# Non-Invasive Quantification of Cerebral Oxygenation in Ischaemic Stroke Using MRI


Matthew Cherukara

Hertford College

University of Oxford

A thesis submitted for the degree of

*Doctor of Philosophy*

Trinity Term 2019

*To the glory of God alone*

# Acknowledgements


## Personal

I would first like to thank my parents, Tom and Diana Cherukara, for their unwavering love and support throughout my whole life, and especially over the last four years, and my sister, Esther, for her encouragement in spite of her own academic workload, and her great sense of humour.

I would like to thank my supervisors, Nic Blockley and Michael Chappell, for allowing me to work on this fascinating project, and for all their help, advice, and camaraderie. I hope that you are able to pick up where I've left off in this project, as I think it really could be something worthwhile and beneficial.

I'd like to thank all my colleagues at the FMRIB Centre and the IBME. I can't name everyone, but I'm especially grateful to Alan Stone, for helping me with data, and analysis, and all kinds of things, when I was starting out, and Caitlin O'Brien, for going through the whole DPhil process at the same time as me, and always being willing to give time and attention to helping me out. I'm also grateful for advice and helpful conversations with Jack Allen, Joe Woods, Hongbae Jeong, Alex Smith, Ben Tendler, Yan Tong, Harry Mason, Tom Kirk, and many others.

I'm extremely thankful for the support and encouragement given by my family at St Ebbe's Church, who are also too numerous to list here. I'd especially like to thank Vaughan Roberts for putting up with me as a housemate for three years, and Richard Brash, Glenn Nesbitt, Ian Fry, Andi Wang, Tuti, Jon Hunt, Steven Firmin, Ashley Wright, Rick and Sarah Lange, Sam and Jordan Brewitt-Taylor, Sam and Katie Aroney, Jordan and Kristin Cardenas, Nathan and Sophie Wallace, Toni Searles, and Phil Legg, for help, advice, and consistent concern for me. I'd also like to thank Luke and Miriam Markham for continued faithfulness in friendship; Audrey Southgate, for support and encouragement; and Mark Wright, for the timely provision of stamps.

Most of all, I'd like to thank LaRae for being amazingly patient, relentlessly encouraging, and indispensably helpful, especially during the last few months as I've been writing this up. I hope to be able to return the favour when you're writing up your own D.Phil.

## Institutional

I would like to thank: the Engineering and Physical Sciences Research Council, and the Medical Research Council, for funding my DPhil; Hertford College and the Guarantors of Brain for funding that enabled me to present my work at three ISMRM annual meetings; the coordinators and administrators of the ONBI CDT; and the support staff at FMRIB and the IBME.

I'd especially like to thank the AVIC radiographers, Peter Manley and Alison Fletcher, for always being willing to help, and for their superhuman patience when things go wrong.

For Chapter 6 in particular, I would like to thank my collaborators at the Oxford Acute Vascular Imaging Centre, especially Professor James Kennedy, Dr. Davide Carone, Dr. George Harston, and the radiographers, Peter Manley and Alison Fletcher, for acquiring and curating the patient data presented here. I would also like to thank all the patients who participated in the AMICI study and their families.

# Abstract

Measurements of oxygen availability can be used to distinguish regions of the brain that are at risk of permanent damage during and after ischaemic stroke. This has the potential to inform management decisions, or monitor progress after treatment.

Differences in the oxygenation of blood (quantified as oxygen extraction fraction [OEF]) cause changes in the rate of reversible transverse relaxation, as measured using asymmetric spin echo (ASE) magnetic resonance imaging (MRI). This relationship is described by the quantitative blood oxygen level dependent (qBOLD) signal model. A streamlined version of the qBOLD model has recently been used to measure OEF in healthy subjects, and to detect changes in related parameters in ischaemic stroke.

In this thesis, a Bayesian framework for inferring on a multiple-compartment qBOLD model is developed, and applied to simulated and *in vivo* data to estimate OEF and other parameters. This model is then used to test potential improvements to the already established streamlined qBOLD framework. The possibility of acquiring data without a fluid-attenuated inversion recovery (FLAIR) sequence is investigated, and the complications that arise when cerebrospinal fluid contributes to the qBOLD signal are described. Then, modifications to the model that account for the effect of diffusion, and of differences in blood vessel distributions, are tested using Monte Carlo simulations, and validated in healthy subjects. These are tested alongside changes to other acquisition parameters that could lead to more efficient data collection.

Finally, the qBOLD model is used to infer OEF in ischaemic stroke patients. It is shown that oxygenation differs between pathological regions, which suggests that this method could be usefully applied to stroke assessment in the clinic.

# Contents

# Works Arising from this Thesis

## Journal Articles

**Matthew T. Cherukara**, Alan J. Stone, Michael A. Chappell, Nicholas P. Blockley. Model-Based Bayesian Inference of Brain Oxygenation Using Quantitative BOLD. *NeuroImage*, 2019. *Accepted.*

## Conference Proceedings

**Matthew T. Cherukara**, Alan J. Stone, Davide Carone, Radim Licenik, George W. J. Harston, James Kennedy, Michael A. Chappell, Nicholas P. Blockley. Bayesian Inference of Brain Oxygenation and Deoxygenated Blood Volume in Acute Stroke using Streamlined Quantitative BOLD. *Proceedings of the 25th Annual Meeting ISMRM*, Honolulu, Hawaii, 2017.

**Matthew T. Cherukara**, Alan J. Stone, Michael A. Chappell, Nicholas P. Blockley. Correcting for the Influence of Cerebrospinal Fluid in Quantification of $R_2'$ and Deoxygenated Blood Volume Using Quantitative BOLD. *Proceedings of the 26th Annual Meeting ISMRM*, Paris, 2018.

**Matthew T. Cherukara**, Michael A. Chappell, Nicholas P. Blockley. Quantifying and Correcting for the Assumptions of the Static Dephasing Regime in Quantitative BOLD. *Proceedings of the 27th Annual Meeting ISMRM*, Montreal, Quebec, 2019.

# List of Figures

# List of Tables

# List of Abbreviations

**1D, 2D, 3D** . . One-, two-, or three-dimensional

**ADC** . . . . . Apparent diffusion coefficient

**ANOVA** . . . . Analysis of variation

**ARD** . . . . . Automatic relevance determination

**ASE** . . . . . Asymmetric spin echo

**ASL** . . . . . Arterial spin labelling

**ATP** . . . . . Adenosine triphosphate

**BF** . . . . . Bayes factor

**BOLD** . . . . . Blood oxygen level dependent (signal)

**CBF** . . . . . Cerebral blood flow

**CBV** . . . . . Cerebral blood volume

**$CMRO_2$** . . . . Rate of cerebral oxygen metabolism

**CNR** . . . . . Contrast-to-noise ratio

**CSF,** $\lambda$ . . . . Cerebrospinal fluid

**CT** . . . . . x-ray Computed tomography

**DBV,** $\zeta$ . . . . Deoxygenated blood volume

**DCE** . . . . . Dynamic contrast enhanced

**dHb** . . . . . Deoxyhaemoglobin

**DSC** . . . . . Dynamic susceptibility contrast

**DWI** . . . . . Diffusion weighted imaging

**EMF** . . . . . Electromotive force

**EPI** . . . . . Echo planar imaging

**FID** . . . . . Free induction decay

**FLAIR** . . . . Fluid attenuated inversion recovery

**fMRI** . . . . . Functional magnetic resonance imaging

**GASE** . . . . . GESEPI asymmetric spin echo

**GESEPI** . . . Gradient echo slice excitation profile imaging

**GESFIDE** . . Gradient echo sampling of free induction decay and echo

**GESSE** . . . . Gradient echo sampling of the spin echo

**GM** . . . . . Grey matter

**GRE** . . . . . Gradient echo

**Hb** . . . . . Haemoglobin

**HMRF** . . . . Hidden Markov random field

**HRF** . . . . . Haemodynamic response function

**ISF** . . . . . Interstitial fluid

**MCMC** . . . . Markov chain Monte Carlo

**MH** . . . . . Metropolis-Hastings

**MLE** . . . . . Maximum likelihood estimation

**MR** . . . . . Magnetic resonance

**MRF** . . . . . Markov random field

**MRI** . . . . . Magnetic resonance imaging

**MTT** . . . . . Mean transit time

**NIHSS** . . . . National Institutes of Health stroke scale

**NLLS** . . . . . Nonlinear least squares

**NMR** . . . . . Nuclear magnetic resonance

**OEF** . . . . . Oxygen extraction fraction

**PCASL** . . . . Pseudo-continuous arterial spin labelling

**PET** . . . . . Positron emission tomography

**PLD** . . . . . Post-labelling delay

**PWI** . . . . . Perfusion weighted imaging

**qBOLD** . . . . Quantitative blood oxygen level dependent

**RBC** . . . . . Red blood cell

**RF** . . . . . Radio frequency

**ROI** . . . . . Region of interest

**rt-PA** . . . . . Recombinant tissue plasminogen activator

**SDR** . . . . . Static dephasing regime

**SE** . . . . . Spin echo

**SNR** . . . . . Signal-to-noise ratio

**SSS** . . . . . Superior sagittal sinus

**TE** . . . . . Echo time

**TI** . . . . . Inversion time

**TR** . . . . . Repetition time

**TRUST** . . . . $T_2$ relaxation under spin tagging

**TTP** . . . . . Time to peak

**VB** . . . . . Variational Bayes

**WM** . . . . . White matter

# 1 Introduction

## 1.1 Motivation

Acute ischaemic stroke caused 2.98 million deaths worldwide in 2015[1] and causes a severe reduction in survivors' quality of life,[2,3] due to disability, depression and anxiety, and recurrent stroke.[4] Treatment by intravenous thrombolysis within the first few hours after stroke onset has been repeatedly demonstrated to improve outcomes,[5,6] although it has been suggested that the presence of an ischaemic 'penumbra' may be predictive of both the effectiveness of treatment, and of final patient outcome.[7]

The ischaemic penumbra is defined as the region in which blood flow is reduced, but cellular metabolic function continues.[8] It therefore ought to be possible to identify the penumbra by quantifying the rate at which oxygen is metabolized throughout the brain, which is related to the proportion of oxygen that is taken up from the blood by the tissue.[9,10] This oxygen extraction fraction (OEF) can be measured using oxygen-15 positron emission tomography (PET).[11] This is considered the 'gold standard' in OEF measurement; however, it requires expensive PET hardware (including a source of $^{15}$O) and so has only limited clinical availability. It is also invasive, requiring the intravenous injection of a radiotracer.

Magnetic resonance imaging (MRI) offers an alternative that is both much more widely available and more versatile than PET. Several MRI modalities are used in ischaemic stroke assessment, which typically detect either cell death (as the result of infarction) or changes in blood flow.[7,12] A more direct measure of oxygen uptake in the brain can be measured using blood oxygen level dependent (BOLD) MRI, which exploits the difference in magnetic susceptibility between deoxyhaemoglobin and brain parenchyma to detect changes in the amount of deoxygenated blood present.[13]

The quantitative BOLD (qBOLD) model relates OEF to measured MRI contrast[14] and has been shown to be a reliable method for measuring OEF in animals[15] and healthy human subjects.[16,17] More recently, it has been used in acute stroke with promising results.[18] There is substantial potential for this progress to be developed further, and for the qBOLD model to be used to help delineate the ischaemic penumbra, and to quantify changes in oxygenation (or metabolism) over time. Given the complex nature of the interaction between deoxygenated blood and the MR signal,[14] and the number of parameters that must be accounted for, simple fitting techniques (such as least squares regression) have some limitations when applied to the qBOLD model.[19]

Bayesian inference is a body of techniques that can be used to estimate parameters from noisy data using complicated, nonlinear models (such as the qBOLD model).[20] The Bayesian framework deals with parameters as distributions of probable values, rather than point estimates, and so it can quantify uncertainty explicitly. It also enables the incorporation of prior knowledge about specific model parameters and the range of values they are expected to take. Bayesian inference has been used to fit models in several MRI modalities[21–23] and could be applied to qBOLD data with similar effectiveness.

### 1.1.1 Aims of the Thesis

The aims of this thesis are as follows: to develop a framework for inferring on physiological parameters using the qBOLD model and MRI data; to use this framework to validate the assumptions that underlie the qBOLD model, with

respect to the brain's anatomy and physiology; to develop practical improvements to the way qBOLD data are acquired; and finally to apply these techniques to data from ischaemic stroke patients, in order to identify the ischaemic penumbra reliably at the earliest time point.

## 1.2 Thesis Outline

The remainder of this thesis consists of the following chapters:

- **Chapter 2** presents theory and background information on MRI and its uses in quantifying brain physiology, ischaemic stroke, and Bayesian inference techniques, and reviews the relevant literature.
- **Chapter 3** describes using the qBOLD model to infer physiological parameters from simulated and *in vivo* data, and compares model-based Bayesian inference with a simpler linear fitting procedure.
- **Chapter 4** deals with the signal contribution from extracellular fluid, and presents several possible mechanisms for correcting for it, comparing these in data from healthy volunteers.
- **Chapter 5** discusses several assumptions made in the qBOLD model, particularly to do with diffusion of water in brain tissue, and uses Monte Carlo simulations and *in vivo* data to develop corrections for the effect of diffusion and other processes.
- **Chapter 6** applies the developed qBOLD model to data from acute ischaemic stroke patients, and compares estimates of OEF and other physiological parameters in clinically relevant regions of interest, demonstrating the utility of the methods developed in previous chapters.
- **Chapter 7** summarizes the work presented in this thesis, and describes several possible avenues for further investigation that could be undertaken, following on from this work.

# 2

# Background and Literature Review

## Contents



This chapter contains the theoretical background of all the topics considered as well as a review of relevant literature. It is structured around four themes: in

Section 2.1, the theoretical background that underpins MRI is described. Section 2.2 presents the motivating clinical problem, acute ischaemic stroke, and explains and reviews the clinical imaging methods currently and historically used in stroke diagnosis. Next (in Section 2.3) follows an explanation of how MRI can be used to detect and quantify changes in physiology, in particular, the blood oxygen level dependent (BOLD) signal. Finally, the Bayesian statistical framework under which much of this work is analysed is explained in Section 2.4.

## 2.1 Magnetic Resonance Imaging

This section sets out the relevant theory of magnetic resonance imaging, which forms the basis of the work described in later chapters. It begins with a description of nuclear magnetic resonance (Section 2.1.1) and its extension to magnetic resonance imaging (Section 2.1.2), which is based on descriptions in relevant textbooks[24–26] and other sources.[27–29] Then several specific acquisition strategies that are relevant to this work are presented and described, based on the literature.[26,30–33]

### 2.1.1 Nuclear Magnetic Resonance

Nucleons have an intrinsic property called spin, which is equivalent (for present purposes) to classical angular momentum. Nuclei with non-zero spin (resulting from having unpaired protons and/or unpaired neutrons) act as spinning charged particles, and therefore have an induced magnetic moment $\boldsymbol{\mu}$.

In the presence of a static external magnetic field $\boldsymbol{B_0}$, the energy of these particles is split into discrete levels; this is known as the Zeeman effect. Since protons have spin-$\frac{1}{2}$, they split into two energy levels, with components parallel and antiparallel to $\boldsymbol{B_0}$. The energy difference between the two levels is

$$\Delta E = \gamma \hbar B_0 \tag{2.1}$$

where $\gamma$ is the proton gyromagnetic ratio (42.6 MHz $\mathrm{T}^{-1}$) and $\hbar$ is the reduced Planck's constant.

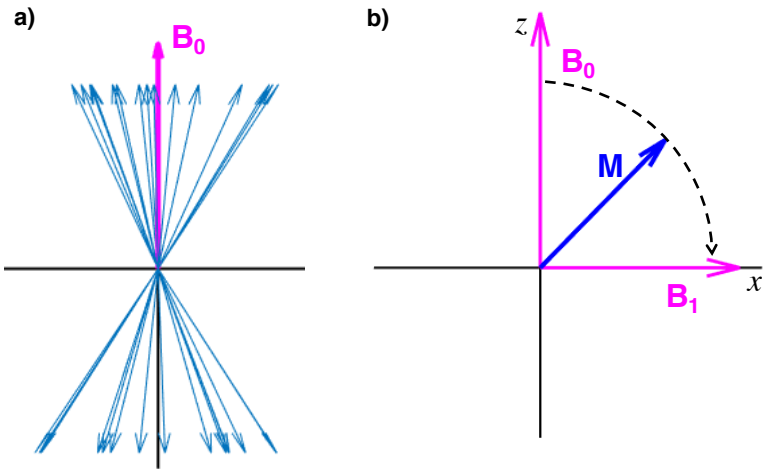


**Figure 2.1: a)** Illustration of the magnetic moments $\mu$ of several spins in the presence of a static field $\boldsymbol{B_0}$. **b)** Illustration of the movement of the net magnetization $\boldsymbol{M}$ with the addition of another field $\boldsymbol{B_1}$. This is shown in the rotating frame, so $\boldsymbol{B_1}$ appears as a static field.

In neither of these energy states does $\boldsymbol{\mu}$ align perfectly with $\boldsymbol{B_0}$, so the static field will exert a torque on the magnetic moment, causing it to precess around $\boldsymbol{B_0}$ with angular velocity $\omega_0$, given by the Larmor equation:

$$\omega_0 = \gamma \boldsymbol{B_0} \tag{2.2}$$

$\omega_0$ is referred to as the Larmor frequency.

At thermal equilibrium, the ratio of populations in each energy state is given by the Boltzmann equation:

$$\frac{N_1}{N_2} = e^{\frac{\Delta E}{kT}} \tag{2.3}$$

where $k$ is Boltzmann's constant. In the case where $T$ is 310 K, and $B_0$ is 3 T, this results in a ratio of 1.0000031. While this seems small, given the abundance of hydrogen nuclei in the human body, this results in a measurable net magnetization $\boldsymbol{M}$. At thermal equilibrium, $\boldsymbol{M}$ has no component perpendicular to $\boldsymbol{B_0}$, since the magnetic moments are distributed at random angles around that direction. Figure 2.1a illustrates such a distribution of spins.

### Excitation

Only the component of $\boldsymbol{M}$ that is perpendicular to $\boldsymbol{B_0}$ can be detected, so it is necessary to perturb the system out of equilibrium in order to conduct measurements. By convention, $\boldsymbol{B_0}$ points in the positive $z$-direction, and the $x$- and $y$-axes are perpendicular to it. Applying a second magnetic field $\boldsymbol{B_1}$ oscillating at the Larmor frequency, perpendicular to $\boldsymbol{B_0}$, causes $\boldsymbol{M}$ to tip towards the transverse ($x$-$y$) plane. In a 'rotating frame' (which rotates around the $z$-axis at the Larmor frequency), $\boldsymbol{B_1}$ is seen as a static field. This is illustrated in Figure 2.1b.

The $\boldsymbol{B_1}$ field is applied as a pulse (referred to as a radio frequency [RF] pulse, since the Larmor frequency of $^1$H and other commonly used nuclei are in the radio frequency range of the electromagnetic spectrum), and the angle through which $\boldsymbol{M}$ is tipped $\alpha$ depends on the amplitude and duration $T$ of the pulse, as well as on $\gamma$:

$$\alpha = \gamma \int_0^T B_1(t)dt \tag{2.4}$$

The transverse component of $\boldsymbol{M}$ experiences a torque from the resulting field (the sum of $\boldsymbol{B_0}$ and $\boldsymbol{B_1}$), and precesses around it at the Larmor frequency. This produces an oscillating magnetic field, which can induce an electromotive force (EMF) in a nearby RF receiver coil. It is this induced EMF, which is proportional to $M_{xy}$, that forms the basis of the nuclear magnetic resonance (NMR) signal, and of MRI.

### Relaxation

After excitation, the system will return to the thermal equilibrium state over time. This is driven by two processes. Spin-lattice relaxation is the means by which the longitudinal magnetization $M_z$ returns to its original magnitude $M_0$. Its rate is described by

$$M_z(t) = M_0(1 - e^{-\frac{t}{T_1}}) \tag{2.5}$$

where $T_1$ is the longitudinal relaxation time constant, and depends on the rate of tumbling and rotation of the water molecules. Spin-spin relaxation, in which

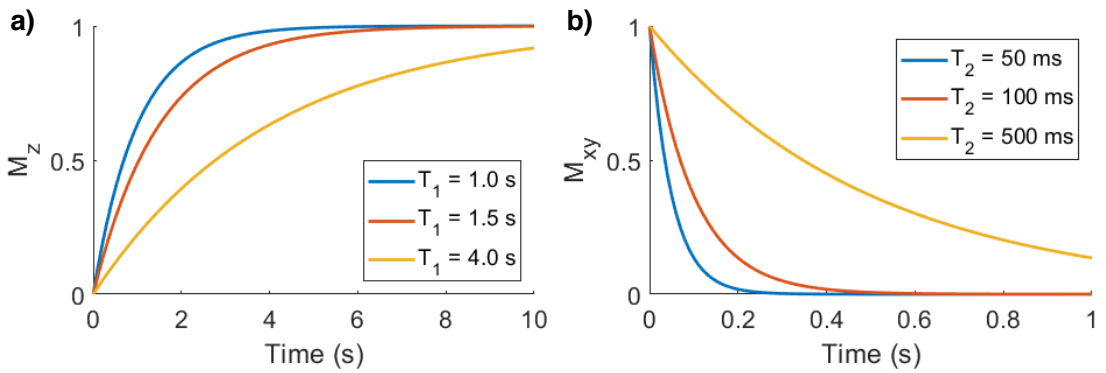


**Figure 2.2:** Examples of **a)** longitudinal ($T_1$) and **b)** transverse ($T_2$) relaxation with different time constants.

protons exchange energy and lose phase coherence, causes a decay in transverse magnetization $M_{xy}$ and is described by

$$M_{xy}(t) = M_0 e^{-\frac{t}{T_2}} \tag{2.6}$$

where $T_2$ is the transverse relaxation time constant, which depends on the local magnetic field $\boldsymbol{B}$ and other tissue properties. Figure 2.2 illustrates the longitudinal and transverse components of $\boldsymbol{M}$ relaxing with different $T_1$ and $T_2$ constants after an $\alpha$=90° excitation RF pulse. Equations 2.5 and 2.6 are the solutions to the Bloch equations in the case of a free induction decay (FID) experiment.

### 2.1.2 Forming an Image

In order to generate an image from the measured EMF, it is necessary to encode the spatial locations of the spins in some way. This can be done through the application of magnetic field gradients $\boldsymbol{G}$, which change the magnitude of $B_z$ through space. This causes the resonant frequency of the spins to vary across the sample, which allows for spatial discrimination of both excitation and readout signals. By applying gradients to $B_z$ across all three directions, it is possible to localize a signal in 3D. Typically, this is done in different ways in each direction. Note that in this section, relaxation and off-resonance effects are neglected.

A slice-selective gradient $G_z$ is applied during excitation, which causes $B_z$ (and hence the Larmor frequency) to vary along the $z$-axis. If the RF pulse is constrained

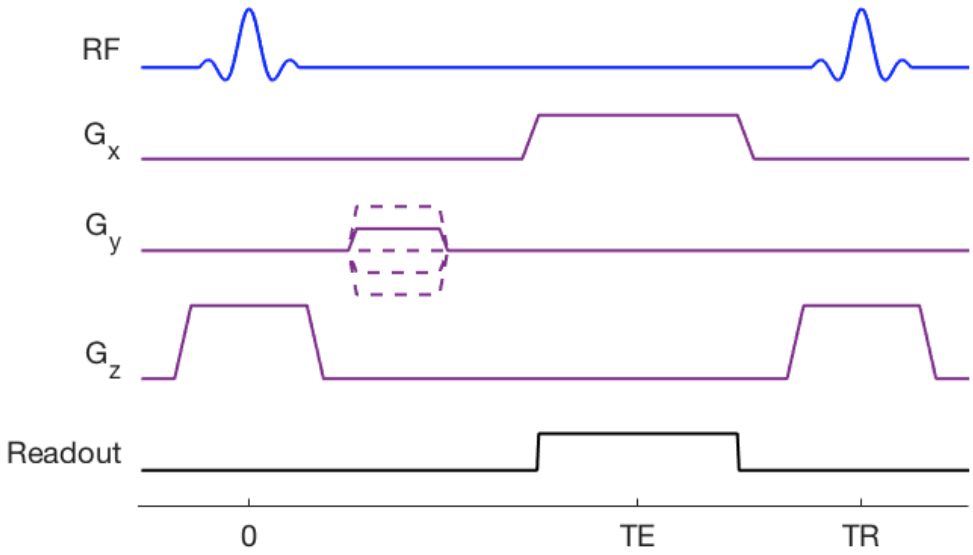


**Figure 2.3:** Example MRI pulse sequence. A slice-selective $G_z$ gradient is applied at the same time as a 90° excitation RF pulse, which tips $\boldsymbol{M}$ into the transverse plane. A $G_y$ phase-encoding gradient blip causes all the spins along a line in the $y$-axis to accrue a fixed amount of phase. Then a readout $G_x$ gradient is applied to vary phase accrual along the $x$-direction, while data is read out at time $TE$. The sequence then repeats after time $TR$, with the amplitude of $G_y$ changed in each repetition, to raster along the $y$-direction.

to a small range of frequencies, only spins within a certain $z$-direction slice (or slab) will be excited. The thickness of the slice depends on the bandwidth of the RF pulse and the strength of $G_z$.

Gradients $G_x$ and $G_y$ change the rate at which phase is accrued by spins throughout the $x$-$y$ plane. In a typical MRI experiment (such as the one exemplified in Figure 2.3), a $y$-gradient is applied briefly and then switched off, after excitation, to introduce a phase gradient in the $y$-direction (this is referred to as phase encoding). An $x$-gradient is applied throughout the readout, so that the Larmor frequency varies linearly along the $x$-axis for each line that is read out (this is referred to as frequency encoding). A single 2D readout can therefore be decoded to assign $x$ and $y$ co-ordinates to each measurement.

### The $k$-space Formalism

The relationship between frequency and phase encoding, and spatial distribution of sources, can be simplified through the use of the $k$-space formalism. The signal

measured from a 2D slice during an MRI experiment is given by

$$S(t) = \int\int \rho(\boldsymbol{r}) e^{-i\phi(\boldsymbol{r},t)} dxdy \tag{2.7}$$

where $\rho$ is the proton density, and $\phi(\boldsymbol{r}, t)$ is the accumulated phase at spatial location $\boldsymbol{r} = [x, y]$ and time $t$, given by

$$\phi(\boldsymbol{r}, t) = \gamma \int_0^t \boldsymbol{G}(\tau) \cdot \boldsymbol{r} dt \tag{2.8}$$

By substituting $\boldsymbol{k} = \gamma \int \boldsymbol{G} dt$ (which is based on the $0^{\text{th}}$ order moment of the gradient), Equation 2.8 can be simplified to

$$S(\boldsymbol{k}) \propto \int\int \rho(\boldsymbol{r}) e^{-i\boldsymbol{r}\cdot\boldsymbol{k}(t)} dxdy \tag{2.9}$$

From this, it can be seen that the measured MRI signal $S(\boldsymbol{k})$ is the Fourier Transform of the proton density map $\rho(\boldsymbol{r})$ (or equivalently, of transverse magnetization $M_{xy}$). The aim of an MRI acquisition is therefore to sample $k$-space as efficiently as possible. Procedures for doing so are described in Section 2.1.4.

A number of important imaging parameters can be considered in terms of their $k$-space equivalents. The large-scale variations across an image, with low spatial frequency, are encoded near the centre of $k$-space, whereas high spatial frequency information is at the periphery. In-plane image resolution is determined by the extent of $k$-space sampled, and field of view is the inverse of the distance in $k$-space between samples (this is the Nyquist sampling limit).

Applying gradients $G_x$ and $G_y$ is equivalent to moving along a trajectory through 2D $k$-space, so pulse sequences can be designed to sample the greatest extent of $k$-space evenly and in the most efficient manner. In order to use the Fast Fourier Transform (an algorithm which calculates the Fourier Transform of discrete data) to convert rapidly from $k$-space to image space, it is necessary that $k$-space samples fall on a rectangular Cartesian grid.

#### Imaging Artefacts

Using $\boldsymbol{B_1}$ gradients to localize spins is only possible in a homogeneous $\boldsymbol{B_0}$ field. In general, at higher field strengths it becomes more difficult to create a homogeneous static field across a head-sized area, although this can be achieved through optimally designing the coil distribution in the magnet, and through the use of mechanical shims. These are a set of small ferromagnets that are distributed around the bore to maximise homogeneity.

When a living subject is placed in the scanner, the interfaces between tissue types (especially next to large spaces of air such as the sinuses) create inhomogeneities in $\boldsymbol{B_0}$ which affect local Larmor frequencies, leading to two typical imaging artefacts.[26]

Image distortion occurs when macroscopic inhomogeneities (i.e. those on a scale larger than an imaging voxel) cause additional field gradients which sum with the applied gradients $G_x$ and $G_y$. This leads to spins being encoded in the wrong spatial position. Depending on the direction of the additional gradient, this can either cause shifting of signal along the readout direction, or 'shearing' perpendicular to it.

Echo shifting occurs when additional gradients mean that the centre of $k$-space (where the total area under the gradients is zero) does not occur at the point where the area under the applied gradients (only) is zero. This reduces signal (since a proportion of spins in the voxel are not covered by the readout at all) or causes 'dropout' in the extreme case when the centre of $k$-space is shifted by an amount greater than the length of the voxel.

### 2.1.3 Contrast Manipulation

By applying specific gradients and RF pulses, it is possible to manipulate the type of contrast in an MR image. Several pertinent strategies for doing so are outlined here.

#### Gradent Echo and Spin Echo

In a gradient echo (GRE) sequence, such as the one shown in Figure 2.3, a single RF pulse generates a free induction decay (FID) in which the net transverse magnetization rapidly decreases. This is due to the fact that imaging voxels

contain variations in the magnetic field on the microscopic (sub-voxel) scale. These differences cause spins within the voxel to lose phase coherence with one another. The time constant which governs this process is $T_2'$. The relaxation rate measured in FID is the sum of this effect, and the spin-spin interactions described above, such that

$$\frac{1}{T_2^*} = \frac{1}{T_2} + \frac{1}{T_2'} = R_2^* = R_2 + R_2' \tag{2.10}$$

where the transverse relaxation rates $R_2$ (and their longitudinal counterpart $R_1$) are the inverse of the relaxation time $T_2$. Given the additive relation of $R_2$ and $R_2'$, it is often simpler to describe transverse relaxation with rates rather than times.

Because microscopic field variations do not change over time, it is possible to reverse their effect by applying a second RF pulse at time $TE/2$ after the excitation pulse, now chosen to induce a flip angle $\alpha$=180°. Having had their instantaneous phase-state 'flipped', spins will continue to accrue phase at the same rate; so, if the magnetization is read out at time $TE$, the spins will be in phase, and the effects of local microscopic inhomogeneities will have been reversed. This is referred to as a spin echo (SE) sequence,[35] and is illustrated in Figure 2.4.

By tuning the timings $TR$ and $TE$ of an SE (or GRE) protocol, it is possible to manipulate the relative weightings of longitudinal and transverse relaxation ($T_1$ and $T_2$ effects, respectively) and so produce images with a desired contrast. Using a long $TR$ minimises the effect of $T_1$ differences, while using a short $TE$ minimises $T_2$ effects. So an imaging sequence with long $TR$ and short $TE$ will have contrast that is weighted by proton density alone; a sequence with short $TR$ and short $TE$ will have $T_1$-weighted contrast; and a sequence with long $TR$ and long $TE$ will have a $T_2$-weighted contrast. (Short $TR$ and long $TE$ does not produce a useful contrast in most applications.)

It is possible to measure $T_2$ (or equivalently, $R_2$) by acquiring a series of SE images with different $TE$[35] and fitting an exponential decay function of the form

$$S(TE) = Me^{-R_2 \cdot TE} \tag{2.11}$$

where $M$ is the steady-state magnetization.

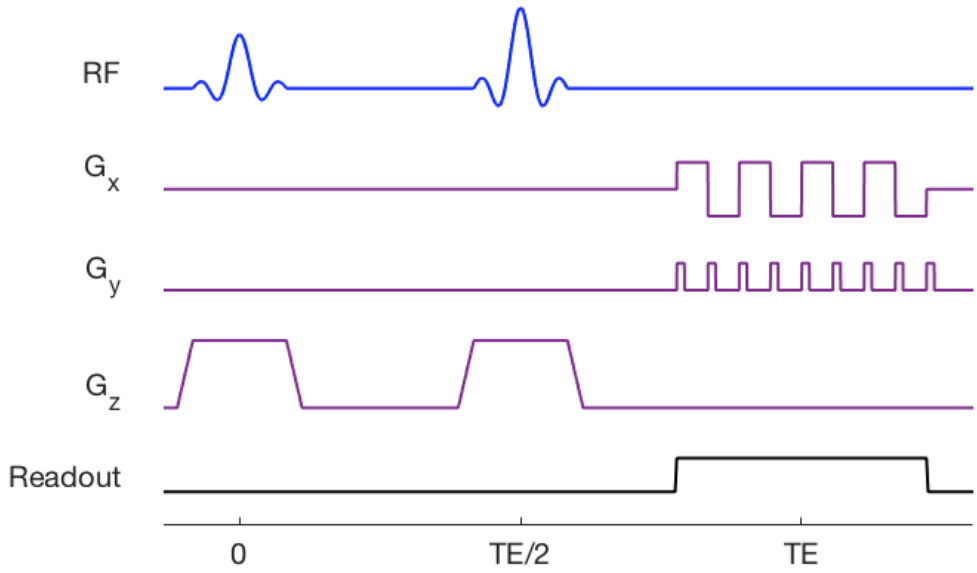


**Figure 2.4:** An EPI spin echo sequence. A 90° excitation pulse at time 0 is followed by a 180° inversion pulse at $TE/2$, then the signal is read out at $TE$. The EPI readout is able to cover all of $k$-space in a single shot by acquiring lines of points up and down the $x$-direction, with $G_y$ blips that move across the $y$-direction.

### GESSE

It is often desirable to measure $R_2'$ simultaneously with $R_2$. This can be done using gradient echo sampling of the spin echo (GESSE), which was proposed by Yablonskiy & Haacke[36] as a development of the gradient echo sampling of FID and echo (GESFIDE) sequence by Ma & Werhli.[37]

Under GESFIDE, an SE sequence with a 90° excitation pulse followed by a 180° refocussing pulse is played out, and two sets of gradient echo images are read out on either side of the refocussing pulse. These can then be fit to a model of both $R_2^*$ (the rate of signal decay during the dephasing stage, before the inversion) and $R_2^-$ (the rate of signal recovery in the rephasing stage, between the inversion and the spin echo), where $R_2^- = R_2 - R_2'$. These can then be used to calculate $R_2$ and $R_2'$. A major disadvantage of this approach is that it relies on the assumption that there are no inhomogeneities in $B_0$ and that the refocussing pulse is applied without slice profile imperfections.[36]

By contrast, the GESSE sequence acquires sets of gradient echoes in the rephasing stage, after the refocussing pulse, and also in the second dephasing stage, after the

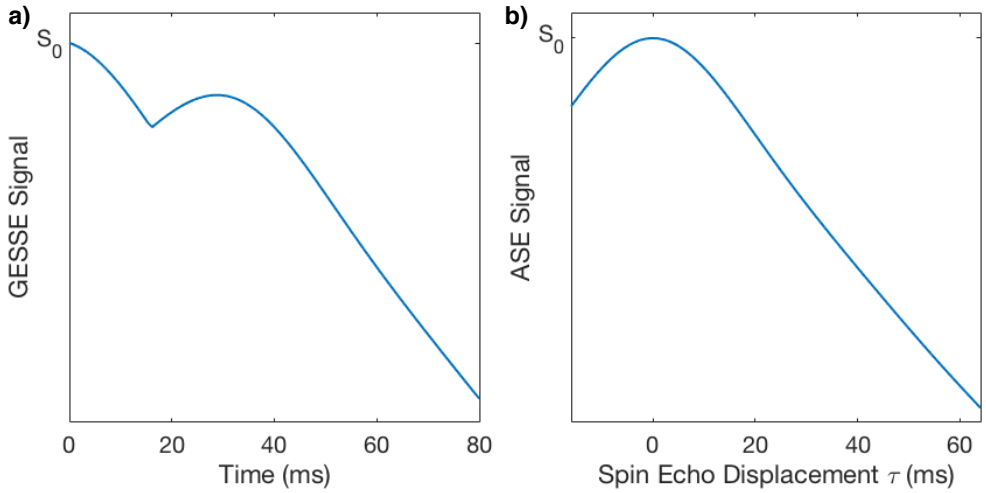


**Figure 2.5:** Example signal curves for **a)** GESSE and **b)** ASE sequences, simulated using the same parameters, except that the GESSE data uses $TE$=32ms, and $t$ from 0 to 80ms, and the ASE data uses $TE$=64ms, and $\tau$ from -16 to 64ms.

spin echo. $R_2$ and $R_2'$ can then be fitted, as before, from the resulting signal. An example of the GESSE signal as a function of time is shown in Figure 2.5a.

### ASE

The rate of reversible transverse relaxation $R_2'$ contains information about the local magnetic susceptibility of a voxel, so a sequence which is sensitive to differences in $R_2'$ can be useful. One way to achieve $R_2'$ contrast in an image is through an asymmetric spin echo (ASE) sequence.[32] This is similar to SE, except that the timing of the 180° refocussing pulse is shifted relative to readout time. This means that the spins will be back in phase at an effective echo time ($TE + \tau$), where the refocussing pulse is shifted by $\tau/2$. If the signal is read out at $TE$, it will be

$$S(\tau) = S_0 \cdot e^{-R_2' \cdot \tau} \cdot e^{-R_2 \cdot TE} \tag{2.12}$$

where $S_0$ is the SE signal (i.e. the signal measured when $\tau = 0$). This has the effect of introducing a controlled amount of $R_2'$ decay into the SE signal. An example of the ASE signal as a function of $\tau$ is shown in Figure 2.5b.

**FLAIR**

Voxels in the brain often do not contain only a single tissue type, so it may be necessary to remove the signal contribution from a particular tissue compartment. When different compartments have significant differences in their $T_1$, this can be done using a fluid-attenuated inversion recovery (FLAIR) sequence.[33] In this sequence, a 180° inversion pulse is applied at time $t = 0$ and the imaging experiment is carried out at time $TI$ after that. The signal is then allowed to recover further, and the process is repeated at time TR. This is illustrated in Figure 2.6. The FLAIR preparation changes the steady state magnetization of each compartment, so Equation 2.5 becomes

$$m_x = 1 - \left(2 - e^{-\frac{TR-TI}{T_1^x}}\right) \cdot e^{-\frac{TI}{T_1^x}} \tag{2.13}$$

which reduces to the non-FLAIR prepared case (Equation 2.36) when $TI = 0$. As well as completely removing the signal from one compartment, FLAIR also has the negative effect of reducing the magnetization of the other compartments, hence the signal measured from them.

$TI$ is chosen so that at $TI$, the signal from the CSF compartment is zero. Optimal $TI$ is found by rearranging Equation 2.13:[38]

$$TI = T_1 \left(\ln(2) - \ln(1 + e^{-\frac{TR}{T_1}})\right) \tag{2.14}$$

### 2.1.4 Acquisition Strategies

When planning an MRI experiment, it is important to consider both the manner in which $k$-space is traversed and sampled during readout, and the way in which RF pulses are used to control the contrast that can be observed in the resulting image. This section describes relevant strategies used in both of these considerations.

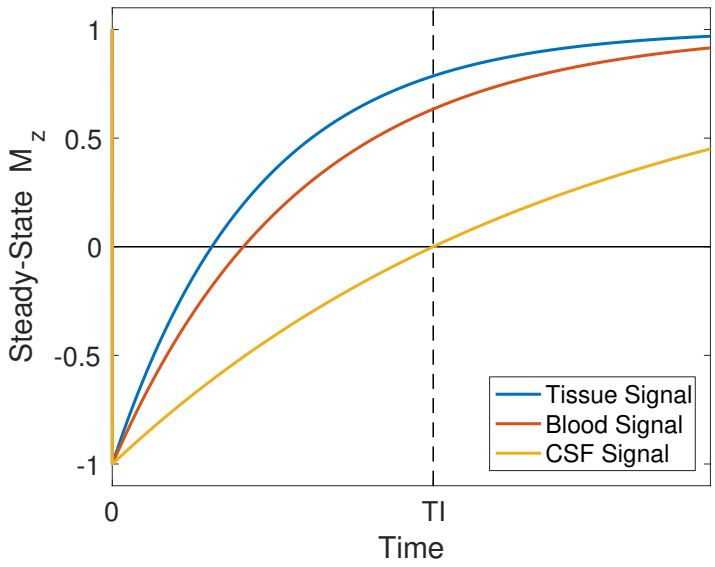


**Figure 2.6:** Simulated signal evolution with FLAIR preparation. TI is chosen so that the signal from the CSF compartment is zero when the ASE excitation pulse is applied. Note that the tissue signal has not fully recovered at TI, which leads to reduced SNR.

### EPI

In a conventional MRI pulse sequence (such as the one shown in Figure 2.3), one line of $k$-space is read out after each RF excitation. Building up a complete 2D slice therefore requires a number of repetitions equal to the matrix size (number of lines) in that direction, which typically ranges between 64 and 256. A much more time-efficient approach would be to sample all of $k$-space after a single excitation.

Echo planar imaging (EPI) was developed by Mansfield in 1977,[31] and it is one such single-shot 2D acquisition method. After excitation, $G_x$ is switched from positive to negative to read up and down the $k_x$ direction. Whenever it reaches the furthest point in $k_x$, $G_y$ is switched on in a short 'blip' to move across the $k_y$ direction. Figure 2.7 shows a typical 2D EPI trajectory.

Although EPI is much faster than a conventional MRI readout, it does have some disadvantages. Off-resonance effects lead to an accrual of phase error, particularly in the blip direction $k_y$, which in turn leads to apparent stretching or compression of the resulting image in the $y$ direction. This can be corrected for by acquiring

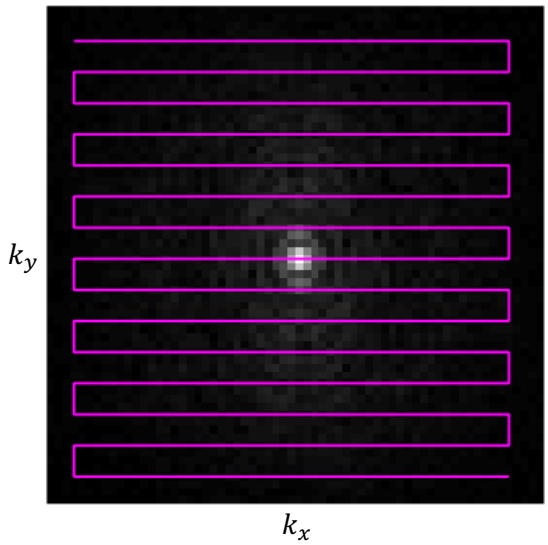


**Figure 2.7:** An example gradient trajectory of a 2D EPI readout sequence. Beginning in a far corner of $k$-space, the trajectory moves along the $k_x$ direction through the application of a continuous $G_x$. Once it reaches the far end, a short 'blip' in $G_y$ moves the trajectory down $k_y$, then $G_x$ is reversed and the readout moves back along the $k_x$ direction the opposite way. This is repeated until all of $k$-space is covered.

two images, one in which the trajectory begins in negative $k_y$ and blips 'up', and another which begins in positive $k_y$ and blips 'down'.

Additionally, since signal decay continues to occur while the readout trajectory is being traversed, $k$-space points that are read out later will have an additional $T_2^*$ weighting. This too can be corrected for in the post-processing stage.[24]

### GESEPI

Images with high $T_2^*$ weighting can also suffer from dropout artefacts due to macroscopic inhomogeneities in the $z$-component of $\boldsymbol{B_0}$. When using a slice-selective gradient $G_z$ to localize readout, macroscopic inhomogeneities cause phase dispersion in the $z$-direction that can lead to signal losses. A solution to this problem is found in the gradient echo slice excitation profile imaging (GESEPI) technique.[34] In this method, a slice-selective gradient is applied while the excitation RF pulse is being transmitted as normal, but $G_z$ is also used to phase-encode the $z$-direction over multiple repetitions.

By partitioning a 3D 'slab' into several thin slices with different gradient offsets,

and integrating over them by averaging them in 3D $k$-space, the effects of $z$-direction inhomogeneities can be removed, since it can be assumed that the differences in susceptibility due to these sources will not change significantly through the depth of a single slice (i.e. they are macroscopic fields, unlike the microscopic susceptibility differences which give rise to $T_2$- and $T_2^*$-weighted contrast).

Since the RF excitation pulse is not perfectly slice-specific (it does not form a perfect top-hat function in the $z$-direction), but also excites spins that are outside the slice, it is necessary to oversample with GESEPI slices in the $z$-direction to avoid the signal from these spins being aliased back into the image. This further increases the GESEPI scan duration (compared to a slice-selective 2D acquisition), which is proportional to the number of slices acquired per slab.

## 2.2 Acute Ischaemic Stroke

This section presents a description of acute ischaemic stroke and the typical treatments and procedures associated with stroke in the clinic (Section 2.2.1). It also provides an overview of the medical imaging techniques used to diagnose and assess ischaemic stroke (Section 2.2.2). This section is based on work presented in several clinical review papers[8,12,39,40] and other sources.[10,41]

### 2.2.1 Stroke

Stroke occurs when blood supply to part of the brain is restricted, which can be the result of either a bleed (haemorrhagic stroke), or a blockage in an artery (ischaemic stroke).

Haemorrhage, which can occur either in the brain tissue itself (intracerebral haemorrhage) or between the membranes that envelope the brain (subarachnoid haemorrhage), has an extremely high mortality: approximately 25% within 24 hours and up to 50% at 30 days.[42–44] It is often the result of small vessel disease resulting from hypertension. Treatment generally involves managing blood pressure and coagulation but can require surgery.[45]

Ischaemic stroke is much more common, accounting for around 75% of all strokes,[42,46–48] although with a lower mortality. In 2015, 2.98 million deaths were attributed to ischaemic stroke, compared with 3.35 million haemorrhagic strokes,[1] despite the large differences in incidence.

### Ischaemic Stroke: Causes and Classification

Ischaemic stroke occurs as the result of occlusion of an artery supplying part of the brain, typically in the middle cerebral artery or the internal carotid artery.[7,12] Adams and colleagues[49] defined three common subtypes of ischaemic stroke: large artery atherosclerosis (in which a major brain or branch cortical artery is occluded), cardioembolism (in which an embolus originating in the heart travels to the brain and occludes a particular artery), and lacune infarction (in which a small artery is occluded, resulting in lacunar syndrome but not any loss of function in the cortex or cerebellum). A range of other aetiologies is possible, many of which are not fully understood.[40]

Stroke severity is typically assessed using the National Institutes of Health Stroke Scale (NIHSS),[50] which consists of a series of eleven tests that are administered to patients upon presentation. The tests cover cognition, memory, sensory and motor skills, vision and attention, and speech and language. Points are added for poor performance in each category, with a higher total score indicating a more severe stroke. An NIHSS score of $\leq$4 indicates minor stroke, and $\geq$16 (up to the maximum of 42) indicates severe stroke. NIHSS score has been shown to be highly consistent across observers,[51] and has been used extensively as a criterion for selecting treatment.[52]

The final outcome of a stroke can be assessed using the modified Rankin Scale,[53,54] which categorizes disability on a discrete scale from 0–6, with 0 indicating no symptoms of disability, up to 6 corresponding to death. In the literature, the modified Rankin Scale is often used to quantify the effectiveness of a particular intervention by categorizing patients into those with 'good' outcomes (typically with a score $\leq$2) and those with 'bad' outcomes (with a score $\geq$ 3).[5,7,55,56]

### Physiological Effects

Brain function is directly related to the availability of oxygen. Since the brain has no capacity for storing oxygen, it must be delivered to each neuron directly through the vascular network. Oxygen diffuses from the blood into the surrounding tissue, so the concentration of oxygen in the plasma must be high enough to create a concentration gradient that will cause diffusion through a series of cells. This ensures that those neurons which are not directly adjacent to a blood vessel to still recieve enough oxygen to function. As dissolved oxygen diffuses out of the vascular system, more oxygen molecules dissociate from haemoglobin into the plasma. The amount of oxygen bound to haemoglobin, relative to its total possible capacity, is the oxygen saturation $SO_2$. The difference between arterial oxygen saturation $SaO_2$ and venous oxygen saturation $SvO_2$ is the oxygen extraction fraction (OEF).[9,10] In healthy adults, whole brain OEF is around 40%.[11,57–59]

Oxygen availability can also be quantified in terms of the rate of cerebral blood flow (CBF), which is measured in mL of blood per 100 g of tissue per minute. Ischaemia, which causes either a reduction or total arrest of blood flow, starves the affected part of the brain of oxygen and prevents normal function. Astrup and colleagues[8] showed that two important thresholds of CBF exist, which are of particular interest, and are illustrated in Figure 2.8.

When CBF falls below approximately 35-40% of its baseline, neurons are no longer able to restore their membrane potentials to their resting levels after firing, so neuronal activity fails.[10,60,61] Once CBF goes below approximately 20% of its baseline, neurons are no longer able to maintain the correct balance of ions on either side of their cell membranes. As ions diffuse across the membrane, the osmotic pressure over it increases, until the influx of water into the cell causes membrane failure and cell death.

Membrane failure is marked by an increase in diffusion of water (since molecules are no longer impeded by cell structures), which can be quantified in terms of the apparent diffusion coefficient (ADC). Electrical failure is accompanied by a decrease in the rate of cerebral metabolism of oxygen ($CMRO_2$). As CBF decreases,

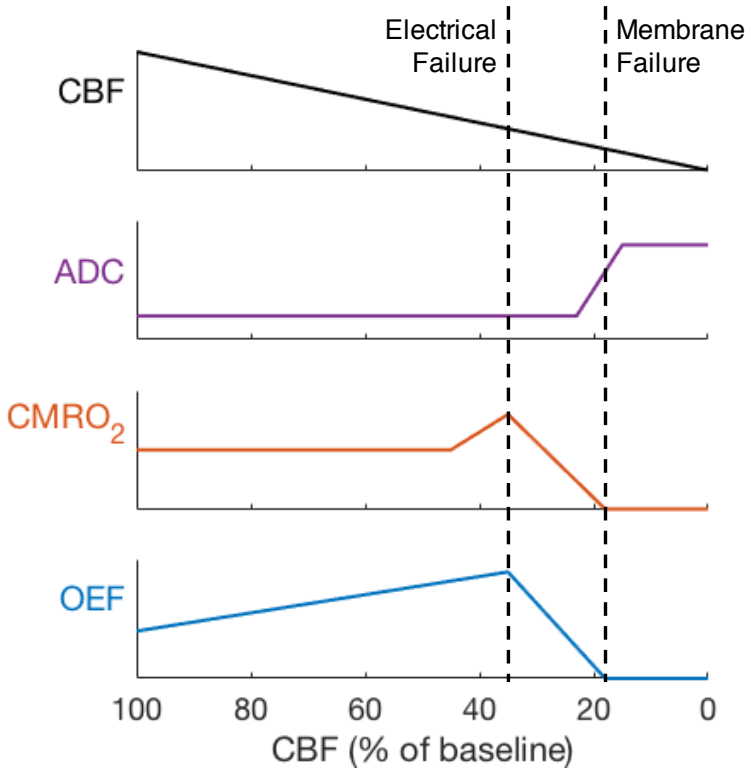


**Figure 2.8:** Illustration of thresholds of electrical and membrane failure as a function of cerebral blood flow (first row). **Second row:** Apparent diffusion coefficient (ADC) increases at the membrane failure threshold. **Third row:** Rate of cerebral oxygen metabolism ($CMRO_2$) decreases once the electrical failure threshold has been reached. **Fourth row:** Oxygen extraction fraction (OEF) increases as CBF decreases, then decreases sharply when metabolism ceases.

but before it reaches the electrical failure threshold, more oxygen dissociates from the haemoglobin to which it is bound, in order to maintain the concentration gradient required to cause diffusion to the most distant cells. This corresponds to an increase in local OEF.

In healthy adults, CBF in grey matter is uniform, and typically on the order of 50-55 mL/100g/min.[62–64] Fick's Principle, based on mass conservation of oxygen, relates these parameters to $CMRO_2$:[62]

$$CMRO_2 = c \cdot [Hb] \cdot CBF \cdot OEF \tag{2.15}$$

where [Hb] is haemoglobin concentration and $c$ is the oxygen carrying capacity of haemoglobin.[65]

### Ischaemic Regions

Ischaemic stroke causes variation in CBF across the brain, which enables definition of clinically relevant regions of interest, based approximately on the thresholds given in Figure 2.8. The region of lowest CBF, where membrane failure has occurred, is the ischaemic core.[12] Here, lack of oxygen has led to cell death, the tissue is irrecoverably lost, and permanent neurological deficit may result.

Often, nearby tissue may be less severely affected. In regions surrounding the core, CBF may be lowered, due to the occlusion of one particular vessel, but it remains high enough that metabolism can continue and neurons can remain intact, even if they do not have sufficient oxygen to work normally. This region is known as the ischaemic penumbra,[8,10,66] and it contains tissue that could be recovered if flow is restored to normal. The penumbral threshold can be extended to higher CBFs, such as those around 60% of baseline, at which protein synthesis is inhibited.[67] In this case, failure to restore adequate blood flow quickly (within a matter of hours) will lead to cell death, and the effective expansion of the infarct core. Oligemia (reduction in CBF) may also occur beyond the penumbra, but this remains benign so long as CBF does not fall below the aforementioned thresholds.[12]

### Treatment

Thrombolysis with recombinant tissue plasminogen activator (rt-PA) is the recommended treatment in most ischaemic stroke cases,[6,68] but it is most effective when administered within 6 hours of stroke onset.[5] It was first trialled in 1995, and it works by releasing bound plasmin from plasminogen, which in turn will degrade the fibrin in the clot causing the occlusion.[55] rt-PA causes increased vascular permeability and can lead to excessive bleeding, so it must not be used in the treatment of haemorrhagic stroke.[6] It is therefore essential to diagnose the type of stroke correctly before treatment.

Recently, endovascular mechanical thrombectomy has been tested as a surgical means for removing clots much more quickly than thrombolysis, and without the risks

associated with rt-PA.[69,70] Reperfusion of affected tissue is almost instantaneous in this case and leads to faster neurological recovery.

### 2.2.2 Medical Imaging

Diagnosis and treatment of acute ischaemic stroke relies on the use of medical imaging to locate and delineate the ischaemic core from surrounding tissue. Identifying the penumbra can also improve outcomes by opening up further treatment options.[10,71]

X-ray computed tomography (CT) scanning is by far the most common, and recommended, tool for imaging stroke.[68] It has the advantage of being extremely fast, widely available, and presents only minimal risk to patients in terms of exposure to ionising radiation.[72]

#### MR Imaging of Acute Stroke

MRI has been used in the assessment of acute stroke since the 1980s,[73–75] at which time proton-density and $T_2$-weighted maps were used to determine the presence of ischaemia and the extent of the regions of infarcted tissue. These data were qualitative, and could only reproduce maps of the ischaemic core that were more readily obtainable using CT. As MRI technology has improved, so has the quality and reliability of these kinds of images. As early as 1991, Bryan and colleagues[76] reported that $T_2$-weighted MR images provided a higher contrast-to-noise ratio (CNR) between healthy and ischaemic tissue than CT images. This has been confirmed by more recent comparisons.[77] MRI measurements have been shown to be increasingly reliable when combined with more traditional methods of stroke assessment.[78,79]

However, MRI is limited by the fact that patients must be screened for magnetically unsafe implants before they can be scanned. Such implants are more common in the elderly, who are at higher risk of acute stroke than the general population, and, depending on the severity of the stroke, patients may not be able to respond to screening questions.

Diffusion-weighted imaging (DWI) can be used to identify the changes in apparent diffusion coefficient (ADC) that define the ischaemic core.[56,80,81] However, since its inception there has been disagreement over the validity of diffusion as a biomarker in ischaemia.[39,41]

In the very acute stage, ion imbalances across the membrane lead to an influx of water into the cells (cytotoxic edema), increasing the relative proportion of intracellular water. This causes a decrease in ADC, since intracellular water is less free to diffuse than extracellular water.[82] This change is reversible, if oxygen supply (blood flow) is restored quickly enough.[83] In the 'sub-acute' stage, cell death leads to an increase in ADC (since cell membranes and structures no longer impede diffusion),[39] although the timescale of this is not certain and has been suggested as between 24 hours[84] and 4 days.[85]

**Imaging Perfusion**

It is also possible to measure CBF directly using MRI, in the form of perfusion-weighted imaging (PWI).[86] In this modality, intravenous injection of a bolus of contrast agent (containing gadolinium) causes a change in local susceptibility which can be measured as a decrease in $T_2^*$ (this is known as Dynamic Susceptibility Contrast [DSC] MRI). Rapid acquisition of EPI images can then be used to calculate the mean transit time (MTT) and cerebral blood volume (CBV) of each voxel.[56,87] MTT alone could be a useful marker of occlusion, or of tissue at risk of infarction, but it can also be combined with CBV to calculate CBF.[88]

Additionally, gadolinium causes a local change in $T_1$, the measurement of which is known as Dynamic Contrast Enhanced (DCE) MRI. Typically, blood flow through a voxel is too fast to allow for reliable measurement of $T_1$ changes; however, this technique can be used to monitor breakdown of the blood-brain barrier, which occurs in some cases around 24 hours after acute stroke onset.[89,90]

While PWI using Gd-based contrast agents is useful in this regard, it is not without risks, as gadolinium has been shown to cause anaphylactic reactions in some patients.[91] It has been recommended that patients on dialysis, or with significant

loss of renal function, not be given Gd-based contrast agents due to the risk of nephrogenic systemic fibrosis,[92–94] even though renal dysfunction significantly increases risk of stroke.[44,95] More recently, it has been shown that gadolinium remains permanently deposited in the brain, even in subjects with fully-functioning kidneys.[96]

### Diffusion-Perfusion Mismatch

A useful advancement to using DWI (which is not always discriminatory of ischaemia) and PWI separately is to combine them and identify regions in which one of these is abnormal but not the other. This method was first used by Neumann-Haefelin *et al.*[97] and exploits the fact that, during the first few hours after onset, the DWI lesion (in which membrane failure has occurred) is often much smaller than the PWI lesion (the entire area of reduced CBF). It was shown that the diffusion-perfusion mismatch (at presentation) was predictive of later growth of the infarct lesion.[98,99]

In the early 2000s, it was pointed out that visual identification of the mismatch area was an unreliable biomarker,[100] although it continued as a clinically useful means of stratifying acute stroke patients in the absence of a better gold standard.[101] The choice of perfusion parameter has also been debated. The earliest studies favoured time-to-peak (TTP),[97] although more quantitative, model-based measures such as MTT and CBF later became preferable.[78,79]

A large ($N = 74$) prospective study conducted by Albers and colleagues[102] between 2001 and 2005 identified diffusion-perfusion mismatches in 54% of acute stroke patients, using TTP perfusion imaging, and the presence of such a mismatch to be a predictor of how effective reperfusion using rt-PA would be: for patients without a mismatch, administration of rt-PA within 6 hours of symptom onset did not, in aggregate, improve their outcome on the modified Rankin Scale; patients with a mismatch had a 'favourable clinical response' after rt-PA in 67% of cases (compared with only 19% 'favourable clinical responses' without reperfusion). This suggests that identifying the ischaemic penumbra (which may be assumed to be synonymous with the DWI-PWI mismatch region) could be valuable in stratifying patients for treatment.

A major limitation of using the mismatch as a diagnostic standard is the variation between studies and centres on the definition of the mismatch region. Yoo *et al.*[79] have suggested that the absolute size of the DWI lesion is a better predictor of final outcome than NIHSS score or mismatch, and that the absolute size of the MTT perfusion lesion could be useful as a predictor of the effectiveness of reperfusion.

### Other MR Applications in Stroke Imaging

Recent advances in computer vision and machine learning techniques have also been applied to stroke imaging. Huang, Shen, and Duong used an artificial neural network to predict tissue fate after middle cerebral artery occlusion in rats, using measurements of CBF, ADC, and $T_2$, validated by histology. They found that this combined machine learning approach performed better than one or two measures alone.[103] Mouridsen and colleagues used level-sets boundary-defining techniques to outline lesions in PWI data automatically with good agreement with manual delineation by experts.[104] Stier *et al.* applied convolutional neural networks to multi-parametric PWI data to predict tissue fates using regional information, and they found this to be much more accurate than single-voxel techniques, although a direct comparison with manual prediction by an expert was not included.[105]

### Physiological Imaging

DWI measures the effects of infarction once it has already occurred, and for the most part it can only delineate unsalvageable tissue. PWI measures blood flow, which is indicative of risk of infarction, but cannot predict outcome directly. Increasingly complex analyses of these data are useful, but they generally do not perform better than expert readers. Clearly, there is a need for direct measurement of physiological processes, in particular, oxygen metabolism (quantified as $CMRO_2$) or uptake.

The gold standard for such measurements is positron emission tomography (PET) using oxygen-15,[106–108] although this is not widely available and therefore of limited application. Recently, MR-based physiological measurements have been applied to acute stroke,[109] but these require further development. The possibility of using MRI to measure physiological parameters directly is described in the following section.

## 2.3 MR Physiology

The magnetic properties of biologically important molecules mean that they can be used as endogenous contrast agents to probe physiology. This section describes the BOLD signal, its origin, and how it can be used in MRI (Subsection 2.3.1), as well as models that describe it quantitatively (Subsection 2.3.2). Then, other quantitative and physiological MRI modalities are described, including Arterial Spin Labelling (ASL) and $T_2$ Relaxation Under Spin Tagging (TRUST), along with the ways in which these methods complement quantitative BOLD (Subsection 2.3.6). This section draws from review papers,[17,110–113] textbooks,[114] and other sources.[59,115–118]

### 2.3.1 The BOLD Signal

The Blood Oxygen Level Dependent (BOLD) signal was first discovered in 1990 by Ogawa and colleagues[13,119–121] as a change in $T_2$ that was correlated with neural stimulation. Since then, it has been the mainstay of functional MRI (fMRI[122]), in which the coupling between neuronal activity and the brain's vascular system is exploited to generate probabilistic maps of brain regions and their association with particular tasks (as in conventional "task-based" fMRI[114]) or their correlation with activity in other regions of the brain, absent any external stimulus (as in resting-state fMRI.[123,124])

Fundamentally, neuronal activations require energy, since the electrical potential across the neuron's membrane must be reset after each firing. The energy for this is provided in the form of adenosine triphosphate (ATP), which is itself created locally in each neuron through glycolysis. Glycolysis can happen anaerobically (without oxygen), but the aerobic reaction is approximately one order of magnitude more efficient.[125] However, aerobic glycolysis requires a constant supply of oxygen. This is provided to each neuron in the brain through the vascular system. Around 2% of the oxygen in the blood is dissolved in the plasma, and the rest is bound to haemoglobin (Hb) molecules within red blood cells.[126]

Hb is an iron-containing protein and is diamagnetic in its oxygenated state, but deoxygenated haemoglobin (dHb) is paramagnetic (relative to water).[13,127,128]

As oxygen is extracted from blood plasma in the capillaries by adjacent neurons, more oxygen dissociates from Hb, leaving dHb behind. This change in the relative concentration of dHb leads to a change in local magnetic susceptibility $\chi$, which in turn affects the time constant of the transverse dephasing of spins $T_2$. Since this effect is local, it is reversible with respect to a spin echo. An MR acquisition protocol that is sensitive to $T_2^*$ (or $T_2'$) can therefore be used to track local changes in dHb concentration.

In fMRI, neuronal electrical activity is coupled with changes in cerebral blood flow (CBF)[129] and cerebral blood volume (CBV), as well as a decrease in local OEF. In healthy conditions, the body responds to task-specific activation by overcompensating with oxygenated blood flow to the relevant region of the brain, leading to a local decrease in dHb concentration, hence an increase in $T_2^*$ that can be observed as the BOLD signal. Without knowledge of CBV or CBF, the BOLD signal is only a measure of change in $T_2^*$ relative to a defined baseline. It is not a quantitative measure, and thus cannot be compared directly between subjects, or used as a sole indicator of disease.

### Calibrated BOLD

One solution to the lack of quantitative information offered in fMRI is the calibrated BOLD method first described by Davis *et al.*[130] This was originally developed as a means of quantifying functional changes in metabolism that would be comparable between subjects, but can also be used to quantify OEF at rest.[131–133]

Calibrated BOLD attempts to calculate the maximum possible signal change $M$ that would be achieved by removing all dHb from a voxel. This can be calculated by manipulating CBV and $CMRO_2$, using an assumed form for their relationship. CBV is assumed to be related to CBF by Grubb's power law:[134,135]

$$\Delta CBV = \Delta CBF^{\alpha} \tag{2.16}$$

where the exponent $\alpha$ was originally measured by Grubb to be 0.38, based on $^{15}O$ PET studies of rhesus monkeys under hypercapnia.[134] It has since been measured

in humans, using hyper- and hypocapnic stimuli, with MRI, as 0.18,[118,135] and investigations with numerical simulations of BOLD data have yielded optimal values of $\alpha$ as low as 0.14.[136]

CBF can be manipulated by controlled inhalation of $CO_2$, which causes hypercapnia, which in turn evokes vasodilation. The resulting increase in CBF is assumed not to change $CMRO_2$.[130] The resulting change to the measured BOLD signal $\Delta BOLD$ is given by the Davis model:[130,131]

$$\frac{\Delta BOLD}{BOLD_0} = M \cdot \left(1 - \left(\frac{CBV}{CBV_0}\right)\left(\frac{[dHb]}{[dHb]_0}\right)^{\beta}\right) \tag{2.17}$$

[dHb] is the concentration of dHb in the veins, the subscript 0 indicates the baseline (normocapnic) state, $\beta$ is a constant,[121] and

$$M = A \cdot TE \cdot CBV_0 \cdot [dHb]_0^{\beta} \tag{2.18}$$

where $A$ is a constant. By applying Fick's principle (Equation 2.15) and the Grubb power law (Equation 2.16) the hypercapnic calibration model becomes

$$\frac{\Delta BOLD}{BOLD_0} = M \cdot \left(1 - \left(\frac{CMRO_2}{CMRO_{2,0}}\right)^{\beta}\left(\frac{CBF}{CBF_0}\right)^{\alpha-\beta}\right) \tag{2.19}$$

Since the relation between end-tidal $CO_2$ and CBF is known,[130,137] it is possible to calculate $M$ using a hypercapnic stimulus and acquired BOLD data. Then, when neuronal activity or a change in physiology causes a change in $CMRO_2$, that change can be quantified in a way that is robust to other factors such as blood volume and oxygen saturation. It is dependent on the assumption that all oxygen extracted from the vascular system by a particular voxel is metabolized in that voxel (contributing to local $CMRO_2$) rather than being transported out.[130]

In order to measure an absolute, rather than a relative, change in metabolism, another calibration is required. When $M$ is calculated by a hypercapnia experiment (Equation 2.19), a similar experiment using hyperoxia (which changes venous oxygen saturation without affecting CBF[131]) yields[65,138]

$$\frac{\Delta BOLD}{BOLD_0} = M \cdot \left(1 - \left(\frac{CBF}{CBF_0}\right)^{\alpha}\left(\frac{[dHb]}{[dHb]_0} + \frac{CBF_0}{CBF} - 1\right)^{\beta}\right) \tag{2.20}$$

which can be used to calculate OEF from the measured change in [dHb].

Calibrated BOLD methods are, in general, limited by the need to deliver gases in a controlled manner. In practical terms, this means that results can be affected by ill-fitting masks or inaccurate measurement of delivered or end-tidal gas fractions. The $CO_2$ challenge that is used to calculate $M$ cannot be tolerated for extended lengths of time and has been shown to affect $CMRO_2$.[139] Similarly, hyperoxia does not affect only oxygen saturation, but also CBF, which may compromise calibration using Equation 2.20.[138]

In clinical populations, especially those suffering from acute stroke, carrying out a calibrated BOLD experiment may not be feasible for these reasons: hypercapnia may not be well tolerated; mask fitting and the necessity for deep, consistent breathing may not be possible; acquisition times are long (typically >15 minutes); and other changes in physiology induced by the ischaemia may undermine the assumptions made in the calibration equations.

### 2.3.2 Quantitative BOLD

The quantitative BOLD (qBOLD) model can be used to quantify physiological parameters based on transverse relaxation without the need for exogenous contrast agents or gas challenges. It was first proposed by Yablonskiy & Haacke[14] and in general terms describes the evolution of signal from bulk tissue in the presence of several paramagnetic susceptibility-altering objects.[14,17] Magnetic susceptibility $\chi$ is the constant of proportionality between tissue magnetization $M$ and $B_0$:

$$M = \chi \cdot B_0 \tag{2.21}$$

Paramagnetic substances have a small positive $\chi$ (as opposed to diamagnetic substances with a small negative $\chi$), because they contain unpaired electrons and thus have a magnetic moment. Importantly, the $Fe^{2+}$ in the centre of a haemoglobin molecule is paramagnetic, but it forms a diamagnetic complex when combined with

oxygen. The result is a susceptibility difference $\Delta\chi_0$ between fully oxygenated and fully deoxygenated red blood cells (RBCs). This can be quantified based on the weighted sum of the susceptibilities of the components of a red blood cell — water, protein, haemoglobin (Hb), and deoxyhaemoglobin (dHb):[140]

$$\chi_{RBC} = (1 - n_{Hb} \cdot \nu_{MHb}) \cdot \chi_{H_2O} + n_{Hb} \cdot (M_{dHb} \cdot \chi_{protein} + OEF \cdot \chi_{dHb}) \quad (2.22)$$

Here $n_{Hb}$ is the intracellular Hb concentration, $\nu_{MHb}$ is the molar volume of dissolved Hb, $\chi_{H_2O}$ is the susceptibility of water, $M_{dHb}$ is the molecular weight of dHb, $\chi_{protein}$ is the diamagnetic susceptibility contribution of Hb per unit mass, and $\chi_{dHb}$ is the paramagnetic susceptibility contribution of dHb per mole. Using literature values from SQUID magnetometry leads to $\Delta\chi_0$=0.264 ppm.[140]

The presence of an embedded object with a different susceptibility from the bulk tissue that surrounds it causes a local change in the magnetic field experienced by the tissue, leading to a change in the rate of phase accrual, which is expressed as a frequency shift $\delta\omega$.

**Signal Averaging in Grey Matter**

Following the general description of an MR signal from a voxel (Section 2.1.2), Equation 2.7 can be written in terms of frequency $\omega$ as a volume integral:

$$S(t) = \frac{1}{V} \cdot \rho \cdot \int_V e^{-i \cdot \omega(\boldsymbol{r}) \cdot t} d\boldsymbol{r} \quad (2.23)$$

where $V$ is the voxel's volume, and $\omega(\boldsymbol{r})$ is the local frequency at position $\boldsymbol{r}$. In the rotating frame, it is defined as the sum of the effect of all the susceptibility-altering objects $n$:

$$\omega(\boldsymbol{r}) = \sum_n \gamma \cdot b_n(\boldsymbol{r} - \boldsymbol{r}_n) \quad (2.24)$$

where $b_n(\boldsymbol{r}-\boldsymbol{r}_n)$ is the inhomogeneous magnetic field created by the $n$th susceptibility-altering object (whose location is $\boldsymbol{r}_n$) at $\boldsymbol{r}$.

The result of averaging over Equation 2.23 depends on the distribution of the susceptibility-altering objects. In the qBOLD case, these are blood vessels containing deoxygenated blood (veins, venules, and capillaries), which can be modelled as infinitely long cylinders with random orientation, random uniform distribution throughout each voxel, and an arbitrary distribution of radii $P(R)$. This leads to[14]

$$S(t) = \rho \cdot (1 - \zeta) \cdot e^{-\zeta \cdot f(\delta\omega \cdot t)} \tag{2.25}$$

where $\zeta$ is the total volume fraction occupied by the susceptibility-altering objects in the voxel, and the function $f(x)$ is defined as

$$f(x) = \frac{1}{3} \cdot \int_0^1 \frac{2+u}{u^2} \cdot \sqrt{1-u} \cdot \left(1 - J_0\Big(\frac{3}{2} \cdot x \cdot u\Big)\right) du \tag{2.26}$$

where $J_0(y)$ is the zero-order Bessel function in $y$.

In this case, $\delta\omega$ is given by

$$\delta\omega = \frac{4}{3} \cdot \pi \cdot \gamma \cdot B_0 \cdot \Delta\chi \tag{2.27}$$

When the susceptibility-altering objects are deoxygenated blood vessels, then $\zeta = DBV$, and under the assumption that arterial blood is fully oxygenated, and that dHb is the only source of a difference in $\chi$, then

$$\Delta\chi = \Delta\chi_0 \cdot Hct \cdot OEF \tag{2.28}$$

Thus the qBOLD MR signal depends on OEF and DBV. This OEF is based on local $SO_2$ of venules and capillaries within each voxel, which may not be as low as the $SvO_2$ in larger draining veins. Thus local OEF measured using qBOLD (or other $R_2'$-based methods) should not necessarily be expected to have the same value as whole-brain OEF measured using other modalities.

### Measuring the qBOLD Signal

Yablonskiy & Haacke observed that Equation 2.26 has two asymptotic forms that are more computationally manageable, based on time scale.[14] Under an ASE acquisition, where $TE$ is kept constant and spin echo offset $\tau$ is varied, Equation 2.25 becomes

$$S(\tau) = \exp\left(\frac{3}{10} \cdot \zeta \cdot (\delta\omega \cdot \tau)^2\right) \qquad |\tau| < t_c \qquad (2.29a)$$

$$S(\tau) = \exp\left(\zeta - \zeta \cdot \delta\omega \cdot \tau\right) \qquad |\tau| > t_c \qquad (2.29b)$$

where $S(\tau)$ is normalized to the spin echo signal $S(\tau = 0)$, and the characteristic time $t_c$ is given by[141]

$$t_c = \frac{1.5}{\delta\omega} \qquad (2.30)$$

In the 'short-$\tau$' regime of Equation 2.29a, $\log(S)$ varies quadratically with $\tau$ whereas the 'long-$\tau$' regime (Equation 2.29b) has a log-linear dependence on $\tau$. From this long-$\tau$ regime, it is possible to define the rate of reversible transverse dephasing $R_2'$ as

$$R_2' = \zeta \cdot \delta\omega \qquad (2.31)$$

Substituting in Equations 2.27 and 2.28 gives

$$R_2' = \frac{4}{3} \cdot \pi \cdot \gamma \cdot B_0 \cdot \Delta\chi_0 \cdot Hct \cdot OEF \cdot \zeta \qquad (2.32)$$

It is therefore possible to re-write Equation 2.29 in terms of $R_2'$ and $\zeta$, thereby removing explicit dependence on OEF:

$$S(\tau) = \exp\left(\frac{3}{10} \cdot \frac{(R_2' \cdot \tau)^2}{\zeta}\right) \qquad |\tau| < t_c \qquad (2.33a)$$

$$S(\tau) = \exp\left(\zeta - R_2' \cdot \tau\right) \qquad |\tau| > t_c \qquad (2.33b)$$

OEF can be recovered by solving Equation 2.32:

$$OEF = \frac{3 \cdot R_2'}{4 \cdot \pi \cdot \gamma \cdot B_0 \cdot \Delta\chi_0 \cdot Hct \cdot \zeta} \qquad (2.34)$$

### 2.3.3 Intravascular Signal Models

The qBOLD model can be extended to include the signal which originates from venous blood. Several models have been proposed which describe this intravascular signal, which are described below. The total signal measured from a voxel in this two-compartment model is the sum of the signal from each compartment, weighted by their apparent volume fractions.[141] Apparent deoxygenated blood volume $\zeta'$ is given by

$$\zeta' = m_b \cdot n_b \cdot DBV \tag{2.35}$$

where $n_b$ is the relative spin density of blood, and $m_b$ is its steady-state magnetization. For an ASE sequence (when $TR \gg TE - \tau$), compartment $x$ has a steady state magnetization $m_x$ given by[142]

$$m_x = 1 - e^{-\frac{TR}{T_1^x}} \tag{2.36}$$

where $T_1^x$ is the $T_1$ of compartment $x$. The total signal is therefore given by

$$S^{total}(\tau) = S_0 \cdot \Big(\zeta' \cdot S^b(\tau) + (1 - \zeta') \cdot S^t(\tau)\Big) \tag{2.37}$$

where $S_0$ is the signal without any transverse relaxation, and $S^t$ is the signal from the tissue compartment (Equation 2.25).

A potential limitation of this approach is the consistent use of $\zeta'$ (or DBV) for both determining signal shape and weighting the several compartments. From a theoretical perspective, the 'volume' term used in the qBOLD model is specifically the volume of blood which has a susceptibility offset from bulk tissue. It is assumed that this corresponds to venous blood, whose lower oxygenation results in $\Delta\chi$. However, it is possible that, since arterial blood is not actually 100% saturated,[110,136,143] it may also contribute to dephasing in the bulk compartment. The same is true of capillary blood. The parameter CBV, or even venous CBV, as measured using calibrated BOLD (or another technique like VASO[115]), does not necessarily correspond to either DBV or $\zeta'$, in terms of its effect on the qBOLD signal.

### Linear Model

The simplest model of the blood signal $S^b$ assumes that it decays monoexponentially and is reversible with respect to the spin echo:[144,145]

$$S^b(\tau) = e^{-R_2^b \cdot TE} \cdot e^{-R_2^{b*} \cdot |\tau|} \tag{2.38}$$

where $R_2^b$ and $R_2^{b*}$ are, respectively, the irreversible and reversible relaxation rates of blood. These are defined empirically, and depend on OEF and $Hct$:[144]

$$R_2^b = 4.5 + 16.4 \cdot Hct + (165.2 \cdot Hct + 55.7) \cdot OEF^2 \tag{2.39}$$

$$R_2^{b*} = 10.2 - 1.5 \cdot Hct + (136.9 \cdot Hct - 13.9) \cdot OEF^2 \tag{2.40}$$

This model does not properly consider the dephasing effects inside the blood vessel, which consists of a bulk (plasma) containing susceptibility altering objects (red blood cells).

### Powder Model

An alternative model, which includes intravascular dephasing, was proposed by Sukstanskii & Yablonskiy:[17,146]

$$S^b(\tau) = e^{-R_2^b \cdot TE + i\frac{\delta\omega \cdot \tau}{2}} \cdot \frac{C(\eta) - iS(\eta)}{\eta} \tag{2.41}$$

where $C(\eta)$ and $S(\eta)$ are the Fresnel cosine and sine functions, and

$$\eta = \left(\frac{3 \cdot \delta\omega \cdot |\tau|}{\pi}\right)^{\frac{1}{2}} \tag{2.42}$$

This is based on dephasing of blood plasma spins by RBCs (all the spins within RBCs are assumed to dephase at the same rate), and therefore follows the same principle as the bulk tissue in the presence of blood vessels.[146] Equation 2.41 can be written asymptotically, with two regimes based on dephasing time ($\tau$ in the case of ASE) and the assumed geometry of the RBCs.

### Motional Narrowing Model

A recently proposed analytical model describes the blood signal under the motional narrowing regime. This is valid because the size of an RBC is significantly smaller than the distance a spin in the plasma will diffuse during time TE. The signal in this regime is:[147,148]

$$S^b(\tau) = e^{-R_2^{b,true} \cdot TE} \cdot \exp\left[-\frac{\gamma^2}{2} G_0 t_D^2 \cdot \left(\frac{TE}{t_D} + \sqrt{\frac{1}{4} + \frac{TE}{t_D}} + \frac{3}{2} - 2\sqrt{\frac{1}{4} + \frac{TE+\tau}{t_D}} - 2\sqrt{\frac{1}{4} + \frac{TE-\tau}{t_D}}\right)\right] \quad (2.43)$$

Here characteristic diffusion time $t_D = R_{rbc}/D_b$, where $R_{rbc}$ is the characteristic size of red blood cells, $D_b$ is their rate of diffusion within blood vessels, $R_2^{b,true}$ is the intrinsic $R_2$ of fully oxygenated blood, and $G_0$ is the mean square field inhomogeneity in blood:

$$G_0 = \frac{4}{45} \cdot Hct \cdot (1 - Hct) \cdot (4\pi \cdot B_0 \cdot OEF \cdot \Delta\chi_0)^2 \quad (2.44)$$

This approach is based on the weak field approximation (which was applied to $R_2$ decay by Jensen & Chandra[149]), and produces the same result as the powder model in the case of FID decay about spherical objects, but better accounts for the evolution of the signal in sequences with several tipping pulses (such as the Carr-Purcell-Meiboom-Gill sequence) or ASE. It was validated against other models using simulated data[147] and *in vivo*.[148]

## 2.3.4 qBOLD Validation Studies

Several papers have been published validating the qBOLD model in a range of conditions. Initially, Yablonskiy used a phantom blood vessel network to measure its volume fraction (equivalent to DBV) and $R_2'$ reliably using GESSE qBOLD.[150] Later, Sedlacik and Reichenbach performed similar phantom experiments and also

measured OEF and DBV *in vivo* in healthy volunteers.[16] They found that simultaneous estimation of OEF and DBV was unreliable but that fixing one parameter to a literature value produced consistent and reasonable results in the other.

He, Zhu, and Yablonskiy validated qBOLD estimates of OEF in rats against oxygen saturation measurements from sampled blood made with a blood gas analyser, finding very strong correlation between the two measurements.[15] Ni and colleagues[151] compared several methods for measuring $R_2'$, including GESSE and ASE which are both used in qBOLD literature.[19,141,142] Here, statistically significant differences were found in GM $R_2'$ estimates between methods, with GESSE resulting in $R_2'$=2.7±0.3 $s^{-1}$, and ASE measuring $R_2'$=3.8±0.6 $s^{-1}$.

The qBOLD model has also been analysed using different techniques. Simon *et al.* used a Bayesian approach to fit a multiple-compartment qBOLD model to *in vivo* data, with modulations of the signal provided by a functional neuronal stimulus and hypercapnia.[152] Most recently, Domsch and colleagues compared fitting of *in vivo* GESSE data with the qBOLD model (through least-squares regression) against the use of an artificial neural network.[153] The results varied significantly between methods: least-squares regression of the full qBOLD model (Equations 2.25 and 2.26) estimated DBV=11.4±2.0% and OEF=26±5%, whereas the artificial network produced DBV=4.2±0.1% and OEF=40±1%. The difference between least-squares regression on the full model and the asymptotic model (Equation 2.29) was almost as large, suggesting that least-squares fitting is not suitable for models of this complexity.

These experiments have shown that qBOLD can be a useful method for estimating OEF and DBV; however, there are limitations to its reliability which warrant further investigation.

### 2.3.5 Other qBOLD Approaches

#### Alternative Dephasing Models

Kiselev & Posse[154] also proposed an analytical model for signal dephasing in the presence of a network of susceptibility-altering objects. In this model, each blood

vessel contributes to the dephasing of a spin within a voxel. Asymptotic solutions were derived for both the static dephasing regime and the diffusion narrowing (motional narrowing) regime. The benefit of such a model is the potential to de-couple the effects of OEF and DBV in the short time regime.[17]

The static dephasing regime of the qBOLD model is expected to hold only in the case of sufficiently large vessels, like veins and venules.[17] To account for the signal originating from capillaries, Sukstanskii & Yablonskiy developed a Gaussian phase approximation model.[155,156] In it, the distribution of phases $\phi$ in a voxel is considered to have a zero-mean Gaussian distribution.[157] This assumes a uniform $B_0$ field which is not the case, but has been shown to be a reasonable approximation.[146] It is the same model that underlies the intravascular 'powder model'. After signal averaging (which is more straightforward with Gaussian $\phi$), the original qBOLD equations are modified by a signal attenuation function $\Gamma(t)$, which has two asymptotic forms based on the characteristic diffusion time $t_D$:

$$\Gamma(TE) = G_0 \cdot t_D^2 \cdot \left( \frac{t^3}{4t_D^3} - C_1 \cdot \left(\frac{t}{t_D}\right)^{7/2} \right) \qquad t << t_D \qquad (2.45a)$$

$$\Gamma(TE) = G_0 \cdot t_D^2 \cdot \left( \frac{3t}{16t_D} \ln \frac{t}{t_D} + C_2 \cdot \frac{t}{t_D} + C_3 \right) \qquad t >> t_D \qquad (2.45b)$$

where $G_0$ is a frequency correlation parameter (which depends on the product of OEF and DBV), and $C_1$, $C_2$, and $C_3$ are numerical constants. Simulations showed that the inclusion of an attenuation function with higher order terms improves model fitting under realistic conditions.[156] The major disadvantage of this approach is that OEF and DBV appear only in the $G_0$ parameter, and so cannot be separated by fitting this model alone.

**Phenomenological Models**

An alternative approach to qBOLD is that taken by Dickson and colleagues. They used Monte Carlo methods to generate simulated GESSE qBOLD signals (following the Boxerman method[158]), and found that water diffusion had a significant impact on the fitted values of OEF, DBV, and $T_2$ when they used the static dephasing regime

qBOLD model.[159] The proposed alternative was to derive a phenomenological model of the form

$$S(t) = S_0 \cdot e^{-DBV \cdot f(t)} \tag{2.46}$$

$$f(t) = A_1 \cdot \left(e^{-A_2 \cdot t} - 1\right) + A_3 \cdot t + A_4 \tag{2.47}$$

where each of the parameters $A_n$ are themselves parametrized

$$A_n = OEF \cdot \left(B_1 - B_2 e^{-B_3 \cdot OEF}\right) \tag{2.48}$$

and the constants $B_n$ are found by fitting to simulated data.[160] This approach was found to be reliable in estimating OEF from GESSE data; however, the values of the parameters vary strongly with the radius (or distribution of radii) of vessels simulated, and on an assumed value for DBV. If an unrealistic vessel distribution is used, the final estimates of OEF will be inaccurate and not easily correctable. This and all Monte Carlo-based diffusion experiments rely on the assumption of isotropic diffusion in grey matter, which, if combined with an anisotropic arrangement of vessels, may lead to very different signal shapes.

A similar phenomenological model was used by Pannetier *et al.*[161] to assess the affect of vessel radius on simulated data and to compare with the analytical model proposed by Kiselev & Posse.[154] Using DWI and $T_2$ mapping to provide additional information for dictionary fitting of their numerical model of GESSE data, it was found that the effect of vessel radius could be accounted for to estimate DBV and $\Delta\chi$ (analogous to OEF) in a phantom study.

### Combining Methods

Incorporating additional information has been shown to improve model fitting. Initially, An & Lin showed that $B_0$ inhomogeneities caused overestimation of DBV, but that this could be mitigated by retrospectively correcting for it using a field map.[162] This was extended to prospective correction using GESEPI (see Section 2.1.4) in the streamlined qBOLD method.[19,163]

Christen and colleagues demonstrated the feasibility of combining estimates of $R_2$ and $R_2^*$ with measures of CBF and CBV from other methods to quantify OEF and $CMRO_2$.[164] This method, referred to as multiparametric qBOLD, was validated against other qBOLD methods in healthy subjects. It is, in theory, robust against the effects of diffusion, because of the short echo time required to estimate $R_2^*$, though it relies on the same assumptions as the SDR qBOLD model. This method required a total scan time of 15 minutes, which may make it impractical for use in an acute clinical setting.

Recently, Lee, Englund, and Wehrli[165] proposed an 'interleaved' qBOLD method, which combined SDR qBOLD estimates of $R_2'$ in grey matter with velocity-selective spin labelling estimates of $R_2^b$ in the veins,[166] to fit a combined model of intravascular and extravascular signal and thereby estimate OEF and DBV simultaneously. This method is currently limited to a single slice implementation, although it could be expanded at the cost of scanning time; it also relies on the imposition of strong priors (see Section 2.4) for accurate parameter estimation.

### 2.3.6 Quantitative MRI

Other aspects of brain physiology can be quantified using other MR techniques, some of which are particularly relevant to acute stroke and OEF quantification.

#### Arterial Spin Labelling (ASL)

Arterial spin labelling (ASL) was first used by Williams, Detre, and colleagues in 1992[167,168] as a non-invasive, endogenous-contrast-based method of perfusion imaging.[112] In a typical ASL experiment, blood water is labelled by inverting the magnetization of blood in the feeding arteries of the brain. Then, after a suitable post-labelling delay (PLD), an image of the brain is acquired (typically using an EPI readout). A control image of the brain is acquired without the preceding inversion and is subtracted from the labelled image. The result is an image which is weighted by the amount of labelled blood that has flowed into each voxel during

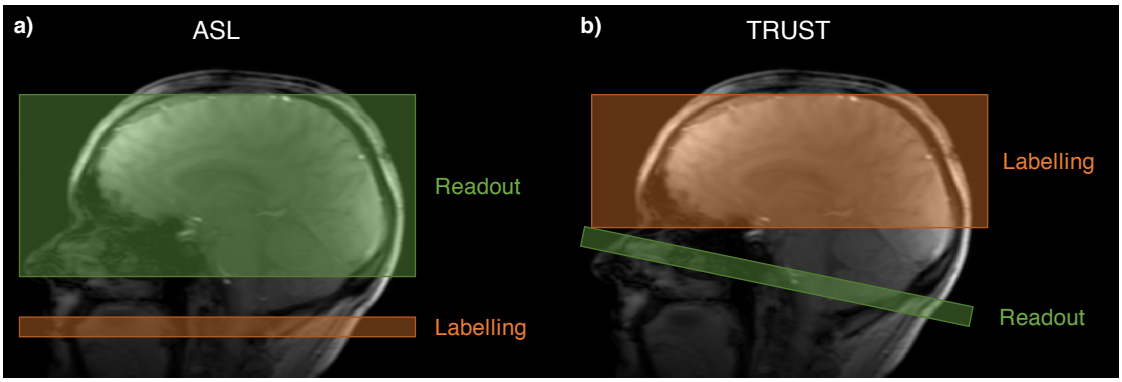


**Figure 2.9:** Illustration of typical labelling and readout regions for **a)** (pseudo-continuous) ASL and **b)** TRUST. In ASL, the labelling plane is placed in the neck so that all inflowing arterial blood is labelled, then signal from the whole brain is read out. In TRUST, labelling is applied to the whole brain, inverting the magnetization in venous blood, which drains through the readout slice by the sagittal sinus.

the PLD time. Typical labelling and readout planes for a pseudo-continuous ASL (PCASL) experiment are indicated in Figure 2.9a.

Buxton and colleagues[169] derived a kinetic model that described the signal in a voxel as the convolution of an arterial input function and a residue function.[113] The arterial input function depends on the $T_1$ of blood (which undergoes longitudinal relaxation as it is travelling from the labelling plane in the neck up to the brain) and on the arterial transit time (ATT), or the time taken for blood to travel from the labelling plane to the voxel. The residue function describes the $T_1$ decay that continues after the labelled blood has arrived in the voxel, as well as other physiological clearance functions. By acquiring ASL data with a range of PLDs and assuming the form of the residue function, it is possible to calculate CBF and ATT. ASL can therefore be used to measure perfusion quantitatively, without the need for a contrast agent as in dynamic contrast enhanced (DCE) MRI.

In the clinic, single-PLD ASL can be used to identify acute stroke, while a quantitative CBF measurement from multi-PLD ASL can be used in the traditional diffusion-perfusion mismatch imaging (see Section 2.2) to identify the ischaemic core and penumbra, or it can be combined with a measurement of OEF to estimate $CMRO_2$.[61]

Because blood occupies a small volume fraction of a typical voxel, and the $T_1$ of blood is around 1600ms at 3T[63] (which is of the same order of magnitude as a typical PLD), the SNR of ASL is intrinsically very low. PCASL[170] uses a series of low flip-angle RF pulses applied in a narrow labelling slice to adiabatically invert a large bolus of blood. This approach has a higher SNR per unit time than other continuous ASL methods and is preferred clinically.[60,61,64]

### $T_2$ Relaxation Under Spin Tagging (TRUST)

$T_2$ relaxation under spin tagging (TRUST) was developed by Lu & Ge[59] as a non-invasive technique to quantitatively measure whole brain oxygenation by measuring the $T_2$ of venous blood.[59,171,172] In its acquisition protocol, it can be thought of as the reverse of ASL: in TRUST, a large slab high in the brain is labelled by a inverting the magnetization; then after a delay of $TI$ an image is read out from a single inferior slice. This is shown schematically in Figure 2.9b. The imaging slice is chosen to contain the superior sagittal sinus (SSS), through which cerebral blood drains.

As in ASL, labelled and control images are acquired and their difference computed, but only in voxels that are located wholly within the SSS (which ought to be the only voxels in which the signal changes between the labelled and control images). The difference in signal is given by[59]

$$\Delta S = S_0 \cdot e^{TE_e\left(\frac{1}{T_1^b}-\frac{1}{T_2^b}\right)} \tag{2.49}$$

where $S_0$ is the signal without $T_2$ weighting, $TE_e$ is the effective echo time determined by the $T_2$ preparation pulse timing, and $T_1^b$ and $T_2^b$ are the relaxation times of blood. OEF can be derived from $T_2^b$ through the use of a calibration function, which also depends upon $Hct$[172] and uses constants obtained from *ex vivo* experiments in the literature.[173]

Since the SSS, in which the TRUST signal is measured, drains blood from the entire brain, TRUST provides a whole-brain measure of OEF, which has been shown to be reliable and reproducible, when compared with other methods for whole-brain OEF estimation.[9,172] It therefore has potential utility as a validation

method against other measures of whole-brain OEF. However, it is not sensitive to regional variation of OEF, such as occurs in ischaemic stroke. Recently, work has been carried out to localize TRUST measurements using spatial saturation pulses to suppress signal from certain areas and retain signal only from one region of interest.[174] This has been tested at the hemispheric level with promising results and could be extended to greater spatial specificity.

## 2.4 Bayesian Inference

Bayesian inference is a general class of techniques for model inference that differs from traditional frequentist statistics in several important ways. It is centred around Bayes' Theorem, which relates one's belief about model parameters to observed data and prior beliefs. This section contains a theoretical introduction to Bayes' Theorem (Section 2.4.1), followed by a description of two alternative approaches to solving Bayes' Rule, by sampling (Section 2.4.2) and approximation (Section 2.4.3). Examples of how Bayesian methods are applied to relevant problems in MRI are also presented (Section 2.4.4). This section draws from material in textbooks,[175–179] relevant journal articles,[22,23,180,181] and other sources.[182–184]

### 2.4.1 Bayes' Theorem

Bayesian inference is built upon Bayes' Theorem (or Bayes' Rule), which was originally stated by Thomas Bayes in these words:[185]

> If there be two subsequent events, the probability of the second b/N, and the probability of both together P/N, and it being first discovered that the second event has happened, from hence I guess that the first event has also happened, the probability I am right is P/b.

In the inference terminology, the 'first event' is the occurrence of some parameters $\Theta$, and the 'second event' is some observed data $Y$. The 'probability of both together' is the joint probability of $(Y, \Theta)$, so the probability that Bayes' 'guess' was correct is $P(\Theta|Y)$, known as the posterior. Bayes' Theorem can be stated mathematically:

$$P(\Theta|Y,\mathcal{M}) = \frac{P(\Theta|\mathcal{M}) \cdot P(Y|\Theta,\mathcal{M})}{P(Y|\mathcal{M})} \tag{2.50}$$

where the prior $P(\Theta|\mathcal{M})$ is one's *a priori* belief about the parameters, $P(Y|\Theta,\mathcal{M})$ is the likelihood of the data being generated by $\Theta$, and $P(Y|\mathcal{M})$ is the evidence of the data. The evidence is the probability that $Y$ was observed at all (regardless of the value of $\Theta$) given the model $\mathcal{M}$. It can be obtained by marginalizing $\Theta$ out of the joint distribution $P(Y,\Theta|\mathcal{M})$ (for this reason, it is also referred to as the marginal likelihood, in frequentist statistics). The posterior probability $P(\Theta|Y,\mathcal{M})$ is what one should *a posteriori* believe about $\Theta$ after having observed $Y$. $\mathcal{M}$ represents a model that, in general, maps $\Theta$ to $Y$ through a function $Y = S(\Theta)$. The choice of $\mathcal{M}$ can be left aside temporarily, reducing Equation 2.50 to

$$P(\Theta|Y) = \frac{P(\Theta) \cdot P(Y|\Theta)}{P(Y)} \tag{2.51}$$

In Bayesian statistics, the probabilities $P$ are not single values, but distributions that describe random events, such that an actual probability can be obtained by integrating over $P$ with respect to a variable of interest. This allows for the explicit handling of uncertainty in an analytical way, which is a key advantage of the Bayesian method. Inferences can be made about a model or its parameters on the basis of their probability distributions $P$, in particular, those of the posterior or the likelihood. Summary statistics such as the mean posterior probability can be used to provide an estimate of a parameter's values, and measures such as variance (or standard deviation) can quantify the uncertainty in that estimate. The frequentist technique of maximum likelihood estimation (MLE) is equivalent to finding the modal value of $\Theta$ in the probability distribution $P(Y|\Theta)$.[184]

Bayesian inference differs from MLE by representing the entire likelihood, not just its mode, and by the inclusion of the prior $P(\Theta)$, which represents existing knowledge about the distribution of values in $\Theta$. When the model is assumed, the model evidence $P(Y)$ can be treated as a normalizing constant, and ignored too, leading to

$$P(\Theta|Y) \propto P(\Theta) \cdot P(Y|\Theta) \tag{2.52}$$

which reduces to an equation when the probability distributions are normalized. Evaluating it analytically is generally not possible, so $P(\Theta|Y)$ can be obtained either by sampling from it, or by approximating it. These methods will be considered in turn below (in Sections 2.4.2 and 2.4.3).

### Comparing Models

The choice of model $\mathcal{M}$ was left aside earlier, but it is an important consideration. Two models can be compared using the Bayes Factor $BF$, which is defined as the ratio of their evidences, or the ratio of the probability that $Y$ could have occurred, given a particular model:[186–188]

$$BF = \frac{P(Y|\mathcal{M}_1)}{P(Y|\mathcal{M}_2)} \tag{2.53}$$

where $BF \gg 1$ suggests that the data support model $\mathcal{M}_1$, and $BF \ll 1$ suggests that the data support model $\mathcal{M}_2$. In practice, $P(Y|\mathcal{M})$ can be evaluated by marginalizing the numerator of Equation 2.51 over all $\Theta$. This is, as above, usually intractable, and must therefore be either sampled numerically (see Section 2.4.2) or approximated.[189] In the event of multiple models with similar evidences, a committee approach could be used, in which the the final posterior is the sum of $n$ posteriors $P(\Theta|Y, \mathcal{M}_n)$, each weighted by $P(Y|\mathcal{M}_n)$.[184]

Alternatively, models can be tested using the Bayesian information criterion (BIC),[190] which does not depend on the priors, but which is approximately proportional to the natural logarithm of $BF$.[189] This also includes a weighting based on the number of individual parameters within $\Theta$, and so favours simpler models, which are able to explain the same data in fewer variables.

Model simplification can also be achieved using automatic relevance determination (ARD — also known as a shrinkage prior),[23,191] in which parameters $\theta$ that are suspected of being superfluous, are assigned Gaussian prior $P(\theta) \approx \mathcal{N}(0, v)$, and their variance $v$ is inferred as another model parameter. If the presence of $\theta$ within the model is not supported by $Y$, then $v \to 0$, leading to the posterior $P(\theta|Y) \to 0$ and $\theta$ being excluded from the final inferred results.

### Advantages of the Bayesian Approach

Bayesian methods offer several advantages over frequentist inference techniques, especially in modelling biological systems: the ability to incorporate knowledge of parameter distributions *a priori* allows constraints to be placed on the parameters in line with physical or biological limits in order to prevent noisy data from producing extreme or implausible estimates.[184] In imaging data, in which the model is fit to data from each voxel, priors can be used to incorporate local or regional information for each voxel, based on its neighbours, to enforce spatial smoothness or to enhance or suppress expected features.[181,192]

Bayesian methods also allow for inference on complicated models which cannot be solved analytically. These can include noise models, whose form and parameters (such as variance) can be inferred simultaneously alongside parameters of interest. Combining multiple models and adapting them on-line is also possible in a Bayesian framework.[193]

Since Bayesian inference explicitly handles uncertainty in parameters, rather than simply providing point estimates, it is possible to construct hierarchical models which compare uncertainty across multiple levels, such as from the individual subject up to a group of subjects.[194,195]

## 2.4.2 Posterior Sampling Methods

Since it is often not possible to evaluate the posterior (Equation 2.52) analytically, it can be found by sampling. The crudest method for doing this is to generate a uniform grid of points in parameter space and evaluate the likelihood using the chosen model for each $\Theta_n$. In high dimensions (that is, with a large number of parameters being inferred), this method becomes prohibitively time-consuming, and can be extremely inefficient, since a large amount of time will be spent evaluating the model in regions of very low $P(Y|\Theta)$.

### Metropolis Hastings

The exact posterior distribution can also be obtained by sampling it using the Metropolis Hastings (MH) algorithm.[196–198] This is a Markov Chain Monte Carlo (MCMC) method that generates samples from a probability distribution by making random steps through parameter space. In the most general case, parameters are initialized at $\Theta_1$, then for each of $N$ steps, a new set of parameter values $\Theta_{n+1}$ is proposed, drawn from a distribution $Q$. In the original Metropolis algorithm,[196] $Q$ is a Gaussian distribution centred on $\Theta_n$, although the algorithm was generalized by Hastings to asymmetric or arbitrary $Q$.[197].

The likelihoods at $\Theta_n$ and $\Theta_{n+1}$ are evaluated, and the new parameter values are accepted with a probability proportional to their ratio:

$$p(\Theta_{n+1} accepted) = \min\left(\frac{P(Y|\Theta_{n+1})}{(P(Y|\Theta_n)}, 1\right) \tag{2.54}$$

so steps where $P(Y|\Theta_{n+1})$ is greater than $P(Y|\Theta_n)$ are always accepted, but steps in the lower likelihood direction are also sometimes accepted. This prevents the chain from becoming trapped in local maxima and ensures that the entire posterior space will be explored given sufficiently large $N$. If the candidate parameters are not accepted, then $\Theta_{n+1}$ takes the values of $\Theta_n$, and the chain does not move.

The width of $Q$ can be adjusted iteratively based on the acceptance rate $c$, which is the ratio of proposed points accepted to total points proposed, within a pre-determined range of recent points. This allows for large steps to be made when the relative local likelihood is low, and for a larger number of steps to be concentrated in regions of parameter space where the likelihood is highest, allowing for finer delineation of $P(\Theta|Y)$. The optimal $c$ depends on the dimension $d$ of the parameter space.[175] For $d = 2$, $c_{optimal} = 0.352$; for $d = 3$, $c_{optimal} = 3.16$; and as $d \to \infty$, $c_{optimal} \to 0.234$.

Steps can be made in a single dimension of parameter space at a time (in which case each dimension has a separate $Q$ distribution), or in the entire parameter space (in which case $Q$ is a multivariate normal distribution). In either case, a set

of points $\Theta$ is built up in parameter space with the same form as the likelihood $P(Y|\Theta)$. It is much more efficient than the 'grid search' method described above, whose computation time scales exponentially with $d$.

The MH algorithm (specifically, Gibbs sampling of MH[199]) has been applied to MRI data in a range of ways, including reduction of heteroscedastic noise (that is, noise with non-uniform variance) in fMRI time series data.[200] In this case, careful evaluation of a posterior that includes variable-selection parameters allows for adaptive modelling of large noise spikes.

### 2.4.3 Variational Bayes

In cases where the analytical form of the posterior cannot be solved exactly, it may be possible to approximate it as $q(\Theta|Y)$, which is a distribution that takes the form of a well-defined function (parametrized by a set of hyper-parameters) that can be solved analytically.[20,22] The variational Bayes (VB) method is based on minimizing the Kullback-Liebler (KL) divergence (or KL distance) of $q(\Theta|Y)$ from $P(\Theta|Y)$, which can be written as $D_{KL}\Big(P(\Theta|Y)\Big|\Big|q(\Theta|Y)\Big)$. The KL divergence between the two distributions is a measure of the information gained when one revises one's beliefs from the approximation $q(\Theta|Y)$ to the truth $P(\Theta|Y)$.[180]

By rearranging Equation 2.51 and taking logs, the log evidence (or marginal likelihood) can be written as

$$\log P(Y) = \log P(Y,\Theta) - \log P(\Theta|Y) \tag{2.55}$$

into which the approximation $q(\Theta|Y)$ can be introduced. Integrating over $\Theta$, and re-arranging further, gives

$$\log P(Y) = \int q(\Theta|Y) \log \frac{P(Y,\Theta)}{q(\Theta|Y)} d\Theta + \int q(\Theta|Y) \log \frac{q(Y|\Theta)}{P(\Theta|Y)} d\Theta \tag{2.56}$$

where the first term on the right-hand side is defined as the free energy $\mathcal{F}$, and the second is $D_{KL}\Big(P(\Theta|Y)\Big|\Big|q(\Theta|Y)\Big)$. So

$$\mathcal{F} = \int q(\Theta|Y) \log \frac{P(Y,\Theta)}{q(\Theta|Y)} d\Theta \tag{2.57}$$

and

$$D_{KL}\Big(P(\Theta|Y)\Big|\Big|q(\Theta|Y)\Big) = \int q(\Theta|Y) \log \frac{q(Y|\Theta)}{P(\Theta|Y)} d\Theta \tag{2.58}$$

Since the true $P(\Theta|Y)$ is not known, $D_{KL}\Big(P(\Theta|Y)\Big|\Big|q(\Theta|Y)\Big)$ cannot be evaluated.[180] However, Jensen's inequality (which is $\phi(E[X]) \leq E[\phi(X)]$, where $X$ is a random variable, $\phi$ is a convex function (such as $\phi(x) = -\log x$), and $E[\cdot]$ is the expected value) shows that

$$D_{KL}\Big(P(\Theta|Y)\Big|\Big|q(\Theta|Y)\Big) \geq 0 \tag{2.59}$$

which is an equality when $q(\Theta|Y) = P(\Theta|Y)$.

The same can be shown in the case of discrete distributions by Gibbs' inequality,[179] which states that the information entropy of a distribution $P$ is less than the cross entropy of $P$ with any other probability distribution $Q$, or

$$-\sum_x P(x) \log P(x) \leq -\sum_x P(x) \log Q(x) \tag{2.60}$$

which can be rearranged

$$D_{KL}\Big(P\Big|\Big|Q\Big) \equiv \sum_x P(x) \log P(x) - \sum_x P(x) \log Q(x) \geq 0 \tag{2.61}$$

Thus, since the evidence $P(Y)$ is constant, minimizing $D_{KL}\Big(P(\Theta|Y)\Big|\Big|q(\Theta|Y)\Big)$ is equivalent to maximising $\mathcal{F}$ with respect to $q(\Theta|Y)$. This requires a tractable form for $q(\Theta|Y)$, which in VB is defined such that the mean field approximation applies:

$$q(\Theta|Y) = \prod_i q_{\theta_i}(\theta_i|Y) \tag{2.62}$$

where each group of parameters $\theta_i$ has its own posterior distribution. This assumes that each parameter group is independent, but it allows for correlation of the individual parameters within a group.[20] For simplicity, it will be assumed that

$\Theta = \{\theta, \phi\}$, where $\theta$ are the model parameters (or the hyper-parameters on the original model parameters), and $\phi$ are the parameters of the noise (which Attias refers to as 'hidden nodes'[20]).[22] The approximate posterior $q(\Theta|Y)$ in Equation 2.57 can be factorized using Equation 2.62, and the resulting expression for free energy optimized:

$$\mathcal{F} = \int q(\theta|Y)q(\phi|Y) \log \frac{P(Y, \theta, \phi)}{q(\theta|Y)q(\phi|Y)} d\theta \leq \log P(Y) \tag{2.63}$$

where the evidence acts as the upper bound on $\mathcal{F}$.

**Expectation Maximization**

Equation 2.63 is optimized by an iterative two-step process that is analogous to expectation maximization. In the first step ('expectation'), the posterior is computed over the noise parameters $\phi$ by setting

$$\frac{\partial \mathcal{F}}{\partial q(\phi)} = 0 \tag{2.64}$$

This is followed by a second step ('maximization'), in which

$$\frac{\partial \mathcal{F}}{\partial q(\theta)} = 0 \tag{2.65}$$

It is usually necessary for the chosen priors to be conjugate to the posterior (and the likelihood), in order to make the calculations tractable. The choice of exponential functions (such as Gaussians) for the priors is sufficient to satisfy this condition.[201]

In the case of a nonlinear forward model, of the form

$$Y = S(\theta) + e(\phi) \tag{2.66}$$

$P(\theta)$ takes the form of a multivariate normal distribution (MVN) with means $\boldsymbol{m_0}$ and variances $\boldsymbol{v_0}$, and $P(\phi)$ is a gamma distribution with parameters $\{\boldsymbol{s_0}, \boldsymbol{c_0}\}$. The approximate posteriors have the same form: $q(\theta|Y) \sim \text{MVN}(\theta; \boldsymbol{m}, \boldsymbol{v})$ and $q(\phi|Y) \sim \text{Ga}(\phi; \boldsymbol{s}, \boldsymbol{c})$.[22] The key to ensuring generality is the approximation of $S(\theta)$ by a first-order Taylor expansion about $\boldsymbol{m}$:

$$S(\theta) \approx S(\boldsymbol{m}) + \boldsymbol{J}(\theta - \boldsymbol{m}) \tag{2.67}$$

where $\boldsymbol{J}$ is the Jacobian.[22] Making this approximation allows Equation 2.63 to be written explicitly, differentiated (as in Equations 2.64 and 2.65), and optimized with respect to $\theta$ and $\phi$.

It can be noted here that the Gauss-Newton solution to the process of nonlinear least squares (NLLS) fitting is equivalent to VB without priors.

### Comparing Models with Free Energy

The free energy $\mathcal{F}$, which is evaluated throughout the VB optimization process (Equation 2.57), can also be used to compare models. Since $\mathcal{F}$ acts as a bound on $-P(Y|\Theta, \mathcal{M})$, a model which better explains the data will have a greater $\mathcal{F}$.[202,203] In the limit of an infinitely large sample size, and without priors, $\mathcal{F}$ is the same as the BIC.[20,204]

### Spatial Regularization

In most medical imaging applications, it is assumed that structures are spatially larger than the dimensions of an imaging voxel, and that the property of the structure which provides contrast in the image (to distinguish it from other structures) is roughly equal in value throughout the structure. It is this principle, applied to the property of $T_1$ relaxation time, that enables the segmentation of $T_1$-weighted brain images into compartments of white matter, grey matter, and cerebrospinal fluid.[205]

This is especially true of many physiological parameters in the healthy brain (such as OEF, CBF, and the BOLD HRF), in which it is expected that neighbouring voxels will not have very different values for these parameters. This assumption can be enforced in a model inference framework in several ways: first, spatial smoothing can be applied retrospectively to parameter maps after inference has been performed, for example by the use of a Gaussian filter. However, this approach risks removing genuine variation in the data, and depends on the manual selection of a filter type and its parameters (e.g. the width or variance of the Gaussian function). Spatial

smoothing can also be applied to the raw data $Y$ before inference, although again this relies on arbitrary selection of smoothing parameters. Furthermore, in the case of models with multiple parameters, prospective smoothing implies a uniform degree of smoothness across all parameters, which may not be desired.

In a Bayesian framework, it is possible to define the priors $P(\Theta)$ in such a way as to encourage spatial smoothness.[181,192] In this case, the prior on parameter $\theta_i$ is defined

$$P(\theta_i) \sim \mathcal{N}\Big(0, (\alpha_i \boldsymbol{L}^T \boldsymbol{L})^{-1}\Big) \tag{2.68}$$

where $\boldsymbol{L}$ is the unweighted graph Laplacian[206] and $\alpha_i$ is a smoothness hyperparameter, which is itself inferred upon. This has the form of an MVN, and so can be used within the VB framework. This can be combined with a non-spatial prior (which encodes belief about the range of values $\theta_i$ is expected to take) through a Gaussian process prior.[181]

### 2.4.4 Applications to MRI

The concepts behind Bayesian inference have existed for quite some time, but it has only been in the last two decades that methodological advancements (like VB) and increasing computing power have combined to make the use of Bayes feasible on large, real datasets with high dimensions. In recent years, Bayesian inference, and in particular VB, has been used in a wide range of MRI applications.

The use of Bayesian methods to solve General Linear Models in functional MRI was developed by Friston and colleagues[21,207] in the early 2000s, being based first on the Empirical Bayes method[207] and later on VB.[208] In this field, VB is used to handle both the weights of the linear model and the parameters that define autoregressive noise, which is present in fMRI time series. Penny and colleagues used VB model selection, based on maximization of $\mathcal{F}$, to select the most appropriate noise model; they validated their results by comparison with Gibbs Sampling (an MCMC method).[208] The parameters of the haemodynamic response function (which relates physiological changes to the measured BOLD

signal) have also been modelled in a spatially varying VB framework, which resulted in increased sensitivity to functional activations.[209,210]

VB methods have also been used for determining regions of activation[180,211] and analysing patterns across groups of voxels.[212] Inferring the parameters of more complex models of connectivity is also possible in a Bayesian framework.[213,214] Furthermore, these methods enable the incorporation of spatial priors to improve localization of activation events[215] and the simultaneous use of data from multiple modalities.[216]

Beyond fMRI, Bayesian methods have also recently been used in analysis of diffusion MRI,[217] quantitative susceptibility mapping,[218] intravoxel incoherent motion imaging,[219] and for partial volume correction in MR fingerprinting.[220]

VB has been especially useful in ASL model fitting, where models that describe the change in magnetization of a voxel over time are nonlinear and depend on several parameters which must be estimated simultaneously.[22,113] Some parameters, such as the $T_1$ of tissue and blood have known literature values but may vary slightly between (or within) healthy subjects; thus they can be inferred with priors with small standard deviation $\sigma$, as can biophysical model parameters like ATT or the bolus arrival time. Others, such as CBF, are expected to have similar values in localized areas, so spatial priors can be used.[181] Some, such as the arterial signal contribution, are expected to occur only in certain voxels, and so an ARD (shrinkage) prior can be used to estimate such parameters only when they are warranted by the data.[22]

Bayesian methods have also been recently used in calibrated BOLD model fitting. Simon and colleagues used sampling-based Bayesian inference to infer parameters, including $CMRO_2$, on hypercapnia- and functional-stimulus dual-echo GESSE and ASL data, using a multiple-compartment qBOLD model.[152]

## 2.5 Summary

The purpose of this chapter was to present the necessary background theoretical information for the rest of the Thesis and to survey relevant literature.

The first section dealt with the physical basis for MRI, with a particular focus on the acquisition strategies and contrast manipulations used later. It showed that the GESEPI readout sequence[34] can be used to acquire $R_2'$- or $R_2^*$-weighted data that is robust against larger-scale magnetic field inhomogeneities. It also showed that the ASE sequence[32] produced a contrast based on $R_2'$. These are combined in the GASE sequence,[163] which was used throughout this work to acquire qBOLD data.

The second section discussed acute ischaemic stroke, which is the motivating application for this Thesis. It was proposed that rapid identification of the ischaemic penumbra could improve patient stratification and treatment, and that this could be done through quantification of physiological parameters $CMRO_2$ and/or OEF. The aim of this work was to improve upon existing techniques for quantifying OEF non-invasively. The resulting information can be combined with non-invasive measures of perfusion (such as ASL), and validated against other clinical imaging techniques often used in stroke, such as DWI and diffusion-perfusion mismatch.

The third section described how physiological processes can affect measured MR signals, and in particular presented the quantitative BOLD model,[14] which relates $R_2'$-weighted signal to the parameters OEF and DBV, and which forms the basis of this work. The calibrated BOLD method was also presented as a means of quantifying OEF and $CMRO_2$. Other quantitative MRI methods were also presented, including ASL (which can be used to measure perfusion) and TRUST (which can be used to measure OEF).

The final section presented Bayes' theorem and described how Bayesian inference could be useful when applied to a model like the qBOLD model to infer on physiological parameters. The advantages of the Bayesian approach over frequentist model-fitting techniques are its ability to incorporate prior information (of different kinds) about parameters and to infer on nonlinear models in a hierarchical manner. The variational Bayes approach,[20] which was presented and compared with other techniques for evaluating or estimating the posterior, offers a viable method for performing Bayesian inference on data from a nonlinear model like the qBOLD model.

It is clear that there is significant potential clinical utility in a method that can quantify OEF quickly and non-invasively, and that the qBOLD model, being inferred in a Bayesian framework, offers the best option for doing so.

# 3

# Model Based Bayesian Inference in Quantitative BOLD

## Contents



In this chapter the quantitative BOLD model (presented in Section 2.3.2) is used, in a variational Bayesian framework, to infer physiological parameters (OEF and DBV) from simulated and *in vivo* data from healthy volunteers. Several of the issues which surround this, such as the choice of the precise form of the model, and some of its key parameters, are explored and assessed. The results are compared with a simpler method applied to the same data, and to values of OEF and DBV from

the literature. It was found that simultaneously fitting $R_2'$ and DBV in a Bayesian framework was more accurate at estimating parameter values from simulated data than previous methods. OEF estimates from *in vivo* data were generally lower than what would be expected from the literature, and the causes of this were explored.

## 3.1 Introduction

Quantitative measurements of the BOLD signal can be used to construct maps of parameters related to brain metabolism in a non-invasive way. OEF is of particular relevance as a measure of activity, and can be combined with measurements of cerebral blood flow to quantify metabolism directly. Recently, a streamlined quantitative BOLD (sqBOLD) methodology has been developed and applied to clinical stroke populations.[19,109] This uses ASE data to quantify $R_2'$ and DBV, from which OEF can be calculated.

sqBOLD offers several advantages over other methods: the GESEPI ASE (GASE) acquisition[32,34,163] minimises the effect of macroscopic magnetic field gradients, and the use of a FLAIR preparation removes confounding signal from CSF.[19] However, the stepwise calculation of $R_2'$, then DBV, then OEF, could propagate noise resulting in poor signal-to-noise ratio (SNR), and could introduce bias into the estimates. A curve-fitting approach in which multiple parameters are fitted simultaneously to a more complete qBOLD model[141,152] could overcome the limitations imposed by fitting the linear model required in the existing analysis.

Non-linear model fitting, as is required for the qBOLD model, is notoriously challenging on data with limited SNR. The Bayesian approach (in particular, variational Bayesian (VB) inference - see Section 2.4.3) provides a valuable framework for approaching this problem and have been used in similarly challenging applications such as for perfusion estimation from Arterial Spin Labelling.[22]

In this chapter, simulated ASE data are used to evaluate different versions of the qBOLD model, with the aim of selecting a model that can provide the most reliable estimates of OEF. Certain model parameters and inference parameters are

tested and selected. Then, *in vivo* data are used to compare a fully model-based parameter estimation procedure against the existing method.

## 3.2 Theory

The qBOLD model, proposed by Yablonskiy & Haacke[14] describes how transverse magnetisation in bulk tissue changes in the presence of susceptibility-altering objects. In this case, those objects are blood vessels whose susceptibility difference is proportional to OEF, and the protons in the surrounding tissue are assumed to be relatively stationary with respect to the vessels (the static dephasing regime). The full analytical form of the signal in this case is given by Equations 2.25 and 2.26.

This model assumes that deoxyhaemoglobin is the dominant source of magnetic susceptibility. Therefore, the presence of an additional source of susceptibility, such as myelin in white matter or iron deposited in deep grey matter structures, will confound estimates of OEF and DBV. This has previously been shown to result in the overestimation of $R_2'$ and DBV.[19] Hence the analyses in this chapter (and Chapters 4 and 5) are restricted to grey matter.

**One-Compartment Model**

Under ASE (see Section 2.1.3), a refocussing pulse is applied at time $(TE-\tau)/2$, and the signal is read out at time $TE$. Since signal originating from CSF is nulled by the FLAIR preparation, and since, in grey matter, blood vessels carrying deoxygenated blood are expected to account for less than 5% of the total volume,[221] it could be assumed that the entire measured GASE signal is that which originates from the bulk tissue. In the asymptotic form of Equation 2.25, this can be written either in terms of $\delta\omega$ (which is proportional to OEF) or $R_2'$ (Equations 2.29 and 2.33, respectively). In the former case, the total measured signal at $TE$ can be written:

$$S^t(\tau) = S_0 \cdot \exp\left(R_2^t \cdot TE\right) \cdot \exp\left(\frac{3}{10} \cdot \zeta \cdot (\delta\omega \cdot \tau)^2\right) \qquad |\tau| < t_c \qquad (3.1a)$$

$$S^t(\tau) = S_0 \cdot \exp\left(R_2^t \cdot TE\right) \cdot \exp\left(\zeta - \zeta \cdot \delta\omega \cdot \tau\right) \qquad |\tau| > t_c \qquad (3.1b)$$

where $S_0$ is a factor controlling for constant terms, such as inter-voxel differences in signal, and $R_2^t$ is the $R_2$ of tissue. Similarly, Equation 2.33 can be re-written:

$$S^t(\tau) = S_0 \cdot \exp\left(R_2^t \cdot TE\right) \cdot \exp\left(\frac{3}{10} \cdot \frac{(R_2' \cdot \tau)^2}{\zeta}\right) \qquad |\tau| < t_c \tag{3.2a}$$

$$S^t(\tau) = S_0 \cdot \exp\left(R_2^t \cdot TE\right) \cdot \exp\left(\zeta - R_2' \cdot \tau\right) \qquad |\tau| > t_c \tag{3.2b}$$

These two equations offer alternative versions of a one-compartment (1C) qBOLD model, which each depend on DBV and one other parameter: either OEF or $R_2'$.

**Log-Linear Model**

The sqBOLD technique uses the long-$\tau$ regime of Equation 3.2 to fit $R_2'$ and DBV.[19] $R_2'$-weighted images, acquired at $\tau > t_c$, can be fit to a log-transformed model (L model):

$$\ln S^t(\tau) = -R_2' \cdot \tau + \ln S_{SE}^t + \zeta \tag{3.3}$$

Here $R_2'$ can be calculated as the gradient of $\ln S^t(\tau)$, and $\zeta$ can be obtained by subtraction of $\ln S_{SE}^t$ from the intercept, where $S_{SE}^t$ is the signal measured at the spin echo ($\tau = 0$). OEF can then be calculated using Equation 2.34.

**Two-Compartment Model**

Since the measured GASE signal likely does not originate solely from the bulk tissue, it may be beneficial to model the signal contribution from deoxygenated blood vessels explicitly. This can be done using several different models (described in Section 2.3.3), namely the linear model[144] (Equation 2.38), the 'powder' model[146] (Equation 2.41), and the 'motional narrowing' model[148] (Equation 2.43). For any choice of intravascular model, a two-compartment (2C) model is the weighted sum of it with the $S^t$ (Equation 2.37).

The qBOLD model is expected to have most value in voxels which have a relatively small blood volume and where this additional compartment can correct for the presence of intravascular signal. In the presence of larger blood volume

fractions, whilst the intravascular signal would be appropriate, the assumptions of the extravascular signal model would be invalidated.

## 3.3 Methods

### 3.3.1 Simulations

Simulated qBOLD data were used to examine whether a Bayesian model-based approach was able to estimate OEF more accurately than least-squares fitting to a simplified log-linear model. In MATLAB (MathWorks, Natick, MA), simulated two-compartment ASE qBOLD signals were generated using a 2C model consisting of Equations 2.25, 2.26, 2.43, and 2.37. Signals were simulated with 50 OEF values from 20% to 70% (which includes the expected range of healthy values[222]) and 50 DBV values from 0.3% to 15% (based on the expected range of total blood volume[221]), for a total of 2500 artificial ASE signals.

Gaussian noise was added to simulate 7 SNR values between 5 and 500. Each signal consisted of 24 $R_2'$-weighted images with spin-echo offsets $\tau$ in steps of 4ms between -28ms and +64ms. This optimised range of $\tau$ values were chosen to maximise the SNR of the $R_2'$ parameter estimate.[19] Fractional haematocrit $Hct$ was set at 0.40, the literature value for general circulation,[223] which is similar to what has been used in other related studies.[147,152,165] Previous studies have used lower values such as 0.34,[19,141] in accordance with the Fahraeus effect,[224] which suggests that Hct in small vessels (including capillaries and venules) is lower than in general circulation. This effect has been quantified as a reduction of between 14%[225] and 25%.[226] It is not clear to what extent the range of $Hct$ values present throughout the brain affect the qBOLD signal, or whether an average value can be assumed throughout. Other physiological and sequence parameters were held to constant values, which are given in Table 3.1.

#### Model Parameter Selection

In order to assess the differences between the OEF-based and $R_2'$-based models (Equations 3.1 and 3.2 respectively), a single simulated dataset (OEF=40%, DBV=3%)

| Parameter | Value | Reference |
|---|---|---|
| $Hct$ | 0.40 | Nicoll *et al.*, 2012[223] |
| $\Delta\chi_0$ | 0.264 ppm | Spees *et al.*, 2011[140] |
| $R_2^t$ | 11.5 $s^{-1}$ | He & Yablonskiy, 2007[141] |
| $R_2^{b,true}$ | 5.29 $s^{-1}$ | Berman *et al.*, 2018[148] |
| $t_D$ | 4.51 ms | Berman *et al.*, 2018[148] |
| $B_0$ | 3 T | |
| $TE$ | 74 ms | |
| $TR$ | 3 s | |
| $\tau$ range | -28 to 64 ms | |
| $\tau$ step size | 4 ms | |

**Table 3.1:** Parameter values used for simulating ASE-qBOLD data.

was analysed in a grid search scheme. The posterior probability of each pair of values in the intervals $OEF \in \{20\%, 70\%\}$ and $DBV \in \{0.3\%, 15\%\}$, given the 2C model, was evaluated. The OEF-based and $R_2'$-based models were compared in their accuracy of DBV estimation by marginalizing over OEF and $R_2'$ respectively. Whilst the grid search technique is prohibitive for analysis of *in vivo* data, it enables direct comparison of parameter distributions to determine separability. Grid searches were used to determine which of the OEF-based or $R_2'$-based models were more suitable, based on whether the OEF-DBV or $R_2'$-DBV distributions were more separable.

Another aspect of the qBOLD model was tested using simulated data. The point at which the asymptotic models transition, $t_C$ (Equation 2.30), was defined originally as $t_C = 1.5/\delta\omega$,[14] whereas, more recently, Lee *et al.* used $t_C = 1/\delta\omega$.[165] Since the model itself is phenomenological, parameters such as $t_C$ should be chosen so that the asymptotic model most closely matches the analytical version. For all OEF-DBV pairs, in the absence of noise, the analytical qBOLD model (Equations 2.25 and 2.26) was compared with the asymptotic model (Equation 2.29), and an optimal value for the transition constant $\tau \cdot \delta\omega$ was found using a golden section search (MATLAB's fminbnd).

### Prior Distribution Selection

The full set of simulated data was analysed in a VB scheme, using the Fast ASL and BOLD Bayesian Estimation Routine (FABBER).[22,180,181] The 1C and 2C models were used, with parameters DBV and either OEF or $R_2'$. Prior means $\mu_0$ were taken from the literature for healthy subjects[11,221] and are presented in Table 3.2. The effect of different $\mu_0$ and prior standard deviation $\sigma_0$ were investigated in order to choose values that would not bias the results in the case of very different (e.g. pathological) true values.

VB inference was performed using the 2C model with a range of $\sigma_0$ (between $10^{-1/2}$ and 1000) for each parameter at the highest simulated SNR (SNR=500), with $\mu_0$ fixed to the values in Table 3.2. The absolute difference between the estimate of each parameter and its true value was then computed and averaged over all simulated pairs of OEF and DBV values. In order to minimise the risk of biasing the parameter estimates, the least precise prior which still resulted in a low error was chosen for each parameter, and used in all later inference. Once appropriate precisions were chosen, extreme values of $\mu_0$ were tested to ensure that the chosen prior mean did not significantly affect the results. $\mu_0(R_2') = \{3\text{s}^{-1}, 7\text{s}^{-1}, 15\text{s}^{-1}\}$ and $\mu_0(DBV) = \{0.5\%, 3.6\%, 10\%\}$ were tested, and errors in estimates of DBV and $R_2'$ calculated as above.

### qBOLD Model Comparison

Least-squares regression (LS) and VB inference using each model (L, 1C, and 2C) were performed on the same data, for all OEF-DBV pairs and SNR values. The absolute error between true and estimated OEF and DBV values were averaged across all OEF and DBV values for each SNR, in order to assess the utility of a more complete model, and the effect of noise on estimates. These were compared at the voxel level using two-way ANOVA and Tukey-Kramer (honestly significant difference) pairwise comparisons.

In light of recent efforts to reduce the scan duration for application in clinical research,[109] the same analysis was performed using alternative acquisition

parameters. This acquisition consisted of 11 $R_2'$-weighted images with spin-echo offsets $\tau$ in steps of 8ms between -16ms and +64ms, which represents a scan time reduction of 54%. This data was formed by retroactively removing $\tau$ values from simulated data used in the previous section.

### 3.3.2 Data Collection

Scan data from seven healthy participants (aged 24-32, 4 female), which were collected as part of a previous study,[19] were used to compare non-linear model inference using VB against a linear-least-squares fitting procedure *in vivo*. All imaging was performed on a 3 T Siemens Verio system (Siemens Healthineers, Erlangen, Germany) using the body transmit coil and the vendor's 32-channel receive coil. Subjects were scanned under a technical development protocol agreed with local ethics and institutional committees.

For each subject, a GESEPI ASE (GASE) scan (see Section 2.1.4) with FLAIR preparation ($TI_{FLAIR}$=1210ms) was acquired, with $TR/TE$=3000/74ms, 64×64 matrix, ten slabs, 3.75×3.75×5 mm resolution, and 24 $\tau$ values ranging from -28ms to 64ms in steps of 4ms. Each 5mm slab was constructed by averaging four 1.25mm slices (acquired as 8 k-space partitions including 100% partition oversampling to reduce aliasing) to correct for macroscopic field gradients.[163] Total acquisition time was 9 min 36s.

A high resolution structural MPRAGE image[227] was acquired from each subject, with $TR/TI/TE$=2040/900/4.7ms, flip angle 8°, 192×192×174 matrix, 1×1×1mm resolution. This had a total scan duration of 3 mins 58s, and was acquired for segmentation, in order to generate grey matter masks in which qBOLD model analysis would be performed.

### 3.3.3 Image Analysis

#### Pre-Processing

Data pre-processing was performed in FSL.[228] GASE data were motion-corrected using MCFLIRT,[229] and smoothed with a Gaussian kernel ($\sigma$=0.85mm). This

smoothing procedure was used to reduce the impact of very noisy voxels on overall fitting; however, the kernel was defined such that its full-width-half-maximum is smaller than the size of a voxel, in order to prevent excessive blurring of the images. This maintains the effective spatial resolution of the parameter estimates. Gibbs ringing artefacts were corrected by an iterative process of local subvoxel shifts and resampling, constrained by total variation.[230]

The spin-echo volumes ($\tau$=0) were brain extracted using BET,[231] and segmented using FAST[205] to create grey matter masks that were used to define the region of interest. Structural MPRAGE data were also brain extracted and segmented, then registered to GASE space using FLIRT.[229,232]. From both datasets, grey matter masks were obtained by thresholding the segmented partial volume estimates at 80%, to exclude voxels where partial volumes of white matter or nulled CSF (where the assumptions of the qBOLD model are violated) may severely affect the signal. Visual inspection showed that segmented GASE data produced more consistent maps that overlapped with GM voxels, and had the advantage of not requiring registration and interpolation.

Grey matter SNR was calculated for each subject across all $\tau$ values, in order to determine the approximate range of values from simulation that would be most appropriate. This was done by dividing the mean voxel intensity values within the grey matter mask by the standard deviation of values outside the head.

### qBOLD Model Comparison

*In vivo* ASE data were analysed using the L model, implemented in MATLAB, and the $R_2'$-DBV 1C and 2C models in VB both with and without spatial regularization. The 1C and 2C models were fit to data for all 24 $\tau$ values; whereas the L model only applies to $\tau$=0 and $\tau > t_C$ (for a total of 14 data points). In addition to the motional narrowing model for intravascular signal (2.43), a supplementary analysis of the linear and powder models (Equations 2.38 and 2.41) was also performed. Inference was performed using a 2C model incorporating each different intravascular

| Parameter | Prior Mean $\mu_0$ | Prior Standard Deviation $\sigma_0$ |
|---|---|---|
| DBV (%) | 3.6 | $10^{3/2}$ |
| $R_2'$ ($s^{-1}$) | 2.6 | $10^2$ |
| $S_0$ | 500 | $10^3$ |

**Table 3.2:** Variational Bayes parameters used in FABBER for inference on the qBOLD models. The same prior means and standard deviations were used to initialize the approximate posterior. Mean values for $R_2'$ and DBV are taken from sqBOLD literature.[19]. All other model parameters were fixed to assumed values (Table 3.1).

signal for all subjects (without spatial regularization) in order to compare their impact on final parameter estimates.

Priors and initial posteriors were defined using literature mean values and the standard deviations determined from testing simulated data (see Section 3.4.1). These are given in Table 3.2. Mean GM parameter estimates were compared for each analysis method, for each subject and across the group. Under spatial regularization, each voxel's prior was defined by aggregating the posterior distributions from the 6 adjacent voxels, across 10 iterations. This imposes a degree of spatial smoothness in the parameter distributions.[181]

To determine similarity, estimates were subjected to a two-way ANOVA test to determine whether the group means for each method were equal. In the case of significantly different group means, the Tukey-Kramer (honestly significant difference) method was used to perform pairwise comparisons.

Median GM free energy $\mathcal{F}$ (Equation 2.57) was used to compare the goodness of fit with each regularization method. Group-average $\mathcal{F}$ was –235±53 and –208±51 for the 1C model (without and with spatial regularization, respectively), and –230±58 and –207±50 for 2C. Both differences are statistically significant ($p < 0.001$), but there was no significant difference in $\mathcal{F}$ between the two models (1C and 2C) when the same regularization was used.

A comparison of L, 1C, and 2C models (using VB inference) was also carried out on the same data, analysing only 11 of the originally acquired 24 $\tau$ values, from

-16 ms to +64 ms in steps of 8 ms. The resulting GM mean parameter values were compared between models, and between the 24-$\tau$ and 11-$\tau$ datasets.

To determine the impact of the assumed value of $Hct$=0.40, a further analysis was performed in which the same data (with 24 $\tau$ values) were analysed with all models with $Hct$=0.34 (as used by He & Yablonskiy). It was expected that in the L and 1C models, $Hct$ will act purely as a scaling constant on OEF (Equation 2.34); but since it occurs in the intravascular compartment (Equation 2.44) its effect on $R_2'$ and DBV estimates from the 2C model should also be investigated.

## 3.4 Results

### 3.4.1 Simulated Data

#### Model Parameter Selection

Asymptotic qBOLD models given in terms of OEF and $R_2'$ were compared using grid search posterior sampling of simulated data. The results of this are shown in Figure 3.1. In OEF-DBV space, there was a large region of collinearity between the two parameters, which is likely to prevent accurate estimation of both parameters, as it does not correspond to the Gaussian-like form required for VB (as implemented in FABBER). In contrast, the $R_2'$-DBV space had a posterior distribution in which the two parameters were largely separable and also which could more readily be approximated as a multivariate normal distribution within the VB inference method. Marginalizing over these results with respect to OEF and $R_2'$ yielded DBV likelihood distributions that were directly comparable. The standard deviation in DBV was 1.05% for the OEF-based model, and 1.14% for the $R_2'$ model, suggesting that there was very little difference between the two in their estimation of DBV. The same analysis of OEF estimates derived from each method yielded a standard deviation of 14.5% for the OEF-based model, and 15.8% for the $R_2'$ model.

Simulated data were also used to determine the optimal transition point between the two asymptotic regimes, as a function of $\delta\omega$. This was calculated for each simulated OEF and DBV value, in the intervals OEF$\in \{20\%, 70\%\}$ and DBV$\in \{0.3\%, 15\%\}$. After averaging across the entire parameter space, the optimal

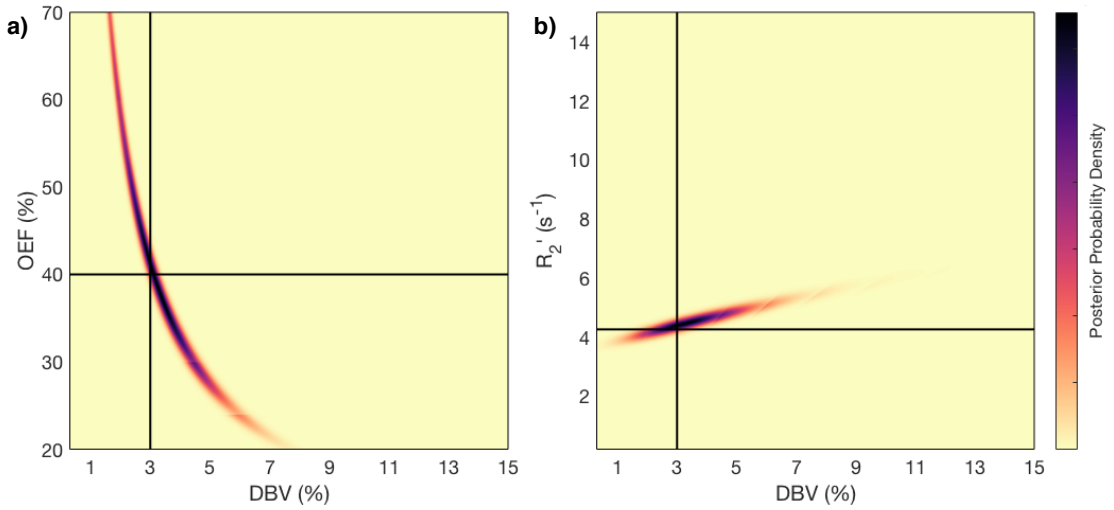


**Figure 3.1:** Results of grid-search posterior sampling on simulated ASE qBOLD data, with SNR 50. **(a)** Posterior probability of OEF-DBV parameter pairs, with true (simulated) values shown as solid black lines. **(b)** Posterior probability of $R_2'$-DBV pairs, using the same data.

transition point was found to be $1.76/\delta\omega$. This value was used in all further analyses of simulated and *in vivo* data, for all models.

### Prior Distribution Selection

Simulated ASE signals were used to compare the L model with the more complicated 1C and 2C models analysed in VB. First, the optimal parameters for VB inference were determined by testing a range of standard deviations for the priors on $R_2'$ (between $10^{-1/2}$ and $10^3$) and DBV (between $10^{5/2}$ and 1). The results of these are shown in Figure 3.2. The error in $R_2'$ was not strongly affected by $\sigma_0$, except at $\sigma_0(R_2') \leq 1$. Similarly, the errors in DBV and OEF diverged quickly at low $\sigma_0(R_2')$, but were consistently low at $\sigma_0(R_2') \geq 10$.

This suggests that $\sigma_0(R_2') = 10^2$ and $\sigma_0(DBV) = 10^{3/2}$ are the least precise values that consistently produce reasonable results, although using an even broader $\sigma_0(R_2')$ was not detrimental. Compared to expected effect sizes on the order of $10^0$ in both $R_2'$ and DBV, these priors are very flat, and should not have a strong effect on the fitting.

Using these $\sigma_0$, the choice of prior mean $\mu_0$ was also investigated by testing extreme values. The error in $R_2'$ and DBV estimates was calculated using each

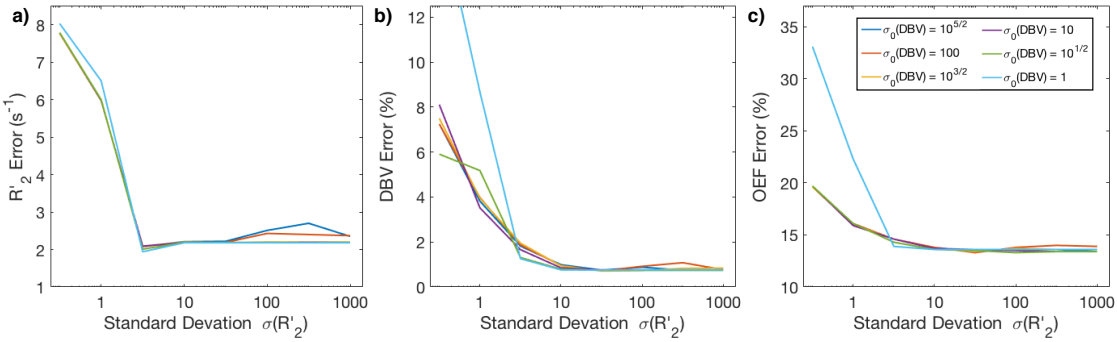


**Figure 3.2:** Optimization of prior standard deviations $\sigma_0$ based on error in parameter estimates on simulated data. **(a)** The effect of priors of $R_2'$ error; **(b)** DBV error; **(c)** OEF error.

combination of $\mu_0(R_2') = \{3\text{s}^{-1}, 7\text{s}^{-1}, 15\text{s}^{-1}\}$ and $\mu_0(DBV) = \{0.5\%, 3.6\%, 10\%\}$, and the standard deviation across all of these was 0.76 $\text{s}^{-1}$ for $R_2'$, and 0.47% for DBV, showing that the choice of $\mu_0$ does not significantly bias the results. This is likely because of the broad priors that were used.

### qBOLD Model Comparison

Using optimized parameters, the simulated ASE signals were analysed using each of the three models (L, 1C, and 2C) at 7 SNR values. Each model was evaluated with both least squares regression (LS) and VB. For each signal, the absolute error between the true value of each parameter and the estimate was calculated. The average errors across the whole parameter space, at each SNR and for each model, are shown in Figure 3.3. The 2C model in LS performed better than any other at estimating $R_2'$. Two-way ANOVA with pairwise comparisons showed that there were not significant differences in estimates of $R_2'$ between all the other methods. The 1C and 2C models in LS performed significantly worse in estimating DBV, and there were no significant differences between the others. At all tested SNRs except 100, the 1C and 2C models in VB performed significantly ($p < 0.001$) better than the L model, or any LS implementations, at estimating OEF. Apart from at very low SNR (SNR$\leq$10) and at SNR=500 there were not significant differences in parameter estimates between the LS and VB implementations of the L model.

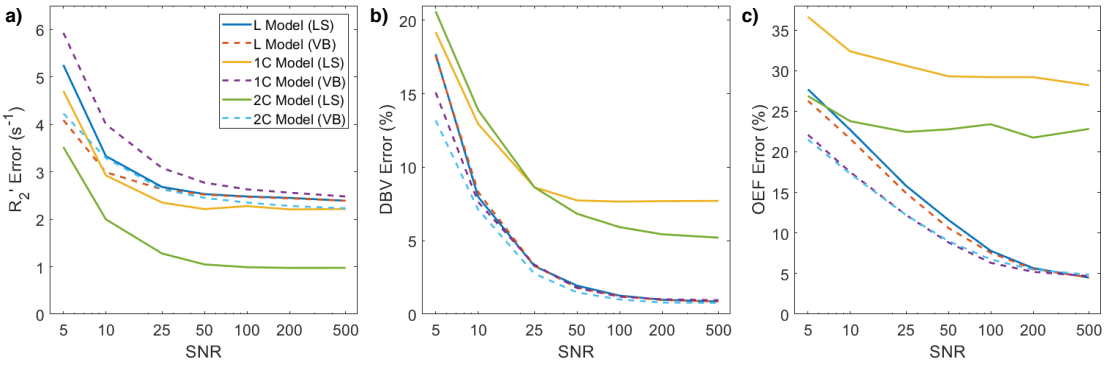


**Figure 3.3:** Error in parameter estimates of **(a)** $R_2'$, **(b)** DBV, and **(c)** OEF as a function of simulated SNR for all three models, under both least squares (LS) and variational Bayes (VB) fitting. Across all SNR levels, the LS implementations of the 1C and 2C models performed poorly in estimating DBV and OEF. At SNRs below 100, the VB implementations of the 1C and 2C models estimated OEF significantly ($p < 0.001$) more accurately than other models.

Across the range of data, with simulated $OEF \in \{20\%, 70\%\}$ and $DBV \in \{0.3\%, 15\%\}$, the 1C and 2C models performed similarly well; however, in the high DBV regime (DBV>10%), the 2C model estimated both $R_2'$ and DBV more accurately than L or 1C models. $R_2'$ error was 14±3% lower with 2C estimation ($p < 0.001$, based on a one-sample t-test), and DBV error was 24±9% lower ($p < 0.05$).

The results of the analysis using an alternative, shorter acquisition protocol are presented in Figure 3.4, which parallels Figure 3.3 in showing the error in estimations of $R_2'$, DBV, and OEF, as a function of SNR. The errors in OEF estimation across all SNRs were higher in the case of fewer $\tau$ values, but in this case the 2C model offered an even greater improvement over the L model than 1C, especially at lower SNR (SNR≤50).

### 3.4.2 *In Vivo* Data

The analysis methods (L model in least squares fitting, and 1C and 2C models in VB, with and without spatial regularization) were tested on GASE data from 7 healthy subjects. Computation time for the L model analysis averaged 2.5 seconds per subject, for the entire volume, and for both 1C and 2C models in VB was 10.3 seconds each per subject. VB with spatial regularization took, on average, 11.8 seconds per subject (for 1C and 2C models).

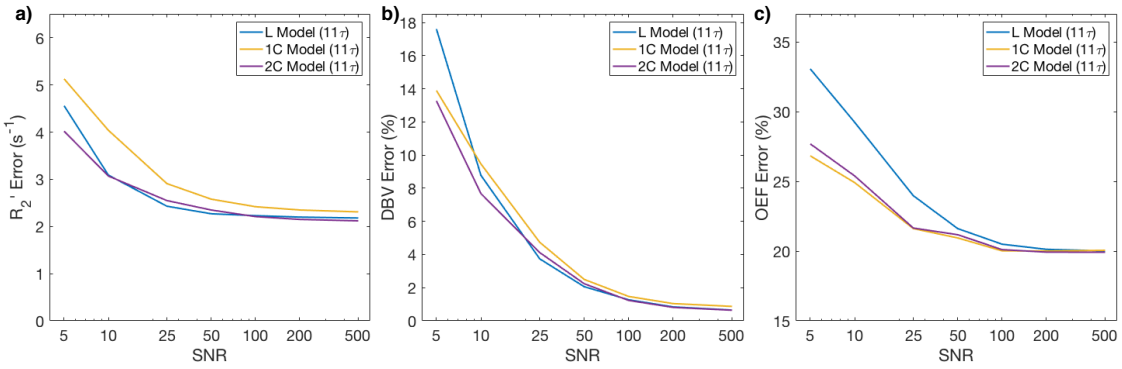


**Figure 3.4:** Error in parameter estimates of **(a)** $R'_2$, **(b)** DBV, and **(c)** OEF as a function of SNR for all three models with VB fitting, using a reduced simulated dataset with 11 $\tau$ values from -16ms to +64ms (in steps of 8ms). Results are comparable for $R'_2$ and DBV estimation between all three models, but the 1C and 2C models perform better at OEF estimation, especially at low SNR.

Grey matter SNR was calculated by dividing the mean GASE voxel intensity within GM by the standard deviation of the noise in empty space outside the head. Across all subjects and $\tau$ values, SNR was 89±16.

In order to confirm that the VB model fitting was working as intended, histograms of the GM parameter values were plotted, which are shown in Figure 3.5. These show that the parameter estimates tended to fall in Gaussian-like distributions (although OEF and DBV values are hard-thresholded at 0), which validate using the mean grey matter value as a representative summary of the entire distribution of values.

### qBOLD Model Comparison

Mean GM estimates for $R'_2$, DBV, and OEF for each subject are presented in Table 3.3, as well as inter-voxel standard deviations of parameter estimates, which account for physiological variation as well as uncertainty in model fitting. Maps from an example subject are shown in Figure 3.6, and a group-level comparison is shown in Figure 3.7. The group-average grey matter OEF estimate from the L model was 21±2%, the 1C model estimated 17±2% without spatial regularization, and 19±2% with spatial regularization. The 2C model estimated OEF at 18±2% and 20±2% (without and with spatial regularization, respectively). Group-average

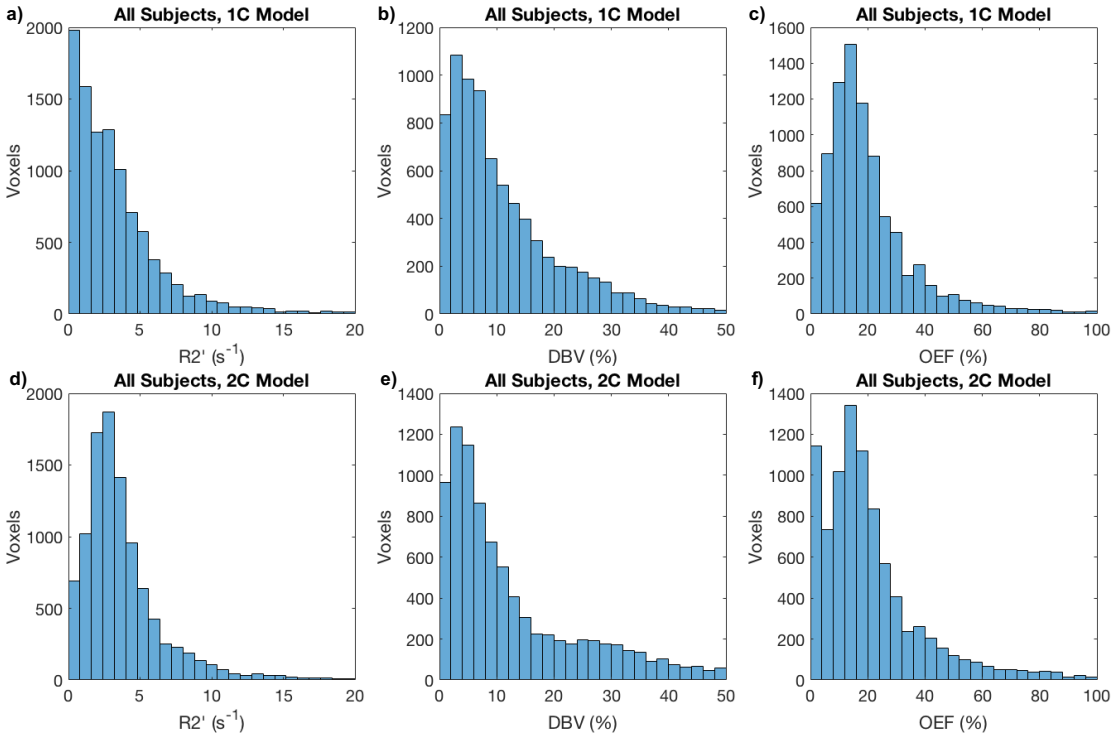


**Figure 3.5:** Grey matter estimates of **(a,d)** $R_2'$, **(b,e)** DBV, and **(c,f)** OEF, across all subjects (N=7) from VB model fitting using the 1C model (first row) and 2C model (second row). In all cases, there is a clear modal range of values, which corresponds approximately to the mean values reported in Table 3.3 and shown in Figure 3.7.

grey matter DBV was 5.38±0.62%, 5.99±0.43%, and 6.58±0.26% for L, 1C, and 2C models respectively.

Since it was necessary to exclude voxels with certain very high parameter values, it is possible that the mean estimate across a subject may have been skewed. The mode could be a more useful comparison, and Table 3.4 shows these results. When calculating the mode on continuous data, it is necessary to group values into bins. The choice of number of the total number of bins to use affected the modal values in all cases. Since there are approximately 1500 grey matter voxels for each subject, $\sqrt{1500} \approx 40$ bins were used.

| | Mean Grey Matter $R_2'$ ($s^{-1}$) | | | | |
|---|---|---|---|---|---|
| **Model** | **L** | **1C** | **1C** | **2C** | **2C** |
| **Regularization** | **None** | **None** | **Spatial** | **None** | **Spatial** |
| 1 | 3.1±1.9 | 3.6±1.1 | 3.6±1.0 | 3.6±1.3 | 3.6±1.0 |
| 2 | 3.7±2.8 | 3.9±1.4 | 4.2±1.4 | 4.0±1.8 | 4.2±1.4 |
| 3 | 3.0±2.7 | 3.2±1.1 | 3.4±1.2 | 3.5±1.7 | 3.5±1.2 |
| 4 | 3.5±3.2 | 3.9±1.3 | 4.3±1.3 | 4.1±1.8 | 4.4±1.4 |
| 5 | 3.1±2.9 | 3.4±1.4 | 3.4±1.5 | 3.9±2.1 | 3.3±1.8 |
| 6 | 3.5±2.9 | 3.9±1.1 | 4.1±1.2 | 4.0±1.4 | 4.2±1.2 |
| 7 | 2.8±2.6 | 3.9±1.4 | 3.0±1.8 | 3.5±2.7 | 2.8±2.0 |
| Mean | 3.2±0.3 | 3.5±0.4 | 3.8±0.4 | 3.8±0.4 | 3.6±0.4 |
| | **Mean Grey Matter DBV (%)** | | | | |
| **Model** | **L** | **1C** | **1C** | **2C** | **2C** |
| **Regularization** | **None** | **None** | **Spatial** | **None** | **Spatial** |
| 1 | 4.9±3.9 | 6.7±3.2 | 6.7±3.6 | 6.4±3.0 | 6.4±3.5 |
| 2 | 6.3±5.4 | 7.4±4.0 | 7.6±4.4 | 7.1±3.8 | 7.1±4.2 |
| 3 | 4.4±3.9 | 6.6±3.1 | 6.6±3.4 | 6.4±2.9 | 6.4±3.2 |
| 4 | 5.4±5.1 | 7.3±3.4 | 7.5±3.8 | 6.7±3.1 | 7.4±3.7 |
| 5 | 5.8±5.4 | 6.9±3.4 | 6.9±3.6 | 6.1±3.0 | 6.8±3.6 |
| 6 | 5.8±5.8 | 6.9±3.3 | 6.5±3.6 | 6.0±2.9 | 6.5±3.6 |
| 7 | 5.2±5.1 | 6.1±3.5 | 6.2±3.7 | 5.8±3.1 | 6.6±3.7 |
| Mean | 5.4±0.6 | 6.8±0.4 | 6.9±0.5 | 6.4±0.4 | 6.7±0.4 |
| | **Mean Grey Matter OEF (%)** | | | | |
| **Model** | **L** | **1C** | **1C** | **2C** | **2C** |
| **Regularization** | **None** | **None** | **Spatial** | **None** | **Spatial** |
| 1 | 24±17 | 19±11 | 22±12 | 20±11 | 23±13 |
| 2 | 20±14 | 17±11 | 18±11 | 17±11 | 20±12 |
| 3 | 23±17 | 16±11 | 19±12 | 17±11 | 19±12 |
| 4 | 21±14 | 17±10 | 17±10 | 19±11 | 18±11 |
| 5 | 20±14 | 16±11 | 18±12 | 18±12 | 20±14 |
| 6 | 23±17 | 19±12 | 20±12 | 21±12 | 22±12 |
| 7 | 18±15 | 16±13 | 16±13 | 16±15 | 18±15 |
| Mean | 21±2 | 17±2 | 19±2 | 18±2 | 20±2 |

**Table 3.3:** Parameter estimates of $R_2'$, DBV, and OEF using the three qBOLD models: linear model (L) considering only tissue signal at long-$\tau$ and $\tau = 0$ data points; a one-compartment (1C) model considering tissue signal across all $\tau$; and a two-compartment model (2C) that includes intravascular signal. Results are given for 1C and 2C models with and without spatial regularization. Table shows grey matter mean ± grey matter inter-voxel standard deviation, for 7 healthy subjects, and group mean ± group standard deviation.

| | Modal Grey Matter $R_2'$ ($s^{-1}$) | | | | |
|---|---|---|---|---|---|
| **Model** | **L** | **1C** | **1C** | **2C** | **2C** |
| **Regularization** | **None** | **None** | **Spatial** | **None** | **Spatial** |
| 1 | 2.4 | 2.4 | 2.4 | 2.5 | 3.4 |
| 2 | 2.5 | 2.8 | 2.8 | 2.8 | 2.8 |
| 3 | 1.9 | 1.3 | 1.6 | 1.0 | 2.0 |
| 4 | 2.5 | 2.8 | 2.8 | 2.8 | 3.2 |
| 5 | 1.9 | 2.8 | 1.3 | 2.8 | 1.3 |
| 6 | 2.2 | 2.8 | 2.9 | 2.8 | 2.2 |
| 7 | 1.6 | 1.4 | 3.1 | 1.3 | 0.5 |
| Group Mode | 2.2 | 2.8 | 2.9 | 2.2 | 1.9 |
| | **Modal Grey Matter DBV (%)** | | | | |
| **Model** | **L** | **1C** | **1C** | **2C** | **2C** |
| **Regularization** | **None** | **None** | **Spatial** | **None** | **Spatial** |
| 1 | 4.2 | 0.1 | 3.1 | 0.1 | 2.5 |
| 2 | 4.3 | 0.1 | 6.2 | 0.1 | 1.5 |
| 3 | 1.7 | 0.1 | 1.3 | 0.1 | 0.5 |
| 4 | 3.5 | 0.1 | 7.5 | 0.1 | 2.5 |
| 5 | 1.3 | 0.1 | 2.5 | 0.1 | 0.5 |
| 6 | 2.3 | 0.1 | 3.5 | 0.1 | 2.5 |
| 7 | 3.5 | 0.1 | 1.4 | 0.1 | 1.5 |
| Group Mode | 2.5 | 0.1 | 2.5 | 0.1 | 1.5 |
| | **Modal Grey Matter OEF (%)** | | | | |
| **Model** | **L** | **1C** | **1C** | **2C** | **2C** |
| **Regularization** | **None** | **None** | **Spatial** | **None** | **Spatial** |
| 1 | 17.8 | 17.9 | 13.4 | 17.9 | 13.0 |
| 2 | 17.2 | 14.0 | 12.6 | 17.8 | 14.6 |
| 3 | 18.0 | 17.7 | 13.7 | 17.7 | 14.0 |
| 4 | 21.8 | 17.9 | 13.4 | 17.8 | 12.5 |
| 5 | 14.0 | 14.0 | 11.7 | 14.0 | 8.7 |
| 6 | 17.0 | 17.9 | 16.1 | 18.0 | 16.9 |
| 7 | 13.5 | 14.0 | 4.8 | 18.0 | 6.0 |
| Group Mode | 18.0 | 16.5 | 13.7 | 18.0 | 13.0 |

**Table 3.4:** Modal parameter estimates of $R_2'$, DBV, and OEF using the three qBOLD models: linear model (L) considering only tissue signal at long-$\tau$ and $\tau = 0$ data points; a one-compartment (1C) model considering tissue signal across all $\tau$; and a two-compartment model (2C) that includes intravascular signal. Results are given for 1C and 2C models with and without spatial regularization. Voxel values for each subject and model were collected into 40 bins of equal widths. The table shows the central value of the modal bin in each case. The values of 0.1 for DBV under 1C and 2C model suggest that 0 is the modal value in those cases.

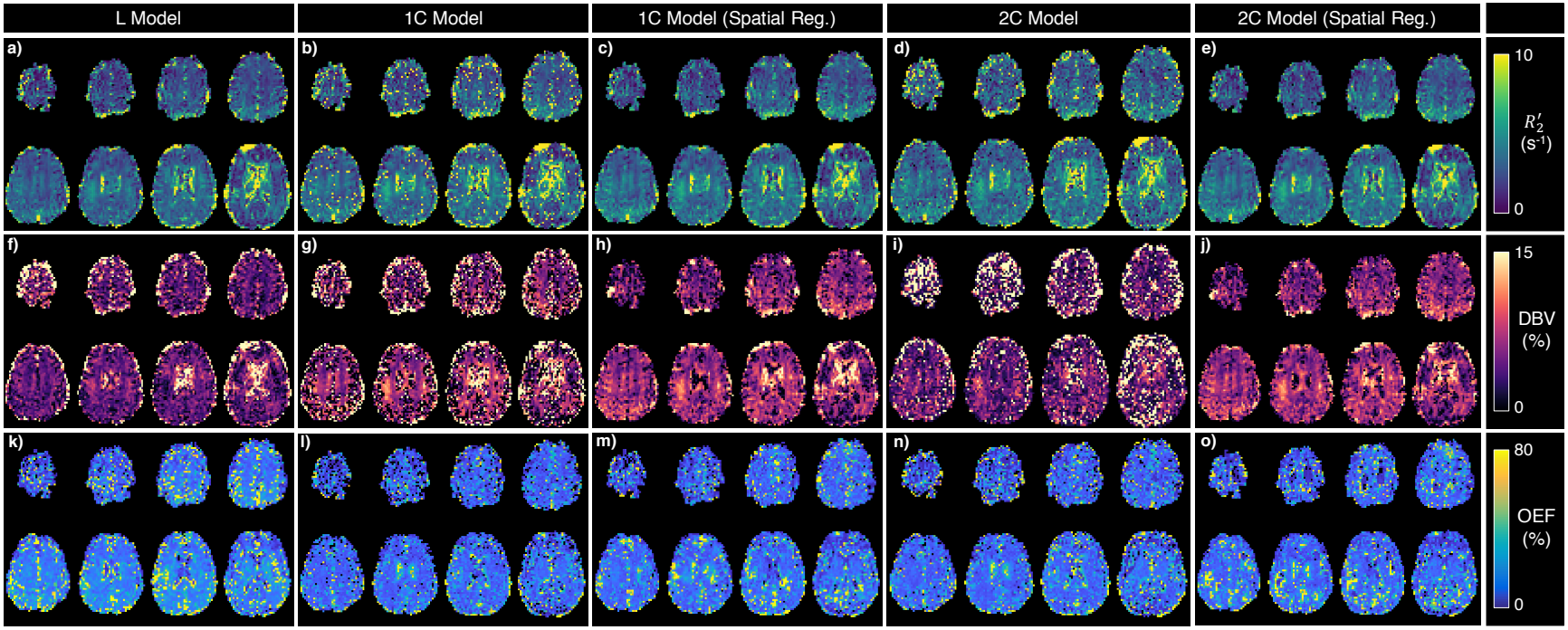


**Figure 3.6:** Example parameter maps for a single subject, showing estimated $R_2'$ (top row), DBV (middle row) and OEF (bottom row), using the L model (first column), 1C model (second column), 1C model with spatial regularization (third column), 2C model (fourth column), and 2C model with spatial regularization (fourth column). For all parameters, the use of spatial regularization drastically reduces the number of bright voxels, where parameters were previously estimated as extreme values.

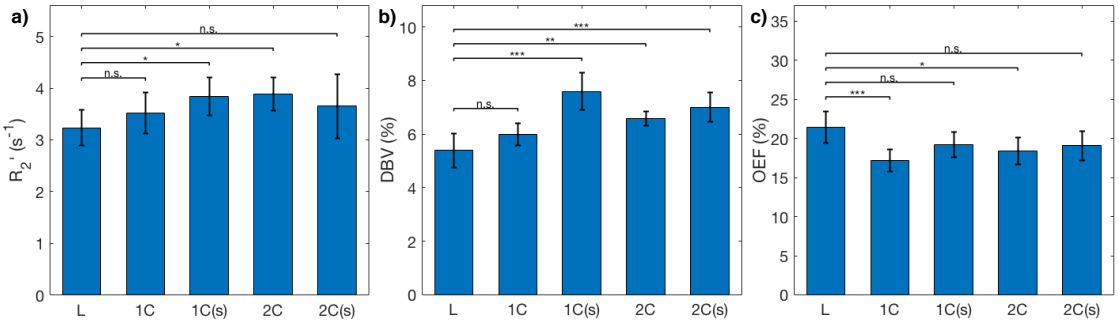


**Figure 3.7:** Group (N=7) average GM estimates of **(a)** $R_2'$, **(b)** DBV, and **(c)** OEF, with error bars indicating inter-subject standard deviation, for the L model, and 1C and 2C models; (s) indicates spatial regularization. Two-way ANOVA and pair-wise comparisons show significant differences (marked with asterisks *) between groups.

In almost all cases, the mean parameter estimates were higher than the modal estimates, suggesting that the means were being skewed by a small number of voxels with very high values. In the case of DBV in the non-spatial regularized models, the modal bin was the one closest to zero, suggesting that the distribution of values throughout the brain is not Gaussian (as illustrated in Figure 3.5b,e).

At the inter-subject level, the variance in $R_2'$ improved significantly (based on an F-test with $\alpha$=0.05) with the 1C model (both with and without spatial regularization) compared to the L model. Group-average grey matter standard deviation of $R_2'$ was 2.7s$^{-1}$ in least-squares fitting, compared to 1.21s$^{-1}$ under VB. Variances in OEF and DBV were lower in spatially-regularized VB, but were not statistically significant. At the intra-subject level, the improvements of VB were statistically significant in all subjects for $R_2'$, and in 4 of 7 subjects for DBV and OEF (based on an F-test with 100 degrees of freedom). Spatially regularized VB made a significant improvement in the variances of all parameters across all subjects. This effect can be seen in the relative number of voxels which contain values that are not physically plausible, such as those with OEF or DBVs greater than 100%. Across the group, the proportion of grey matter voxels with OEF estimates greater than 100% was 33.7% under VB without spatial regularization, compared to 8.6% with spatial regularization (under the L model, the proportion was 18.8%). Figure 3.6 illustrates this improvement. Using the 2C model also resulted in a decrease in

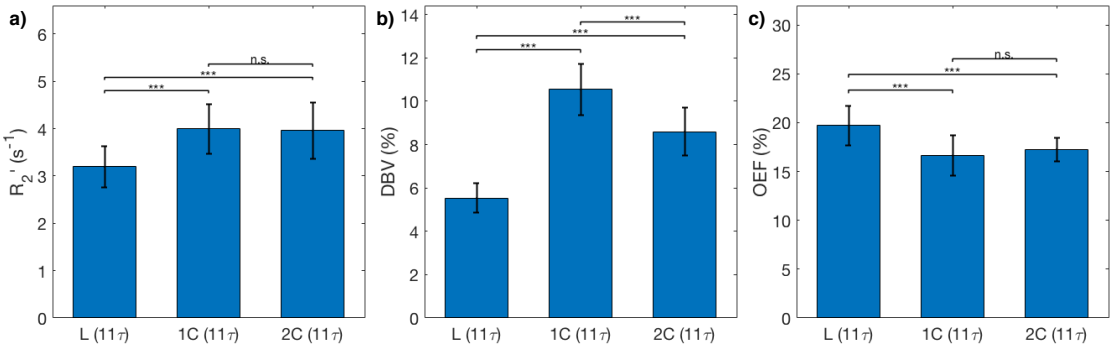


**Figure 3.8:** Group average GM estimates of **(a)** $R_2'$, **(b)** DBV, and **(c)** OEF, with error bars indicating inter-subject standard deviation, for the L model, and 1C and 2C models (VB inference, without spatial regularization), on data with 11 $\tau$ values (from -16ms to 64ms in steps of 8ms).

the proportion of voxels with OEFs or DBVs above 100% (17.7% and 8.1% without and with spatial regularization, respectively).

Two-way ANOVA showed statistically significant differences in average GM estimates of $R_2'$ between L model and the 1C and 2C models inferred under VB. There was a significant difference between L model and 1C model estimates of DBV, but not between L and 2C. There were significant differences between the L model and all others (except non-spatially regularized 1C model) in estimates of OEF. For both 1C and 2C, across all parameters, there were no group-level statistically significant differences between estimates made with and without spatial regularization.

The same comparison was carried out between the L, 1C, and 2C models on the same data with only 11 $\tau$ values. Inter-subject GM average parameter estimates are shown in Figure 3.8, which parallels Figure 3.7. The 1C model estimated DBV to be much higher than the other models. There was a statistically significant difference ($p < 0.001$) between OEF estimates made with the L model on 11-$\tau$ versus 24-$\tau$ data, but no significant difference between estimates made with the 1C or 2C models, suggesting that these more complete models are more robust to changes introduced by undersampling in $\tau$.

Median GM free energy was used to compare the goodness of fit with each regularization method. Group-average free energy was –235±53 and –208±51 for 1C model (without and with spatial regularization, respectively), and –230±58 and

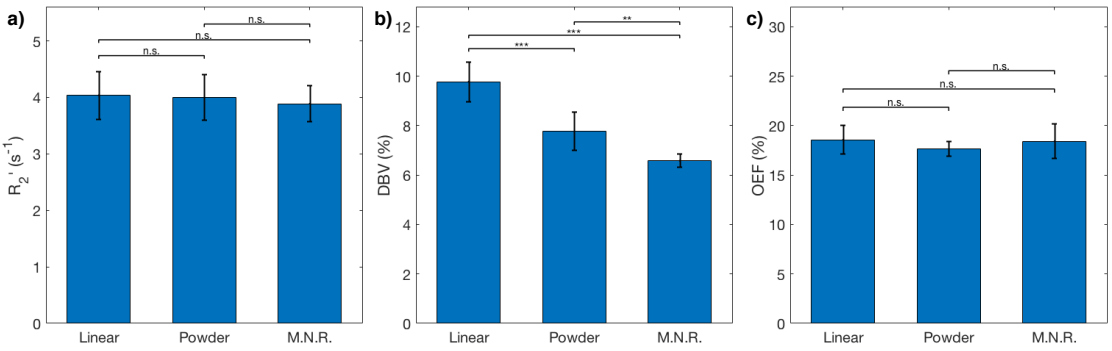


**Figure 3.9:** Group average GM estimates of **(a)** $R_2'$, **(b)** DBV, and **(c)** OEF, with error bars indicating inter-subject standard deviation, for the 2C model using three different models of the intravascular signal contribution $S^b$: linear model (Equation 2.38), powder model (Equation 2.41), and motional narrowing model (MNR - Equation 2.43). Two-way ANOVA and pair-wise comparisons showed that there was no significant difference in estimates of $R_2'$ or OEF, but that all three methods resulted in different average DBV estimates.

–207±50 for 2C. Both these differences were statistically significant with $p < 10^{-3}$. There were no significant differences in free energy between the two models when the same regularization was used.

### Intravascular Model Comparison

An additional analysis of the 2C model was performed using different models of the intravascular signal, which is shown in Figure 3.9. This shows that there was no significant difference in $R_2'$ or OEF estimation between the three intravascular signal models. There was a significant difference in DBV estimation, and the motional narrowing model resulted in DBV estimates that were closest to what was expected from the literature.

Table 3.5 (which parallels Table 3.3) shows the results of inference using the 2C model, with an assumed $Hct$ of 0.34. DBV estimates were higher under the spatially-regularized 2C model with $Hct$=0.34, which is to be expected given the dependence on $Hct$ in the intravascular compartment model's field inhomogeneity parameter $G_0$ (Equation 2.44). OEF estimates were also higher with a lower $Hct$ for the 2C model, both with and without spatial regularization. As expected, there was no difference in $R_2'$ or DBV estimates based on $Hct$ using the L or 1C models

| | $R_2'$ ($s^{-1}$) | | DBV (%) | | OEF (%) | |
|---|---|---|---|---|---|---|
| **Regularization** | **None** | **Spatial** | **None** | **Spatial** | **None** | **Spatial** |
| 1 | 3.7±2.4 | 3.9±2.3 | 6.6±3.3 | 8.1±2.6 | 22±15 | 22±14 |
| 2 | 4.0±3.5 | 4.3±3.3 | 6.8±5.1 | 9.4±3.5 | 20±17 | 20±15 |
| 3 | 3.4±3.2 | 3.4±3.2 | 5.9±3.6 | 7.5±3.0 | 20±16 | 21±15 |
| 4 | 4.1±3.6 | 4.4±3.8 | 6.4±4.4 | 9.3±3.8 | 22±17 | 20±15 |
| 5 | 3.5±3.2 | 3.7±3.5 | 6.0±5.6 | 8.7±4.0 | 20±18 | 19±16 |
| 6 | 4.1±3.7 | 4.2±3.6 | 7.1±4.9 | 8.3±4.2 | 19±17 | 23±16 |
| 7 | 3.5±3.0 | 3.0±3.3 | 5.5±3.7 | 7.1±3.0 | 20±16 | 19±15 |
| Mean | 3.6±0.4 | 3.9±0.5 | 6.3±0.5 | 8.4±0.9 | 21±1 | 21±1 |

**Table 3.5:** Parameter estimates of $R_2'$, DBV, and OEF using the 2C qBOLD model, with $Hct$ fixed to 0.34 (as opposed to $Hct$=0.40 as in Table 3.3). The table shows GM mean ± GM inter-voxel standard deviation, for 7 healthy subjects, and group mean ± group standard deviation.

(not shown). Therefore, the OEF estimates from the L or 1C model were scaled as the ratio of the $Hct$ values: a 17.5% increase in OEF with $Hct$=0.34.

## 3.5 Discussion

### 3.5.1 Improvements to Model Fitting

#### Parameter Selection

Previously published work[165,233] has shown that the qBOLD model is not optimally suited for simultaneous estimation of OEF and DBV, which are important parameters in research or clinical assessment of brain metabolism. In this chapter, simulated data were used to demonstrate the collinearity between OEF and DBV that makes accurate estimation difficult. It also showed that the likelihood distribution in $R_2'$-DBV space (Figure 3.1) had visibly lower correlation between the parameters, providing the opportunity to estimate them accurately and simultaneously. Furthermore, the distribution was relatively smooth and symmetrical in both the $R_2'$ and DBV dimensions, so the assumption of a multivariate normal distribution is reasonable, making these parameters suitable for VB analysis.

Simulated ASE-qBOLD data were used to optimize parameters for VB inference. In particular, prior standard deviations were chosen that resulted in the most

accurate estimation across a broad range of OEF values (from 20% to 70%, encompassing both healthy and pathological values[222]) and DBV values (from 0.3% to 15%[221]). The prior mean values were chosen based on relevant prior work.[19] It would also be possible to use values from other imaging modalities to define prior means. For example, a hyperoxia experiment could be used to estimate venous cerebral blood volume in grey matter,[234] which could be used to inform the prior on DBV. It was shown, however, that significantly changing the prior means does not have a detrimental effect on the accuracy of parameter estimation. This is to be expected given the deliberate choice of broad standard deviations for the priors.

**Model Comparison**

Simulated data with a range of SNRs were also used to compare least-squares fitting of a log-linear model with VB inference on the asymptotic qBOLD model with one or two compartments. The model used for the second (intravascular) compartment was one that accounts for the fact that spins inside blood vessels diffuse over a significantly greater distance than the size of a red blood cell in TE, so they are in the motional narrowing regime.[147] Figure 3.3 showed that VB inference using the 1C or 2C models produced OEF estimates that were significantly more accurate than the L model at SNRs below 100, and estimated both OEF and DBV more accurately than the 1C and 2C models fit using least squares regression. Though LS regression of the 2C model estimated $R_2'$ more accurately than other methods, it also performed worse in DBV estimation, leading to poorer OEF estimates overall, compared with the VB implementation of the same model.

Across all parameters, there was not a substantial difference in performance between the 1C and 2C models. This is likely to be due to the fact that, in voxels with normal DBV, the intravascular compartment contributes a very small amount to the overall signal, and so could potentially be ignored. Similarly, additional analysis showed that the 1C and 2C models were more accurate at estimating $R_2'$ and OEF on sparser data, particularly at low SNR (see Figure 3.4). The difference in OEF error between L and 2C models in Figure 3.4 is greater than in Figure 3.3,

suggesting that the use of this analysis framework is even more important when used with shorter acquisition times, such as in a clinical protocol.

One of the limitations of this study was the use of the analytical qBOLD model as the ground truth. Generation of synthetic qBOLD signals using a more detailed model incorporating different vascular compartments and vessel sizes would be more representative of *in vivo* data. Chapter 5 deals with the integration of such models to validate and optimise new streamlined qBOLD implementations.

### 3.5.2 *In Vivo* Validation

The same analyses were applied to GASE data from 7 healthy subjects, and GM mean parameter estimates were compared at the group level. Statistically significant differences were found between the L model and 1C and 2C models in $R_2'$ and OEF estimation (but not between 1C and 2C), and between the L model and 1C model (but not 2C) in DBV estimation. The grey matter inter-voxel standard deviations of all parameters were significantly lower in VB estimation than with the L model. This suggests that VB inference with a more complete model is less susceptible to fitting extreme values. Inter-voxel standard deviations were higher than the errors reported for simulated data of the same SNR because they also account for physiological variation across grey matter. The number of voxels with un-physiological values was reduced when using the 2C model compared with the 1C model, suggesting that modelling the blood signal provides an improvement to overall model fitting. The choice of intravascular signal model within the 2C model affected estimates of DBV, but not of $R_2'$ or OEF, at the group level. The motional narrowing model was preferred, because it has been shown from a theoretical perspective to model signal evolution accurately in the blood following a refocussing pulse.[147]

The expectation of spatial homogeneity in parameters can be incorporated into VB analysis using spatial regularization, in which the estimated posterior distributions of adjoining voxels are used as priors in an iterative process. The effect of spatial regularization was tested in both the 1C and 2C models. In both cases, though there was not a significant change in group-level parameter averages,

the median free energy increased significantly, suggesting a better fit of the model to the signal. The resulting parameter maps (exemplified in Figure 3.6) were also more homogeneous, and had fewer voxels where parameters had been estimated as having un-physiological values (such as OEFs above 100%).

The parameter estimates obtained from all methods are susceptible to partial volume effects from infiltrating white matter (where the assumptions of the qBOLD model do not hold), especially given the large voxel size used. By defining the grey matter segmentation threshold more strictly, it is possible to reduce this effect and to obtain a more accurate grey matter average, although the whole-brain maps still contain mixed voxels where estimates are not accurate. A model that describes the qBOLD signal in white matter could be used alongside a partial volume correction paradigm, as used in the analysis of arterial spin labelling data,[235] to correct for this effect. Alternatively, acquiring data with a larger matrix size (such as 96×96 instead of 64×64) could result in more voxels that are almost entirely grey matter, and thereby mitigate the influence of partial GM voxels.

### 3.5.3 Comparison with Literature Values

Parameter estimates and comparable literature values can be found in Table 3.6. The average grey matter $R_2'$ estimate of 3.7±0.4s$^{-1}$ was higher than the 2.9±0.4s$^{-1}$ reported by He & Yablonskiy[141] and the 3.1±0.3s$^{-1}$ reported by Simon *et al.*[152] However, both of those apply the qBOLD model to GESSE data, which requires simultaneous quantification of $R_2$ and $R_2'$, whereas the GASE data used here is not sensitive to $R_2$.

Grey matter DBV was here estimated to be 7.00±0.55%, which is significantly higher than reported elsewhere, although there is considerable variation in the literature, with DBV ranging from 1.75±0.13%[141] to 4.9±2.0%[165] or up to 5%.[142] This may be due to uncertainty introduced by assuming values of parameters used to calculate actual DBV from apparent DBV (Equation 2.35), or due to the signal transient often observed at $\tau$=0 (see, in particular, He & Yablonskiy, 2007,[141] Figure 1C). Here, signal was consistently higher at $\tau$=0 than would be expected, which

| **Method** | $R_2'$ ($s^{-1}$) | **DBV (%)** | **OEF (%)** |
|---|---|---|---|
| Log-Linear qBOLD | 3.2±0.3 | 5.39±0.62 | 21.4±2.1 |
| 1C qBOLD (spatially regularized) | 3.8±0.3 | 7.59±0.70 | 19.2±1.6 |
| 2C qBOLD (spatially regularized) | 3.7±0.4 | 7.00±0.55 | 19.1±1.8 |
| GESSE qBOLD[141] | 2.9±0.4 | 1.75±0.13 | 38.3±5.3 |
| GESSE qBOLD[16] | - | 2.54±0.40 | 26.9±2.5 |
| GESSE qBOLD[152] | 3.1±0.4 | - | - |
| GESFIDE[151] | 2.7±0.4 | - | - |
| GESSE[151] | 2.7±0.3 | - | - |
| Neural network qBOLD[153] | - | 4.2±0.1 | 40±1 |
| Conventional qBOLD[165] | - | 4.9±2.0 | 31.8±6.0 |
| Interleaved qBOLD[165] | - | 3.1±0.5 | 39.9±3.3 |
| TRUST[59] | - | - | 35±6 |
| PET[11] | - | - | 41±9 |

**Table 3.6:** Group GM average parameter estimates for $R_2'$, DBV, and OEF, showing group mean ± group standard deviation, with comparisions with other methods from the literature.

may have led to underestimation of $\zeta'$ in the linear model. The 1C and 2C models, which are not dependent on a single data point for their DBV estimation, should be more robust against this error than the L model. In this study, the 2C model had less inter-subject variation in DBV estimates than the 1C model.

### Sources of OEF Error

OEF estimates obtained using sqBOLD (with any analysis method) are significantly lower than those obtained using GESSE-qBOLD[141,153] or non-qBOLD methods such as TRUST[59] and oxygen-15 tracer-based PET.[11] This is in part due to the over-estimation of DBV that is consistently reported in ASE-based qBOLD studies. It may also be due to the assumed value of $Hct$=0.40. The analysis with $Hct$=0.34 led to an increase in estimated OEF to 21% (with the 2C model), which is closer to literature values, but was accompanied by an increase in estimated DBV to 8.4%, which is even further from what would be expected. The exact value of average $Hct$ in GM is not known, although a reduction of around 15% compared to the arteries (where $Hct \approx 0.40$) is supported by Calamante *et al.*[225] It is possible

that larger veins (with $Hct$=0.40) may contribute more to the ASE qBOLD signal than smaller vessels with lower $Hct$. Similarly, this study assumed $\Delta\chi_0$=0.264 ppm,[140] as opposed to $\Delta\chi_0$=0.18 ppm used in older studies.[142] However, despite this systematic offset it has been demonstrated elsewhere that OEF estimates using this experimental technique are modulated by pathology.[109]

Comparing qBOLD-based OEF methods with other modalities (such as TRUST) is not necessarily the most useful, since $R_2'$ may vary most significantly with capillary oxygen saturation, as opposed to the whole-brain arterial-venous difference measured with TRUST. It may be that the lower OEF values obtained here are closer to a mean OEF, as measured in the capillaries. However, since GESSE-qBOLD methods have obtained higher OEF estimates that the ASE-based qBOLD methods used here, this may account for only part of the discrepancy.

OEF overestimation may also be due to error in $R_2'$ estimation, which could be caused by diffusion in the tissue compartment, which is ignored in the static dephasing model.[14] Simulation and *in vivo* studies have shown that diffusion of water in brain parenchyma affects the BOLD signal measured under the GESSE sequence[154,159] and ASE.[151] A qBOLD model which accounts for diffusion in ASE, like that constructed by Dickson and colleagues,[160] may enable more accurate estimation of $R_2'$ and DBV, although it requires quantification (or assumption) of the rate of diffusion, and the distribution of vessel sizes in grey matter. The GESEPI acquisition used[34,163] reduces the effect of magnetic field inhomogeneities, and thereby improves the physiological specificity of $R_2'$ estimation, but does not perfectly remove them, which may explain why DBV estimates are higher than those obtained after retrospective magnetic field gradient correction.[150]

A further source of potential error is the use of the mean parameter estimate across grey matter as the point of comparison. This may be skewed by outlying values, and is affected by the fact that very high parameter values were excluded at a particular cut-off point (100%, in the case of OEF). The data show that, at the subject and group level (see Figure 3.5) the parameters do not always fall in a Gaussian distribution. The mode may convey useful information, and

could instead be used as the 'whole brain' average; however, this would make results not directly comparable to those in the literature (in which the mean is typically reported[141,151,152,162,236]), and would preclude the use of whole brain standard deviation as a measure of spread.

**Advantages of the Present Method**

The clinical utility of OEF estimation is primarily in quantitative inter-subject and inter-regional comparisons. The group-level standard deviation of OEF among young healthy subjects reported here was similar to, or smaller than, those of other methods. Normalized variance, accounting for differences in mean OEF, was lower under spatially regularized VB than other methods. This suggests that the 2C, spatially regularized method proposed here may be useful in identifying differences across a population. Similarly, OEF is expected to be uniform across the healthy brain, and the spatially regularized 1C and 2C models produced smooth maps. These methods may, therefore, be useful in identifying regions of altered OEF, such as the ischaemic penumbra, by comparison with healthy tissue.

Other literature methods required precise initialization of parameter values in order to obtain reasonable results after model fitting. This is not required in a Bayesian framework, as broad, minimally-informative priors can be used to produce accurate results across a range of parameter values, as was shown in simulated data. Model-based fitting of sqBOLD data does, therefore, have considerable potential utility, although there are significant limitations which must be investigated further.

## 3.6 Conclusions

This chapter has shown that a Bayesian framework can be used to estimate parameters in the qBOLD model reliably and consistently, when compared with previous analysis methods. It showed first that using the $R_2'$-DBV model (Equation 3.2) on simulated data was more suitable for VB inference (and parameter estimation in general) than the original OEF-DBV model, because it resulted in clearer separation of parameters. It then showed that the non-linear model used can

be extended in a number of ways, such as including contributions to the signal from the intravascular compartment.

Grey matter average parameter estimates obtained from simulated data using VB had significantly lower variation than those of the simpler L model, leading to more homogeneous distributions and more precise average values. The distributions were even more homogeneous, and the average values more precise, when using a model that includes the intravascular signal contribution.

On *in vivo* data, this chapter showed that ASE-qBOLD consistently estimated parameter values that were different from those obtained through other methods. In particular, DBV estimates tended to be higher than literature values, leading to lower OEF estimates. The possibility that these differences were the result of motional narrowing (diffusion) effects in the tissue compartment was explored further in Chapter 5. The utility of these estimates in still providing clinically relevant information was considered in Chapter 6.

Future work ought to include a direct comparison with alternative qBOLD techniques, including those that use data acquired by other modalities such as GESSE, analysed in the same VB framework. A comparison with another method of OEF estimation (TRUST) is demonstrated in Chapter 5. An external estimate of blood volume, obtained by a technique like calibrated BOLD (see Section 2.3.1), would also be useful for validation.

The method presented in this chapter, and used throughout the rest of this work, estimates parameters more accurately from simulated data, and leads to significantly less variance at the intra-subject level *in vivo*.

# 4

# Correcting for the Extracellular Signal Contribution

## Contents



This chapter considers the effect of extracellular water on the qBOLD signal. Section 4.1 describes the way in which cerebrospinal fluid (CSF) has been dealt with in similar qBOLD experiments, and the FLAIR preparation which is used

in the current streamlined-qBOLD method. In Section 4.2 simulated qBOLD data which includes a contribution from CSF is analysed using sampling-based Bayesian inference. It is shown that cerebrospinal fluid (CSF) confounds estimates of physiological parameters of interest, especially DBV. It is proposed that by incorporating prior knowledge of CSF volume, a correction may be made that will result in more accurate parameter estimation. This would have the added benefit of removing the need for a FLAIR preparation in GASE qBOLD data acquisition. In Section 4.3 several methods for CSF partial volume estimation are described and compared. Then, in Section 4.4, they are used to inform inference on OEF and DBV with the qBOLD model, on non-FLAIR-prepared GASE data. It was found that CSF volume estimates obtained by biexponential model fitting were effective in correcting estimates of OEF in four out of five healthy subjects. The large variation between subjects, and other confounding factors, are discussed.

## 4.1 Introduction

In a typical voxel of grey matter, 3-5% of the volume is taken up by extracellular fluid,[159] which consists of interstitial fluid (ISF) and cerebrospinal fluid (CSF). Water can freely exchange between these two fluids, so they can be considered as a single compartment for the purposes of this work (as in He & Yablonskiy[141]). In the streamlined qBOLD protocol,[19] a FLAIR preparation[33] is used to null the signal contribution from extracellular fluid. This method is effective, but it has a number of disadvantages: it limits slice coverage (due to the inversion time delay), it reduces SNR (since the tissue signal will not have fully recovered at inversion time), and it is sensitive to motion (since slice-selective inversion pulses are required). These factors are all particularly important when applying qBOLD to ischaemic stroke assessment.

In a Bayesian framework, in which data is analysed by inferring the parameters of a non-linear model, the signal contribution from CSF could be accounted for by instead acquiring data without the FLAIR preparation, then modelling the total signal from all three compartments (tissue, intravascular, and extracellular). This can be enhanced by the incorporation of a spatially-varying prior for the

extracellular fluid volume parameter $\lambda$, in the form of a CSF partial volume map. This can be obtained through a number of different methods by taking into account differences in the relaxation parameters of CSF and bulk grey matter tissue.

The original formulation of the quantitative BOLD model considered brain tissue to be a single uniform mass, with some susceptibility-altering objects embedded in it, although not contributing directly to the measured signal.[14] Early *in vivo* validations, in which $R_2'$ was measured using the GESSE sequence,[36] found that estimates of $R_2'$ varied as a function of TE.[236] This was hypothesised to be due to the presence of multiple compartments with different $T_1$ and $T_2$ within a given voxel. This was supported by studies which quantified relaxation parameters in different tissue types.[140,237,238] One of these compartments had a much longer $T_2$, of up to 1600ms,[239] and corresponded to extracellular fluid. He and Yablonskiy (2007)[141] proposed a multiple-compartment qBOLD model which took this compartment, and the intravascular signal, into account.

Further investigations using the qBOLD model either incorporated the same model for CSF signal[15,159,160] or ignored its contribution altogether.[153,165] Simon and colleagues[152] used a similar model of the CSF compartment in Bayesian model-fitting of GESSE data using a hypercapnic stimulus. They found that using a FLAIR preparation improved the sensitivity of estimated $R_2'$ to changes in $CO_2$. They also report that model-based accounting for the CSF compartment provided a significant improvement in consistency of results. This supports investigation into a similar correction applied to GASE data.

## 4.2 Three Compartment qBOLD Simulation

A qBOLD model incorporating signal from three compartments (bulk tissue, intravascular water, and extracellular fluid) was simulated, and Bayesian inference of model parameters performed, in order to assess the feasibility of performing inference on *in vivo* data that included a signal contribution from CSF.

### 4.2.1 Theory: Extracellular Compartment Model

Under an asymmetric spin echo (ASE) acquisition, a 180° refocussing pulse is applied at time $(TE - \tau)/2$ (leading to an effective echo time of $TE - \tau$) and the signal is read out at time TE. The extracellular compartment's normalized signal $S^e$ contains an additional term, resulting from the differences in protein and lipid content between it and intracellular water:[110,141]

$$S^e(\tau) = S^t(\tau) \cdot e^{-2\pi i \cdot \Delta f \cdot \tau} \tag{4.1}$$

The measured ASE signal consists of the weighted sum of each of these signal compartments. The contribution of the extracellular compartment is given by its apparent volume $\lambda'$:

$$\lambda' = \frac{m_e \cdot n_e \cdot \lambda}{m_t \cdot n_t \cdot (1 - \lambda) + m_e \cdot n_e \cdot \lambda} \tag{4.2}$$

where $\lambda$ is the actual volume fraction of the extracellular compartment, $m_e$ and $m_t$ are the steady-state magnetizations of CSF and tissue respectively, and $n_e$ and $n_t$ are their relative spin densities. Ernst and colleagues found $n_t = 0.723$ in cortical grey matter,[240] and CSF can be approximated as water, with $n_e = 1$. However, in the ischaemic core, where membrane failure has occured and intracellular macromolecules are moving freely through the CSF, $n_e$ may decrease to a value approaching that of grey matter.

The total ASE signal is therefore:

$$S(\tau) = S_0 \cdot (\lambda' \cdot S^e(\tau) + \zeta' \cdot S^b(\tau) + (1 - \lambda' - \zeta') \cdot S^t(\tau)) \tag{4.3}$$

where $S^b$ and $S^t$ are the signals from the intravascular and tissue compartments, respectively, and are defined in Equations 2.33 and 2.43. Apparent deoxygenated blood volume $\zeta'$ is approximated as $\zeta' = m_b \cdot n_b \cdot \zeta$, and $n_b$ is given as 0.775.

| Parameter | Value | Reference |
|---|---|---|
| OEF | 40 % | Lu & Ge, 2008[59] |
| $\zeta$ | 3 % | Roland et al., 1987[221] |
| $\lambda$ | 5 % | Whittall et al., 1997[237] |
| $\Delta f$ | 5 Hz | He & Yablonskiy, 2007[141] |
| $R_2^t$ | 11.5 $s^{-1}$ | He & Yablonskiy, 2007[141] |
| $R_2^e$ | 4.0 $s^{-1}$ | He & Yablonskiy, 2007[141] |
| $T_1^t$ | 1200 ms | Lu et al., 2005[241] |
| $T_1^e$ | 3817 ms | Lu et al., 2005[241] |
| $B_0$ | 3 T | |
| TR | 3 s | |
| TE | 74 ms | |
| $\mathrm{TI}_{FLAIR}$ | 1210 ms | |
| $\tau$ range | -16 to 64 ms | |
| $\tau$ step size | 8 ms | |

**Table 4.1:** Parameter values used for simulating data. Other parameters use the values given in Table 3.1.

### 4.2.2 Methods

#### Simulated Data Generation

The three-compartment qBOLD model (Equation 4.3) was used to generate a set of simulated ASE data, with parameters set to values given in Table 4.1. In order to assess the model's sensitivity to each parameter, and the relations between parameters, Bayesian inference was performed. A set of data with no extracellular compartment signal ($\lambda = 0$) was also generated with other parameters kept constant.

The choice of $T_1$ values for each compartment is important for ensuring that simulated data is useful, because the FLAIR preparation relies on an assumed value of $T_1^e$ in order to remove the CSF signal, and the contribution of the other compartments after the inversion recovery are also weighted by their $T_1$ (Equation 2.13). The values used (Table 4.1) were based on measurements conducted by Lu and colleagues[241], although there is substantial variation in the literature. In the CSF compartment, He & Yablonskiy[141] used $T_1^e = 3700$ms, based on Clare & Jezzard;[242] whereas Simon & colleagues[152] used $T_1^e = 4000$ms, as a mean of literature values.

| **Relaxometry literature** | | |
|---|---|---|
| **Source** | $T_1^t$ **(ms)** | $T_1^e$ **(ms)** |
| Wansapura et al., 1999[238] | 1300 | - |
| Clare & Jezzard, 2001[242] | 1060 | 3700 |
| Gelman et al., 2001[244] | 1760 | - |
| Ethofer et al., 2003[245] | 1470 | - |
| Lu et al., 2005[241] | 1200 | 3817 |
| Stanisz et al., 2005[243] | 1820 | - |
| **qBOLD literature** | | |
| Source | $T_1^t$ (ms) | $T_1^e$ (ms) |
| He & Yablonskiy, 2007[141] | 1000 | 3700 |
| Simon et al., 2016[152] | 1200 | 4000 |
| Stone & Blockley, 2017[19] | - | 3817 |

**Table 4.2:** Measurements of $T_1$ of grey matter and CSF at 3T from relaxometry literature; and values used in qBOLD literature.

The FLAIR inversion time $TI_{FLAIR}$ used was calculated using Equation 2.14.

There is even greater variation in the literature regarding grey matter $T_1$. Values reported at 3T, and those used in qBOLD related experiments, are shown in Table 4.2. In this case, there was a difference of over 70% between the $T_1^t = 1060$ms reported by Clare & Jezzard[242] and $T_1^t = 1820$ms reported by Stanisz *et al.*[243] For consistency, the values for $T_1^e$ and $T_1^t$ from Lu *et al.*[241] were used throughout this chapter.

### Grid Search Inference

The joint likelihood distributions of pairs of parameters were sampled using a 2D grid search, in which a 1000x1000 grid of uniformly distributed parameter values were used to generate sample signals using the same model. The sum of squares difference between the original signal and each tested signal is proportional to the likelihood that the tested parameter pair explains the original data. The following parameter pairs were tested: $(R_2', \zeta)$, $(R_2', \lambda)$, $(R_2', \Delta f)$, $(\zeta, \lambda)$, $(\zeta, \Delta f)$, $(\lambda, \Delta f)$.

### Metropolis-Hastings Inference

When inferring on *in vivo* data, where the ground truth is not known, better fitting can generally be achieved by allowing more degrees of freedom, but only if the

parameters are truly independent. A Metropolis-Hastings (MH) algorithm[196,197] (see Section 2.4.2) was used to test combinations of parameters in higher dimensions for independence, with respect to ASE contrast.

The MH algorithm is much more time-efficient than a grid search, since only a minimal amount of time is spent evaluating the model in areas of very low likelihood. In order to mitigate the impact of the choice of starting position, a burn-in period is typically employed, in which the first several steps are not included in the final results. In this case, distributions were sampled over $10^7$ MH steps, following a 2000-step burn-in period.

First, the same pairs of parameters were inferred on in order to confirm that the MH algorithm produced comparable likelihood distributions to the 2D grid search. Then, the MH algorithm was used to generate sample likelihood distributions from the following combinations of parameters: $(R_2', \zeta, \lambda)$, $(R_2', \zeta, \Delta f)$, and $(R_2', \zeta, \lambda, \Delta f)$.

### 4.2.3 Results

A set of simulated ASE data without FLAIR was analysed in a series of 2D grid searches, in which pairs of parameters were tested by generating a uniformly spaced likelihood distribution in each case. These are presented in Figure 4.1. The likelihood of $(R_2', \zeta)$ (Figure 4.1a) was close to a normal distribution in each dimension, although there was some correlation between the parameters, and the distribution in the $\zeta$-direction did not appear uniform about the maximum. For other pairs of parameters: $(R_2', \lambda)$, $(R_2', \Delta f)$, and $(\zeta, \lambda)$ (Figure 4.1b-d), there was clear negative correlation between the two parameters, while in the case of $(\zeta, \Delta f)$ (Figure 4.1e) the likelihood was not linear across all $\Delta f$. For the final pair, $(\lambda, \Delta f)$ (Figure 4.1f), there was strong collinearity between the two parameters, and the distribution was clearly non-Gaussian, suggesting that simultaneous inference on both $\lambda$ and $\Delta f$, from a single set of NF ASE data, would not be feasible.

In each of the grid search cases, all other parameters were held to constant ground-truth values. Metropolis-Hastings (MH) inference in two dimensions produced sample likelihood distributions that were very similar to those from the grid searches,

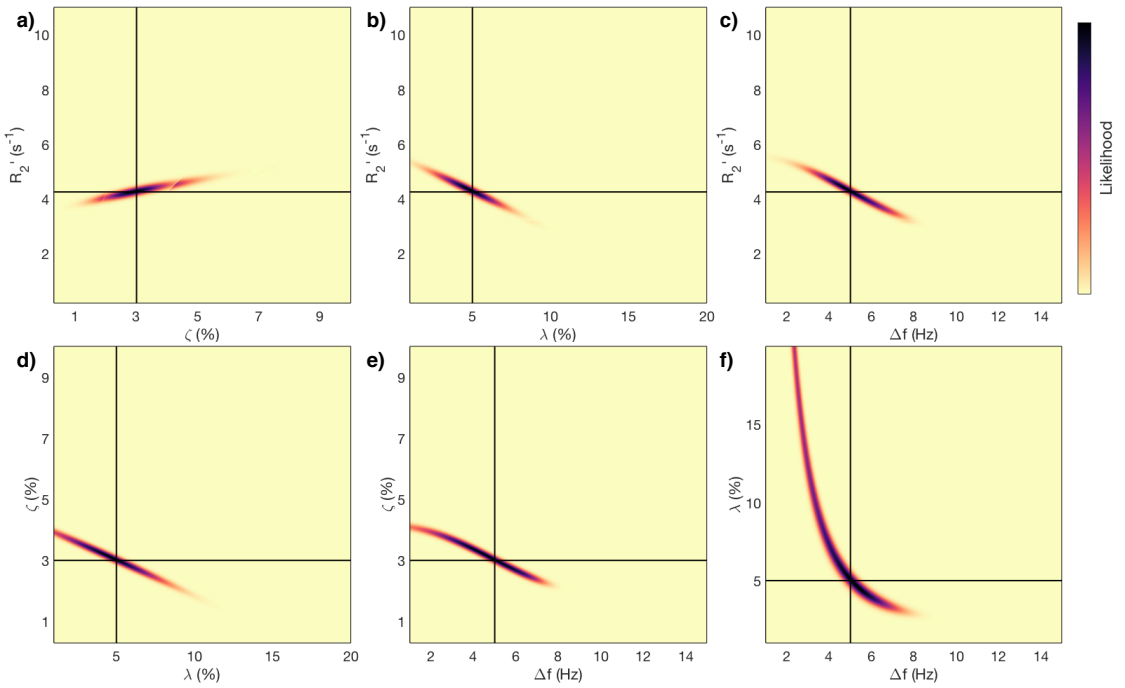


**Figure 4.1:** Results of a set of 2D grid searches with various pairs of parameters, illustrating pairs of values that were likely to correspond to the true simulated values. **a)** $R_2'$ and $\zeta$. **b)** $R_2'$ and $\lambda$. **c)** $R_2'$ and $\Delta f$. **d)** $\zeta$ and $\lambda$. **e)** $\zeta$ and $\Delta f$. **f)** $\lambda$ and $\Delta f$. Solid black lines indicate true values: $R_2' = 4.26$ s$^{-1}$, $\zeta = 3\%$, $\lambda = 5\%$, $\Delta f = 5$ Hz.

although it was necessary to search over a wider range of parameter space. MH enables simultaneous inference of more parameters, which would be prohibitively time-consuming in the grid-search method. The results of 4D MH inference (on $R_2'$, $\zeta$, $\lambda$, and $\Delta f$) are shown in Figure 4.2. The first row shows samples representing the likelihood distribution of $R_2'$ (Figure 4.2a), and the joint likelihood distributions of $R_2'$ and each of the other parameters (Figure 4.2b-d), which suggest that $R_2'$ would be over-estimated when the other parameters are also unknown (as opposed to the 2D grid search cases represented in Figure 4.1a-c, where the centre of the distribution in the $R_2'$-axis fell along the line of the true value.) The second row showed that the likelihood distribution of $\zeta$ (Figure 4.2e), and the joint likelihoods ($\zeta$,$\lambda$) (Figure 4.2f) and ($\zeta$,$\Delta f$) (Figure 4.2g) had very little variation in the $\zeta$-axis, suggesting that accurate estimation of blood volume was not possible at all in this case. The bottom two rows (particularly the joint distribution of ($\lambda$,$\Delta f$) in 4.2i) showed a large region of collinearity between $\lambda$ and $\Delta f$, as was seen in Figure 4.1f.

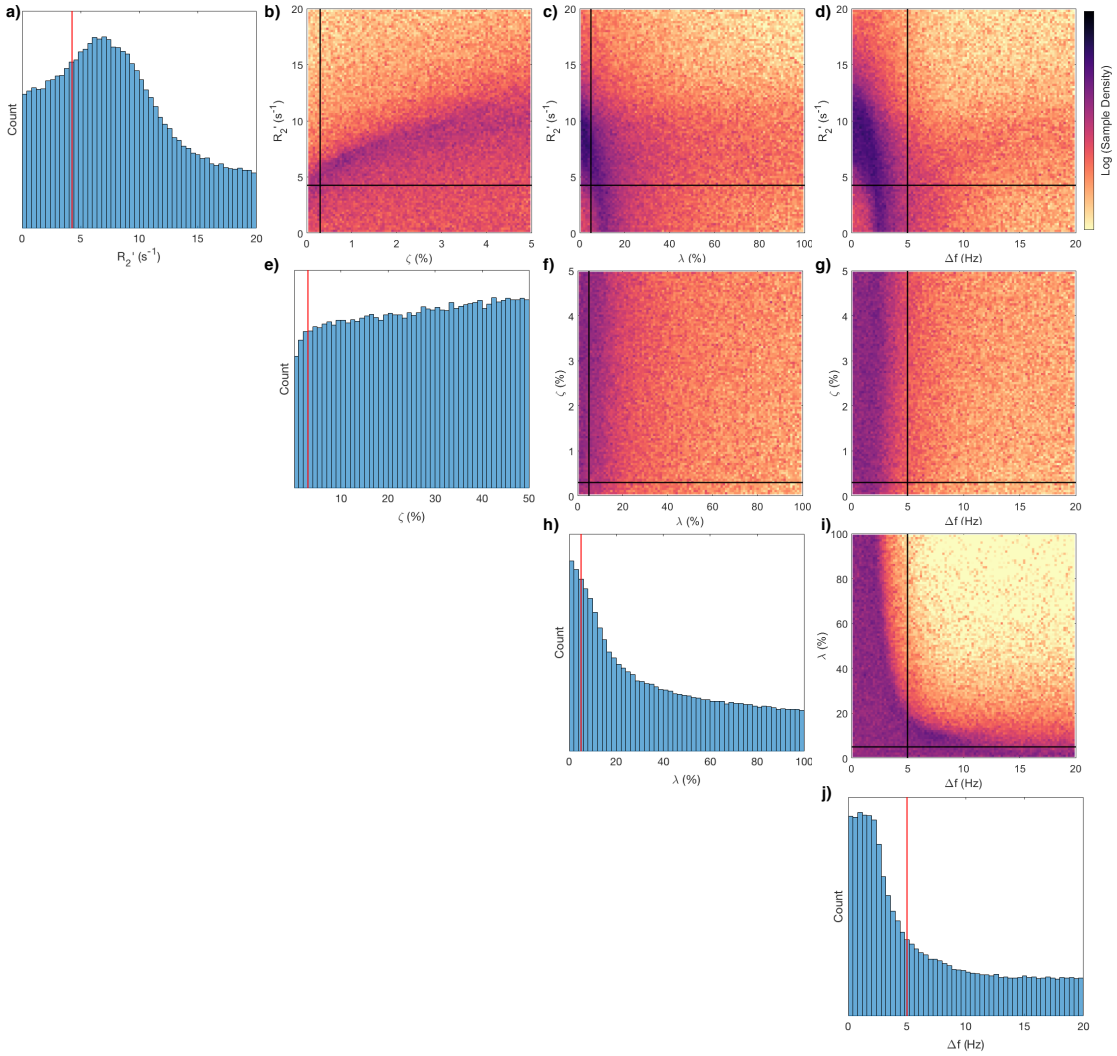


**Figure 4.2:** Results from 4D Metropolis-Hastings inference on non-FLAIR-prepared ASE data. 1D histograms in the main diagonal show the number of MH steps that were accepted in each interval of parameter values, with ground truth indicated by red vertical lines ($R_2' = 4.26$ s$^{-1}$, $\zeta = 3\%$, $\lambda = 5\%$, $\Delta f = 5$ Hz). The other figures show the MH sample density (log scaled) for each pair of parameters, with ground truth values indicated by solid black lines.

The lack of accuracy in $\zeta$ estimation persisted even when $\Delta f$ was fixed, as the 3D MH inference presented in Figure 4.3 shows. In this case, the $R_2'$ likelihood distribution (Figure 4.3a) had a broad peak around the ground truth value of $R_2' = 4.26$ s$^{-1}$, but the $\zeta$ likelihood distribution (Figure 4.3d) was extremely broad, and appeared to trend away from the ground truth of $\zeta = 3\%$ towards very high values. This can also be seen in the broad dispersion along the $\zeta$ axes in the joint likelihood distributions with $R_2'$ and $\lambda$ (Figure 4.3b and e respectively). Finally,

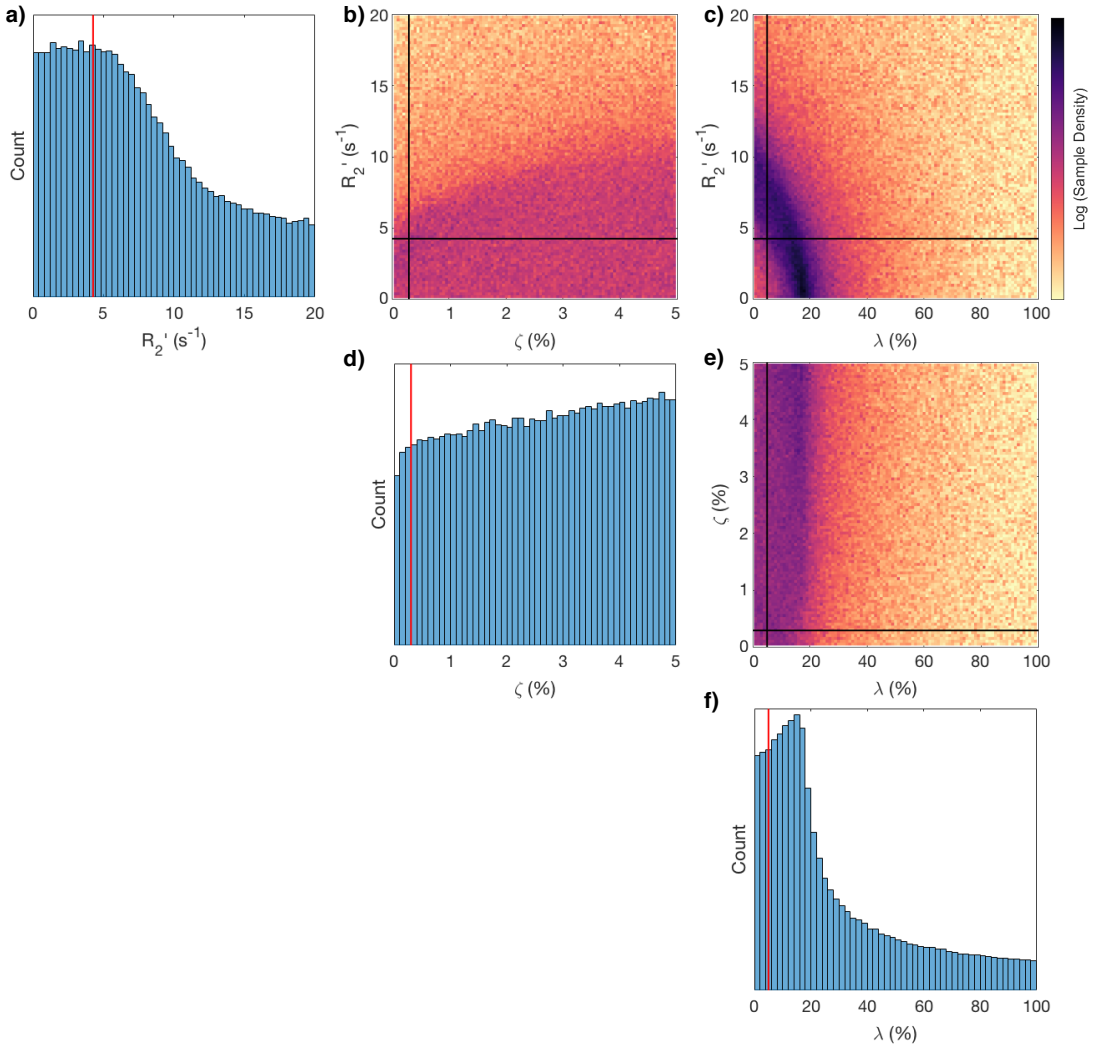


**Figure 4.3:** Results from 3D Metropolis-Hastings inference on non-FLAIR-prepared ASE data. 1D histograms in the main diagonal show the number of MH steps that were accepted in each interval of parameter values, with ground truth indicated by red vertical lines ($R_2' = 4.26$ s$^{-1}$, $\zeta = 3\%$, $\lambda = 5\%$). The other figures show the MH sample density (log scaled) for each pair of parameters, with ground truth values indicated by solid black lines. $\Delta f$ was fixed to its true value of 5 Hz throughout.

the $\lambda$ likelihood (Figure 4.3f) had a well-defined peak at around $\lambda = 20\%$, as opposed to the ground truth $\lambda = 5\%$.

### 4.2.4 Discussion

Inference on simulated ASE-qBOLD data showed that, in the presence of a non-negligible signal contribution from the extracellular compartment, it is not possible to accurately estimate $R_2'$ and $\zeta$ (which are needed to calculate OEF). Even in the 3D

case, where other parameters including $R_2^t$, $R_2^e$, and $\Delta f$, are perfectly known, there was no clear optimal value of $\zeta$ in terms of its likelihood to explain the simulated data.

By adding terms to the model of the qBOLD signal, more degrees of freedom are introduced. This has the potential to result in more accurate fitting, since the more complicated model ought to describe more of the biological reality. However, when certain parameters are fit without constraints, error in estimation may result either from local minima, or from lack of sensitivity to particular parameters. This can be overcome in part by the selection of an appropriate model-fitting technique. Linear least-squares fitting is unsuitable for complex models, but several Bayesian techniques offer different advantages. Since the posterior distributions cannot be evaluated analytically in the qBOLD model, they must either be approximated or sampled.

Sampling-based methods (as described in Section 2.4.2) can be highly time-consuming, but reproduce the exact posterior distribution. When dealing with simulated data, in which the posterior only needs to be evaluated once, this time cost is acceptable. As detailed above (Section 4.2.2), the Metropolis-Hastings algorithm offers a significant time improvement compared to the simple grid search, especially in situations with dimensions higher than two. The resulting samples are drawn exactly from the true posterior, but they are limited in that the possible range of parameter values must be constrained in some way. This is particularly problematic in that the $\zeta$ samples shown in Figures 4.2e and 4.3d are distributed throughout all of the possible parameter space, meaning that the mean and median values are strongly dependent upon the chosen upper limit ($\zeta = 50\%$ in this case).

Another solution to the problem of inaccurate fitting (due to collinearity between parameters) is to define priors that constrain the values certain parameters can take. This can be done either by assuming parameter values from the literature (as was done throughout with $T_1$ values), or by using information derived from other imaging data.

In the single-compartment qBOLD model acquired under ASE (Equation 2.33), reversible transverse decay ($R_2$) effects are removed from the signal by the sequence

design, allowing $R_2'$ to be fitted alone, without requiring any knowledge of $R_2$. However, in the multiple-compartment qBOLD model (Equation 4.3), the relative contribution of each compartment depends on both $R_1$ and $R_2$ (Equation 2.13).

Ischaemia is known to cause changes in $R_1$[246] and $R_2$[80], which may render the assumed relaxation rates incorrect, leading to incorrect weighting of each compartment's signal, and hence misestimation of other parameters. It may therefore be necessary either to acquire ASE data with inherent $R_2$ contrast (this is investigated further in Section 5.3.3) or to acquire separate quantitative $R_1$ and $R_2$ maps and use those values as priors in the model fitting.

Another possibility is to include prior knowledge of $\lambda$ and $\Delta f$ from other data, which could improve $\zeta$ inference. This potential correction is presented in the remainder of this chapter.

## 4.3 CSF Volume Estimation

Given that key parameters in the three-compartment qBOLD model $(R_2', \zeta, \lambda)$ do not appear independent, it is necessary to incorporate additional information about at least one of them in order to accurately infer on the others. The most natural candidate for this is $\lambda$, which can be quantified in a number of ways, as described below. In this section, *in vivo* data were collected and partial volume maps of $\lambda$ generated and compared.

### 4.3.1 Tissue Segmentation Methods

#### $T_1$-weighted Segmentation

A $T_1$-weighted image can be segmented based on the assumption that the different tissue types each have a different $T_1$. This is implemented in FSL's FAST,[205] which uses a Hidden Markov Random Field (HMRF) model to categorise voxels. In simpler methods of image segmentation, such as finite mixture models, voxels are assigned to one of a fixed number of classes based solely on their intensity. This is highly susceptible to noise, and can produce very patchy parameter maps.

It is generally assumed that the major tissues of the healthy brain (white matter, grey matter, and CSF) are relatively homogeneous (in terms of parameters like $T_1$), and are distributed throughout the brain in large neighbourhoods of adjacent voxels. This spatial information is incorporated into a Markov Random Field (MRF) model, through constraints placed upon neighbouring voxels. In MRI images, this reality is degraded by noise, by field inhomogeneity effects (bias fields), and by partial volume effects that occur when a single voxel contains multiple tissue classes. Thus, the state of a voxel is not directly observed. The HMRF model in FAST takes this into account with a model that relates hidden states to observed states. This, along with the labels of each voxel, and an estimate of the bias field, is updated in an iterative process using an expectation maximization algorithm.[205]

This results in maps of posterior probabilities for each tissue class being the one that describes each voxel.

### $T_2$-weighted Segmentation

A $T_2$-weighted image can be segmented in the same way, making use of differences in $T_2$ between tissue types. TE can be varied in order to change the amount of weighting each tissue type will have. Since CSF has a relatively long $T_2$ (between 250ms[141] and 1600ms[239]), compared to grey and white matter (80ms and 110ms respectively[238]), a spin-echo image acquired at a longer TE (on the order of 250ms) will be dominated by signal from the extracellular compartment.

### $T_2$ Biexponential Fitting

Since grey matter voxels are expected to contain some volume fraction $\lambda$ of CSF and/or ISF, and since this fracton has a different $T_2$ to the intracellular water, by collecting a series of $T_2$-weighted spin-echo images with different TEs, a biexponential decay model could be fit to the data in order to quantify $\lambda$. The biexponential decay model takes the following form:

$$S(TE) = S_0\Big[\lambda \cdot e^{-\frac{TE}{T_2^e}} + (1-\lambda) \cdot e^{-\frac{TE}{T_2^t}}\Big] \tag{4.4}$$

where $T_2^t$ and $T_2^e$ are the $T_2$ of tissue and extracellular water respectively.

Work has been done to define the optimal sampling procedure for monoexponential[247] and multi-exponential[248,249] decaying data. In the monoexponential case, with only two unknowns, the optimal strategy (based on minimization of the Cramer-Rao lower bound) is to measure at only two $TE$s: 0 (or as close to 0 as possible, given the acquisition) and $1.28T_2$, but with additional repeats to increase SNR. The proportion of volumes acquired at each of these $TE$s is not equal, because the SNR decreases with time as $T_2$ decay occurs. In an alternative linear-spacing paradigm, values spaced between 0 and $2.02TE$ are optimal.[247]

In the biexponential case, the optimal sampling procedure depends on which parameter's uncertainty must be minimized,[249] of the four parameters in Equation 4.4: $S_0$, $\lambda$, $T_2^t$, and $T_2^e$. If the ratio of $T_2^e$ to $T_2^t$ is sufficiently large, sampling patterns can be optimised for each compartment separately, as if they were monoexponentials. In the case of closer $T_2$s, or greater uncertainty in *a priori* estimates of them, exponential spacing between two defined TEs is optimal, with the maximum TE optimised based on the ratio of expected uncertainty in $T_2^e$ and $T_2^t$ and the number of samples to be acquired.[248]

Given the number of data points available for fitting, and SNR levels, it is necessary to use fixed values of $T_2$ for both compartments, and to fit for $S_0$ and $\lambda$ only. It was decided that eight multi-slice 2D volumes with eight $TE$s should be collected because this acquisition would take the same amount of time as a single GASE volume. Since the separation between $T_2^e$ and $T_2^t$ is so large, linear spacing is only marginally worse than optimal exponential spacing, provided an appropriate maximum $TE$ is selected.

### FLAIR Contrast Fitting

A FLAIR preparation[33] exploits the differences in $T_1$ between CSF and other tissues in order to null the signal coming from the extracellular compartment. The total signal at $TI$ is the sum of the magnetizations of both compartments:

$$S(TI) = S_0 \cdot \Big(\lambda \cdot m_{csf}(TI) + (1 - \lambda) \cdot m_{tissue}(TI)\Big) \tag{4.5}$$

where $m_{csf}(TI)$ and $m_{tissue}(TI)$ are defined by Equation 2.13, and include assumed values for the $T_1$ of CSF and grey matter.

By collecting a spin-echo ($\tau = 0$) GASE volume with and without FLAIR (that is, with $TI = \{0\text{s}, 1.2\text{s}\}$), $S_0$ and $\lambda$ can be inferred by fitting Equation 4.5. Acquiring additional volumes at a range of $TI$s would also enable fitting of $T_1$, but this entails similar problems as with fitting $T_2$ in the above biexponential fitting method.

### 4.3.2 Data Collection

Scan data from five healthy participants (aged 24-35, 2 female) were collected using a 3T Siemens Verio system (Siemens Healthineers, Erlangen, Germany), under a technical development protocol agreed with local ethics and institutional committees. For each subject, GASE[163] data were collected with and without FLAIR ($TI$=1210ms); $TR/TE$=3s/82ms, 96×96 matrix, eight slabs, 2.29×2.29×5mm resolution, and 11 $\tau$ values ranging from -16 to 64ms in steps of 8ms. The acquisition time for each GASE volume was 24 seconds, leading to a total acquisition time of 4 mins 24 seconds for each of the FLAIR-prepared and non-FLAIR GASE datasets.

A high resolution structural MPRAGE[227] image was also acquired for each subject, with $TR/TI/TE$ = 2040/900/4.7ms, flip angle 8°, 192×192×174 matrix, 1×1×1 mm resolution. This had an acquisition time of 3 mins 58 seconds.

A single GASE volume was acquired at $TE$=250ms, $\tau$=0ms, which took 24 seconds. A set of eight 2D spin echo volumes were acquired at the same resolution as the GASE data, with $TE$s equally spaced from 66 to 248ms. In this case, it was possible to acquire volumes made up of 2D slices, rather than the 3D slabs acquired in the GASE acquisition. The 3D slabs are the result of slice averaging in the GESEPI technique which reduces the effect of macroscopic $B_0$ inhomogeneities, which would affect $R_2'$ fitting in ASE data.[34] In GASE acquisition, eight slices are averaged to form each slab,[19] but since there is no $R_2'$ contrast in the spin-echo ($\tau$=0) data points, the effect of $B_0$ inhomogeneity is reversed by the spin echo,

so this additional step is not necessary. It is therefore possible to acquire eight separate volumes (with different $TE$s) in the same amount of time.

#### Image Registration

The data required for $T_2$-weighted segmentation, $T_2$ biexponential fitting, and FLAIR-contrast model fitting, were all acquired at the same resolution as the GASE data used for the main qBOLD model fitting, which meant that, apart from rigid body motion correction using MCFLIRT,[229] no complicated registration is required, and the CSF maps ought to align precisely with the GASE data.

In the case of $T_1$-weighted segmentation, however, the data were acquired at very different resolutions, and must therefore be registered. There are several considerations regarding registration methods, the two most important factors being the number of degrees of freedom used in the transformation, and the method of interpolation used to transfer data over. Since the resolutions are different between MPRAGE and GASE, rigid body transformation (with only 6 degrees of freedom) is not suitable. Since EPI data contain geometric distortions that approximate stretching and skewing, affine transformation (with 12 degrees of freedom) was used. Non-linear registration (with many more degrees of freedom) is generally not used for intra-subject registration.[229,232] In order to preserve the partial volume values (or any other quantitative data), and to avoid inconsistencies such as apparent gaps in the CSF compartment, intermediate supersampling (to match MPRAGE resolution) and trilinear interpolation were used.

### 4.3.3 Comparison Methods

#### Similarity Metrics

In the absence of any ground truth knowledge of CSF distribution in the brain, it is not possible to evaluate the various methods for CSF partial volume estimation directly. In the context of improving qBOLD parameter inference, it is possible to use the FLAIR-prepared GASE data as a 'gold standard' with no CSF signal

contribution, and to compare the resulting parameter estimates with non-FLAIR-prepared data. This comparison is performed in Section 4.4.

The segmentation methods can be compared on the basis of their similarity, under the assumption that a method whose results are very different from the average result of several other methods is likely to be wrong. The Dice Similarity Coefficient (DSC) has been shown to be a valuable measure of spatial overlap in image segmentation experiments.[250] It is defined as

$$DSC(A, B) = \frac{2(A \cap B)}{A + B} \tag{4.6}$$

where $A$ and $B$ are the two (binarized and vectorized) images to be compared, and $A \cap B$ is the intersection of $A$ and $B$.

In the case of several comparable results, it is also possible to identify deviation from consensus. This can be done with binary classification data by counting the percentage of voxels in which the outcome of one method is different from all the others (or from a majority of the others). The method which produces the most 'odd-one-out' voxels may be inferred to be the least reliable.

Quantitative, non-thresholded voxel-wise partial volume estimates could also be used to determine similarity. Calculating the mean and standard deviation of CSF volume fraction across all methods, for each voxel, would result in an average partial volume map. The number of voxels that differ significantly from this (based on a $t$-test) from each method, could then be used to determine consistency between methods. Given the small number of methods being compared here (four), the statistical power of such a test would be too low to render it useful.

### Comparison Analyses

The CSF volume estimation methods described above (Section 4.3.1) were applied to data from all five subjects to produce 4 CSF partial volume maps. $T_1$-weighted (MPRAGE) images were brain-extracted using FSL's BET[231] and segmented using FAST[205] into three classes (white matter, grey matter, and CSF). The CSF partial volume maps were registered into GASE-space using FLIRT[229,232] and applywarp.[228]

$T_2$-weighted images ($TE = 250$ms, $\tau = 0$ GASE volumes) were segmented using FAST with a fourth class for non-brain tissue. Equation 4.4 was implemented as a forward model in FABBER[22,180,181] with parameters $\lambda$ and $S_0$, and used to infer on variable-$TE$ GASE volumes under VB inference. Equation 4.5 was also implemented as a forward model in FABBER with the same parameters $S_0$ and $\lambda$ and used to infer on $\tau = 0$ GASE volumes acquired with and without FLAIR.

Variations to the above methods were also tested, including: transforming $T_1$-weighted images into GASE space first, then segmenting them; upsampling $T_2$-weighted images into MPRAGE resolution, segmenting them, then downsampling back to GASE space; segmenting shorter $TE$, FLAIR-prepared ASE images; and fitting the biexponential and FLAIR contrast methods using least-squares rather than VB. In each case, these were found to produce qualitatively poorer CSF partial volume maps, based on visual inspection.

The resulting maps were thresholded at 5%, 20%, 40%, 60%, 80%, and 95% to create binary CSF masks, which were compared by calculating the DSC for each subject and threshold. These were also subjected to an odd-one-out analysis, where the proportion of voxels that differ from the majority was calculated for each subject, threshold, and CSF volume estimation method.

### 4.3.4 Results

A set of CSF partial volume maps from a typical example subject are shown in Figure 4.4. In the $T_1$ segmented images, the ventricles and cortical channels did not have 100% CSF volume, though they should have. This effect may have been caused by the transformation and interpolation of the segmented maps. The images from $T_2$-weighted segmentation suffered from bright artefacts in the anterior of the brain. These are caused by signal pile-up due to distortion of the EPI acquisition trajectory by $B_0$ inhomogeneity. The biexponential fitting results had many features in common with the $T_1$ and $T_2$ segmented maps, especially in the details of the cortical folding, but there is also higher CSF partial volume in the GM regions of the brain, which have 0% CSF according to the segmentation methods. This

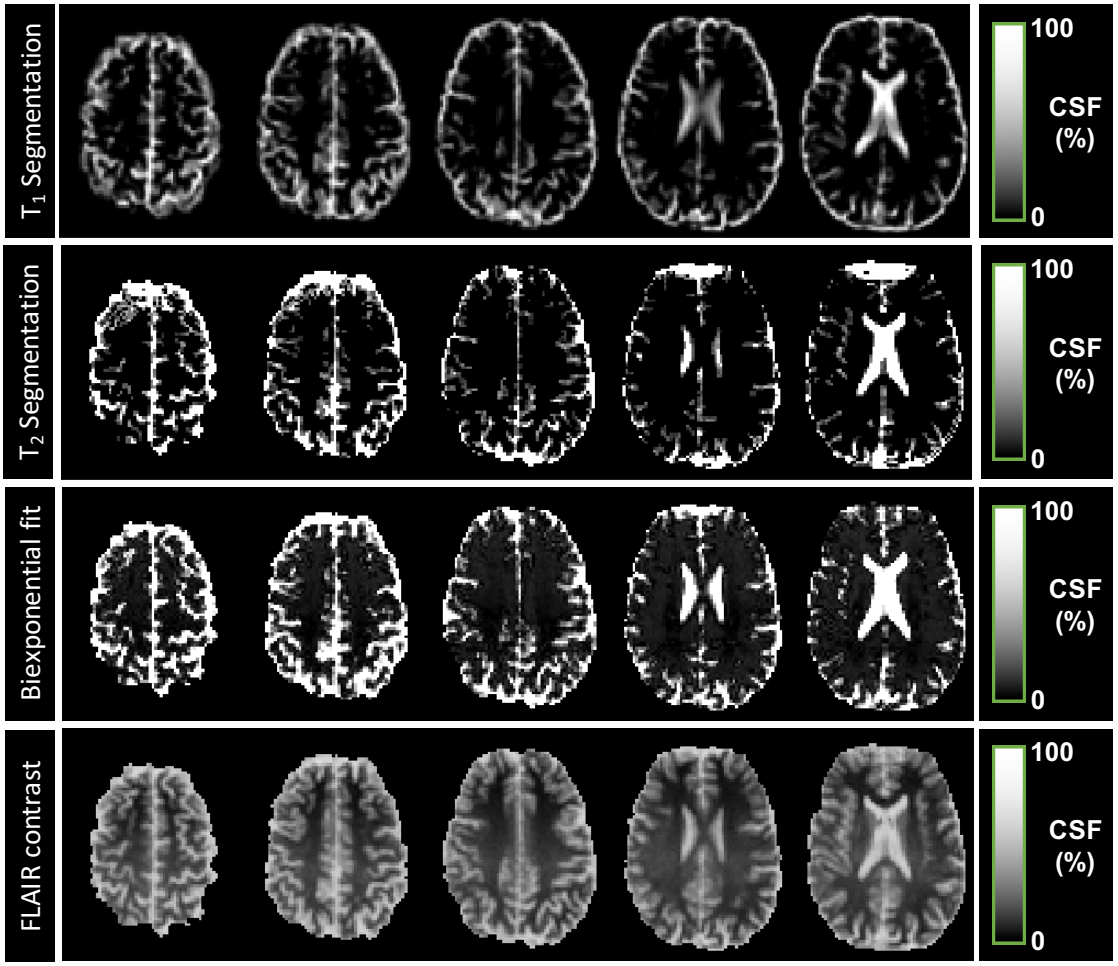


**Figure 4.4:** Example maps of CSF partial volume from a single healthy subject, obtained by four methods: **First row:** Segmentation of $T_1$-weighted image. **Second row:** Segmentation of $T_2$-weighted image. **Third row:** Biexponential model-fitting to $T_2$ data. **Fourth row:** FLAIR contrast model fitting.

may be beneficial when correcting for signal originating from the interstitial fluid within grey matter voxels. The FLAIR contrast maps were visibly the most different from the other methods, and estimated particularly high values of CSF content in grey and white matter regions inside the cortex. There was also less contrast between tissue areas and ventricles under this method.

The resulting CSF partial volume maps were compared with one another to assess consistency, and identify methods which produced results that differed significantly from others. Figure 4.5 shows the DSC of each pair of methods based on two CSF partial volume thresholds: 5% and 20%. Segmentation of $T_1$- and $T_2$-weighted images produced maps with a high similarity when thresholded at low

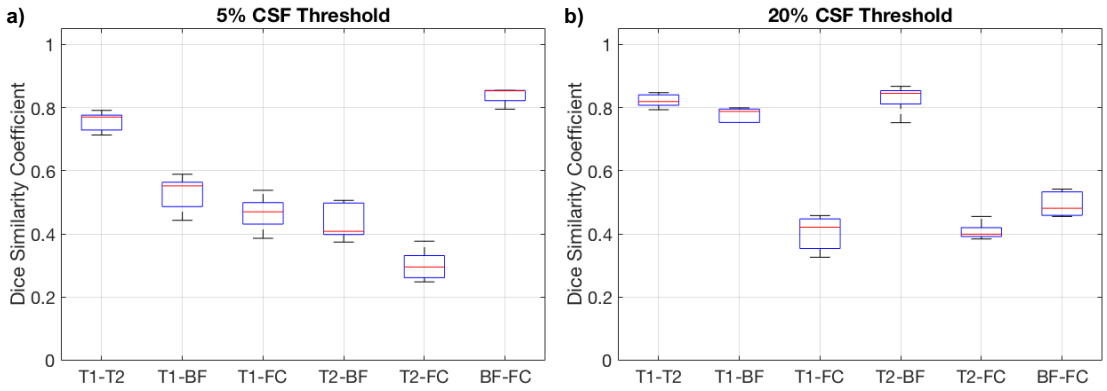


**Figure 4.5:** Pairwise inter-subject average Dice Similarity Coefficients (DSCs) for the four CSF partial volume estimation methods, using binarized CSF maps thresholded at **(a)** 5% and **(b)** 20% CSF partial volume. **T1:** segmentation of $T_1$-weighted images. **T2:** segmentation of $T_2$-weighted images. **BF:** biexponential fitting of $T_2$ data. **FC:** FLAIR contrast model fitting.

CSF partial volumes. FLAIR contrast derived maps were generally least similar to others, as can be seen visually in Figure 4.4. At the higher partial volume threshold, the biexponential model fitting results were highly similar to those from $T_1$- and $T_2$-weighted segmentation.

Figure 4.6 shows the results of an 'odd-one-out' comparison of the four resulting CSF maps, after binarizing at several CSF partial volume thresholds. Generally, the biexponential model fitting produced the maps with the most consistent voxels at both 5% and 20% thresholds. When averaging across all threshold values, the $T_2$-weighted segmentation produced the most consistent maps, and FLAIR contrast fitting the least. The larger variation and higher inconsistency in $T_1$-weighted segmentation may be the result of mismatches after transforming the maps into GASE space.

### 4.3.5 Discussion

Since it was not possible to obtain a ground truth map of CSF distribution, the segmentation methods cannot be assessed in an absolute sense against a gold standard. Given that only four methods were fully tested, and other considerations, such as the need for co-registration of the data, consensus (or measurement of similarity between methods) does not necessarily guarantee accuracy.

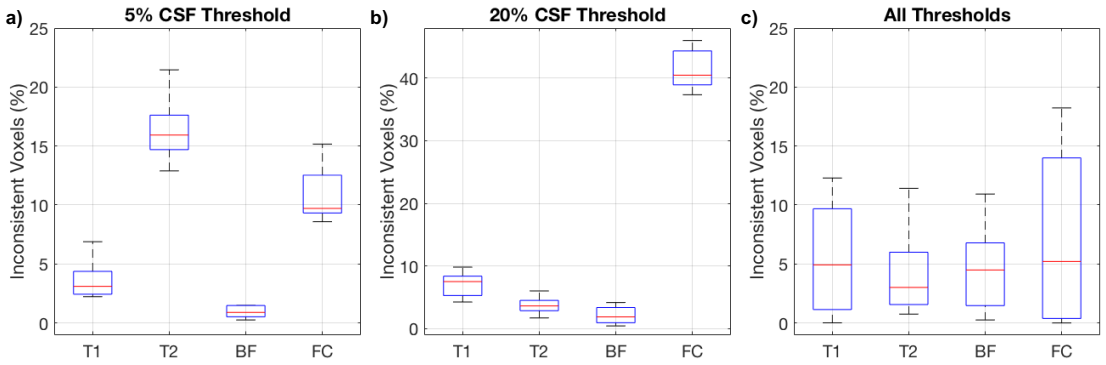


**Figure 4.6:** Comparison of four CSF partial volume estimation methods, based on the proportion of voxels classified as CSF or non-CSF at thresholds of **(a)** 5% CSF partial volume, **(b)** 20% CSF partial volume, and **(c)** average across six thresholds: $\{5\%, 20\%, 40\%, 60\%, 80\%, 95\%\}$. Each box-and-whisker point is the inter-subject average number of voxels classified differently by that particular method, compared to all three other methods. **T1:** segmentation of $T_1$-weighted images. **T2:** segmentation of $T_2$-weighted images. **BF:** biexponential fitting of $T_2$ data. **FC:** FLAIR contrast model fitting.

It is therefore necessary to choose the best method for CSF partial volume estimation based on its usefulness to the desired application: namely in correcting for qBOLD signal originating from the extracellular compartment. By using the CSF maps from each method as spatial priors that constrain the possible values of $\lambda$ in fitting the three-compartment qBOLD model (Equation 4.3), and comparing the resulting estimates of OEF, or other parameters of interest, the best correction method can be determined. This, however, relies on the assumption that the parameter estimates produced from inference on FLAIR-prepared data form a reasonable 'ground truth.'

### Data Acquisition and Analysis

Other considerations, given this application, are important. One such consideration is the manner in which the additional data for CSF correction is acquired, and the time it takes. $T_1$ segmentation makes use of a separate MPRAGE image which is acquired as part of the standard clinical protocol (see Chapter 6). Thus, it does not strictly increase the amount of scanning time required; however, it requires image registration with the GASE data, and is susceptible to future changes in protocol, which might render $T_1$-weighted imaging unneccessary, or involve other

changes that require different sets of imaging data. The need to perform linear registration between MPRAGE and GASE data may have limited the usefulness of the $T_1$-weighted data. Correcting the EPI distortions in the GASE data using a method such as that of Andersson and colleagues[251] may make this process easier, and improve the quality of the final parameter maps.

$T_2$-weighted segmentation can be performed on $\tau = 0$ GASE data at any $TE$, and so may not require any additional scanning time on top of the normal qBOLD GASE acquisition. However, acquiring this volume at longer $TE$ increases the relative weighting of the extracellular compartment (since it has the longest $T_2$), and may therefore make segmentation of the CSF more reliable (at the expense of distinguishing between grey and white matter, which is not necessary in this case).

Sufficient $T_2$-weighted data can be acquired for biexponential fitting in the same time as a single GASE volume (around 24s), if the SE images are acquired as stacks of 2D slices rather than as 3D slabs. If an optimal sampling pattern of $TE$ is employed, it may be possible to reduce this even further, and improve the fitting accuracy. FLAIR-contrast model fitting also requires only one additional GASE volume, and so has only a minor cost in terms of scanning time.

Other methods for estimating CSF partial volume, such as using a surface-based segmentation algorithm, were not considered here, in part due to the additional scanning time that would be required, which would limit its utility in rapid clinical assessment of acute stroke. They may, however, have been useful in providing additional points of comparison for DSC and consensus measurements. The possibility of combining CSF maps from multiple methods into a single averaged map could be explored in the future.

### Application to Acute Stroke

Acquiring NF data from acute stroke patients has the potential to increase SNR, reduce the impact of movement artefacts (which are far more severe in stroke patients than healthy volunteers), and reduce scan duration.

$T_1$-weighted segmentation could be used straightforwardly, since a $T_1$-weighted anatomical image is usually acquired for registration and segmentation already. The ASE data would typically be registered to anatomical space for analysis and comparison with other modalities, so the need for non-linear registration is not a limitation.

$T_2$-weighted segmentation has similar advantages, and the CSF correction can be performed entirely in ASE-space, and then the final paramater estimates transformed to anatomical space, to maintain fidelity.

Biexponential fitting correction requires additional data acquisition, which would increase clinical scan time. Given the fact that the $T_2$ of ischaemic core and penumbral tissue may be singificantly different from literature values, even more $TE$ values than were used here may be required to properly separate the two compartments.

FLAIR correction would require an additional FP volume to be collected (at a single $\tau$), which would increase scan time. It also relies on the assumption that the FLAIR preparation is truly effective, which may be even less likely in acute stroke patients given the likelihood of motion artefacts.

In all, $T_2$-weighted segmentation would probably be the most clinically useful methods for CSF partial volume estimation, although this would need to be tested on acute stroke patients.

## 4.4 *In Vivo* CSF Signal Correction

Since the FLAIR preparation has been shown to remove signal contribution from CSF effectively,[19,152] it can be assumed that fitting a model which explicitly accounts for signal arising in the extracellular compartment ought to produce the same parameter estimates as inference on FLAIR-prepared data. This section compares model inference on FLAIR-prepared (FP) data with non-FLAIR-prepared (NF) data, with a range of potential CSF correction methods. The method which produces inferred parameter values that are closest to the those from FP data could be considered the best. However, since it has been shown that there are differences in

DBV and OEF estimates between ASE-qBOLD and other methods (see Section 3.5), it may be that this is not the ideal ground truth for comparison.

### 4.4.1 Data Collection and Pre-Processing

Collection of GASE data from five healthy subjects is described in Section 4.3.2. GASE data underwent Gaussian filtering (the kernel's full width half maximum was set at 2.29mm, to match the in-plane resolution), and motion correction with MCFLIRT.[229] Gibbs artefacts were removed using iterative subvoxel shifts.[230] Images were then brain extracted using BET.[231]

Structural data were also brain extracted, then segmented using FAST.[205] The resulting GM partial volume map was thresholded at 80% to define a GM region of interest, which was then registered to GASE space. The $\tau = 0$ spin echo volumes, both with and without FLAIR, were also segmented in the same way. Visual inspection showed that, for all five subjects, the masks produced by segmentation of GASE images more closely corresponded to GM areas, than those produced by segmentation of the $T_1$-weighted MRPAGE images. Therefore, GASE-derived GM masks were used to define the region of interest throughout.

The GM partial volume threshold of 80% was chosen to ensure that voxels which would be strongly affected by partial volume effects, either from WM (where GASE signal is not expected to obey the qBOLD model) or CSF, were excluded. Conversely, it is not so strict a threshold as to exclude a large number of voxels that are mostly grey matter, or in which CSF correction has the most useful role to play.

### 4.4.2 Analysis Methods

#### Signal-to-Noise and Contrast-to-Noise

The effect of removing the FLAIR preparation from GASE data acquisition was investigated, first in terms of the effect on SNR and CNR, and then in the effect on parameter inference. SNR was calculated by dividing the average signal within the GM mask by the standard deviation of the signal in a similarly-sized region

outside the brain. SNR was calculated for each $\tau$ value and each subject. CNR was calculated according to:

$$CNR = \frac{\tilde{S}_{GM}(\tau = 0) - \tilde{S}_{GM}(\tau = \tau_{max})}{\sigma_{non-brain}} \tag{4.7}$$

where $\tilde{S}_{GM}$ is the average signal in grey matter, and where $\tau_{max}$ is the longest $\tau$ value acquired.

SNR and CNR were compared between subjects with a two-sampled t-test.

### qBOLD Model Inference

The two-compartment qBOLD model (Equation 2.37) was fit to FP GASE data (using FABBER) to establish ground truth estimates of $R_2'$ and DBV. Then, NF GASE data was inferred using the same two-compartment model, to test whether simply ignoring the signal contribution from the extracellular compartment was a feasible option that would result in similar parameter estimates. Next, the three-compartment model (Equation 4.3) was fit to the NF GASE data, with $\lambda$ as an additional parameter to be inferred upon. $\Delta f$ and $R_2^e$ were held to constant literature values of 5 Hz and 4.0s$^{-1}$ respectively (Table 4.1).

Finally, the three-compartment model was then used to infer on NF data, with a partial volume map of $\lambda$ supplied to FABBER as an image prior, to define prior means $\mu_0$ for each voxel. CSF partial volume maps from each of the four methods described in Section 4.3.1 were tested. A stricter prior on $\lambda$ of $\phi_0(\lambda) = 10^1$ was used to enforce the external partial volume estimate on the rest of the fitting.

The resulting estimates of $R_2'$, DBV, and OEF, from each inference, were compared (using MATLAB) both within each subject and across the group. This was done by subjecting estimates to a two-way ANOVA test to determine whether the intra- or inter-subject means from each inference were equal. In the case of significantly different group means, the Tukey-Kramer method was used to perform pairwise comparisons, as in Chapter 3.

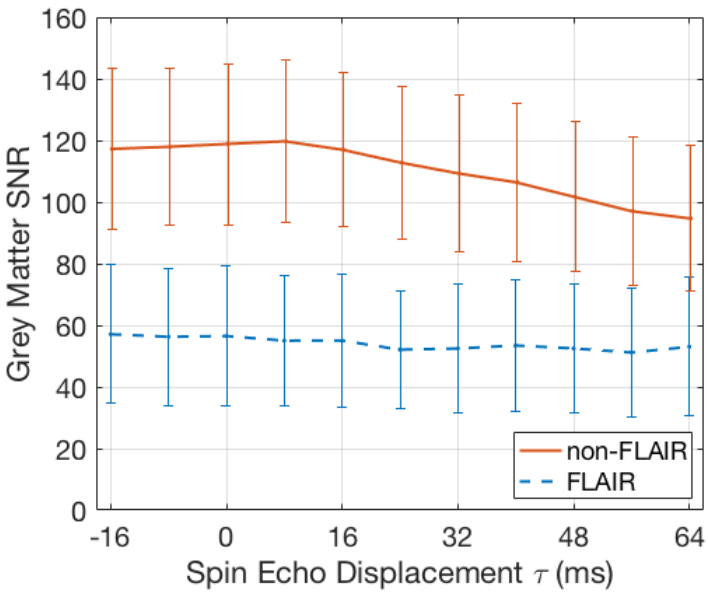


**Figure 4.7:** Average signal-to-noise ratio (SNR) in grey matter across five subjects, for each GASE volume, acquired with and without FLAIR preparation.

### 4.4.3 Results

#### Signal-to-Noise and Contrast-to-Noise

Grey matter SNR was calculated for every GASE volume for each subject, with and without FLAIR, and is presented in Figure 4.7. SNR was consistently higher across all $\tau$ values in NF data; although there was more variation between short-$\tau$ and long-$\tau$ volumes.

Average GM SNR and CNR (across volumes) for each subject are shown in Table 4.3. SNR varied considerably between subjects, but was always significantly higher in NF than FP ($p > 0.01$). CNR was also significantly higher in NF than FP ($p > 0.05$). Across all subjects and $\tau$ values, FP SNR was 54±21, whereas NF SNR was 110±25. FP CNR was 16±10, and NF CNR was 34±13.

#### qBOLD Model Inference

VB inference was performed on NF GASE data from all five subjects, under the following conditions: a two-compartment qBOLD model (ignoring extracellular signal contribution entirely), the three-compartment qBOLD model (with $\lambda$ as an inferred parameter), and the three-compartment qBOLD model with an external

| | SNR | | CNR | |
|---|---|---|---|---|
| **Subject** | **FLAIR** | **non-FLAIR** | **FLAIR** | **non-FLAIR** |
| 1 | 71.5±4.0 | 133.9±16 | 28.7±8.3 | 52.8±18 |
| 2 | 70.5±3.7 | 108.7±9.0 | 21.2±7.6 | 39.4±14 |
| 3 | 64.6±1.1 | 94.5±13 | 14.9±6.3 | 24.8±8.1 |
| 4 | 40.2±1.5 | 135.4±4.3 | 7.1±3.7 | 31.5±11 |
| 5 | 23.4±1.6 | 78.8±5.4 | 5.6±2.8 | 20.2±8.1 |

**Table 4.3:** Grey matter average signal-to-noise ratio (SNR) and contrast-to-noise ratio (CNR) for GASE data acquired with and without FLAIR preparation (FP and NF respectively).

estimate of CSF partial volume used to define the priors on $\lambda$. Maps used for prior $\lambda$ were generated from: segmentation of $T_1$-weighted images (referred to as T1); segmentation of $T_2$-weighted images (T2); biexponential fitting of $T_2$ (BF); and fitting of FLAIR contrast (FC).

Mean GM estimates for $R_2'$, $DBV$, $OEF$, and $\lambda$ for each subject and condition are given in Table 4.4, and the difference between each correction method and the FP dataset are presented in Figure 4.8. Two-way ANOVA with pairwise comparisons were used to determine whether the distributions from each NF condition were similar or dissimilar to the FP results.

Figure 4.9 shows example OEF maps under different FLAIR-correction conditions for a single healthy subject (the same as was shown in Figure 4.4). The OEF distributions were very similar in all cases.

The large inter-subject variability in DBV (and to a slightly lesser extent, $R_2'$) meant that there were no statistically significant differences between conditions of the group-level data. The exception was $R_2'$ estimation, where the uncorrected NF-2C and NF-3C results were significantly different from FP (although correction with any of the four CSF maps rectified this).

Intra-subject (voxelwise) data was tested with ANOVA and pairwise comparisons to determine whether any correction condition produced parameter estimates in GM that were not statistically significantly different from those obtained from inference on FP data. Uncorrected NF data, with both 2C and 3C models, produced

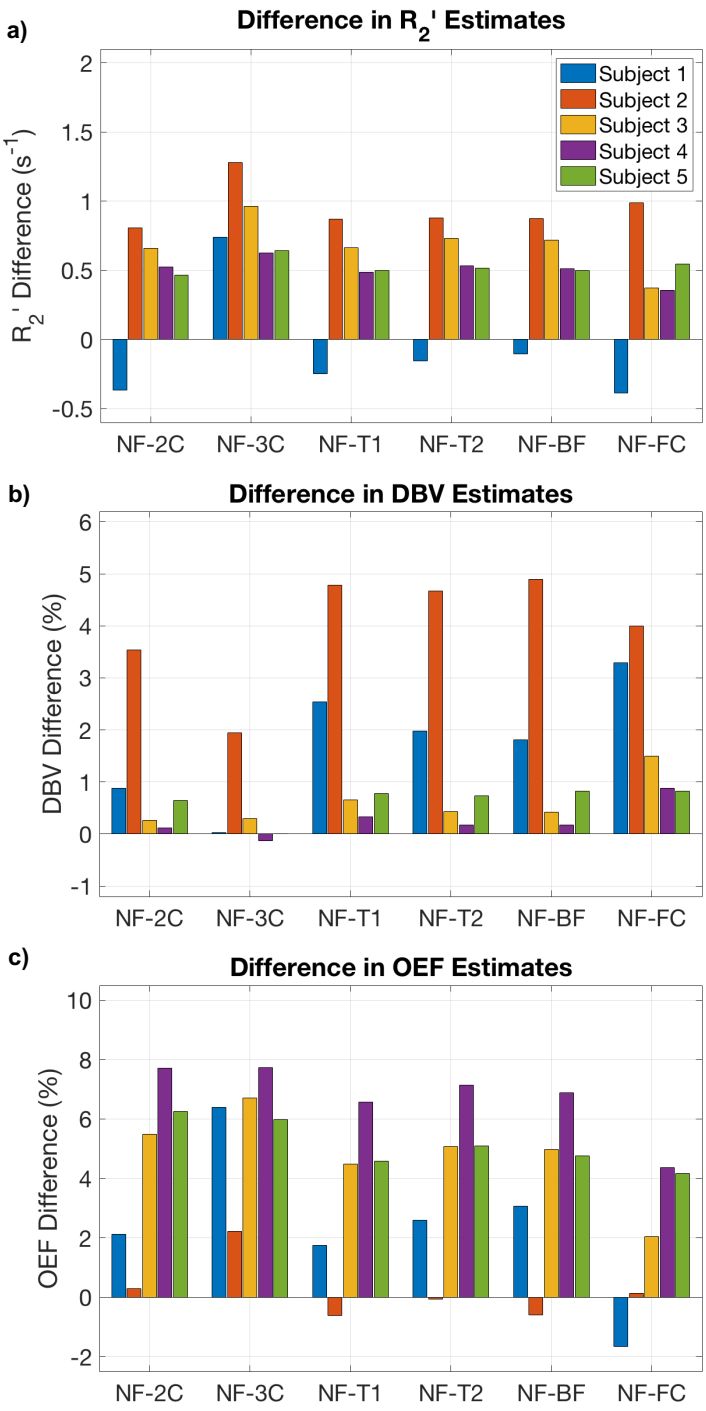


**Figure 4.8:** Differences in GM mean estimates of **(a)** $R'_2$, **(b)** DBV, and **(c)** OEF for five healthy subjects, under different conditions of CSF correction, compared to FLAIR-prepared acquisition. **NF:** non-FLAIR acquisition; **2C:** inference with two-compartment qBOLD model; **3C:** inference with three-compartment qBOLD model; **T1:** 3C model with $T_1$-weighted CSF spatial prior; **T2:** 3C model with $T_2$-weighted CSF spatial prior; **BF:** 3C model with biexponential fitting model CSF spatial prior; **FC:** 3C model with FLAIR contrast model CSF spatial prior.

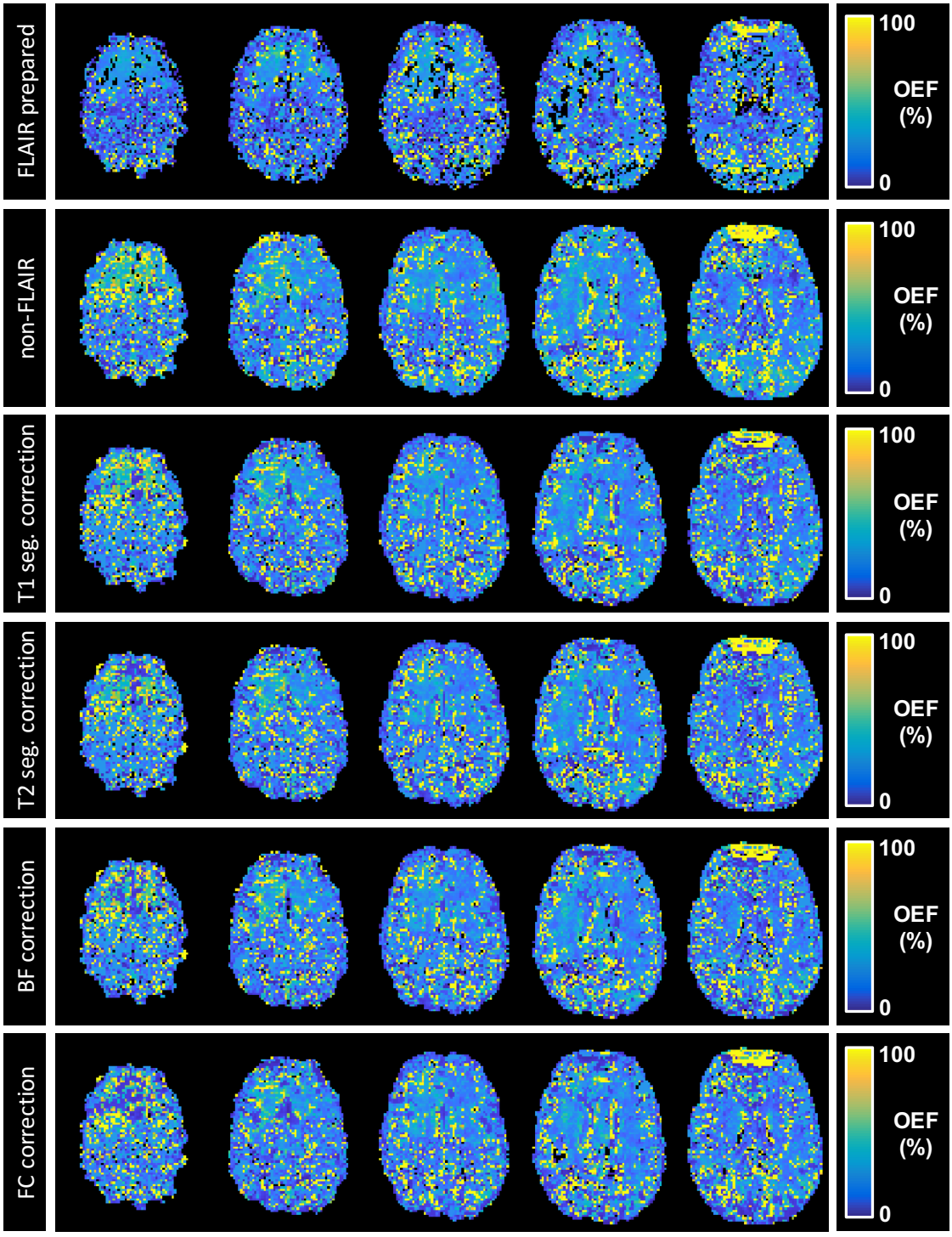


**Figure 4.9:** Example maps of estimated OEF from a single subject, under different conditions of CSF correction: **First row:** FLAIR-prepared acquisition; **Second row:** non-FLAIR acquisition (uncorrected 3C model); **Third row:** non-FLAIR acquisition with CSF correction using segmented $T_1$ data; **Fourth row:** non-FLAIR with $T_2$ segmentation CSF correction; **Fifth row:** non-FLAIR with biexponential fit CSF correction; **Sixth row:** non-FLAIR with FLAIR-contrast correction.

| | Grey matter $R_2'$ ($s^{-1}$) | | | | | | |
|---|---|---|---|---|---|---|---|
| **Subject** | **FP-2C** | **NF-2C** | **NF-3C** | **NF-T1** | **NF-T2** | **NF-BF** | **NF-FC** |
| 1 | 3.6±3.1 | 3.4±2.1 | 4.8±3.6 | 3.5±2.2 | 3.6±2.2 | 3.5±2.6 | 3.3±2.6 |
| 2 | 3.6±3.0 | 3.2±2.2 | 4.3±3.9 | 3.4±2.4 | 3.4±2.3 | 3.4±2.7 | 3.4±2.7 |
| 3 | 2.8±1.4 | 3.1±1.5 | 3.6±2.0 | 3.1±1.5 | 3.2±1.6 | 3.0±1.5 | 2.8±1.3 |
| 4 | 2.5±1.6 | 2.7±1.4 | 3.0±2.0 | 2.6±1.5 | 2.7±1.5 | 2.5±1.4 | 2.4±1.5 |
| 5 | 2.9±2.9 | 2.7±1.5 | 3.3±2.7 | 2.9±2.0 | 2.9±1.8 | 2.9±2.1 | 3.0±2.3 |
| | **Grey matter DBV (%)** | | | | | | |
| **Subject** | **FP-2C** | **NF-2C** | **NF-3C** | **NF-T1** | **NF-T2** | **NF-BF** | **NF-FC** |
| 1 | 4.6±2.9 | 3.9±1.7 | 4.9±2.1 | 3.1±0.8 | 3.2±0.8 | 3.3±0.9 | 3.1±0.8 |
| 2 | 3.7±2.0 | 3.1±1.6 | 4.5±2.7 | 2.9±1.4 | 3.1±1.6 | 3.0±1.5 | 3.1±1.6 |
| 3 | 2.7±1.5 | 3.1±1.1 | 3.6±1.3 | 2.7±0.9 | 2.7±0.9 | 2.7±0.9 | 2.6±0.8 |
| 4 | 1.9±1.2 | 2.5±0.8 | 2.5±1.1 | 1.9±0.7 | 2.0±0.7 | 1.9±0.7 | 1.8±0.7 |
| 5 | 4.6±2.3 | 2.5±0.9 | 3.2±1.7 | 2.5±0.9 | 2.4±1.1 | 2.4±1.1 | 2.4±1.1 |
| | **Grey matter OEF (%)** | | | | | | |
| **Subject** | **FP-2C** | **NF-2C** | **NF-3C** | **NF-T1** | **NF-T2** | **NF-BF** | **NF-FC** |
| 1 | 17±10 | 15±15 | 7.9±7.0 | 21±18 | 22±18 | 20±18 | 18±17 |
| 2 | 18±10 | 14±14 | 9.8±8.9 | 17±16 | 17±16 | 18±15 | 17±16 |
| 3 | 18±12 | 16±14 | 6.4±5.3 | 21±15 | 22±15 | 19±14 | 20±15 |
| 4 | 21±11 | 16±16 | 8.4±7.3 | 24±16 | 23±16 | 22±16 | 23±15 |
| 5 | 18±12 | 13±12 | 9.4±8.1 | 19±14 | 21±14 | 18±14 | 16±13 |

**Table 4.4:** Grey matter mean ± standard deviation of estimates of $R_2'$, DBV, and OEF from five healthy subjects, under different conditions of CSF correction. **FP:** FLAIR-prepared acquisition; **NF:** non-FLAIR acquisition; **2C:** inference with two-compartment qBOLD model; **3C:** inference with three-compartment qBOLD model; **T1:** 3C model with $T_1$-weighted CSF spatial prior; **T2:** 3C model with $T_2$-weighted CSF spatial prior; **BF:** 3C model with biexponential fitting model CSF spatial prior; **FC:** 3C model with FLAIR contrast model CSF spatial prior.

estimates of OEF that were significantly different from FP in all subjects ($p < 0.001$). Correction with the $T_1$-derived CSF map was effective in two out of five subjects, in that the corrected parameter estimates were not statistically significantly different from those obtained from FLAIR-prepared data; correction with a $T_2$-derived CSF map in two subjects (not the same two); BF correction in four subjects; and FC correction in one subject.

This suggests that no one method for CSF partial volume correction stands

above the others. But using a partial volume map derived from biexponential fitting may be useful in many, but not all, cases.

### 4.4.4 Discussion

#### SNR Improvement

The grey-matter average SNR and CNR, across all volumes and subjects, was roughly twice as high in non-FLAIR-prepared data than FLAIR-prepared data. This is also reflected in the lower grey matter standard deviations $\sigma$ seen in parameter estimates using the same 2C model on NF data compared to FP data (Table 4.4), where there was an improvement in $\sigma(R_2')$ (a 28% reduction) and $\sigma(DBV)$ (a 38% reduction) between NF and FP. This, as well as the other limitations of the FLAIR preparation (namely, that it requires longer acquisition time to achieve the same slice coverage, and is sensitive to motion) provide ample reason for attempting to model and correct for CSF signal contribution in NF data.

#### CSF Signal Correction

Inference on NF data was performed under a range of conditions, and the results compared with inference on FP data. The consistent lack of similarity in estimates of OEF and DBV between FP-2C and NF-2C demonstrate that simply ignoring the extracellular compartment leads to misestimation of physiological parameters. Similarly, in all but one case, fitting the 3C model with $\lambda$ as a free parameter is not sufficient to account for CSF signal.

The FP data, as shown in the first row of Figure 4.9 (and in Figure 3.6), still contains some signal in the ventricles, which suggests that the CSF signal may not have been entirely suppressed by the FLAIR preparation. This may mean that part of the signal in grey matter arises from CSF, as well as tissue, so it may be that the 3C model should be used even when inferring on FP data.

There is a clear potential for an externally defined spatial prior on $\lambda$ to offer some improvement to parameter estimation of NF data. Four methods for $\lambda$ estimation were presented in Section 4.3, and their use as spatial priors was compared. It

was assumed that the GM parameter estimates obtained from FLAIR-prepared data were accurate, and that effective correction ought to produce values that were not significantly different from those. By this standard, $T_2$ biexponential model fitting resulted in the best correction, although all methods were inconsistent across subjects, and parameters. In general, there is correlation between effective $R_2'$ correction, and OEF correction, but not with DBV, despite the fact that $R_2'$ and DBV estimates are together required to produce OEF.

There were 3 (of 15) subjects-parameter combinations in which all correction methods appeared to work equivalently well, and 4 in which they all performed equally poorly. And two subjects for which $R_2'$ estimation did not appear to require correction at all, since there was no significant difference between the FP and NF conditions, after inference with the 2C model.

DBV estimates seemed to be more strongly affected by the presence or absence of the FLAIR preparation than the $R_2'$ estimates. This may be because, to a first approximation, the signal models used to describe the intravascular compartment (Equation 2.43) and the CSF compartment (Equation 4.1) behave similarly in the regimes of $\tau$ used here. The assumptions made in relating apparent DBV to actual DBV $\zeta$ may also have been a source of error in the estimates.

**Other Assumptions and Limitations**

One explanation for the large variation of results between subjects (both the parameter estimates themselves, and the effectiveness of the various correction methods) may be that the values assumed for $R_2$ throughout are not accurate. As well as the large variation in $T_1$ (or $R_1$) values found in the literature (discussed in Section 4.2.2) there is considerable variation in literature estimates of $R_2^e$ and $R_2^t$ at 3 T, and in the values used in qBOLD related experiments.

Literature $R_2^t$ varies from 10.1 $s^{-1}$ ($T_2$=99 ms)[243] to 14.1 $s^{-1}$ ($T_2$=71 ms).[245] The value used here, $R_2^t$=11.5 $s^{-1}$ falls near the middle of this range, and is the value used by He & Yablonskiy,[141] as well as being similar to that of other qBOLD related literature.[159,165] It is, however, lower than tissue $R_2$ measurements reported

from recent qBOLD experiments: Ulrich & Yablonskiy[252] found $R_2^t$=15.1 $s^{-1}$, and Domsch and colleagues[153] found $R_2^t$=18.7 $s^{-1}$.

There is even greater variation in $R_2^e$, which was measured as 0.625 $s^{-1}$ by Qin,[239] and 4.0 $s^{-1}$ by He & Yablonskiy.[141] This chapter has used the latter value, since it is based on an application to the qBOLD model; however, it is possible that using alternative values for $R_2^e$ and $R_2^t$ may have resulted in differences in the final GM parameter estimates, and in the BF correction. In the absence of a ground truth measurement of $R_2$, it is not possible to compare these values directly.

Using the FP data as the ground truth against which to compare correction methods may also have negatively influenced results. Since SNR and CNR were higher in the NF case, it may be that parameter estimates resulting from those data were more accurate, and that the apparent lack of difference between FP and NF estimates in some cases is the result of larger uncertainty in the FP results. In all cases, however, the ratio of mean to standard deviation of estimated parameters is still significantly higher than the SNR or CNR, which suggests that there was additional uncertainty in the model itself, and that it does not perfectly describe the data.

## 4.5 Conclusions

This chapter has described the impact of the signal from extracellular fluid (CSF and ISF) on the qBOLD signal, and has explored the possibility of correcting for this signal in the analysis pipeline.

An analytical model of the CSF signal, taken from the literature, was used to simulate qBOLD data, and inference using sampling-based techniques showed that the additional parameters used to describe the CSF signal were collinear with one another and with other model parameters, especially DBV. *In vivo* data showed significant differences in estimates of OEF (and other model parameters) in the absence of a FLAIR preparation. This pointed towards the need for an external estimate of the CSF model parameters, particularly CSF volume $\lambda$. A correction

of this kind may also be useful even in the FLAIR-prepared case, as there could be residual CSF signal that contributes to the measured ASE signal.

Several methods for CSF partial volume estimation were described and tested, including segmentation of $T_1$- and $T_2$-weighted images, and fitting models of the biexpoential decay of $T_2$, and the $T_1$-weighted contrast introduced by the FLAIR preparation. The resulting partial volume maps were compared with one another, and then used as spatial priors to inform inference on qBOLD data.

Analysis of the results showed that there was substantial variation in the effectiveness of each correction method between subjects. This was also a function of the parameter of interest. $T_2$ biexponential model fitting was found to be the most effective correction method in most subjects, in terms of OEF estimation.

There is significant scope for further investigation, both of the assumptions which underlie the model of CSF signal, and of additional methods for correcting for it.

# 5

# Correcting for qBOLD Model Assumptions

## Contents



In this chapter, possible modifications to the qBOLD protocol are explored which could correct for, or mitigate, the effect of diffusion and other effects on

the final parameter estimates. In Section 5.1 the problem of diffusion is explained, and literature methods for dealing with it are presented. Section 5.2 contains the theoretical basis for the static dephasing model, and its alternatives, and the means by which a model can be assessed. The methods used for simulating data, deriving model corrections, and acquiring *in vivo* data to test these corrections, are given in Section 5.3. The results of each of these steps are presented in Section 5.4, and discussed in Section 5.5. Section 5.6 summarizes this chapter.

## 5.1 Introduction

The qBOLD model described in Section 2.3.2, has been shown (in Chapter 3 and elsewhere[16,19,165]) to overestimate DBV and underestimate OEF compared with expected values from the literature. It has been suggested that diffusion of protons in the tissue results in signal attenuation that is not accounted for in the model,[18,159] which leads to this misestimation of physiological parameters.

The effect of diffusion on $T_2$ in the presence of susceptibility altering objects was described by Gillis & Koenig for the example of very small ferro- or paramagnetic spheres.[253] Given the size of the objects (with radii on the order of tens of nanometres), water protons are considered to be in the motional narrowing regime.

The analytical qBOLD model of Equation 2.25 describes protons in the static dephasing regime (SDR),[14] in which it is assumed that diffusion does not affect the tissue signal. This is valid when the objects (blood vessels) are sufficiently large ($R > 6\mu m$),[17] but does not hold in the presence of smaller objects. In that regime the effect of differences in susceptibility is moderated by the fact that protons are rapidly moving closer or further away. The aggregate rate of phase accrual (equivalent to frequency $\delta\omega$) across all the protons in a voxel changes as a result, and becomes less sensitive to differences in the susceptibility offset $\Delta\chi$ between the vessels and the bulk tissue. The system is therefore approaching the so-called motional narrowing regime.[147,148]

Several authors have proposed methods for accounting for these differences, which are presented in Section 2.3.5. These include new qBOLD models, derived from

first principles, such as that of Kiselev & Posse,[154] or the use of the Gaussian phase approximation.[146] The alternative approach, pursued by Dickson and colleagues, is to use a phenomenological model derived from simulated data.[160]

The effect of diffusion on the ASE signal can be tested using Monte Carlo simulations,[158] as well as a number of other assumptions made in the analytical qBOLD model. These include the assumed distribution of blood vessel radii that contribute to the signal, and the variation in OEF between different blood vessels. The results can then be compared to those obtained from other models that explicitly include diffusion.[154]

In this chapter, Monte Carlo simulations are also used to test other aspects of the qBOLD model, such as the assumptions it makes including the distribution of blood vessel radii and oxygenation, and the use of scaling constants based on their assumed geometry. They are also used to determine optimal acquisition schemes. The results are then applied to *in vivo* data acquired from healthy volunteers, and compared with the existing method.

## 5.2 Theory

### 5.2.1 The Static Dephasing Criterion

The motional narrowing regime[253] applies when the characteristic diffusion time $t_D$ (defined as the average time taken for a spin to diffuse a distance equal to the radius $R$ of the susceptibility altering object) is significantly shorter than the time in which it will dephase, or

$$t_D = \frac{R^2}{D} \ll \frac{1}{\delta\omega} \tag{5.1}$$

where $D$ is the rate of diffusion, and $\delta\omega$ is the characteristic frequency defined in Equation 2.27.

The static dephasing regime applies when the opposite condition is true, or when $t_D \gg \delta\omega^{-1}$. Yablonskiy & Haacke clarified that when the density of susceptibility altering objects is higher (such as in the case of blood vessels, as opposed to the tiny

magnetized particles modelled by Gillis[253]), the average distance between objects $\bar{r}$ is a more important consideration, leading to the static dephasing criterion (for 3D diffusion about randomly oriented cylinders):[14]

$$\frac{\bar{r}^2}{24 \cdot D \cdot DBV} \gg \frac{1}{\delta\omega} \tag{5.2}$$

since, in this case, if the average distance a proton travels in time $T_2'$ (which is given by $T_2' = {R_2'}^{-1} = (DBV \cdot \delta\omega)^{-1}$) is comparable to half the average distance between nearest particles, $\bar{r}$, then its phase may average out as it diffuses.

With a field strength of 3 T, $OEF = 40\%$, $DBV = 3\%$, $D = 1\mu\text{m}^2\ \text{ms}^{-1}$, and other parameters fixed to the constant values used in previous chapters (see Table 3.1), the static dephasing criterion requires vessels with radius $R_c \gg 3\mu\text{m}$. This means that for most venules and veins, the static dephasing regime ought to be applicable. However, the presence of smaller vessels containing deoxygenated blood (whether small venules or capillaries), will affect the rate at which spins dephase, and hence estimates of physiological parameters.[254]

### 5.2.2 Deoxyhaemoglobin Content Quantification

Although OEF is the primary parameter of interest in qBOLD, in the streamlined approach (of Chapter 3), it is a derived measure, based on the ratio of $R_2'$ and DBV (which is another parameter of interest). Other physiological parameters can similarly be derived from the qBOLD model. One that is particularly relevant is deoxyhaemoglobin content (dHb), which is the total volume of deoxyhaemoglobin molecules in a voxel, measured in units of millilitres of dHb per 100 grams of tissue (ml/100g). When considering only the extravascular tissue signal, dHb content is:

$$dHb_{content} = \frac{3 \cdot R_2'}{4\pi \cdot c_{Hb} \cdot \gamma \cdot B_0 \cdot \Delta\chi_0 \cdot \rho} \times 100\ \text{g}^{-1} \tag{5.3}$$

where the $c_{Hb}$ is the conversion factor between haematocrit and haemoglobin concentration, 0.03,[255] and $\rho$ is the density of brain tissue, 1.04 g/ml.[256]

In functional MRI (see Section 2.3.1), the BOLD signal measured in a $T_2^*$-weighted acquisition is a measure of dHb, since it is the combined effect of changes

in blood volume, flow, and oxygenation.[111,129] In acute stroke, it is known that several of these factors change through time, and vary between regions with different levels or stages of ischaemia. It is therefore possible that an uncalibrated measurement of dHb alone may be sufficient to identify the ischaemic penumbra.

Equation 5.3 amounts to a scaling of $R_2'$ from a MRI relaxometry parameter to a physiological one, which may therefore be useful to compare between individuals or between brain regions within a single subject. Since it does not depend on DBV, it can also be used as an intermediate parameter around which to design an optimal ASE-qBOLD experiment, without needing a correction for DBV overestimation.

Using dHb as the sole parameter of interest is limited by the fact that the intravascular compartment has been shown to contribute to the ASE signal (see Chapter 3) but this is not taken into account in Equation 5.3. The fact that DBV is expected to vary throughout the healthy brain, and potentially even more so in the presence of ischaemia, means that dHb content is not necessarily a direct quantification of the availability of oxygen for metabolism, as OEF is.

## 5.3 Methods

Monte Carlo methods were used to simulate qBOLD data with the effect of diffusion included. These were used to test corrections to the qBOLD model, and to optimize certain parameters used to acquire the data. *In vivo* ASE data from healthy volunteers were acquired, and the model corrections used assessed on these. TRUST data was also acquired from a subset of the volunteers, and the average OEF results compared across the two methods.

### 5.3.1 Diffusive Vessel Simulation

A qBOLD signal was simulated for a single proton according to the following method,[18] which was implemented in MATLAB:

1. A system of vessels was generated by randomly selecting a large number of vessel origin points within, or on the surface of, a sphere, and placing a

randomly oriented infinitely long cylinder of radius $R_c$ at each origin point until the total volume occupied by cylinders equals the target volume fraction $V_f$.

2. A proton's random walk path was simulated by placing a proton at the centre of the vessel system, and independently selecting steps along each direction from a normal distribution with zero mean and standard deviation $\sigma_d$:

$$\sigma_d = \sqrt{2D\Delta t} \tag{5.4}$$

where $\Delta t$ is the time interval between steps.

3. The phase accrued $\Delta\phi$ at each step is calculated by summing over the field contribution from all $N$ vessels:[158]

$$\Delta\phi = 2\pi \cdot \gamma B_0 \cdot \Delta\chi_0 \cdot \Delta t \cdot OEF \cdot Hct \cdot \sum_{i=1}^{N} \left(\frac{R_c}{r_i}\right)^2 \cos 2\phi_i \sin^2\theta_i \tag{5.5}$$

where $\theta$ is the angle of the vessel with respect to $B_0$, $\phi$ is the angle of the projection of $B_0$ onto a plane orthogonal to the vessel, and $r$ is the perpendicular distance from the proton to the vessel. This is only valid when $r \geq R_c$, that is for protons outside vessels.

4. An ASE signal is generated by summing $\Delta\phi$ for all intervals prior to the refocussing pulse (at time $\frac{TE-\tau}{2}$), then subtracting all $\Delta\phi$ from then until readout at $TE$.

5. Steps 1–4 are repeated for $P = 10^5$ protons, and the phase evolutions summed to simulate an ASE signal measurement:

$$S(\tau) = \left| \frac{1}{P} \sum_{j=1}^{P} e^{i\phi(\tau)} \right| \tag{5.6}$$

6. Steps 1–5 are repeated for each radius $R_c$ to be tested, and the resulting signals summed, with weightings proportional to the relative fractional volume of $R_c$.[18]

Data simulated in this manner were used to test aspects and assumptions of the qBOLD model. In the following cases, the parameters used were: $TE$=84ms, $\tau$ from -28 to 68 ms, in steps of 4 ms.

**OEF Distributions**

The analytical qBOLD model, and other attempts to quantify OEF, assume a single OEF value for a given voxel, which is typically defined as $(1 - Y)$, where $Y$ is the oxygen saturation of venous blood. This assumes, firstly, that arterial blood is fully saturated, secondly, that only venous blood contributes to the qBOLD signal, and thirdly, that all veins and venules in the voxel have the same saturation.

These assumptions were tested by simulating distributions of vessels with differing combinations of OEF values. Arterioles were simulated with $OEF = 5\%$ to test the possibility that incoming arterial blood is not fully oxygenated; venules were simulated with the literature $OEF = 40\%$; and capillaries were simulated as having $OEF = 30\%$. This distribution of oxygenations was combined with radii drawn from the Sharan distribution (Table 5.1) to model the combined effects of a more realistic vascular system. This distribution was compared to one of a single OEF (chosen to be equal to the weighted average OEF in the multiple-OEF case). The total volume of vessels $\zeta$ was held constant at 5% throughout.

**Vessel Radius Distributions**

Since the radius of the vessels determines the characteristic diffusion time $t_d$ (Equation 5.1), and hence whether the proton is in the static dephasing regime, the effect of simulated vessel radius on signal can be tested. It is possible to simulate all vessels as having the same radius, or to model a distribution of radii. Single radii simulations were performed with logarithmically spaced $R_c = \{3, 10, 30, 100\}$ μm, and three anatomically derived distributions were also tested:

- **Sharan distribution**. This is based on the distribution of vessel radii found in sheep[257] and divides the vasculature into 11 vessel sizes: five of arterioles, five of venules, and one of capillaries. The radii of the capillary and venous

| **Vessel** | **Capillary** | **Venules** | | | | |
|---|---|---|---|---|---|---|
| Radius (μm) | 2.8 | 7.5 | 15 | 22.5 | 45 | 90 |
| Fractional Volume | 0.412 | 0.113 | 0.117 | 0.116 | 0.121 | 0.121 |

**Table 5.1:** Sharan distribution vessel radii and relative volume fractions.[109] Arterioles were excluded from this model.

compartments are given in Table 5.1, along with the relative volume fractions for each radius. Arterioles were not included in the simulated data.

- **Jochimsen distribution**. This is based on *in vivo* human vessel size imaging measurements using hypercapnia-induced BOLD.[258259] Here it was found that the relation between vessel radius and volume fraction followed a Fréchet distribution:

$$V_f(R_c) = \frac{\alpha}{s}\left(\frac{R_c - m}{s}\right)^{-1-\alpha} \exp\left(-\left(\frac{R_c - m}{s}\right)^{-\alpha}\right) \tag{5.7}$$

with shape parameter $\alpha = 0.41$, scale parameter $s = 5.8$ and minimum $m = 10.1$.

- **Lauwers distribution**. This is based on *ex vivo* human anatomical studies,[260] which found that the vascular network accounted for 2.7% of the total volume in the cortex of the right temporal lobe, and that vessels were normally distributed with respect to the inverse square root of their diameter, that is,

$$\frac{1}{\sqrt{D_c}} \sim \mathcal{N}(0.38, 0.07) \tag{5.8}$$

where $D_c = 2R_c$ is the vessel diameter, and the distribution's mean (0.38) and standard deviation (0.07) were derived empirically. This distribution includes capillaries and arterioles, as well as venules, so the total effective DBV simulated may be less than with the other distributions.

The radii and relative volume fractions of these three distributions are shown in Figure 5.1.

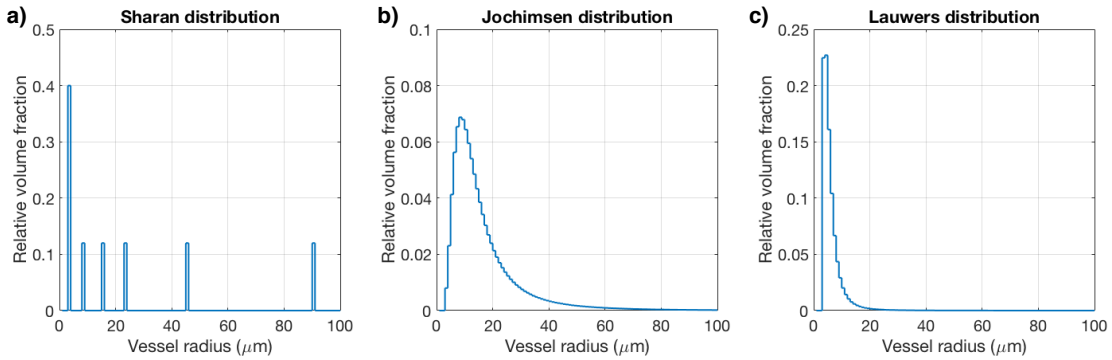


**Figure 5.1:** Relative volume fractions for vessels of each radius, between 1 and 100 μm, for three possible real distributions of vessels.

### Other Parameters

Throughout, the diffusion coefficient of tissue water was set as $D = 1.0\mu m^2$ $ms^{-1}$, based on similar estimates from the literature: Kiselev & Posse,[154] following Le Bihan,[261] used $D = 0.76\mu m^2$ $ms^{-1}$, while Dickson and colleagues used $D = 1\mu m^2$ $ms^{-1}$,[159] and Berman *et al.* used $D = 0.8\mu m^2$ $ms^{-1}$ (based on Equation 5.2).[148]

## 5.3.2 Model Corrections

In order to test the qBOLD model across the entire range of possible values, data were simulated (using the above method) using each vessel distribution, for 1000 pairs of OEF and DBV values, drawn randomly from OEF= $\{0, 100\}$ and DBV= $\{0, 10\}$. For each pair, ASE signals were computed with $TE$=80ms, and $\tau$ from -16 to 64 ms in steps of 8 ms.

The two-compartment (2C) qBOLD model (Equation 2.37) was used to infer $R_2'$ and DBV from the simulated signals, using VB implemented in FABBER.[22,181] dHb and OEF were then calculated (using Equations 5.3 and 2.34, respectively). For each simulated OEF-DBV pair, the error was computed between the estimated and simulated (ground truth) values of OEF, DBV, and dHb.

### Linear Correction

Given the disparity between true (simulated) dHb, and dHb estimated using the SDR qBOLD model (see Section 5.4.2, below), it is likely that both simulated and

*in vivo* estimates could be improved by making a correction to the SDR model's inference of $R_2'$. In the long-$\tau$ regime (when $\tau >> t_c$, Equation 2.33b) the ASE signal is linear-exponential in $R_2'$ so a scalar multiplier $\kappa$ applied to $R_2'$ could correct for the influence of diffusion in this particular case. So, Equation 5.3 becomes

$$dHb_{content} = \frac{3 \cdot \kappa \cdot R_2'}{4\pi \cdot c_{Hb} \cdot \gamma \cdot B_0 \cdot \Delta\chi_0 \cdot \rho} \times 100 \text{ g}^{-1} \tag{5.9}$$

where $\kappa = 1$ in the default (non-diffusive) case.

The value of $\kappa$ was optimized over simulated ASE signals with 1000 known pairs of OEF and DBV, using MATLAB's fminbnd function (searching across the interval $\kappa = \{0.0, 2.0\}$). This process was repeated for data simulated with each of the three realistic vessel radius distributions.

**Non-Linear Corrections**

A scalar correction to $R_2'$ alone will not correct for the effect of diffusion on DBV estimates, so a further correction is needed. It can be noted that the short-$\tau$ regime of the SDR model (Equation 2.33a) contains a factor of 0.3, which is the result of integrating over a distribution of infinitely long, randomly oriented cylinders.[14] If this factor is replaced by a parameter $\eta$, and the above scalar $\kappa$ included, then Equation 2.33a becomes

$$\log\left(S^t(\tau)\right) = -\eta \cdot \frac{(\kappa \cdot R_2' \cdot \tau)^2}{DBV} \tag{5.10}$$

in which $\eta$ can be optimised to account for deviations from the SDR model, either from diffusive effects, or from differences in vessel distributions. Optimal values for $\eta$ and $\kappa$ were found simultaneously using MATLAB's fminsearch function, optimising over 1000 ASE signals generated from new random pairs of OEF and DBV. Optimization was initialized at the default SDR values of $\kappa = 1$ and $\eta = 0.3$, but other initializations ($\kappa = \{0, 2\}$, $\eta = \{0, 0.5, 1\}$) were tested to reduce the risk of finding only local minima.

The characteristic time $t_C$, which determines the transition between the short-$\tau$ and long-$\tau$ regimes of the asymptotic model (Equation 2.33) was optimised in

Chapter 3 against the complete analytical SDR qBOLD model. It is possible that the effect of diffusion, or $R_c$ distribution, may affect the time through which the short-$\tau$ quadratic exponential decay holds true. To test this, $t_C$ was also optimised, both alone, and simultaneously with $\kappa$, and $\kappa$ and $\eta$, in the same way.

The Davis model (Equation 2.17) follows Ogawa and colleagues' original description of the BOLD signal[120] and suggests that [dHb] relates to the BOLD signal by means of a power law with exponent $\beta$. If this relation is incorporated in the definition of characteristic frequency of the qBOLD signal, then Equation 2.27 can be written

$$\delta\omega = \frac{4}{3} \cdot \pi \cdot \gamma \cdot B_0 \cdot \Delta\chi_0 \cdot (Hct \cdot OEF)^{\beta} \tag{5.11}$$

since $[dHb] \propto Hct \cdot OEF$. The parameter $\beta$ can then be optimised in the same way as $\kappa$ and $\eta$, individually or simultaneously with them.

A different correction can be made to the way in which OEF is calculated from $R_2'$ and DBV. Prior work[18] (and the results in Section 5.4.2, below) shows that the relation between true (simulated) OEF and estimated OEF is not linear, so a correction is needed that will non-linearly map estimated OEF (which is proportional to the ratio of $R_2'$ and DBV, according to Equation 2.34) onto true OEF:

$$OEF_{true} = f(R_2', DBV) \tag{5.12}$$

Given that the shape of the curve in Figure 5.5d-e (below) is approximately sigmoidal, an inverse-sigmoid function could be used to transform the ratio of $R_2'$ and DBV into OEF. A tangent function was chosen:

$$OEF_{true} = a_1 \cdot \tan\left(a_2 \cdot \frac{R_2'}{DBV}\right) + a_3 \tag{5.13}$$

where $a_1$, $a_2$, and $a_3$ are parameters that must be optimised for a particular vessel distribution and acquisition protocol. In this case, optimization of the $a$ parameters was performed using MATLAB's Curve-fitting toolbox and the fminsearch function on simulated ASE data.

**Assessing the Corrections**

The effectiveness of each correction method was determined by fitting the corrected model (with parameters $R_2'$ and DBV) to simulated ASE data using VB. ASE signals were simulated for 1000 OEF-DBV pairs, drawn freshly from the same intervals as above. dHb was calculated using Equation 5.9, and OEF using Equation 2.34 and Equation 5.13.

The difference between the true (simulated) and estimated values were computed for each parameter, and averages of the absolute error, and the relative error (defined as absolute error divided by true value), were calculated. These quantities were minimized in order to determine the optimal correction method that would work across a broad range of possible physiological values for OEF and DBV.

The versatility of the optimized correction parameters was tested by fitting data generated using one $R_c$ distribution using the parameters of the others (i.e. Sharan-distribution simulated data were inferred using $\kappa_{Jo}$, $\eta_{Jo}$, $\kappa_{La}$, and $\eta_{La}$). The errors in the resulting physiological parameter estimates were compared across each of the $R_c$ distributions.

### 5.3.3 Optimizing qBOLD Acquisition

Simulated qBOLD signals were also used to optimize the acquisition protocol for streamlined qBOLD. In particular, $TE$ and the choice of $\tau$ values were assessed for their suitability to fitting OEF, DBV, and dHb. It was assumed throughout that 11 ASE volumes would be acquired, in line with the current sqBOLD protocol,[19] so as to avoid changing the total scan duration.

First, data were simulated with four $TE$s: $TE = \{48\text{ms}, 66\text{ms}, 80\text{ms}, 112\text{ms}\}$. Three sets of $\tau$ values were also tested, with even spacings between -8 and 32ms (for all $TE$s), between -16 and 64ms (for $TE = 80$ms and $TE = 112$ms), and between -24 and 96ms (for $TE = 112$ms only). This was repeated for all three vessel radius distributions. A jackknife analysis of the $\tau$ values was performed on data at $TE = 48$ms and $TE = 80$ms, in which one $\tau$ value's data was removed, and the remaining 10 inferred as normal. This was repeated for each of the 11 $\tau$s, and the

| | Spin Echo Displacement $\tau$ (ms) | | | | | | | | | | |
|---|---|---|---|---|---|---|---|---|---|---|---|
| **Set Number** | **1** | **2** | **3** | **4** | **5** | **6** | **7** | **8** | **9** | **10** | **11** |
| 1 | -16 | -8 | 0 | 8 | 16 | 24 | 32 | 40 | 48 | 56 | 64 |
| 2 | -16 | -8 | -4 | 0 | 4 | 8 | 16 | 24 | 32 | 48 | 64 |
| 3 | -16 | -12 | -8 | -4 | 0 | 4 | 8 | 12 | 16 | 24 | 32 |
| 4 | 0 | 2 | 4 | 6 | 8 | 10 | 20 | 30 | 40 | 50 | 60 |
| 5 | -10 | -6 | -2 | 2 | 6 | 10 | 20 | 30 | 40 | 50 | 60 |
| 6 | -4 | -2 | 0 | 2 | 4 | 6 | 32 | 40 | 48 | 56 | 64 |

**Table 5.2:** Spin echo displacement $\tau$ values (in ms) tested using simulated data, for $TE = 80$ms. Set 1 corresponds to the evenly-spaced values typically used in streamlined qBOLD.[19]

error between true and estimated parameters was compared across the results, to determine which individual data points were more or less important to overall fitting.

Then, for $TE = 80$ms, several other sets of $\tau$ values that were not evenly spaced were tested. These are shown in Table 5.2. As in the previous part (Section 5.3.2), 1000 simulated signals (with pairs of OEF and DBV values) were generated for each $\tau$ set, and VB inference was performed using the uncorrected, $\kappa$-corrected, and $\kappa, \eta$-corrected models. The average error between true (simulated) and estimated parameter values was calculated, as was the correlation between both sets of values.

### 5.3.4 *In Vivo* Data

GASE[163] data were acquired from six healthy volunteers (aged 25–41, 3 female) using a 3T Siemens Verio system (Siemens Healthineers, Erlangen, Germany), under a technical development protocol agreed with local ethics and institutional committees. GASE parameters were: $TR/TE$=3s/84ms, $TI_{FLAIR}$=1210ms, 96×96 matrix, eight slabs, 2.29×2.29×5mm resolution, and 11 $\tau$ values ranging from -16 to 64ms in steps of 8ms.

To test other acquisition parameters, GASE data were also collected from a single subject at $TE$=66ms (the shortest $TE$ at which a 96x96 matrix could be acquired on the available hardware) with 11 $\tau$ values evenly spaced between -8 and $\tau_{max}$=32ms; and at $TE$=112ms with two sets of 11 evenly-spaced $\tau$ values, between -8 and $\tau_{max}$=32ms and between -24 and $\tau_{max}$=96ms. Additionally, 11 $\tau$ values

(evenly spaced between -8 and $\tau_{max}$=32ms) were collected at $TE$=84ms. From another single subject, GASE data were collected at $TR$=2s (with $TI_{FLAIR}$=870ms), and all other parameters kept constant, to compare the effect of a shorter $TR$ acquisition. In the remaining 4 subjects, GASE data were collected with the same parameters, but in an 80×80 matrix.

A high resolution structural MPRAGE[227] image was acquired for each subject, with $TR/TI/TE$ = 2040/900/4.7ms, flip angle 8°, 192×192×174 matrix, 1×1×1 mm resolution. TRUST[59] data were acquired for four subjects, with 6 $TE$s, from 0 to 200ms in steps of 40ms, two repeats (for a total of 24 volumes).

### Pre-Processing

GASE data were processed in the same way as all previous datasets (see Sections 3.3.3 and 4.4.1), with Gaussian filtering, motion correction, and Gibbs artefact removal. Data were brain extracted using BET,[231] and the SE ($\tau$=0) volume was segmented in FAST[205] to produce a GM mask for each subject.

### VB Analysis

VB (implemented in FABBER) was used to infer the parameters of the two-compartment $R_2'$-DBV qBOLD model under conditions of: no correction, $\kappa$ correction, and $\kappa, \eta$ correction. OEF was calculated from the resulting estimates of $R_2'$ and DBV using Equation 2.34. OEF was also calculated using the results from the $\kappa, \eta$ corrected analysis using Equation 5.13. For each correction method, the values of $\kappa$, $\eta$, and the parameters of Equation 5.13, were taken from simulated data for all three $R_c$ distributions (see Table 5.5 and Equations 5.16a–5.16c) and each one was tested in turn.

A two-way ANOVA test, followed by pairwise comparisons with the Tukey-Kramer method, was used to compare GM average values for each parameter between the different correction conditions.

**TRUST Validation**

TRUST data (see Section 2.3.6) were analyzed using the following process. First, the superior sagittal sinus (SSS) was manually segmented (based on the scale of the intensity changes between the labelled and unlabelled conditions). Then, labelled and unlabelled images of the same effective echo time $TE_e$ were subtracted, and the result fit to Equation 2.49 using VB, to determine $R_2^b$. $R_1^b$ was assumed to $0.62\text{s}^{-1}$.[171] In whole blood, $R_2^b$ is related to OEF by[172,174]

$$R_2^b = A + B \cdot OEF + C \cdot OEF^2 \tag{5.14}$$

where

$$A = -13.5 + 80.2 \cdot Hct - 75.9 \cdot Hct^2 \tag{5.15a}$$

$$B = -0.5 \cdot Hct + 3.4 \cdot Hct^2 \tag{5.15b}$$

$$C = 247.4 \cdot Hct \cdot (1 - Hct) \tag{5.15c}$$

The coefficients in 5.15 are taken from the literature.[172] Equation 5.14 was solved for OEF using a fixed value of $Hct = 0.40$ to obtain whole-brain OEF estimates for each subject.

## 5.4 Results

### 5.4.1 Diffusive Vessel Simulation

Figure 5.2 shows the effect of simulating vessels with a range of OEF values, as opposed to the situation in which all vessels have the same OEF (but with the same distribution of radii), in the non-diffusive and diffusive case. The root mean square (RMS) difference between the two normalized signals, without diffusion, was 0.0238. With diffusion, RMS=0.0422. Since the RMS error is less than 5% (in both cases) and since, by inspection, the signals are extremely similar in the short-$\tau$ regime (in the diffusive case), it seems reasonable to approximate each voxel as having a single value for OEF, even if the actual OEFs of each vessel vary widely.

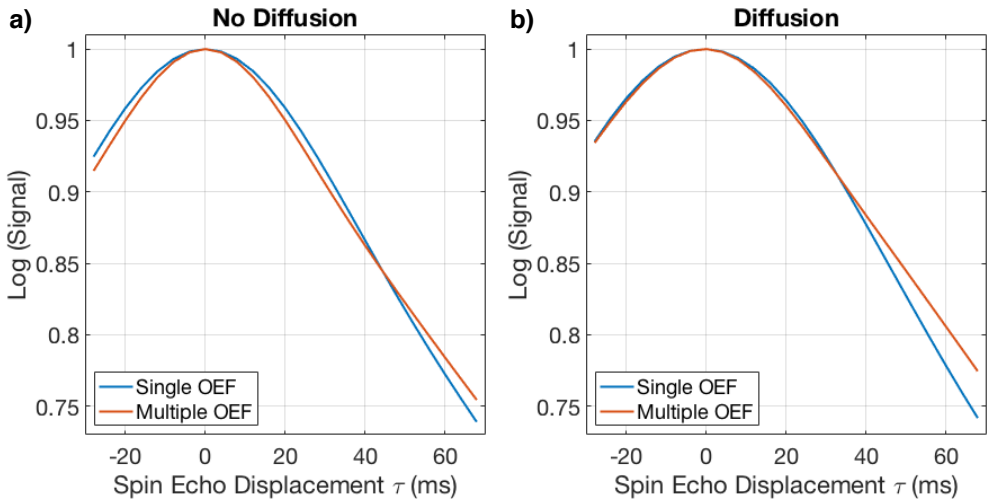


**Figure 5.2:** ASE signal curves generated from simulated data with a distribution of vessel radii $R_c$, with either a single OEF value shared among all vessels, or a different OEF for each radius. **a)** without and **b)** with diffusion. Average OEF and total DBV are the same in all cases.

Figure 5.3 shows the effect of diffusion on simulated ASE signals generated with different $R_c$. Table 5.3 shows the error in estimates of $R_2'$, DBV, and OEF made using the SDR qBOLD model across a range of OEFs between 20 and 70%, and DBVs between 1 and 10%. These both show that the accuracy of the SDR model is not strongly affected by large vessels ($R_c \sim 100\mu m$), but small vessels ($R_c \leq 10\mu m$) change the shape of the ASE curve significantly, and cause mis-estimation of $R_2'$ and hence $OEF$.

Figure 5.4 shows the effect of diffusion on ASE signals generated using *in vivo* distributions of $R_c$. There is some qualitative differentiation between distributions in the static case, but the diffusive case is very different, and has a lot more variation between distributions. This means that parameter estimates using the qBOLD model will be affected by the choice of distribution. Also shown are simulated signals generated using vessels of a single size (in each case, chosen as the mean $R_c$ of each distribution), with diffusion. There is some difference between single-radius and multiple-radii in all cases. This is especially so for the Sharan distribution (Figure 5.4a), which has a high mean radius, but also a significant contribution from a very small radius (2.8 μm). The Jochimsen and Lauwers distributions have lower mean radii, and less contribution from larger vessels (which can be

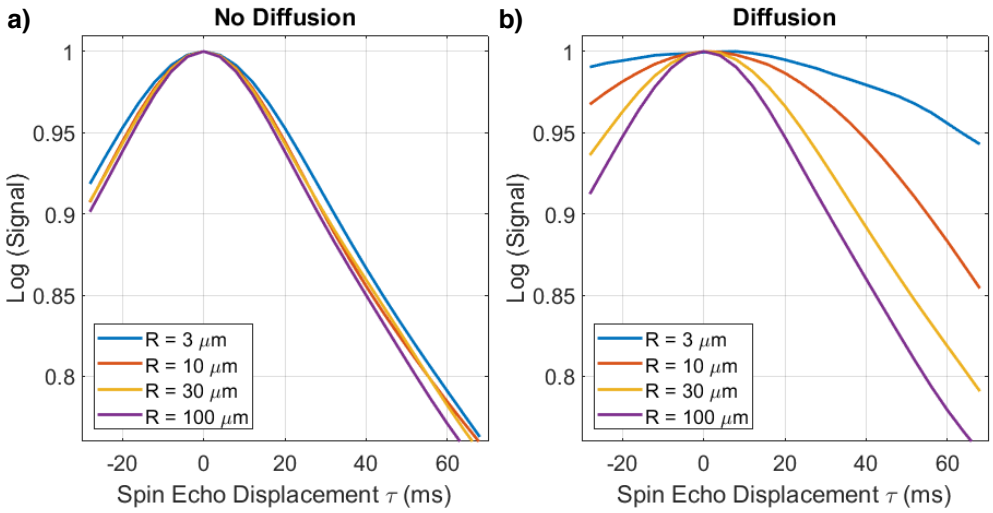


**Figure 5.3:** ASE signal curves generated from simulated data, each with uniform vessel radii $R_c$, **a)** without and **b)** with diffusion. These data were generated with $OEF = 40\%$ and $DBV = 3\%$.

| | | Parameter Error | | |
|---|---|---|---|---|
| | **Radius (μm)** | $R_2'$ ($s^{-1}$) | **DBV (%)** | **OEF (%)** |
| Static | 3 | 2.4 ± 1.7 | 3.7 ± 2.6 | 15.8 ± 11.0 |
| | 10 | 2.7 ± 1.9 | 3.6 ± 2.5 | 16.8 ± 12.2 |
| | 30 | 2.6 ± 1.9 | 3.3 ± 2.3 | 15.7 ± 11.0 |
| | 100 | 2.9 ± 2.0 | 3.3 ± 2.3 | 16.7 ± 12.0 |
| Diffusive | 3 | 5.3 ± 3.4 | 3.5 ± 2.8 | 37.3 ± 17.0 |
| | 10 | 2.9 ± 2.0 | 3.9 ± 2.3 | 36.4 ± 20.0 |
| | 30 | 2.2 ± 1.5 | 4.0 ± 2.5 | 20.1 ± 12.5 |
| | 100 | 2.7 ± 1.9 | 3.6 ± 2.5 | 14.6 ± 10.3 |

**Table 5.3:** Error in estimation of $R_2'$, DBV, and OEF from simulated qBOLD data, for vessels with a single radius, with both static and diffusive simulations, averaged across simulated (true) OEF values between 20% and 70%, and simulated (true) DBV values between 1% and 10%.

modelled with the SDR). In every case, the ASE signal generated using a full distribution of $R_c$ is different to the SDR model (and the non-diffusive simulations) than the equivalent single-radius simulation.

Table 5.4 shows the error in estimates of $R_2'$, DBV, and OEF made using the SDR qBOLD model across a range of OEFs between 20 and 70%, and DBVs between 1 and 10%, for simulated data generated using the three *in vivo* distributions of $R_c$, with and without diffusion.

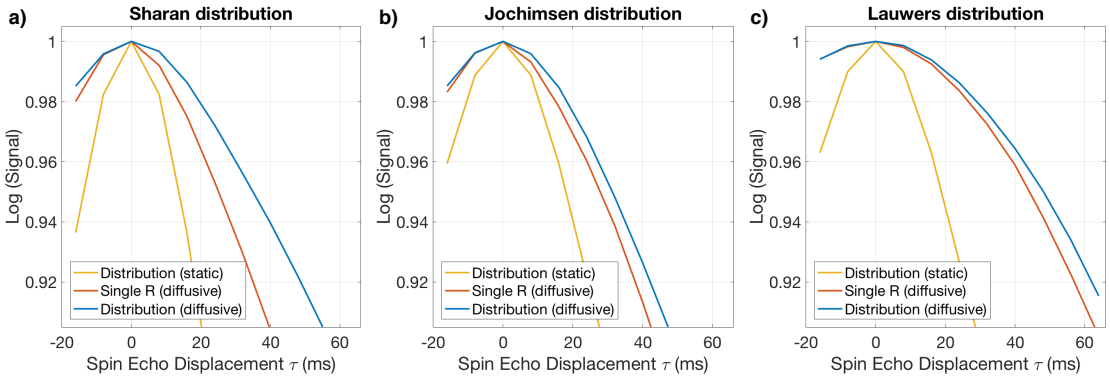


**Figure 5.4:** ASE signal curves generated from simulated data, with vessel radii following three *in vivo* distributions: **a)** Sharan distribution,[257] **b)** Jochimsen distribution,[258] **c)** Lauwers distribution.[260] In each case, data were simulated with and without diffusion, and with diffusion around vessels with a single radius. In all cases, OEF= 40% and DBV= 3%.

| | **Vessel size distribution** | **Parameter Error** | | |
|---|---|---|---|---|
| | | $R_2'$ ($s^{-1}$) | **DBV (%)** | **OEF (%)** |
| Static | Sharan | 6.8 ± 4.0 | 4.5 ± 3.3 | 15.7 ± 10.7 |
| | Jochimsen | 2.8 ± 2.0 | 3.4 ± 2.4 | 17.1 ± 12.7 |
| | Lauwers | 2.7 ± 1.9 | 3.7 ± 2.5 | 16.5 ± 11.4 |
| Diffusive | Sharan | 3.2 ± 2.2 | 2.8 ± 2.2 | 22.5 ± 12.4 |
| | Jochimsen | 2.6 ± 1.7 | 3.5 ± 2.2 | 25.6 ± 12.9 |
| | Lauwers | 4.1 ± 2.7 | 2.9 ± 2.3 | 38.0 ± 15.9 |

**Table 5.4:** Error in estimation of $R_2'$, DBV, and OEF from simulated qBOLD data, for vessels with radii drawn from three distributions, with both static and diffusive simulations.

### 5.4.2 Model Corrections

#### Uncorrected Model Fitting

Results from parameter estimation using the qBOLD model fitted to data simulated with the Sharan distribution are shown in Figure 5.5. The first row shows estimated dHb as a function of true dHb, where for all $TE$s, the relationship observed appears approximately linear. This suggests that a simple linear correction to the definition of dHb, such as in Equation 5.9 could be sufficient to overcome this discrepancy in the model. The same phenomenon is observed in data simulated using both the Jochimsen and Lauwers distributions of $R_c$, and for different $\max(\tau)$ values at $TE = 112$ms.

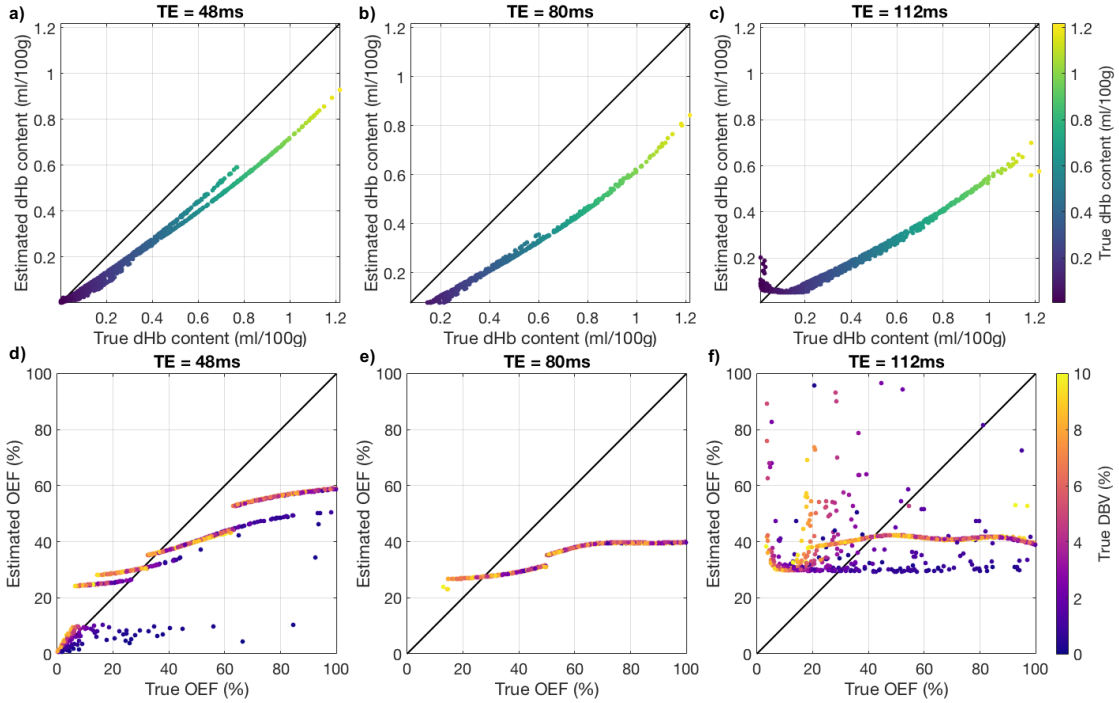


**Figure 5.5:** Estimates of **(a-c)** dHb and **(d-f)** OEF, compared to the true values (with unity line shown in black) made on data simulated using the Sharan distribution, with true dHb from $\{0, 1.25\text{ml}/100\text{g}\}$ and true OEF from $\{0, 100\%\}$. For three different $TE$s: **(a,d)** 48ms, **(b,e)** 80ms, **(c,f)** 112ms.

The second row of Figure 5.5 shows estimated OEF as a function of $\text{OEF}_{true}$. In both Figure 5.5d and 5.5f there are a number of data points (usually corresponding to very low DBV values) that are scattered away from the main 'line' of points. Ignoring those outliers, the differences between the true and estimated do not follow a linear relationship, for any $TE$. As $TE$ increases, the total dynamic range of estimated OEF values decreases, from between 20–60% at $TE = 48$ms, to only 30–40% at $TE = 112$ms. This same phenomenon was also observed in the other distributions, and exemplifies the need for a non-linear correction to the SDR qBOLD model in order to accurately estimate OEF in the presence of diffusion.

The average error in dHb, OEF, and DBV was calculated for each distribution (at $TE = 80$ms) by taking the absolute value of the difference between the true (simulated) and estimated parameter values. The error in dHb estimation was 0.10 ml/100g, 0.09 ml/100g, and 0.28 ml/100g, for Sharan, Jochimsen, and Lauwers distributions, respectively. The error in DBV was 4.9%, 6.2%, and 13.9%; and

| | Optimal $\kappa$ only | | | $\kappa$ and $\eta$ Simultaneously | | | | | |
|---|---|---|---|---|---|---|---|---|---|
| | | | | Optimal $\kappa$ | | | Optimal $\eta$ | | |
| $TE$ (ms) | 48 | 80 | 112 | 48 | 80 | 112 | 48 | 80 | 112 |
| Sharan dist. | 0.84 | 0.67 | 0.66 | 0.66 | 0.57 | 0.52 | 0.36 | 0.37 | 0.38 |
| Jochimsen dist. | 0.97 | 0.78 | 0.77 | 0.74 | 0.64 | 0.57 | 0.34 | 0.36 | 0.37 |
| Lauwers dist. | 0.97 | 0.64 | 0.48 | 0.56 | 0.43 | 0.38 | 0.37 | 0.40 | 0.40 |

**Table 5.5:** Optimal values for the dHb scaling parameter $\kappa$ and short-$\tau$ geometric factor $\eta$, for each vessel radius distribution, as a function of $TE$. Showing results of optimization of $\kappa$ alone, and $\kappa$ and $\eta$ simultaneously. Note that the default (uncorrected) case is $\kappa = 1$.

the error in OEF was 31.1%, 29.1%, and 37.2%. As expected from previous simulated and *in vivo* results (see Chapter 3), the relative error was highest in DBV estimation (greater than 100% in all cases) and lowest in dHb estimation (29.7% in the case of the Jochimsen distribution).

### Optimising Correction Parameters

The scaling parameter $\kappa$ was optimized to minimise the error in dHb estimation. It was found that $\kappa$ varied significantly both with $TE$ and with the choice of vessel distribution. The results are presented in Table 5.5. At low $TE$ only a very small correction ($\kappa \approx 1$) is required, and $\kappa$ decreases as $TE$ increases, although the rate of this varies between the $R_c$ distributions.

The parameters $\kappa$ and $\eta$ were optimized simultaneously to minimise error in OEF estimation. The results of this are also presented in Table 5.5. Here it was also found that $\kappa$ varied significantly with $TE$ and $R_c$ distribution. There was some variation in $\eta$ across these parameters, but not to the same degree, and the optimal value was consistently higher than the default (uncorrected) value $\eta = 0.3$.

It was found that $t_C$ did not vary significantly from the value of $1.76/\delta\omega$ found in Chapter 3, regardless of the choice of TE or $R_c$ distribution. Similarly, when the exponent $\beta$ was optimised, both alone, and simultaneously with $\kappa$, and $\kappa$ and $\eta$, it did not deviate significantly from its default value $\beta = 1$.

Optimal parametrizations for Equation 5.13 were found for each of the three $R_c$ distributions, at $TE = 80$ms, which were:

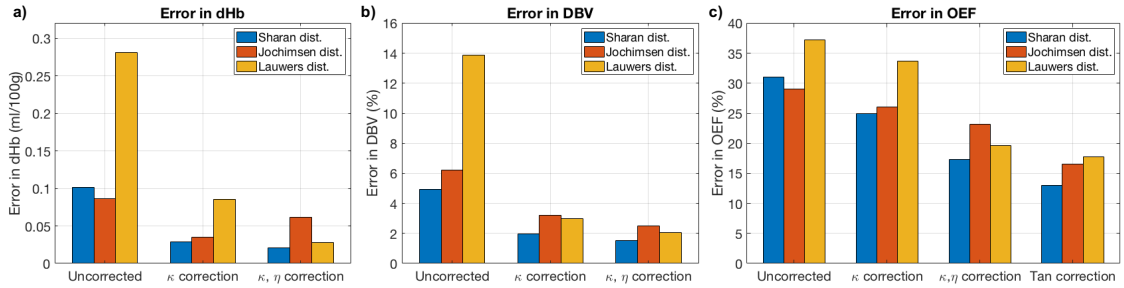


**Figure 5.6:** Average error in estimates of **(a)** dHb, **(b)** DBV, and **(c)** OEF, from simulated data for all three $R_c$ distributions. Estimates were made with the SDR qBOLD model without correction, with linear $\kappa$ correction, and with non-linear $\kappa, \eta$ correction for all three parameters. The use of the tan function (Equation 5.16) to map $R_2'$ and DBV to OEF is also shown in OEF only, since this step is performed after $R_2'$ and DBV estimation (on $\kappa, \eta$ corrected results).

$$OEF_{Sh} = 0.117 \cdot \tan\left(0.0861 \cdot \frac{c \cdot R_2'}{DBV}\right) + 0.312 \tag{5.16a}$$

$$OEF_{Jo} = 0.125 \cdot \tan\left(0.0922 \cdot \frac{c \cdot R_2'}{DBV}\right) + 0.404 \tag{5.16b}$$

$$OEF_{La} = 0.0376 \cdot \tan\left(0.00272 \cdot \frac{c \cdot R_2'}{DBV}\right) + 0.202 \tag{5.16c}$$

where $c = \frac{4}{3}\pi \cdot \gamma B_0 \cdot \Delta\chi_0 \cdot Hct$. The outlying points mentioned above were excluded, in order to ensure consistent fitting to the corrected models.

### Corrected Parameter Estimation

The proposed corrections to the qBOLD model make a significant difference to the accuracy of parameter estimates from simulated data, as shown in Figure 5.6. The absolute errors between true (simulated) parameter values and their estimates were compared using two-way ANOVA with correction for multiple comparisons (all differences are statistically significant at $p < 0.05$ unless otherwise stated). Data points in which estimated parameter values were outside a physiologically reasonable range (i.e. where DBV or OEF were estimated as being greater than 100%) were excluded from all analyses.

Using the linear $\kappa$ correction to $R_2'$ reduced the error in dHb estimation by 60% using Jochimsen distribution data (from 0.0860 ml/100g to 0.0346 ml/100g), and

by 72% and 70% for the Sharan and Lauwers distributions respectively (although the magnitude of the error in the Lauwers distribution was still significantly higher than for the other distributions).

Adding a correction $\eta$ in the short-$\tau$ regime of the SDR model further improved dHb estimation for the Lauwers distributions, but worsened dHb estimation with the Jochimsen distribution, and did not have a statistically significant effect on the Sharan distribution. This was compensated for by the fact that combined $\kappa$ and $\eta$ correction improved DBV estimation for both the Sharan and Jochimsen distribution (but not Lauwers), and improved OEF estimation in all three $R_c$ distributions.

Using a non-linear function to obtain OEF from estimates of $R_2'$ and DBV (after $\kappa, \eta$ correction) improved the accuracy of OEF estimation for all three distributions. The average absolute error between true and estimated OEF was lowest for the Sharan distribution, at 13.0%, but highest for the Lauwers distribution at 17.8% (and 16.5% for the Jochimsen distribution). The use of the non-linear tan function had the greatest impact on Jochimsen distribution data, providing a relative 29% improvement to OEF error compared with $\kappa, \eta$ correction, and a total of a 43% improvement against the uncorrected SDR qBOLD model.

Simulated data generated with each $R_c$ distribution were also inferred on using the optimized parameters from the other distributions. It was found that for dHb (or $R_2'$) estimation with linear $\kappa$ correction, $\kappa_{Jo}$ was only effective in correcting Jochimsen distribution data, but $\kappa_{Sh}$ and $\kappa_{La}$ were almost equally effective at correcting both Sharan and Lauwers distribution data. For OEF estimation with $\kappa, \eta$ correction, all three sets of $\kappa, \eta$ values were approximately equally effective in correcting Sharan or Jochimsen simulated data, but Lauwers distribution data was only corrected effectively using $\kappa_{La}, \eta_{La}$. Any linear or non-linear correction always improved dHb and OEF estimates when compared to the uncorrected results of the same distribution.

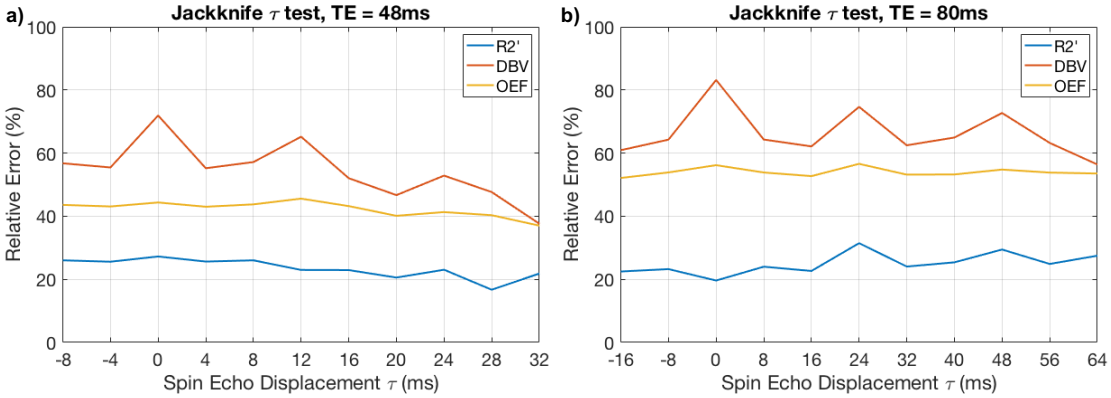


**Figure 5.7:** Relative error in parameters ($R_2'$, DBV, and OEF) between true (simulated) and estimated values (using the uncorrected qBOLD model) under a jackknife test, in which each $\tau$ value was omitted in turn, and the parameters estimated without that datum. The $x$-axis indicates which $\tau$-value was omitted. **(a)** $TE$=48ms, **(b)** $TE$=80ms.

### 5.4.3 Acquisition Optimization

The results of the jackknife analysis of $\tau$ values in the evenly spaced acquisition are shown in Figure 5.7. In general, $R_2'$ and OEF estimation were affected uniformly by omitting any single $\tau$ value. There were certain $\tau$ values whose omission caused a sharp increase in DBV error, particularly $\tau = 0$. This trend is seen at both $TE$=48ms and $TE$=80ms.

The comparison of six different sets of $\tau$ values (from Table 5.2) is shown in Table 5.6. It shows that error in $R_2'$ estimation was relatively consistent across the $\tau$ sets, although Set 3 (which included the fewest points in the long-$\tau$ regime) performs significantly worse than the others. The opposite was true of DBV estimation, in which the relative error was much lower (only 36.5%) with Set 3 (compared to an average of 88% across the other 5 Sets). The same result was seen in the correlation results of $R_2'$ and DBV.

The lowest OEF error was obtained with Set 3, although the difference between the highest OEF error (55.2% with Set 5) and the lowest (45.2% with Set 3) was much smaller than the difference in DBV error (10%). However, it is likely that OEF uncertainty is driven by uncertainty in DBV; since in $R_2'$ relative error was consistently lower and correlation was consistently higher. Since $R_2'$ was relatively unaffected by the set of $\tau$ values chosen (provided there were at least some in the

| Set Number | Relative Error (%) | | | Estimate Correlation | | |
|---|---|---|---|---|---|---|
| | $R_2'$ | DBV | OEF | $R_2'$ | DBV | OEF |
| 1 | 32.3 | 81.5 | 53.4 | 0.92 | 0.57 | 0.60 |
| 2 | 34.7 | 84.3 | 54.0 | 0.66 | 0.37 | 0.55 |
| 3 | 47.5 | 36.5 | 45.2 | 0.98 | 0.69 | 0.67 |
| 4 | 37.8 | 87.6 | 54.7 | 0.76 | 0.38 | 0.61 |
| 5 | 38.2 | 91.7 | 55.2 | 0.81 | 0.34 | 0.63 |
| 6 | 35.7 | 95.8 | 54.8 | 0.84 | 0.27 | 0.58 |

**Table 5.6:** Comparison of the relative error in parameter estimates (true value – estimated value / true value) and correlation between true and estimated values, for six arbitrarily defined sets of $\tau$ values (given in Table 5.2), with $TE$=80ms. Results are the average across 1000 simulated data points, drawn from intervals OEF=$\{0, 100\%\}$ and DBV=$\{0, 10\%\}$.

long-$\tau$ regime, unlike Set 3), the best acquisition, which minimizes OEF error, is likely to be one which acquires a sufficiently large number of data points in the short-$\tau$ regime to infer DBV as accurately as possible.

### 5.4.4 *In Vivo* Data

Example parameter maps of dHb and OEF from a single subject, under different correction conditions (using Sharan parameters), are shown in Figure 5.8. Both $\kappa$ and $\kappa, \eta$ correction had the effect of raising dHb uniformly across the brain, whereas the effect on OEF was less smooth (although there was still a visible increase in average OEF estimate). The tan correction resulted in more voxels with unphysical values (thresholded black or bright yellow).

Group-average ($N = 6$) GM estimates of parameters dHb, DBV, and OEF, under all tested correction conditions, are shown in Figure 5.9. Across the group, both the $\kappa$ and $\kappa, \eta$ correction caused a significant increase in average dHb estimates, for all sets of correction parameters. $\kappa$ correction did not affect DBV estimates, but did produce significantly different OEF estimates in all cases. Using $\kappa_{Sh}$, average dHb increased from 0.12±0.01ml/100g to 0.17±0.02ml/100g, and OEF increased from 19.7±3.6% to 29.6±5.1%.

Combined $\kappa, \eta$ correction caused a further increase in average OEF relative to $\kappa$ correction, although this was not statistically significant in the case of $\kappa_{Sh}, \eta_{Sh}$.

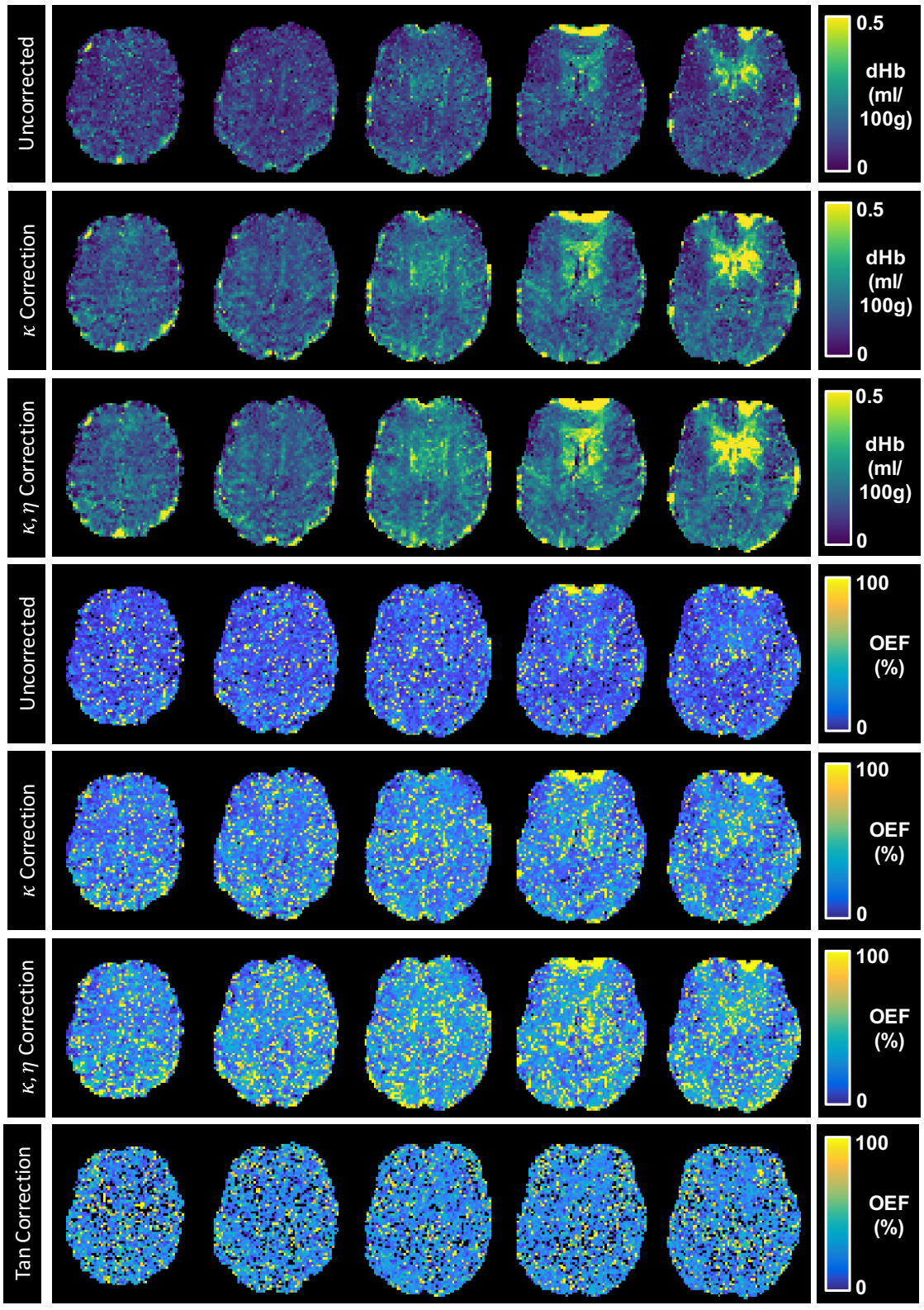


**Figure 5.8:** Example parameter maps of dHb (first three rows) and OEF (latter four rows) from a single subject, under different model correction conditions: uncorrected (first and fourth rows), linear $\kappa$ correction (second and fifth rows), non-linear $\kappa, \eta$ correction (third and sixth rows), and non-linear tan correction (seventh row, OEF only).

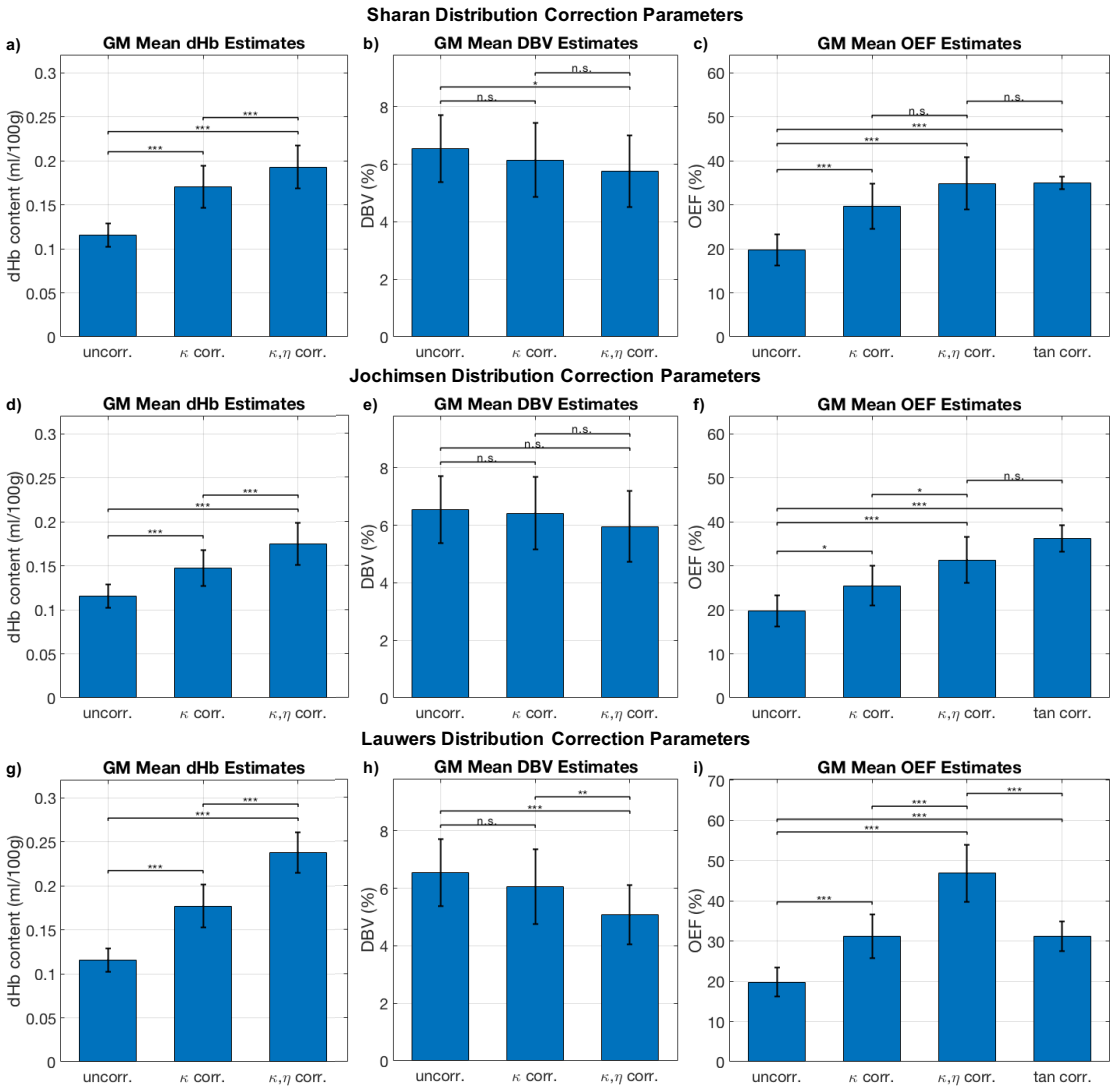


**Figure 5.9:** Average grey matter estimates of dHb (first column), DBV (second column), and OEF (third column) on *in vivo* data ($N = 6$) with different correction conditions: uncorrected, linear $\kappa$ correction, non-linear $\kappa, \eta$ correction, and tan function fitting (OEF only). Three sets of correction parameters were used, obtained from optimizing three simulated vessel distributions: Sharan (first row), Jochimsen (second row), Lauwers (third row). Statistically significant differences (based on two-way ANOVA followed by pairwise comparisons) are indicated by asterisks.

There was a statistically significant reduction in average DBV estimates using Sharan and Lauwers parameters, from 6.6±1.2% without corrections to 5.1±1.0% using $\kappa_{La}, \eta_{La}$. Tan correction did not produce significantly different OEF estimates from $\kappa, \eta$ correction, except when using the Lauwers parameters (Equation 5.16c).

Under linear $\kappa$ correction, the choice of $\kappa$ (from Table 5.5) affected some parameter estimates. There was no statistically significant difference between $\kappa$-corrected average dHb estimates using Sharan or Lauwers parameters, but both of these were significantly different ($p < 0.001$) from the average dHb obtained using $\kappa_{Jo}$. The same differences were also found in the OEF estimates. There were no significant differences in DBV estimates between the different $\kappa$ values.

Under non-linear $\kappa, \eta$ correction, the choice of $R_c$ distribution led to significantly different estimates of $R_2'$ in all cases. The only statistically significant difference in DBV estimates was observed between the Jochimsen and Lauwers values for $\kappa$ and $\eta$ ($p < 0.05$), and there were significant differences in OEF estimates between the Lauwers values and the other two distributions, but not between Sharan and Jochimsen.

When the tan correction was applied to the resulting $R_2'$ and DBV estimates, the choice of parameters (whether Equation 5.16a, 5.16b, or 5.16c) did produce sets of OEF values that were statistically significantly different.

**TRUST Validation**

TRUST data were acquired and analysed for four subjects, and compared with ASE-qBOLD data analysed using several correction methods. The resulting OEF estimates are shown in Table 5.7. The inter-subject variation was low in the qBOLD OEF results, however the intra-subject standard deviations were very high across all correction methods. They were lower in the tan-corrected case because voxels with already high OEF estimates (under $\kappa, \eta$ correction) tended to take even higher values after the tan correction, and those voxels with a total estimated OEF of above 100% were excluded. The $\kappa, \eta$-optimized qBOLD OEF results were compared

| Subject | qBOLD OEF (%) uncorrected | $\kappa_{Sh}, \eta_{Sh}$ corr. | $\kappa_{Jo}, \eta_{Jo}$ corr. | $\kappa_{La}, \eta_{La}$ corr. | TRUST OEF (%) |
|---|---|---|---|---|---|
| 1 | 22±12 | 39±14 | 35±13 | 51±17 | 47.2±1.4 |
| 2 | 23±13 | 39±15 | 35±14 | 53±18 | 38.7±4.8 |
| 3 | 22±12 | 38±15 | 34±14 | 50±18 | 46.5±2.5 |
| 4 | 18±12 | 33±15 | 30±15 | 43±18 | 41.2±3.3 |
| Mean | 21±2 | 37±3 | 34±2 | 49±4 | 43.4±4.1 |

**Table 5.7:** Average OEF estimates for four healthy subjects obtained using qBOLD with $\kappa, \eta$ corrections applied (using parameters optimized from all three realistic vessel disributions), and TRUST. The qBOLD results show grey matter mean ± grey matter standard deviation; TRUST results are for the whole brain measured in the superior sagittal sinus. The final row shows group mean ± inter-subject standard deviation.

with TRUST, since they represent the best correction (producing the OEF values closest to the expected 40% value from the literature[11,141,153]).

TRUST OEF estimates were higher than those obtained using qBOLD in all cases except with $\kappa_{La}, \eta_{La}$ correction, which produced OEF estimates that were much higher than the others. The next closest qBOLD correction to TRUST was $\kappa_{Sh}, \eta_{Sh}$, which estimated an average OEF of 37±3%, compared to 43.4±4.1% in TRUST.

### Acquisition Optimization

GASE data acquired from one subject at $TE = 66\text{ms}, 84\text{ms}, 112\text{ms}$ were analysed using the qBOLD model under various correction conditions, the results of which are presented in Table 5.8. Using the uncorrected qBOLD model, there was considerable variation in estimated DBV as a function both of $TE$ and $\tau_{max}$, and some variation in OEF, although the GM standard deviations were very high (as in previous *in vivo* datasets, such as Tables 3.3 and 4.4).

The same trends continued when $\kappa$ correction was applied, although in all cases the average DBV estimate was reduced, and the average OEF estimate increased, by the correction. Non-linear $\kappa, \eta$ correction further improved both parameters, across all acquisitions. The largest relative change in DBV (a 39% relative decrease) was seen when $\kappa, \eta$ correction was applied to $TE$=112ms/$\tau_{max}$=96ms data. The same dataset also experienced the largest increase (of 240% relative to the uncorrected

| $TE$ (ms) | $\tau_{max}$ (ms) | Uncorrected DBV (%) | Uncorrected OEF (%) | $\kappa$ Correction DBV (%) | $\kappa$ Correction OEF (%) | $\kappa, \eta$ Correction DBV (%) | $\kappa, \eta$ Correction OEF (%) |
|---|---|---|---|---|---|---|---|
| 66 | 32 | 4.6±2.2 | 19±11 | 4.0±1.9 | 27±14 | 3.2±1.7 | 41±18 |
| 84 | 32 | 5.1±3.0 | 24±14 | 4.1±2.2 | 37±17 | 3.4±1.7 | 48±20 |
| 84 | 64 | 7.3±3.7 | 19±12 | 6.3±3.0 | 30±15 | 5.6±2.7 | 43±18 |
| 112 | 32 | 4.8±2.6 | 17±11 | 3.8±2.0 | 35±17 | 3.3±1.5 | 41±19 |
| 112 | 96 | 9.8±4.8 | 17±12 | 7.2±3.2 | 33±15 | 6.0±2.5 | 43±17 |

**Table 5.8:** Estimates of DBV and OEF with different acquisition parameters $TE$ and $\tau_{max}$ (in all cases, 11 evenly spaced $\tau$ values were acquired). Results are grey matter mean ± grey matter standard deviation, for inference using the uncorrected qBOLD model, $\kappa$ correction, and $\kappa, \eta$ correction (using values optimized from the Lauwers distribution).

estimate) in OEF when $\kappa, \eta$ correction was applied. The corrections had the smallest effect on OEF estimation for $\tau_{max}$=32ms data.

When other correction parameters (derived from the Sharan or Jochimsen distributions) were used, the same trends were observed, albeit to a lesser degree. DBV estimates are consistently lower at $\tau_{max}$=32ms, and correction to the models generally had the largest effect on longer $TE$ data.

Parameter estimates from GASE data acquired at $TR$=2s were compared with those from $TR$=3s data from a single subject. Average grey matter $R_2'$ was 3.7±2.7s$^{-1}$ at $TR$=3 and 3.9±2.7s$^{-1}$ at $TR$=2. Average GM DBV was 6.7±6.3% and 7.0±6.6%, and OEF was 19±11% and 18±11%, at $TR$=3 and $TR$=2 respectively. Two-sampled $t$-tests showed that none of these differences were statistically significant ($p > 0.05$).

Parameter estimates were also made using GASE data from four subjects on an 80×80 matrix (as opposed to the normal 96×96 matrix). Two-sampled $t$-tests showed a statistically significant difference in OEF estimates in one out of four subjects; although DBV estimates were significantly different in three out of four subjects.

## 5.5 Discussion

### 5.5.1 Vessel Radius Distributions

For all but the largest of vessels, the addition of diffusion has a significant impact on the resulting simulated ASE signals, and hence on estimates of $R_2'$, OEF, and DBV made using the SDR model.

The change in shape of the ASE curves in Figures 5.3b and 5.4 shows that the effect of $R_c$ on the log of the signal is not linear. This means that performing Monte Carlo simulations with a single $R_c$, and scaling the results in some way, will not accurately capture the effect of changing radius, nor can a mean (or other average) radius be used to accurately model the range of radii present *in vivo*. This is unlike the case of other physiological parameters (namely OEF and DBV), for which a single set of simulations can be scaled linearly to effectively model the entire physiological range.[18]

Three different *in vivo* radius distributions were considered, each of which was obtained in a different manner. The Sharan distribution is based on *ex vivo* investigation of sheep (following a similar experiment on dogs), and involved rounding measurements of radius into broad bins.[257] It is possible, therefore, that this distribution may be less useful for *in vivo* studies in humans.

The Lauwers distribution is based on human *ex vivo* investigation, albeit only of the right temporal lobe.[260] It may be a better standard for the whole human cortex, but it deliberately ignores large veins (which have the greatest relative effect on the qBOLD signal, given their high OEF) and so may not be the most appropriate for this work.

The Jochimsen distribution was obtained from humans *in vivo* using BOLD contrast (with hypercapnia induced changes) as its measurement.[258] It is necessarily less precise than an *ex vivo* study would be, but it is reasonable to assume that the effect of vessel size on BOLD signal should be similar in Jochimsen *et al.*'s experiments as in the ones carried out in this work.

All distributions include capillaries (the Lauwers distribution additionally includes arteroiles), which would be expected to have lower OEF than veins/venules, or conversely, a lower volume of deoxygenated blood (relative to the total CBV). Since all the blood vessels are simulated with the same OEF, this could lead to DBV misestimation when these distributions are applied to *in vivo* data.

Since it is not possible from simulation alone to determine which vessel distribution is best or most appropriate, all three were investigated further for determining model corrections, and for use in fitting *in vivo* data.

### 5.5.2 Model Corrections

In Section 5.3.2, three modifications to the static dephasing regime qBOLD model (of Equations 2.33, 2.37 and 2.43) were proposed: a linear correction to $R_2'$ estimation using a scaling parameter $\kappa$; a non-linear correction to the model using parameters $\kappa$ and $\eta$; and an alternative method for computing OEF from estimated $R_2'$ and DBV using a tan function (Equation 5.13). The parameters of these corrections were optimized on simulated data, which was generated using a Monte Carlo approach with a realistic distribution of vessel radii. The correction methods were then tested on *in vivo* data from five healthy subjects.

#### Simulated Data

For linear correction, the optimal value of $\kappa$ (Table 5.5) was found to depend strongly on echo time, with longer $TE$ requiring a more significant correction. This was to be expected, given the assumption that parameter misestimation was due to the effect of diffusion, which becomes more prominent as $TE$ increases. The choice of $R_c$ distribution also affected $\kappa$, with the Jochimsen distribution generally requiring the least correction ($\kappa$ closest to 1 at each $TE$) and the Lauwers distribution requiring the most. This accords with what was seen in Table 5.4, where the error in $R_2'$ estimation was highest with the Lauwers distribution and lowest with the Jochimsen. This is because (as Figure 5.1 shows) the Lauwers distribution is heavily dominated by capillaries and other very small $R_c$ vessels, where the static dephasing regime

does not apply; whereas the Sharan and Jochimsen distribution contain significant numbers of larger vessels where Equation 5.2 is satisfied.

The same phenomenon is observed in the optimal values for non-linear $\kappa, \eta$ correction. It can also be noted that the parameters for tan correction of the Lauwers distribution (Equation 5.16c) are markedly different from those of the Sharan and Jochimsen distributions.

When applying the corrections to simulated data, in the presence of noise, $\kappa$ correction significantly improved dHb and DBV estimation in all cases (Figure 5.6), suggesting that this simple modification to the SDR qBOLD model can improve its accuracy and reliability. Non-linear $\kappa, \eta$ correction further improved dHb estimation for two distributions (not Jochimsen), and improved DBV estimation for a different two (not Sharan). This may be because, given the set of $\tau$ values used, there were not enough data points in the short-$\tau$ regime for the $\eta$ correction to make a significant difference.

OEF estimation improved with each correction step, for all distributions. Since this is the primary parameter of interest, this suggests that even if the estimation of intermediate parameters (like $R_2'$) is slightly less accurate, the combined $\kappa, \eta$ correction, and tan correction, ought to improve the overall accuracy of the qBOLD model.

### In Vivo Data

Applying the model corrections to *in vivo* data had a mixed effect. Linear $\kappa$ correction caused an increase in estimated dHb as expected, although the extent of the increase varied depending on the choice of $\kappa$. This continued when $\eta$ correction was also used, though this was most likely due to the fact that, when $\eta$ correction was used, the optimal value for $\kappa$ was lower (such that it has a greater corrective effect) in all cases (Table 5.5). The estimates of dHb appeared to be both more robust and have a greater dynamic range when any of the corrections are used, and using non-linear $\kappa, \eta$ correction was preferable to $\kappa$ only.

The value of estimated DBV did not change significantly with the corrections, except in the cases of $\kappa_{La}, \eta_{La}$. This was in contrast to simulated data, where the error in DBV estimation was significantly reduced by both correction methods (as shown in Figure 5.6). This suggests either, that the overestimation of DBV (see Section 3.5.3) may not simply be due to mismatch in the SDR model (since the corrections did not appropriately correct for DBV); or that the $\tau$ values acquired in this dataset still do not provide sufficient information to estimate DBV accurately.

The $\kappa$ and $\kappa, \eta$ corrections had a significant effect on the estimated OEF values, and in all cases (except $\kappa_{Jo}$) led to OEF estimates that were closer to the expected literature values (see Table 3.6, or references therein[16,141,153,165]). These differences must be attributed solely to the increase in estimated $R_2'$ (or dHb) with the corrections, and not to any change in estimated DBV. Unlike in the simulated case, the tan correction (using Equation 5.16 to map $R_2'$ and DBV onto OEF) did not significantly change the estimated OEF values. This suggests that directly changing Equation 2.34 is not necessarily the best approach, when $\kappa, \eta$ correction produced the same results. This may be due to the fact that, under tan correction, a larger number of voxels were found where estimated OEF took an unphysical value ($OEF > 100\%$ or $OEF < 0\%$), which was more likely to happen in voxels with high OEF (in other methods).

Excluding voxels where model-fitting has failed, or where unreasonable values are estimated, improves the reliability of subject-level GM average parameter values, and therefore allows for useful comparisons of methods in healthy subjects. However, this limits the interpretability of parameter maps (such as Figure 5.8), and may be very detrimental to identifying pathological regions, which may have small numbers of voxels, and parameter values that are already outside normal bounds. With this in mind, it seems that inference on the non-linear $\kappa, \eta$ corrected model, followed by the use of Equation 2.34 to calculate OEF from $R_2'$ and DBV, offers the best method for minimizing the impact of diffusion-related parameter misestimation in ASE-qBOLD.

As well as comparing final estimates of OEF to literature values, it would be worthwhile to test whether applying these corrections to the model improved its

ability to detect changes in OEF. Similar qBOLD experiments have used a simple visual stimulus to evoke changes in the BOLD signal in the visual cortex, which ought to coincide with a decrease in OEF.[19] In the future, further validation of these corrections could be carried out using this kind of fMRI stimulus.

**TRUST Validation**

TRUST provides a robust measurement of whole-brain OEF which can be used as a standard against which to compare qBOLD estimates, under the assumption that OEF is generally uniform across the brain in healthy subjects.[59,172] In the four subjects with TRUST data, OEF was consistently measured to be higher in TRUST, and with lower intra-subject standard deviation, suggesting that the problem of OEF underestimation persists in qBOLD. The correction methods proposed above go some way to fixing this, by increasing estimated $R_2'$, but since they did not improve DBV estimation, OEF remained low.

Like the qBOLD OEF estimates, the TRUST model (Equations 2.49, 5.14, and 5.15) relies on several assumptions. Both models must assume fixed values of $Hct$ and $T_1^b$, since they lack the correct contrast to estimate these simultaneously with OEF. In TRUST, $Hct$ can be quantified through measurement of $T_1^b$ by acquiring TRUST data with a set of different $TR$s.[174] Here, the same fixed value of $Hct = 0.40$ was used throughout. Others have assumed that $Hct$ differs between larger vessels (like the SSS, where the TRUST signal is measured) and smaller vessels (which may dominate the qBOLD signal in grey matter).[19,225,226]

It is important to note that the qBOLD signal in GM is the result of averaging the magnetic susceptibility effects from many blood vessels, which in this chapter are assumed to have differing radii corresponding to different categories of blood vessels. It was shown (in Figure 5.2) that a distribution of OEF values can be accurately approximated by a single (mean) OEF value when simulating ASE-qBOLD data, so it is possible that the GM mean OEF measurements obtained *in vivo* are representative of a distribution of OEF values from different vessels, which would include venules (with a higher OEF closer to that of the SSS, as measured by TRUST) and capillaries

(with a much lower OEF closer to that of the incoming arteries). So the OEF value obtained from a qBOLD method may be expected to be closer to the mean OEF of all blood vessels in a voxel, which would make it significantly lower than the whole brain arterial-venous difference measured by TRUST.

### 5.5.3 Acquisition Optimization

Simulated and *in vivo* data were used to test different parameters (namely $TE$ and the set of $\tau$ values acquired) used in collecting ASE data, in order to ensure that the data collected is the most suitable for fitting with the qBOLD model.

Jackknife testing of $\tau$ values in simulated data showed that acquiring a data point at the spin echo ($\tau$=0) is important for accurate inference of DBV. Multiples of 12ms (namely, 12, 24, and 48ms) also appeared to be important to DBV estimation, although the reason why these data points have a disproportionately high impact is not clear. It is possible that acquiring data at $\tau \approx t_C$ (which is 12.4ms at OEF=40%) is important for finding the ideal point of transition between the short-$\tau$ and long-$\tau$ asymptotic regimes (Equation 2.29).

Testing arbitrary sets of $\tau$ values showed most strongly that acquiring a larger amount of data in the short-$\tau$ regime is greatly beneficial to DBV estimation, at the expense of $R_2'$ (or dHb). This suggests that the previously used paradigm, of 8ms steps from -16 to 64ms, may not be the best, since it includes only 3 values that are reliably in the short-$\tau$ regime (-8, 0, and 8ms) while all the rest are in the long-$\tau$ regime. Only a few points (5 or more out of 11, as in Sets 4-6) are necessary for accurate estimation of $R_2'$, and the remainder ought to be acquired in the short-$\tau$ regime to minimize error in DBV.

Given the GASE acquisition protocols available, it is not possible to acquire unevenly spaced $\tau$ values in the same sequence, so *in vivo* acquisitions were restricted to those with evenly spaced $\tau$ values. This is not a severe limitation, given the similarity in simulated data results between Set 1 (evenly spaced values) and the other sets. However, further investigation should be made into *in vivo* data acquired with uneven $\tau$ spacings.

Simulated data consistently showed that the average error in the estimates of all parameters increased with increasing $TE$ (see Figures 5.5 and 5.7), which was also borne out by *in vivo* results (Table 5.8). This is consistent with the expectation that a significant portion of the misestimation of OEF and DBV using ASE-qBOLD is the result of diffusion of spins in the tissue compartment. At longer $TE$, spins have more time to diffuse and accrue phase irreversibly as a result, leading to the assumptions of the SDR model no longer applying. By acquiring data at shorter $TE$s, this effect is lessened and the error in simulated parameter estimates decreases.

Testing of a single *in vivo* dataset also showed that using a shorter $\tau_{max}$ (which leads to more data points in the short-$\tau$ regime) leads to DBV estimates that are closer to expected literature values (in the range of 3-5%).[16,153,165] The average OEF estimate did not change as strongly as a function of the $\tau$ values used.

The values of the correction parameters $\kappa$ and $\eta$ showed greater deviation from their default values (in the uncorrected SDR-qBOLD model) at higher $TE$, and therefore produced a larger change in physiological parameter estimates. This suggests that if data were acquired at shorter $TE$, and with more data points in the short-$\tau$ regime, the effect of diffusion would be reduced, and the corrections to the qBOLD model less necessary.

Changing the repetition time $TR$ (and adjusting $TI_{FLAIR}$ to match) was tested in a single subject, and no significant differences in parameter estimates were found. This suggests that a shorter-$TR$ protocol (which could enable greater slice coverage in the same total scan time) is equally feasible, although it would be necessary to test this on more subjects.

Similarly, reducing the matrix size to 80×80 (and thereby reducing spatial resolution) did not significantly affect OEF estimates in most (3/4) subjects, although it did affect DBV estimates. This is potentially because partial volume effects became more prominent as voxel size increased, and infiltration from the (nulled) CSF compartment may have affected DBV estimation. However, acquiring a smaller number of $k$-space points (which would enable a shorter $TE$ acquisition)

is not detrimental to OEF estimation, and so may be a useful advancement to the existing acquisition protocol.

## 5.6 Conclusions

This chapter has shown that diffusion of spins in the tissue compartment significantly affects the measured ASE signal, and the subsequent estimates of dHb, OEF, and DBV made using the SDR-qBOLD model. It has shown that basic modifications to the model with which the data are analysed, and to the parameters with which they are acquired, can in large part correct for this effect.

The optimal values of the correction parameters $\kappa$ and $\eta$ are uncertain at this stage, since they depend on the assumed distribution of vessel radii. Three $R_c$ distributions were tested, derived from three different methods in the literature,[257,258,260] and optimal values were found for each one. The Lauwers distribution[260] resulted in the largest corrections, but these resulted in estimates of OEF and DBV that were closest to literature values, especially when data were acquired with a better set of $\tau$ values. This suggests that the ASE-qBOLD signal may be more strongly influenced by capillaries (which dominate the Lauwers distribution) than previously believed.

Acquiring proportionally more data points in the short-$\tau$ regime significantly improved physiological parameter estimation, and even more so when combined with the model corrections. Further work should be done to validate this, and to determine whether an uneven distribution of $\tau$ values may be even more effective. Changing acquisition $TR$ and matrix size did not degrade OEF estimates, and so could be optimized further in an improved acquisition protocol.

# 6
# Application to Acute Stroke

## Contents



In this chapter, data that was acquired from acute stroke patients as part of an ongoing clinical study was analysed using the qBOLD model in the Bayesian framework described in Chapter 3, with corrections based on the work in Chapter 5. The methods of data acquisition and analysis are described in Section 6.2, and the results presented in Section 6.3. Section 6.4 contains the discussion, as well as recommendations for future clinical qBOLD scanning based on this work.

It is shown here that using the corrected qBOLD model (derived in Chapter 5) on GASE data acquired when patients are first presenting acute stroke symptoms

produces estimates of OEF that are significantly different between three regions: the initial ischaemic core, the ischaemic penumbra, and healthy contralateral tissue. This suggests that qBOLD model inference could be useful for delineating and assessing the ischaemic penumbra in acute stroke.

**Acknowledgements**

For this chapter, I would especially like to thank my collaborators at the Oxford Acute Vascular Imaging Centre, especially Professor James Kennedy, Dr. Davide Carone, Dr. George Harston, and the radiographers, Peter Manley and Alison Fletcher, for acquiring and curating the patient data presented here. I would also like to thank all the patients who participated in the AMICI study and their families.

## 6.1 Introduction

The preceding chapters have shown that estimating physiological parameters (namely OEF and DBV) using the qBOLD model is more effective when performing inference in a VB framework, and when using a model that more accurately describes the entire signal, including the component that originates in the vasculature (Chapter 3). Parameter estimation is improved further when the effect of diffusion is corrected for within the model; in particular, the range of OEF values that can be differentiated using the uncorrected qBOLD model is very limited, but it can be expanded through the inclusion of corrective constants in both the short-$\tau$ and long-$\tau$ asymptotic regimes (Chapter 5).

Prior work by Stone and colleagues[109] has shown that linear fitting of the long-$\tau$ regime alone can yield $R_2'$ and DBV estimates that have the potential to usefully distinguish between stages of ischaemia in acute stroke patients. This chapter continues in the same vein and applies the technical advances developed throughout this work to acute stroke patient data with the aim of improving the process of delineating the ischaemic penumbra from other tissues.

The penumbra is a region of the brain, usually surrounding the ischaemic core, in which reduction of CBF has caused a temporary loss of function but no structural

neuronal damage.[8] This is believed to correspond with an area that can be returned to normal function if a supply of oxygen is restored in a timely manner.[10,71] It has been suggested as an indicator of the likelihood of a positive outcome from intervention,[7] and is therefore valuable in prognosis and treatment planning.

Identifying the penumbra requires differentiating it both from the ischaemic core (where loss of oxygen has already caused permanent damage) and from surrounding unaffected tissue and benign oligemia.[12] The core can be reliably identified using DWI,[41,79] but several MRI modalities have been used to delineate the penumbra, most commonly the diffusion-perfusion mismatch.[10] However, since cell survival is dependent on the continuation of normal metabolic processes, a method which directly measures metabolism ought to provide the most reliable indicator of the salvageable penumbra in the presence of reduced blood flow. OEF could be such a biomarker. It is expected that, within the first few hours of stroke onset, OEF will be elevated in both the ischaemic core and the penumbra, in comparison with unaffected tissue. After successful reperfusion, OEF in the penumbra should return to normal, and if reperfusion is unsuccessful, then the core infarcted region will expand into what was the penumbra.

## 6.2 Methods

GASE and other data were acquired from acute stroke patients as part of an ongoing study.[109]

### 6.2.1 Patients

Patients with ischaemic stroke were recruited into a prospective observational cohort study, the Acute MRI In Cerebral Ischaemia (AMICI) programme, under research protocols agreed by the UK National Research Ethics Service (ref: 13/SC/0362). Patients were selected for this analysis on the basis of having a DWI lesion on their presenting scan, and another on a 24-hour or 1-week follow-up scan. Age and stroke severity were not used as inclusion criteria. Patients with lacunar stroke (based on expert analysis of DWI lesion size) were excluded. Follow-up scanning was performed

| Patient | Sex | Age | NIHSS | Syndrome | Time to Scan | Follow-up |
|---|---|---|---|---|---|---|
| 1 | M | 68 | 3 | POCS | 4 hr 11 min | 1 week |
| 2 | F | 69 | 6 | POCS | 10 hr 52 min | 1 week |
| 3 | M | 77 | 22 | POCS | 13 hr 05 min | 1 week |
| 4 | F | 74 | 10 | TACS | 22 hr 17 min | 1 week |
| 5 | F | 80 | 17 | TACS | 17 hr 50 min | 1 week |
| 6 | M | 87 | 19 | PACS | 13 hr 49 min | 1 week |
| 7 | M | 79 | 14 | TACS | 2 hr 20 min | 24 hours |
| 8 | M | 68 | 12 | POCS | 19 hr 33 min | 24 hours |
| 9 | M | 78 | 4 | PACS | 28 hr 19 min | 38 hours |

**Table 6.1:** Details of included acute stroke patients, including NIHSS score (which was assessed at presentation) and stroke syndrome (POCS: Posterior circulation stroke; TACS: Total anterior circulation stroke; PACS: Partial anterior circulation stroke). Also includes the time elapsed between symptom onset and the presentation scan, and the timing of follow-up scans relative to the presentation scan. Patients 7-9 were excluded from later analyses, because they lacked the one week follow-up scan.

at 24 hours, 1 week, and 1 month after the presentation scan where possible. Clinical details of the included patients are presented in Table 6.1. Patients without follow-up scans at the 1 week mark were excluded from subsequent analyses, since these scans were used to determine final infarction. All included patients were treated by intravenous thrombolysis, and Patient 4 also underwent mechanical thrombectomy.

### 6.2.2 Data Acquisition

MRI data were acquired using a Siemens 3T Verio system (Siemens Healthineers, Erlangen, Germany). The following scans were acquired at all time points:

- **Structural.** A high resolution MPRAGE[227] image was acquired for registration and segmentation, with $TR/TI/TE = 2040/900/4.7$ms, flip angle 8°, 192×192×192 matrix, 1.8×1.8×1.8mm resolution. The scan duration was 3 mins 58 seconds.
- **DWI.** Three-direction diffusion-weighted data were acquired for identifying ischaemia on presentation,[262] with $TR/TE = 9000/98$ms, $b = 0$ and 1000s/mm$^2$, four averages, 1.8×1.8×2.0 resolution, 50 slices, and a scan duration of 2 mins 53 seconds.

- **ASL.** Vessel encoded PCASL data (see Section 2.3.6) were acquired for CBF estimation,[63,263] with an EPI readout, $TR/TE$ = 4080/14ms, 64×64×24 matrix, 3.4×3.4×4.5mm resolution, with labelling duration of 1.4s, and six PLDs from 0.25s to 1.5s in steps of 0.25s, and a scan duration of 5 mins 55 seconds.

- **qBOLD.** FLAIR-prepared GASE data were acquired for qBOLD model fitting, with $TR/TI_{FLAIR}/TE$ = 3000/1210/82ms, 96×96 matrix, nine slabs, 2.29×2.29×5mm resolution, and 11 $\tau$ values ranging from -16ms to 64ms in steps of 8ms. The scan duration was 4 mins 30 seconds.

Additionally, on follow-up scans, a $T_2$-weighted FLAIR turbo spin echo image was acquired to identify infarction.[264] This used $TR/TI_{FLAIR}/TE$ = 9000/2500/96ms, 128×128×58 matrix, 1.9×1.9×2mm resolution, and had a scan duration of 2 mins 8 seconds.

Since it was not possible to identify a method that would reliably correct for the extracellular signal contribution (Chapter 4), all patient data were acquired with FLAIR preparations, and it was assumed that the extracellular signal was nulled completely by this.

### 6.2.3 Analysis

As in all previous experiments, GASE data were motion-corrected using MCFLIRT,[229] smoothed using a sub-voxel Gaussian kernel, and corrected for Gibbs ringing artefacts.[230] The spin echo ($\tau$=0) volume was brain-extracted using BET[231] and segmented using FAST[205] to create a grey matter mask in GASE space (in both the presentation and follow-up scans). FLIRT[232] was used to create linear transformation matrices that could register MPRAGE, DWI, GASE, and $T_2$-FLAIR images across both time points.

**Region of Interest Definition**

Five regions of interest were defined for each patient, three of which come directly from imaging data, and two which are derived from those, using the same criteria as Stone *et al.*:[109]

- **Initial Ischaemia**. DWI data acquired at presentation were used to generate ADC maps, which were thresholded at ADC= 620μm$^2$/s (following Purushotham *et al.*[265]). The resulting binary mask was smoothed (using a Gaussian kernel with FWHM of 2.355mm) and clustered iteratively using FSL's Cluster tool.[228] The final ROI, representing the ischaemic region in which cell death has occurred, was manually verified by an expert.[266]

- **Final Infarct**. The $T_2$-weighted FLAIR image acquired at the one week follow-up scan was used to identify the final infarcted region manually, where cell death occured in spite of treatment.[264]

- **Contralateral Grey Matter**. The GM mask produced by FAST segmentation of GASE data was manually modified to include only voxels in the hemisphere contralateral to the ischaemic lesion and in the same range of GESEPI slabs.

- **Infarct Core**. This region is defined as the voxels common to both the initial ischaemia and the final infarct, after registration into the same image space.[109]

- **Infarct Growth**. This region consists of voxels included in the final infarct that are not included in the initial ischaemia after registration to the same image space. These voxels are a subset of the ischaemic penumbra, although it is possible that some areas of at risk tissue were recovered after treatment by thrombolysis.[109]

The ROIs were transformed using FSL's applywarp command into GASE image space for analysis. It has been shown previously that the size of the ischaemic penumbra was predictive of final outcome, and effectiveness of treatment.[98,99,102]

To explore this, ROI sizes (in GASE-space voxels) were compared to NIHSS scores for each subject.

### qBOLD Model Fitting

GASE data were inferred upon using the two-compartment qBOLD model (Equations 2.33, 2.37, and 2.43) under VB, implemented in FABBER[22,181] to produce estimates of $R_2'$ and DBV, which were in turn used to calculate OEF (Equation 2.34). Inference was also performed using the corrected $\kappa, \eta$ model (Equations 5.9 and 5.10) using $\kappa$=0.64 and $\eta$=0.36 (see Section 5.4.2).

For each subject, mean $R_2'$, DBV, and OEF were calculated in three ROIs: the initial ischaemic core, the growth region, and contralateral grey matter, using both the presentation and follow-up GASE data sets. These were compared within subjects and across the group. Two-way ANOVA with pairwise comparisons (using the Tukey-Kramer method) were performed in MATLAB at both the intra- and inter-subject levels.

One week follow-up GASE data were analysed using the uncorrected and corrected qBOLD models in the same way as the presentation data, with ROIs transformed into that GASE image space. The resulting OEF estimates were normalized to the mean contralateral GM value, then compared using ANOVA and pairwise comparisons. The three ROIs (initial ischaemic core, infarct growth, and contralateral GM) were compared with each other within each time point, and between the time points at the group level.

## 6.3 Results

Example results for six acute stroke patients are shown in Figure 6.1. Mean parameter estimates in three regions of interest (ischaemic core, infarct growth, and contralateral GM) are shown in Table 6.3 for six acute stroke patients. These were taken from VB inference of the presentation GASE data, using both the uncorrected and $\kappa, \eta$-corrected qBOLD model.

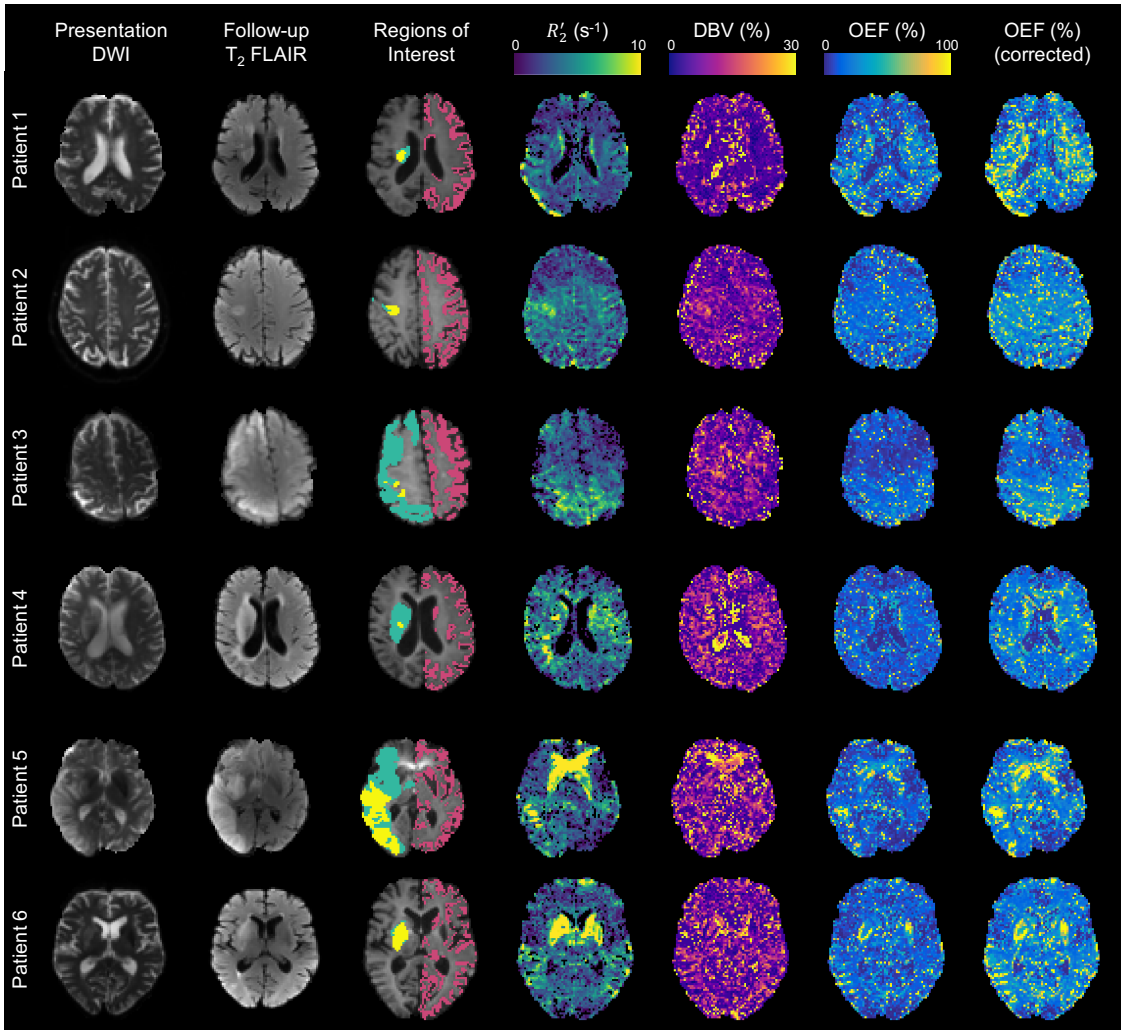


**Figure 6.1:** Results from six acute stroke patients (showing a single exemplary slice in each case). Columns show the presentation DWI; one week follow-up $T_2$-FLAIR; three regions of interest (yellow: ischaemic core; green: infarct growth; pink: contralateral GM); estimates of $R'_2$, DBV, and OEF; and OEF estimated from the corrected qBOLD model.

### 6.3.1 Regions of Interest

The third column of Figure 6.1 shows the initial ischaemic core, growth, and contralateral ROIs on five acute stroke patients, and Table 6.2 shows the number of voxels in the core, final, and growth ROIs, after they were all transformed into presentation GASE space.

There was considerable variation in the size and location of the ROIs between patients. Some, such as Patients 1, 2, and 6, had very small regions of initial ischaemia, which generally grew locally to a lesser degree. Patients 3 and 4 had

| Patient | Voxels in ROI | | |
|---|---|---|---|
| | **Ischaemic Core** | **Infarct Growth** | **Final Infarct** |
| 1 | 19 | 61 | 80 |
| 2 | 63 | 18 | 81 |
| 3 | 21 | 3272 | 3293 |
| 4 | 9 | 502 | 511 |
| 5 | 1543 | 1967 | 3510 |
| 6 | 168 | 57 | 225 |

**Table 6.2:** Sizes (in GASE-space voxels) of three regions of interest in each patient: the initial ischaemic core (determined by ADC at presentation), the infarct growth region (defined as voxels that are in the final infarct but not in the initial core), and the final infarction (determined by $T_2$-FLAIR after one week).

the small cores, but substantially larger growth regions. Patient 5 had a core, and an even larger area of final infarction.

A correlation was found between a patient's final infarct size and their NIHSS score, although this was not statistically significant ($p = 0.067$). There was no correlation found between core or growth region size and NIHSS score.

### 6.3.2 Parameter Inference

Estimates of $R_2'$ were higher in the ischaemic core than in contralateral GM in all subjects but one (Patient 1). This can be seen visually in Figure 6.1 Column 4. This difference was statistically significant in three subjects (Patients 2, 5, and 6). $R_2'$ was significantly higher ($p < 0.001$) in the infarct growth region than contralateral GM in all subjects but one (Patient 6). These trends were the same in both uncorrected and $\kappa, \eta$-corrected datasets.

Uncorrected DBV estimates (Figure 6.1 Column 5) varied substantially between subjects and regions: they were lower in the ischaemic core than contralateral GM (though not statistically significantly) in three subjects (Patients 1, 4, and 6), and higher in the other three (this was statistically significant in Patients 2 and 5 only). There was similar inconsistency in DBV estimates in the growth region, and when the $\kappa, \eta$ corrections were applied.

| | $R_2'$ ($s^{-1}$) | | | | | |
|---|---|---|---|---|---|---|
| | **Uncorrected Model** | | | **$\kappa, \eta$-Corrected Model** | | |
| **Patient** | **Core** | **Growth** | **Contra** | **Core** | **Growth** | **Contra** |
| 1 | 3.0±2.8 | 4.9±3.2 | 3.4±2.9 | 4.3±1.3 | 7.5±1.8 | 5.2±4.2 |
| 2 | 6.8±2.4 | 6.1±1.9 | 3.4±2.7 | 9.8±1.6 | 9.5±1.7 | 5.1±2.6 |
| 3 | 3.8±2.9 | 4.1±3.5 | 3.1±2.8 | 6.6±3.1 | 6.0±4.0 | 4.7±3.0 |
| 4 | 4.2±2.1 | 6.7±4.3 | 3.4±3.2 | 5.4±1.9 | 9.4±6.4 | 5.3±4.6 |
| 5 | 5.1±4.0 | 5.1±4.8 | 3.4±3.3 | 7.5±4.6 | 7.3±5.4 | 4.8±4.0 |
| 6 | 8.5±4.2 | 4.3±3.7 | 3.5±3.2 | 8.7±2.9 | 7.5±2.6 | 5.4±3.3 |
| Mean | 5.2±2.1 | 5.2±1.0 | 3.4±0.1 | 7.1±2.0 | 7.9±1.3 | 5.1±0.3 |
| | **DBV (%)** | | | | | |
| | **Uncorrected Model** | | | **$\kappa, \eta$-Corrected Model** | | |
| **Patient** | **Core** | **Growth** | **Contra** | **Core** | **Growth** | **Contra** |
| 1 | 7.1±6.9 | 6.7±6.4 | 9.7±7.4 | 2.1±1.2 | 6.0±5.2 | 8.1±6.9 |
| 2 | 14.1±9.9 | 10.9±4.7 | 9.8±9.5 | 9.6±3.2 | 8.9±3.4 | 6.9±6.5 |
| 3 | 13.5±8.7 | 9.7±8.6 | 8.4±9.0 | 9.5±4.6 | 7.7±6.2 | 6.8±5.2 |
| 4 | 6.4±6.1 | 11.7±9.2 | 11.1±9.6 | 4.4±3.6 | 10.0±9.5 | 9.7±8.3 |
| 5 | 10.6±9.5 | 9.9±9.4 | 8.3±7.4 | 8.1±6.5 | 8.2±6.7 | 7.8±7.3 |
| 6 | 14.0±9.5 | 17.3±9.9 | 14.8±8.9 | 9.9±6.0 | 11.2±6.4 | 10.9±8.5 |
| Mean | 11.0±3.5 | 11.0±3.5 | 10.4±2.4 | 7.3±3.3 | 8.7±1.8 | 8.4±1.6 |
| | **OEF (%)** | | | | | |
| | **Uncorrected Model** | | | **$\kappa, \eta$-Corrected Model** | | |
| **Patient** | **Core** | **Growth** | **Contra** | **Core** | **Growth** | **Contra** |
| 1 | 46±33 | 33±24 | 21±21 | 65±25 | 54±34 | 32±28 |
| 2 | 16±11 | 23±10 | 20±13 | 32±11 | 35±11 | 30±19 |
| 3 | 27±24 | 23±16 | 21±16 | 22±11 | 33±19 | 29±19 |
| 4 | 26±22 | 34±30 | 20±13 | 61±34 | 44±28 | 28±32 |
| 5 | 26±22 | 27±22 | 23±21 | 38±24 | 40±28 | 29±23 |
| 6 | 30±21 | 23±14 | 21±19 | 46±22 | 30±22 | 26±19 |
| Mean | 29±10 | 27±5 | 21±2 | 44±17 | 39±9 | 29±2 |

**Table 6.3:** Estimates of $R_2'$, DBV, and OEF, from three regions of interest (ischaemic core, infarct growth region, and contralateral grey matter, using the uncorrected and $\kappa, \eta$-corrected qBOLD models) for six acute stroke patients, showing mean ± standard deviation in each ROI, and group mean ± group standard deviation.

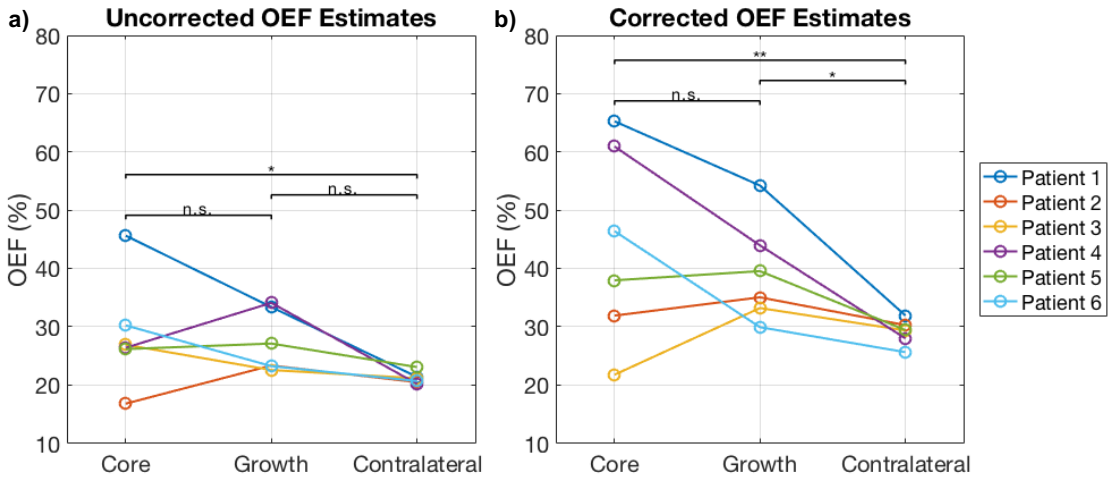


**Figure 6.2:** Average OEF estimates in three regions of interest: ischaemic core, infarct growth, and contralateral grey matter, with group-level significant differences. **(a)** Estimates made using the uncorrected qBOLD model. **(b)** Estimates made using the $\kappa, \eta$-corrected qBOLD model.

OEF was computed from $R_2'$ and DBV, and the results are shown in Figure 6.1 Column 6; OEF estimates with the $\kappa, \eta$ correction are shown in Column 7. In all subjects but one (Patient 2), OEF was higher in the ischaemic core than contralateral GM, and this difference was statistically significant ($p < 0.05$) in three subjects (Patients 1, 5, and 6). OEF was higher in the growth region for all subjects, but this difference was only statistically significant in four subjects (Patients 1, 3, 4, and 5). This remained the case when the corrected qBOLD model was applied.

A group-level comparison of average OEF estimates in three ROIs is shown in Figure 6.2. At presentation, there was a significant ($p < 0.05$) difference in average OEF between the ischaemic core and contralateral GM. This difference was larger when the $\kappa, \eta$-corrected model was used. Using uncorrected OEF estimates, there was no group-level significant difference between the growth region and contralateral GM; however, when the $\kappa, \eta$-corrected model was used for inference, a significant difference was seen between these two ROIs.

It can also be seen from Figure 6.2 that applying the $\kappa, \eta$ correction to the qBOLD model is not equivalent to simply scaling OEF or $R_2'$ estimates uniformly across the brain. Rather, differences in relative OEF values between regions are seen, particularly in Patients 3 (whose core OEF was estimated to be higher in

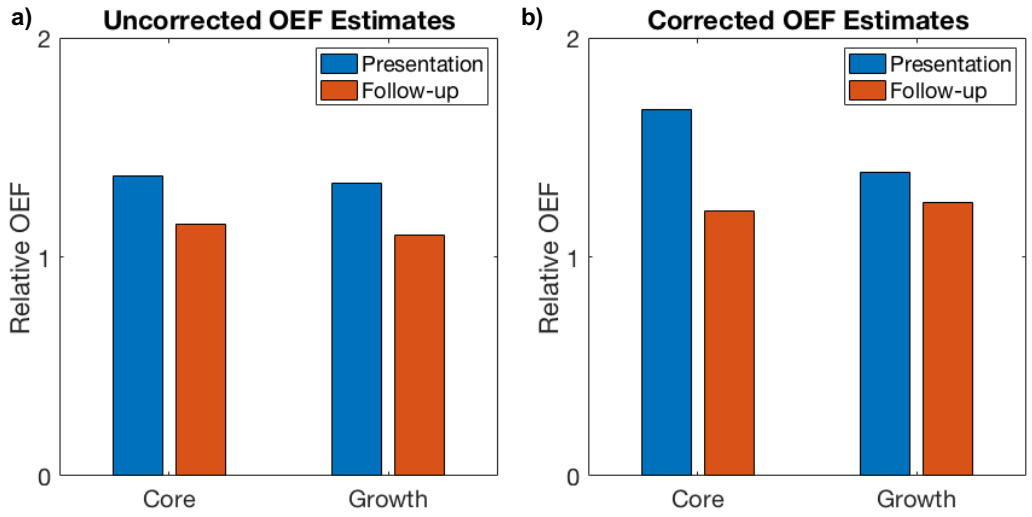


**Figure 6.3:** Group average ($N = 6$) OEF estimates, normalized to contralateral grey matter, in the initial ischaemic core and infarct growth ROIs, at presentation, and after one week. **(a)** Estimates made using the uncorrected qBOLD model. **(b)** Estimates made using the qBOLD model with $\kappa, \eta$ correction.

the core than contralateral using the uncorrected model, but lower in the core than contralateral using the corrected model) and 4 (in whom OEF was estimated to be lower in the core than the growth region without corrections, but higher using the corrected model).

Figure 6.3 shows the group-average OEF estimates in the core and growth regions at presentation and in one week follow-up data. Data in each time point were normalized to the mean contralateral GM estimate. There was very little difference in OEF between core and growth regions at follow-up, which is to be expected given their definitions. The difference between infarcted tissue and contralateral GM was consistently less at follow-up than at presentation.

## 6.4 Discussion

### 6.4.1 Regional Parameter Estimation in Acute Stroke

In this chapter, the two-compartment qBOLD model was used in a Bayesian framework to infer $R_2'$, DBV, and OEF from GASE data acquired from six acute stroke patients. Regions of interest were identified in each subject using other

modalities: DWI was used to define the initial ischaemic core at presentation; $T_2$-FLAIR images acquired one week after the first scan were used to define the final infarct region; and spin echo images were used to segment contralateral grey matter. An infarct growth region was defined to include voxels in the final infarct region that were not in the initial ischaemic core.

Strong, but not statistically significant, correlation was found between the size of the final infarct region and stroke severity (measured by NIHSS). This reinforces the importance of identifying the ischaemic penumbra and rapidly intervening to prevent infarction from spreading beyond the core. All patients were thrombolized intravenously on presentation, but still experienced significant growth of the infarction between presentation and their follow-up scan. This highlights the importance of rapid treatment in all acute stroke cases, as well as the limitations of current procedures. Long term outcomes (such as modified Rankin Scale results for each patient) were not available, though collecting these and comparing them with imaging measures would be useful. Other studies have done so, and found that perfusion metrics, in particular, can be predictive of final patient outcome.[10,102] It is possible that qBOLD parameter estimates could also be useful in this regard.

Average estimates of OEF, and other parameters, were compared across ROIs both within each subject and at the group level. It was found that OEF was statistically significantly higher in the infarct growth region than contralateral GM in four subjects. There was no statistically significant difference in OEF between the core and growth regions in any subject, except Patient 6. This suggests that OEF, as quantified by qBOLD model fitting, is an indicator of hypoperfused tissue that is either infarcted, or at risk of infarction. In the subjects where there was no statistically significant difference between ischaemic and healthy contralateral regions, it is possible that the very small number of voxels included in the core region resulted in this apparent lack of contrast.

Estimates of DBV were highly variable between subjects in the core and growth regions, and were even higher in contralateral GM than was found in previous chapters in healthy subjects' GM (see Tables 3.3 and 4.4). This may be due to

physiological differences between the predominantly young subjects used in previous chapters, but it may also be the result of increased noise, and incomplete nulling of the CSF signal, due to motion during the FLAIR preparation.[109]

Using the corrected qBOLD model developed in Chapter 5 further improved the discriminatory power of this approach, and resulted in statistically significant differences both between the growth region and contralateral GM, and the core and contralateral GM, at the group level. This is likely due to the increased dynamic range in OEF measurements that are made possible by the model corrections.

One week follow-up data showed that there was no statistically significant difference in OEF between infarcted and healthy tissue after that time, although at both the individual subject and group levels there were changes in average OEF in all regions. This may be because there were changes in blood flow in the intervening period that led to a genuine decrease in OEF in the affected area; or it may be that in the absence of any flow, the relative concentration of deoxyhaemoglobin had normalized. The differences between regions, and between time points, were more pronounced, though still not statistically significant, when using the $\kappa, \eta$-corrected qBOLD model.

### 6.4.2 Limitations of the Present Method

The results presented in this chapter show that the qBOLD method has the potential to be useful in the identification of the ischaemic penumbra, although there are several limitations to the approaches used.

The ischaemic core and infarct growth regions were compared against contralateral voxels in a grey matter mask. In several subjects (Patients 2, 3, and 5) this seems more than appropriate, as the final infarct and growth ROIs of these patients occupy mostly GM cortical regions. However, for Patients 1, 4, and 6 the ROIs are based in mostly white matter regions near the ventricles. In this case, it may have been more appropriate to compare core and growth ROIs against equivalently located contralateral tissue, rather than contralateral GM. This was the approach used by Harston and colleagues, who reflected the final infarct ROI through the

midbrain line in order to generate a contralateral ROI.[264] As was noted in Chapters 3 and 5, the qBOLD model was designed to describe signal in grey matter, and it is not clear whether the assumptions of blood vessel distributions, or isotropic diffusion, would hold in white matter. This would not necessarily affect like-for-like comparisons of ipsilateral and contralateral regions, but it may limit the effectiveness of comparing ipsilateral WM against contralateral GM.

There was significant variation in estimates of all parameters between the two time points (presentation and follow-up), which made direct comparison of the ROIs impossible. In this chapter, estimates in the ROIs were normalized to the mean contralateral GM values of the same time point before comparison, although this may have caused differences that were statistically significant to appear not so. It would be useful to compare absolute estimates of OEF across several time points after stroke onset, but the uncertainties inherent in this method made that infeasible.

The qBOLD model used throughout has assumed fixed values of $R_2$ for each of the major signal compartments. In ischaemia, and especially after membrane failure has occurred, this will no longer be the case, and may therefore affect the relative weightings of the compartments inferred in the qBOLD model. Similarly, membrane failure may affect the relative proton density of each compartment, leading to similar misestimation of partial volumes. Furthermore, in areas of infarction, even incoming blood in arterioles may not be fully oxygen saturated, meaning that the relative concentration of deoxyhaemoglobin may not necessarily be indicative of oxygen being extracted in that particular local region.

Although an absolute estimate of OEF would be of great interest, and would enable direct comparison of this method with others, it is not necessarily the only goal of this thesis. Given the number of assumptions made in the qBOLD model (including those explored in the preceding chapters), and the differences in parameter estimates between the ASE-qBOLD model and others from the literature, it is difficult to assert that 'OEF' values given in Table 6.3 (for example) are a true representation of the proportional oxygenation of venous blood (although they are very likely to be closely related to this parameter). This chapter is intended to have

| Parameter | Current Protocol | Recommended Protocol |
|---|---|---|
| FLAIR preparation | YES | NO |
| Repetition time $TR$ (ms) | 3000 | 2000 |
| Echo time $TE$ (ms) | 82 | 48 |
| $\tau$ intervals (ms) | -16:8:64 | -8:4:32 |
| Matrix size | 96×96 | 80×80 |

**Table 6.4:** Details of the recommended parameters for use in acute stroke GASE-qBOLD acquisition, compared with those used in this chapter (Section 6.2.2).

demonstrated that this does not render the qBOLD model useless. The statistically significant differences in OEF between the penumbra and contralateral tissue show that this measure could still be useful in the clinic by providing information on differences in oxygen supply between regions.

A next step which would substantially enhance the utility of this method would be to use the OEF maps produced from the presentation GASE data to automatically outline areas of decreased oxygenation that might correspond to the ischaemic penumbra. This is currently not possible given the low SNR in the OEF maps, so the results presented in this chapter relied on an external definition of the penumbra, using $T_2$-FLAIR data from a later time point. It is possible that maps of another parameter, such as $R_2'$ or dHb could be equally useful in this regard.

### 6.4.3 Recommended Acute Stroke qBOLD Protocol

The results presented in this chapter demonstrate the potential usefulness of qBOLD data to identify the ischaemic penumbra and thereby supplement other MRI modalities in acute stroke diagnosis. However, there is significant scope for further work to be done in order to improve upon this. Some of the improvements to qBOLD model-fitting that have been proposed in this work were tested on the available acute stroke data, but others could not be, due to the way in which the data were acquired.

Nonetheless, based on testing of simulated data and healthy subjects (as described in Chapters 4 and 5) it is possible to make several recommendations for the acquisition of acute stroke qBOLD data in the future. The details of this protocol are given in Table 6.4.

Omitting the FLAIR preparation would improve SNR, reduce sensitivity to noise, and enable greater slice coverage in the same total acquisition time; however, it would lead to a contribution from the CSF compartment being confounded with the tissue signal. It is possible that simply ignoring this contribution, or fitting it using the three-compartment qBOLD model of Equation 4.3 will still yield $R_2'$ and OEF results that display a contrast between the penumbra and contralateral GM. Since a high-resolution structural MPRAGE is acquired as part of the standard protocol already (Section 6.2.2) a $T_1$-weighted segmented map of CSF partial volume could be used as a spatial prior to inform the three-compartment model-fitting.

Testing of simulated and *in vivo* data showed that OEF estimation was more accurate using data that were acquired with shorter $TE$ and a larger proportion of $\tau$-values in the short-$\tau$ asymptotic regime ($\tau < t_C \approx 12$ms). This would mitigate some of the effects of diffusion, and enable more accurate fitting of DBV, which in turn would result in better OEF estimates.

The lower limit of available $TE$s in an EPI acquisition is dependent on the matrix size, which in the current protocol is 96×96. Using a smaller matrix size would allow for a shorter $TE$; however, this would lead to a decrease in in-plane spatial resolution. While a lower resolution may make delineating the exact extent of the penumbra more difficult, it should be noted that the ASL data (which are used to calculate CBF) are currently acquired with a 64×64 matrix (as were the data used in Chapter 3), and so reducing the GASE resolution would not lead to a loss of resolution in any final $CMRO_2$ estimate derived from CBF and OEF. Furthermore, testing in healthy subjects (see Sections 5.4.4 and 5.5.3) showed that this was not detrimental to OEF estimation.

Reducing $TR$ would also increase the number of GESEPI slabs that can be acquired in the same time, although this changes the steady state magnetization (Equation 2.36) as the limit $TR \gg TE - \tau$ is approached. This would be less of a problem if the FLAIR preparation is omitted. However, single-subject testing (see Sections 5.4.4 and 5.5.3) suggested acquiring at a reduced $TR$ did not affect OEF or DBV estimation.

## 6.5 Conclusions

The corrected, two-compartment qBOLD model was used to quantify OEF in three important regions (the ischaemic core, the infarct growth region assumed to correspond to the ischaemic penumbra, and healthy contralateral grey matter) in six acute ischaemic stroke patients. Using data acquired within a few hours of stroke onset, significant differences in estimated OEF were seen between the ischaemic penumbra and contralateral GM, which could not be determined from DWI data alone.

Other parameters, $R_2'$ and DBV, also showed significant differences between regions, and some differences were observed between the presentation scan and the one week follow-up scan, which could provide clinically useful information on the progression of infarction after treatment.

In spite of its limitations, this chapter has shown that the qBOLD model can be used to detect differences in oxygenation between pathological and healthy regions in acute stroke. This could be combined with inferences of blood flow from ASL data to produces maps or regional averages of $CMRO_2$. It is possible that physicians could use this information about oxygen supply and metabolism to plan treatment of acute stroke, or to prepare appropriate long-term care.

# 7 Conclusions and Future Work

## 7.1 Summary of the Thesis

This thesis has described the use of the quantitative BOLD model to infer on parameters describing oxygenation in the brain, in a non-invasive manner, using MRI. The relevant literature was presented in Chapter 2, which described the fundamentals of MR physics, the use of MRI in the management of acute stroke, the ways in which MR signals can be used to quantify brain physiology, and the Bayesian inference techniques used to infer on the nonlinear models used herein.

In Chapter 3, the static dephasing regime qBOLD model was used to infer parameters OEF and DBV from simulated and *in vivo* data. A model which inferred $R_2'$ first was shown to be more suitable than one which inferred OEF directly, and this better model was also shown to be more accurate than previous linear fitting methods. When applied to *in vivo* data from healthy subjects, however, this technique was found to result in estimates of OEF and DBV that were significantly different from those reported in the literature. Several possible reasons for this were examined.

Chapter 4 considered the qBOLD signal originating from extracellular fluid (CSF and ISF) and, using simulated data, showed that the presence of this compartment severely affects estimates of DBV. Several methods for producing CSF partial volume maps were explored, and the results of these were used to inform qBOLD

model inference. The results were mixed, with the performance of the different CSF estimation methods varying across the subjects tested.

In Chapter 5, several assumptions of the static dephasing regime were examined and tested using Monte Carlo simulations of blood vessel networks. The distributions of OEF values and vessel radii $R_c$ were tested, and it was found that $R_c$ had a nonlinear effect on the measured qBOLD signal. Corrections to the SDR qBOLD model were proposed to deal with this effect, and these were shown to be effective on simulated and *in vivo* data. Additionally, simulated data were used to optimize certain acquisition parameters, which would help to define an ideal ASE-qBOLD sequence.

In Chapter 6, the methods developed in this thesis were applied to data from six acute stroke patients. OEF was estimated as being significantly higher in the ischaemic core and penumbra than in unaffected contralateral tissue. Changes in OEF and other parameters one week after stroke onset were also observed. This suggested the potential utility of the qBOLD model in aiding acute stroke assessment at the earliest stages.

## 7.2 Future Work

The work presented in this thesis is, by the nature of such bodies of work, limited in scope, and therefore by no means completed. There are a number of directions in which this work could be continued in the near future, which would help to validate or build upon the results presented above.

### 7.2.1 Extracellular Signal Contribution

Several of the assumptions made about the extracellular signal contribution in Chapter 4 could be investigated further. First, the assumption of a single value for the extracellular compartment's frequency shift $\Delta f$ is not necessarily valid, since CSF (or ISF) could contain different concentrations of proteins or other macromolecules in different parts of the brain. This would be true especially in the case of acute ischaemia, in which cell breakdown may lead to large concentrations

of macromolecules in suspension. Such a lesion may have a signal that evolves very differently from healthy tissue. $\Delta f$ could be measured in each subject by fitting the three-compartment qBOLD model to non-FLAIR GASE data simultaneously with fitting the two-compartment qBOLD model to FLAIR-prepared data, with $\Delta f$ and CSF partial volume fraction $\lambda$ as additional parameters to be inferred.

It was also assumed that CSF and ISF were in free exchange, and could be described by the same model with the same parameters. This assumption could be tested further by using a separately obtained CSF partial volume map to correct for the signal on the cortical surface, and modelling ISF volume fraction as a separate parameter in GM voxels.

No single best source of external CSF volume estimation for CSF signal correction was found; however, there are additional options that could be tested in the future. The results of fitting for $\Delta f$ described above would also produce estimates of $\lambda$ which could be used for correction. Another alternative would be to use a surface-based segmentation technique to define a 3D CSF layer using $T_1$- or $T_2$-weighted data, and to use the resulting surfaces to define CSF partial volumes in each voxel the surface intersects with. This, like other segmentation-based corrections, would be applicable only in voxels at the edge of the cortex, or next to the ventricles, and would not account for the volume of interstitial fluid in each voxel.[159]

### 7.2.2 Diffusive Vessel Simulation

The Monte Carlo methods used for simulating spins in the presence of a network of vessels from Chapter 5 could be extended in several ways, and the results used to inform further corrections to the qBOLD model. A major assumption of the SDR qBOLD model of Equations 2.25 and 2.26 is that vessels are oriented randomly. In their original paper on quantitative BOLD, Yablonskiy & Haacke[14] also detailed a model of dephasing in the presence of an array of parallel cylinders. The signal in this case depends on the orientation of the cylinders with respect to $\boldsymbol{B_0}$.

Human and animal *ex vivo* dissection and *in vivo* laminar fMRI studies[143,267–270] have shown that in the cortex, larger blood vessels including venules are not simply

oriented randomly, but follow a regular structure, with a network of pial vessels running along the surface of the cortex, and a series of penetrating vessels ascending and descending 'vertically' into it. This would suggest that the qBOLD signal in a given GM voxel may be dependent on the orientation of the cortex at that point, since deoxygenated blood vessels will run predominantly parallel to, or perpendicular to, the surface of the cortex, but generally not at other arbitrary orientations.

A qBOLD model which accounted for this anatomy would require an additional orientation parameter, and potentially others that deal with the differing densities of pial and penetrating veins. A surface-based segmentation technique could be used to obtain orientation information, which could then be provided as a spatial prior to further VB inference.

### 7.2.3 Acquisition Optimization

The parameters tested in Chapter 5 represent the first step in determining an optimal acquisition scheme for GASE data to be used in qBOLD model fitting. Further work in testing other acquisitions could be very valuable. In the first instance, acquiring an uneven distribution of $\tau$ values could substantially improve parameter estimation, such as by acquiring a number of points in the short-$\tau$ asymptotic regime to infer DBV accurately, and then some at very long $\tau$ to fit $R_2'$. These could be tested in a Bayesian framework using optimal experimental design techniques,[248,271] or by direct comparison of free energy $\mathcal{F}$.

Similarly, distinguishing between the contributions from the different compartments may be more straightforward when an additional contrast is introduced, such as an $R_2$ weighting. A multiple-ASE sequence[272,273] (in which several echoes are read out at multiples of $TE$) or several sets of GASE data acquired at different $TE$s could be used, with $R_2$ values for each compartment included as additional inferred parameters. This could produce results similar to those obtained from GESSE-qBOLD data.[36,141,152]

The effect of matrix size, $TR$, and other parameters could also be tested in the same framework that was used in Chapter 5. Regardless of the parameter

being optimized, or the method used, it will be important to validate any further advancements to the qBOLD technique on patient data, with the understanding that clinical utility ought to be the standard by which a technique is judged.

### 7.2.4 Clinical Translation

Chapter 6 demonstrated the potential for ASE-qBOLD to be used to assist in acute stroke assessment in the clinic; however, there is significant work that must be done before it can begin to be used prospectively. Given the importance of rapid intervention in ischaemic stroke, and a desire to minimize discomfort to patients, acquisition parameters should be chosen to keep scan durations as short as possible. It is necessary both to acquire enough $\tau$ values to ensure accurate model-fitting, and enough GASE slabs to cover the entire ischaemic penumbra (or ideally, the whole brain), although both of these increase scan duration.

Translation into the clinical setting would also require streamlining of the data analysis process, which in this thesis was done using a sequence of several bespoke scripts. Ideally, a single, clinically interpretable map of OEF (or an equivalently useful parameter) should be produced automatically from a single prescribed GASE acquisition protocol. This would provide information to clinicians as quickly as possible, and should fit into existing clinical workflows by complementing information from other modalities.

## 7.3 Conclusion

This thesis has shown that physiological parameters, especially oxygenation, can be inferred from ASE data using the qBOLD model. It has also shown that the effect of diffusion cannot be ignored by the model, but can be corrected for within it, and thereby used to produce more accurate results. The way in which ASE-qBOLD data are acquired, including the use of the FLAIR preparation, were examined, and improvements were suggested. Finally, this thesis has shown that the qBOLD model can reliably detect differences in oxygenation corresponding to the ischaemic penumbra, which has the potential to improve ischaemic stroke assessment.

# References


[1] H. Wang. "Global, regional, and national life expectancy, all-cause mortality, and cause-specific mortality for 249 causes of death, 1980–2015: a systematic analysis for the Global Burden of Disease Study 2015". In: *The Lancet* 388.10053 (2016), pp. 1459–1544.

[2] Jonathan W. Sturm et al. "Quality of life after stroke: The North East Melbourne Stroke Incidence Study (NEMESIS)". In: *Stroke* 35.10 (2004), pp. 2340–2345.

[3] Seana L. Paul et al. "Long-term outcome in the North East Melbourne stroke incidence study: Predictors of quality of life at 5 years after stroke". In: *Stroke* 36.10 (2005), pp. 2082–2086.

[4] Peter Appelros, Ingegerd Nydevik, and Matti Viitanen. "Poor outcome after first-ever stroke: predictors for death, dependency, and recurrent stroke within the first year". In: *Stroke* 34.1 (2003), pp. 122–126.

[5] J Rother et al. "Effect of Intravenous Thrombolysis on MRI Parameters and Functional Outcome in Acute Stroke <6 Hours". In: *Stroke* 33.10 (2002), pp. 2438–2445.

[6] Joanna M Wardlaw et al. "Recombinant tissue plasminogen activator for acute ischaemic stroke: An updated systematic review and meta-analysis". In: *The Lancet* 379.9834 (2012), pp. 2364–2372. URL: http://dx.doi.org/10.1016/S0140-6736(12)60738-7.

[7] Edward C Jauch et al. "Guidelines for the early management of patients with acute ischemic stroke: A guideline for healthcare professionals from the American Heart Association/American Stroke Association". In: *Stroke* 44.3 (2013), pp. 870–947. arXiv: 1608.04207.

[8] Jens Astrup, Bo K Siesjo, and Lindsay Symon. "Thresholds in Cerebral Ischemia - The Ischemic Penumbra". In: *Stroke* 12.6 (1979), pp. 723–725.

[9] Zachary B Rodgers et al. "Rapid T2- and susceptometry-based CMRO2 quantification with interleaved TRUST (iTRUST)". In: *NeuroImage* 106 (2015), pp. 441–450. eprint: 15334406.

[10] Richard Leigh et al. "Imaging the physiological evolution of the ischemic penumbra in acute ischemic stroke". In: *Journal of Cerebral Blood Flow and Metabolism* (2017).

[11] Colin P Derdeyn et al. "Variability of cerebral blood volume and oxygen extraction: stages of cerebral haemodynamic impairment revisited". In: *Brain* 125.3 (2002), pp. 595–607. URL: http://brain.oxfordjournals.org/content/125/3/595.long.

[12] Shyam Prabhakaran, Ilana Ruff, and Richard A Bernstein. "Acute Stroke Intervention: A Systematic Review". In: *Journal of the American Medical Association* 313.14 (2015), pp. 286–301.

[13] S Ogawa et al. "Brain magnetic resonance imaging with contrast dependent on blood oxygenation." In: *Proceedings of the National Academy of Sciences of the United States of America* 87.24 (1990), pp. 9868–9872.

[14] Dmitriy A Yablonskiy and E Mark Haacke. "Theory of NMR Signal Behavior in Magnetically Inhomogeneous Tissues: The Static Dephasing Regime". In: *Magnetic Resonance in Medicine* 32.6 (1994), pp. 749–763.

[15] Xiang He, Mingming Zhu, and Dmitriy A Yablonskiy. "Validation of oxygen extraction fraction measurement by qBOLD technique". In: *Magnetic Resonance in Medicine* 60.4 (2008), pp. 882–888. eprint: NIHMS150003.

[16] Jan Sedlacik and Jurgen R Reichenbach. "Validation of quantitative estimation of tissue oxygen extraction fraction and deoxygenated blood volume fraction in phantom and in vivo experiments by using MRI". In: *Magnetic Resonance in Medicine* 63.4 (2010), pp. 910–921.

[17] Dmitriy A Yablonskiy, Alexander L Sukstanskii, and Xiang He. "Blood oxygenation level-dependent (BOLD)-based techniques for the quantification of brain hemodynamic and metabolic properties - theoretical models and experimental approaches". In: *NMR in Biomedicine* 26.8 (2013), pp. 963–986. arXiv: NIHMS150003.

[18] Alan J Stone et al. "Simulations of the effect of diffusion on asymmetric spin echo based quantitative BOLD: An investigation of the origin of deoxygenated blood volume overestimation". In: *NeuroImage* 201.7 (2019).

[19] Alan J. Stone and Nicholas P. Blockley. "A streamlined acquisition for mapping baseline brain oxygenation using quantitative BOLD". In: *NeuroImage* 147.July 2016 (2017), pp. 79–88. URL: http://dx.doi.org/10.1016/j.neuroimage.2016.11.057.

[20] Hagias Attias. "A Variational Bayesian Framework for Graphical Models". In: *Advances in Neural Information Processing Systems* (2000).

[21] Karl J Friston et al. "Classical and Bayesian inference in neuroimaging: Applications". In: *NeuroImage* 16.2 (2002), pp. 484–512.

[22] Michael A Chappell et al. "Variational Bayesian Inference for a Nonlinear Forward Model". In: *IEEE Transactions on Signal Processing* 57.1 (2009), pp. 223–236.

[23] Mark W Woolrich. "Bayesian inference in FMRI". In: *NeuroImage* 62.2 (2012), pp. 801–810. URL: http://dx.doi.org/10.1016/j.neuroimage.2011.10.047.

[24] Dwight G Nishimura. *Principles of Magnetic Resonance Imaging*. 2010.

[25] P J Hore. *Nuclear Magnetic Resonance*. 1995.

[26] E Mark Haacke. *Magnetic Resonance Imaging: Physical Principles and Sequence Design*. 1999.

[27] Mark Chiew and Karla L Miller. "Magnetic Resonance Imaging. FMRIB Physics Graduate Course". Lecture. University of Oxford, 2016. Lecture Notes.

[28] William T Clarke. "Human Cardiac Magnetic Resonance Spectroscopy". D.Phil Thesis. Oxford: University of Oxford, Mar. 2016.

[29] Eleanor Berry. "Optimisation of vessel-selective magnetic resonance perfusion imaging and angiography". D.Phil Thesis. Oxford: University of Oxford, Aug. 2016.

[30] M A Bernstein, K F King, and Z J Zhou. *Handbook of MRI Pulse Sequences*. 2004.

[31] Peter Mansfield. "Multi-planar image formation using NMR spin echoes". In: *Journal of Physics C: Solid State Physics* 10 (1977), pp. L55–L58.

[32] G L Wismer et al. "Susceptibility induced MR line broadening: applications to brain iron mapping." In: *Journal of Computer Assisted Tomography* 12.2 (1988), pp. 259–265. URL: http://eutils.ncbi.nlm.nih.gov/entrez/eutils/elink.fcgi?dbfrom=pubmed%7B%5C&%7Did=3351040%7B%5C&%7Dretmode=ref%7B%5C&%7Dcmd=prlinks%7B%5C%%7D255Cnpapers3://publication/uuid/CAA11C12-AA64-409A-8E11-DDC6613B88B4.

[33] Joseph V Hajnal et al. *High signal regions in normal white matter shown by heavily T2-weighted CSF nulled IR sequences*. 1992.

[34] Qing X Yang et al. "Removal of local field gradient artifacts in GE images by slice excitation profile imaging (GESEPI) in high field". In: *Magnetic Resonance in Medicine* 39.3 (1998), pp. 402–409.

[35] E L Hahn. "Spin Echoes". In: *Physical Review* 80.4 (1950), pp. 580–594.

[36] Dmitriy A Yablonskiy and E Mark Haacke. "An MRI method for measuring T2 in the presence of static and RF magnetic field inhomogeneities". In: *Magnetic Resonance in Medicine* 37.6 (1997), pp. 872–876.

[37] Jingfei Ma and Felix W Wehrli. "Method for Image-Based Measurement of the Reversible and Irreversible Contribution to the Transverse-Relaxation Rate". In: *Journal of Magnetic Resonance, Series B* 111.1 (1996), pp. 61–69.

[38] Yuji Shen et al. "A functional magnetic resonance imaging technique based on nulling extravascular gray matter signal". In: *Journal of Cerebral Blood Flow and Metabolism* 29.1 (2009), pp. 144–156.

[39] Norman J Beauchamp et al. "MR diffusion imaging in stroke: review and controversies." In: *RadioGraphics* 18.5 (1998), pp. 1269–1283. URL: http://pubs.rsna.org/doi/10.1148/radiographics.18.5.9747619.

[40] Konstantin Alexander Hossmann. "Cerebral ischemia: Models, methods and outcomes". In: *Neuropharmacology* 55.3 (2008), pp. 257–270.

[41] Christopher H Sotak. "The role of diffusion tensor imaging in the evaluation of ischemic brain injury - a review". In: *NMR in Biomedicine* 15.7-8 (2002), pp. 561–569. URL: http://doi.wiley.com/10.1002/nbm.786.

[42] Joseph Broderick et al. "REPRINT: Guidelines for the Management of Spontaneous Intracerebral Hemorrhage in Adults". In: *Circulation* 116 (2007), pp. 391–413.

[43] Justine Elliott and Martin Smith. "The acute management of intracerebral hemorrhage: A clinical review". In: *Anesthesia and Analgesia* 110.5 (2010), pp. 1419–1427.

[44] Veronique L Roger et al. "Heart disease and stroke statistics-2011 update: A report from the American Heart Association". In: *Circulation* 123.4 (2011), pp. 18–209.

[45] J Alfredo Caceres and Joshua N Goldstein. "Intracranial hemorrhage". In: *Emergency Medicine Clinics of North America* 30.3 (2012), pp. 159–163.

[46] Amanda G Thrift et al. "Incidence of the major stroke subtypes: initial findings from the North East Melbourne stroke incidence study (NEMESIS)". In: *Stroke* 32.8 (2001), pp. 1732–1738.

[47] Valery L Feigin et al. "Stroke epidemiology: A review of population-based studies of incidence, prevalence, and case-fatality in the late 20th century". In: *The Lancet Neurology* 2.1 (2003), pp. 43–53.

[48] Valery L Feigin et al. "Worldwide stroke incidence and early case fatality reported in 56 population-based studies: a systematic review". In: *The Lancet Neurology* 8.4 (2009), pp. 355–369. URL: http://dx.doi.org/10.1016/S1474-4422(09)70025-0.

[49] Harold P Adams et al. "Classification of Subtype of Acute Ischemic Stroke". In: *Stroke* 24.1 (1993), pp. 35–41.

[50] Thomas Brott et al. "Measurements of acute cerebral infarction: a clinical examination scale." In: *Stroke* 20.7 (1989), pp. 864–870.

[51] Larry B Goldstein, Christina Bertels, and James N Davis. "Interrater reliability of the NIH stroke scale". In: *Archives of Neurology* 46.6 (1989), pp. 660–662.

[52] Nishant K Mishra et al. "Mismatch-based delayed thrombolysis: a meta-analysis". In: *Stroke* 41.1 (2010), e25–e33.

[53] John Rankin. "Cerebral vascular accidents in patients over the age of 60: II. Prognosis". In: *Scottish Medical Journal* 2.5 (1957), pp. 200–215.

[54] JT Lindsay Wilson et al. "Improving the assessment of outcomes in stroke: use of a structured interview to assign grades on the modified Rankin Scale". In: *Stroke* 33.9 (2002), pp. 2243–2246.

[55] National Institute of Neurological Disorders and The Stroke rt-PA Stroke Study Group. "Tissue Plasminogen Activator for Acute Ischemic Stroke". In: *New England Journal of Medicine* 333.24 (1995), pp. 1581–1587.

[56] Toshihiro Ueda et al. "Outcome of acute ischemic lesions evaluated by diffusion and perfusion MR imaging." In: *American Journal of Neuroradiology* 20.July (1999), pp. 983–989.

[57] Peter C M Van Zijl et al. "Quantitative assessment of blood flow, blood volume and blood oxygenation effects in functional magnetic resonance imaging". In: *Nature Medicine* 4.2 (1998), pp. 159–167.

[58] Joni M E Oja et al. "Determination of oxygen extraction ratios by magnetic resonance imaging". In: *Journal of Cerebral Blood Flow and Metabolism* 19.12 (1999), pp. 1289–1295.

[59] Hanzhang Lu and Yulin Ge. "Quantitative evaluation of oxygenation in venous vessels using T2-relaxation-under-spin-tagging MRI". In: *Magnetic Resonance in Medicine* 60 (2008), pp. 357–363.

[60] Andrew Bivard et al. "Arterial spin labeling versus bolus-tracking perfusion in hyperacute stroke". In: *Stroke* 45.1 (2014), pp. 127–133.

[61] Greg Zaharchuk. "Arterial Spin Labeled Perfusion Imaging in Acute Ischemic Stroke". In: *Stroke* 45.4 (2015), pp. 1202–1207.

[62] Seymour S Kety and Carl F Schmidt. "the Nitrous Oxide Method for the Quantitative Determination of Cerebral Blood Flow in Man: Theory, Procedure and Normal Values". In: *Journal of Clinical Investigation* 27.4 (1948), pp. 476–483.

[63] Thomas W Okell et al. "Cerebral Blood Flow Quantification Using Vessel-Encoded Arterial Spin Labeling". In: *Journal of Cerebral Blood Flow & Metabolism* 33.11 (2013), pp. 1716–1724. URL: `http://journals.sagepub.com/doi/10.1038/jcbfm.2013.129`.

[64] Takeya Niibo et al. "Arterial spin-labeled perfusion imaging to predict mismatch in acute ischemic stroke". In: *Stroke* 44.9 (2013), pp. 2601–2603.

[65] Peter A Chiarelli et al. "A calibration method for quantitative BOLD fMRI based on hyperoxia". In: *NeuroImage* 37.3 (2007), pp. 808–820.

[66] KA Dani and Steven Warach. "Metabolic imaging of ischemic stroke: the present and future". In: *American Journal of Neuroradiology* 35.6 (2014), S37–S43.

[67] Konstantin Alexander Hossmann. "Viability threshold and the penumbra of focal ischemia". In: *Annals of Neurology* 36.4 (1994), pp. 557–565.

[68] Peter A Ringleb et al. "Guidelines for Management of Ischaemic Stroke and Transient Ischaemic Attack 2008". In: *Cerebrovascular Diseases* 25 (2008), pp. 457–507. URL: `www.karger.com%20www.karger.com/ced`.

[69] Chelsea S Kidwell et al. “A Trial of Imaging Selection and Endovascular Treatment for Ischemic Stroke”. In: *New England Journal of Medicine* 368.10 (2013), pp. 914–923. eprint: NIHMS150003.

[70] Bruce C V Campbell et al. “Endovascular Therapy for Ischemic Stroke with Perfusion-Imaging Selection”. In: *New England Journal of Medicine* 372.11 (2015), pp. 1009–1018. URL: http://www.nejm.org/doi/10.1056/NEJMoa1414792.

[71] Wolf Dieter Heiss. “The concept of the penumbra: Can it be translated to stroke management?” In: *International Journal of Stroke* 5.4 (2010), pp. 290–295.

[72] P. Alan Barber et al. “Imaging of the brain in acute ischaemic stroke: Comparison of computed tomography and magnetic resonance diffusion-weighted imaging”. In: *Journal of Neurology, Neurosurgery and Psychiatry* 76.11 (2005), pp. 1528–1533.

[73] R Nick Bryan et al. “Nuclear Magnetic Resonance Evaluation of Stroke”. In: *Radiology* 149.10 (1983), pp. 189–192.

[74] Jorma T Sipponen. “Visualization of brain infarction with nuclear magnetic resonance imaging”. In: *Neuroradiology* 26 (1984), pp. 387–391.

[75] John F Rothrock et al. “Brain magnetic resonance imaging in the evaluation of lacunar stroke.” In: *Stroke* 18.4 (1987), pp. 781–786. URL: http://www.ncbi.nlm.nih.gov/pubmed/3603605.

[76] R Nick Bryan et al. “Diagnosis of acute cerebral infarction: comparison of CT and MR imaging”. In: *American Journal of Neuroradiology* 12.4 (1991), pp. 611–620.

[77] Pamela W Schaefer et al. “Limited reliability of computed tomographic perfusion acute infarct volume measurements compared with diffusion-weighted imaging in anterior circulation stroke”. In: *Stroke* 46.2 (2015), pp. 419–424.

[78] Ona Wu et al. “Infarct prediction and treatment assessment with MRI-based algorithms in experimental stroke models.” In: *Journal of Cerebral Blood Flow & Metabolism* 27.1 (2007), pp. 196–204.

[79] Albert J Yoo et al. “Combining acute diffusion-weighted imaging and mean transmit time lesion volumes with national institutes of health stroke scale score improves the prediction of acute stroke outcome”. In: *Stroke* 41.8 (2010), pp. 1728–1735.

[80] Michael E Moseley et al. “Early detection of regional cerebral ischemia in cats: Comparison of diffusion- and T2-weighted MRI and spectroscopy”. In: *Magnetic Resonance in Medicine* 14.2 (1990), pp. 330–346.

[81] Helmi L Lutsep et al. “Clinical utility of diffusion-weighted magnetic resonance imaging in the assessment of ischemic stroke”. In: *Annals of Neurology* 41.5 (1997), pp. 574–580. URL: http://www.ncbi.nlm.nih.gov/entrez/query.fcgi?cmd=Retrieve%7B%5C&%7Ddb=PubMed%7B%5C&%7Ddopt=Citation%7B%5C&%7Dlist%7B%5C_%7Duids=9153518.

[82] K A Hossmann and M Hoehn-Berlage. “Diffusion and perfusion MR imaging of cerebral ischemia.” In: *Cerebrovascular and Brain Metabolism Reviews* 7.3 (1995), pp. 187–217.

[83] AL Busza et al. “Diffusion-weighted imaging studies of cerebral ischemia in gerbils. Potential relevance to energy failure.” In: *Stroke* 23.11 (1992), pp. 1602–1612.

[84] K M A Welch et al. “A model to predict the histopathology of human stroke using diffusion and T2-weighted magnetic resonance imaging”. In: *Stroke* 26.11 (1995), pp. 1983–1989.

[85] G Schlaug et al. “Time course of the apparent diffusion coefficient (ADC) abnormality in human stroke.” In: *Neurology* 49.1 (1997), pp. 113–9. URL: http://www.ncbi.nlm.nih.gov/pubmed/9222178.

[86] A Gregory Sorensen et al. “Hyperacute stroke: evaluation with combined multisection diffusion-weighted and hemodynamically weighted echo-planar MR imaging.” In: *Radiology* 199.2 (1996), pp. 391–401.

[87] Masayuki Maeda et al. “Application of Contrast Agents in the Evaluation of Stroke: Conventional MR and Echo-Planar MR Imaging”. In: *Journal of Magnetic Resonance Imaging* 7 (1997), pp. 23–28.

[88] A Gregory Sorensen et al. “Hyperacute Stroke: Simultaneous Measurement of Relative Cerebral Blood Volume, Relative Cerebral Blood Flow, and Mean Tissue Transit Time”. In: *Radiology* 210 (1999), pp. 519–527.

[89] Zamir Merali et al. “Evolution of blood-brain-barrier permeability after acute ischemic stroke”. In: *PLoS ONE* 12.2 (2017), pp. 1–11.

[90] Kersten Villringer et al. “DCE-MRI blood – brain barrier assessment in acute ischemic stroke”. In: *Neurology* 88 (2017), pp. 433–440.

[91] Kieran J Murphy, James A Brunberg, and Richard H Cohan. “Adverse reactions to gadolinium contrast media: a review of 36 cases”. In: *American Journal of Roentgenology* 167.4 (1996), pp. 847–849.

[92] Henrik S Thomsen, Sameh K Morcos, and P Dawson. “Is there a causal relation between the administration of gadolinium based contrast media and the development of nephrogenic systemic fibrosis (NSF)?” In: *Clinical Radiology* 61.11 (2006), pp. 905–906.

[93] Fulvio Stacul et al. “Contrast induced nephropathy: Updated ESUR Contrast Media Safety Committee guidelines”. In: *European Radiology* 21.12 (2011), pp. 2527–2541.

[94] Aurang Z Khawaja et al. “Revisiting the risks of MRI with Gadolinium based contrast agents - review of literature and guidelines”. In: *Insights into Imaging* 6.5 (2015), pp. 553–558.

[95] Stephen L Seliger et al. “Elevated risk of stroke among patients with end-stage renal disease”. In: *Kidney International* 64.2 (2003), pp. 603–609.

[96] Robert J McDonald et al. “Intracranial Gadolinium Deposition after Contrast-enhanced MR Imaging”. In: *Radiology* 275.3 (2015), pp. 772–782. URL: http://pubs.rsna.org/doi/10.1148/radiol.15150025.

[97] Tobias Neumann-Haefelin et al. “Diffusion- and Perfusion-Weighted MRI: the DWI/PWI Mismatch Region in Acute Stroke”. In: *Stroke* 30 (1999), pp. 1591–1597.

[98] Jari O Karonen et al. “Combined Diffusion and Perfusion MRI With Correlation to Single-Photon Emission CT in Acute Ischemic Stroke”. In: *Stroke* (1999).

[99] Ona Wu et al. “Predicting Tissue Outcome in Acute Human Cerebral Ischemia Using Combined Diffusion- and Perfusion-Weighted MR Imaging”. In: *Stroke* (2001), pp. 933–943.

[100] Shelagh B Coutts et al. “Reliability of Assessing Percentage of Diffusion-Perfusion Mismatch”. In: *Stroke* 34.7 (2003), pp. 1681–1683.

[101] Alex de Crespigny. “Editorial Comment—Mismatch or Misconception?” In: *Stroke* 34.7 (2003), pp. 1683–1685.

[102] Gregory W Albers et al. “Magnetic resonance imaging profiles predict clinical response to early reperfusion: The diffusion and perfusion imaging evaluation for understanding stroke evolution (DEFUSE) study”. In: *Annals of Neurology* 60.5 (2006), pp. 508–517.

[103] Shiliang Huang, Qiang Shen, and Timothy Q. Duong. “Artificial neural network prediction of ischemic tissue fate in acute stroke imaging”. In: *Journal of Cerebral Blood Flow and Metabolism* 30.9 (2010), pp. 1661–1670. URL: http://dx.doi.org/10.1038/jcbfm.2010.56.

[104] Kim Mouridsen et al. “Acute Stroke: Automatic Perfusion Lesion Outlining Using Level Sets”. In: *Radiology* 269.2 (2013), pp. 404–412. URL: http://pubs.rsna.org/doi/10.1148/radiol.13121622.

[105] Noah Stier et al. “Deep learning of tissue fate features in acute ischemic stroke”. In: *2015 IEEE International Conference on Bioinformatics and Biomedicine (BIBM)* (2015), pp. 1316–1321. URL: http://ieeexplore.ieee.org/lpdocs/epic03/wrapper.htm?arnumber=7359869.

[106] Robert H. Ackerman et al. “Positron Imaging in Ischemic Stroke Disease Using Compounds Labeled With Oxygen 15: Initial Results of Clinicophysiologic Correlations”. In: *JAMA Neurology* 38.9 (Sept. 1981), pp. 537–543. eprint: https://jamanetwork.com/journals/jamaneurology/articlepdf/580060/archneur_38_9_002.pdf. URL: https://doi.org/10.1001/archneur.1981.00510090031002.

[107] Jean Claude Baron. "Mapping the ischaemic penumbra with PET: Implications for acute stroke treatment". In: *Cerebrovascular Diseases* 9.4 (1999), pp. 193–201.

[108] Jean Claude Baron and Terry Jones. "Oxygen metabolism, oxygen extraction and positron emission tomography: Historical perspective and impact on basic and clinical neuroscience". In: *NeuroImage* 61.2 (2012), pp. 492–504. URL: http://dx.doi.org/10.1016/j.neuroimage.2011.12.036.

[109] Alan J Stone et al. "Prospects for investigating brain oxygenation in acute stroke: Experience with a non-contrast quantitative BOLD based approach". In: *Human Brain Mapping* October 2018 (2019), pp. 2853–2866.

[110] Xiang He and Dmitriy A Yablonskiy. "Biophysical mechanisms of phase contrast in gradient echo MRI". In: *Proceedings of the National Academy of Sciences* 106.32 (2009), pp. 13558–13563.

[111] G Bruce Pike. "Quantitative functional MRI: Concepts, issues and future challenges". In: *NeuroImage* 62.2 (2012), pp. 1234–1240. URL: http://dx.doi.org/10.1016/j.neuroimage.2011.10.046.

[112] Eric C Wong. "An introduction to ASL labeling techniques". In: *Journal of Magnetic Resonance Imaging* 40.1 (2014), pp. 1–10.

[113] Peter Jezzard, Michael A Chappell, and Thomas W Okell. "Arterial spin labeling for the measurement of cerebral perfusion and angiography". In: *Journal of Cerebral Blood Flow & Metabolism* (2017), p. 0271678X1774324. URL: http://journals.sagepub.com/doi/10.1177/0271678X17743240.

[114] Peter Jezzard, Paul M Matthews, and Stephen M Smith. *Functional MRI: An Introduction to Methods*. 1st ed. Oxford: Oxford University Press, 2001.

[115] Hanzhang Lu et al. "Functional magnetic resonance imaging based on changes in vascular space occupancy". In: *Magnetic Resonance in Medicine* 50.2 (2003), pp. 263–274.

[116] Feng Xu, Yulin Ge, and Hanzhang Lu. "Noninvasive quantification of whole-brain cerebral metabolic rate of oxygen (CMRO2) by MRI". In: *Magnetic Resonance in Medicine* 62.1 (2009), pp. 141–148.

[117] Hannah V Hare. "Quantitative Imaging of Cerebral Oxygen Metabolism using MRI". D.Phil Thesis. Oxford: University of Oxford, 2015.

[118] Avery J L Berman. "Basic BOLD Physiology. fMRI: Back to Basics". In: *Proceedings of the 27th Annual Meeting of the International Society for Magnetic Resonance in Medicine*. ISMRM. Montreal, QC, 2019.

[119] Seiji Ogawa et al. "Intrinsic Signal Changes Accompanying Sensory Stimulation: Functional Brain Mapping with Magnetic Resonance Imaging". In: *Proceedings of the National Academy of Sciences* 89.7 (1992), pp. 5951–5955.

[120] S Ogawa, T M Lee, and B Barrere. "The sensitivity of magnetic resonance image signals of a rat brain to changes in the cerebral venous blood oxygenation." In: *Magnetic Resonance in Medicine* 29.2 (1993), pp. 205–10. URL: http://www.ncbi.nlm.nih.gov/pubmed/8429784.

[121] S Ogawa et al. "Functional brain mapping by blood oxygenation level-dependent contrast magnetic resonance imaging. A comparison of signal characteristics with a biophysical model." In: *Biophysical journal* 64.3 (1993), pp. 803–812. URL: http://www.sciencedirect.com/science/article/pii/S0006349593814413.

[122] Kenneth K Kwong et al. "Dynamic magnetic resonance imaging of human brain activity during primary sensory stimulation". In: *Proceedings of the National Academy of Sciences* 89.6 (1992), pp. 5675–5679. URL: papers3://publication/uuid/B967F349-9A1A-47B9-B27D-80E674C7E945.

[123] Bharat Biswal et al. "Functional Connectivity in the Motor Cortex of Resting Human Brain Using Echo-Planar MRI". In: *Magnetic Resonance in Medicine* 34.9 (1995), pp. 537–541.

[124] Stephen M Smith et al. "Correspondence of the brain's functional architecture during activation and rest". In: *Proceedings of the National Academy of Sciences* 106.31 (2005), pp. 13040–13045.

[125] S A Huettel, A W Song, and G McCarthy. *Functional magnetic resonance imaging*. 2004.

[126] R N Pittman. "Oxygen Transport". In: *Regulation of Tissue Oxygenation*. San Rafael, California: Morgan & Claypool Life Sciences, 2011.

[127] John F Schenck. "Magnetic resonance imaging of brain iron". In: *Journal of the Neurological Sciences* 207 (2003), pp. 99–102.

[128] John F Schenck and Earl A Zimmerman. "High-field magnetic resonance imaging of brain iron: Birth of a biomarker?" In: *NMR in Biomedicine* 17.7 (2004), pp. 433–445.

[129] Aaron B Simon and Richard B Buxton. "Understanding the dynamic relationship between cerebral blood flow and the BOLD signal: Implications for quantitative functional MRI". In: *NeuroImage* 116 (2015), pp. 158–167.

[130] Timothy L Davis et al. "Calibrated functional MRI: Mapping the dynamics of oxidative metabolism (hypercapniacerebrovascular reactivity)". In: *Proceedings of the National Academy of Sciences* 95.2 (1998), pp. 1834–1839.

[131] Daniel P Bulte et al. "Quantitative measurement of cerebral physiology using respiratory-calibrated MRI". In: *NeuroImage* 60.1 (2012), pp. 582–591.

[132] Claudine J Gauthier and Richard D Hoge. "A generalized procedure for calibrated MRI incorporating hyperoxia and hypercapnia". In: *Human Brain Mapping* 34.5 (2013), pp. 1053–1069.

[133] Richard G Wise et al. "Measurement of OEF and absolute CMRO2: MRI-based methods using interleaved and combined hypercapnia and hyperoxia". In: *NeuroImage* 83 (2013), pp. 135–147.

[134] Robert L Grubb et al. "The effects of changes in PaCO2 on cerebral blood volume, blood flow, and vascular mean transit time". In: *Stroke* 5 (1974), pp. 630–639. URL: http://www.ncbi.nlm.nih.gov/entrez/query.fcgi?cmd=Retrieve%7B%5C&%7Damp%7B%5C%%7D5Cndb=PubMed%7B%5C&%7Damp%7B%5C%%7D5Cndopt=Citation%7B%5C&%7Damp%7B%5C%%7D5Cnlist%7B%5C_%7Duids=4472361%7B%5C%%7D5Cnpapers3://publication/uuid/B93E8FB2-E18A-4731-AE5C-6FCA05E3E944%20http://stroke.ahajournals.org/cgi/content/abstract/5/5/630.

[135] J. Jean Chen and G. Bruce Pike. "MRI measurement of the BOLD-specific flow-volume relationship during hypercapnia and hypocapnia in humans". In: *NeuroImage* 53.2 (2010), pp. 383–391.

[136] Valerie E M Griffeth and Richard B Buxton. "A theoretical framework for estimating cerebral oxygen metabolism changes using the calibrated-BOLD method: Modeling the effects of blood volume distribution, hematocrit, oxygen extraction fraction, and tissue signal properties on the BOLD signal". In: *NeuroImage* 58.1 (2011), pp. 198–212.

[137] Richard D Hoge et al. "Investigation of BOLD signal dependence on CBF and CMRO2: the Deoxyhemoglobin Dilution Model". In: *Magn. Reson. Med.* 42.5 (1999), pp. 849–863.

[138] Daniel P Bulte et al. "Measurement of cerebral blood volume in humans using hyperoxic MRI contrast". In: *Journal of Magnetic Resonance Imaging* 26.4 (2007), pp. 894–899. URL: http://www.ncbi.nlm.nih.gov/entrez/query.fcgi?cmd=Retrieve%7B%5C&%7Ddb=PubMed%7B%5C&%7Ddopt=Citation%7B%5C&%7Dlist%7B%5C_%7Duids=17896390%7B%5C%%7D5Cnpapers://2869f907-86c9-45b4-b3a1-9fd72ada1eca/Paper/p40190.

[139] Feng Xu et al. "The influence of carbon dioxide on brain activity and metabolism in conscious humans". In: *Journal of Cerebral Blood Flow and Metabolism* 31.1 (2011), pp. 58–67. URL: http://dx.doi.org/10.1038/jcbfm.2010.153.

[140] William M Spees et al. "Water proton MR properties of human blood at 1.5 Tesla: Magnetic susceptibility, T1, T2, T2*, and non Lorentzian signal behavior". In: *Magnetic Resonance in Medicine* 45.4 (2001), pp. 533–542. URL: http://onlinelibrary.wiley.com/doi/10.1002/mrm.1072/abstract%7B%5C%%7D5Cnhttp://onlinelibrary.wiley.com/doi/10.1002/mrm.1072/abstract;jsessionid=CABFE880FF3D9D92EB180A27F52501F4.d02t02%7B%5C%%7D5Cnhttp://onlinelibrary.wiley.com/store/10.1002/mrm.1072/asset/1072%7B%5C_%7Dftp.pdf?v=1.

[141] Xiang He and Dmitriy A Yablonskiy. "Quantitative BOLD: Mapping of human cerebral deoxygenated blood volume and oxygen extraction fraction: Default state". In: *Magnetic Resonance in Medicine* 57.1 (2007), pp. 115–126.

[142] Hongyu An and Weili Lin. "Impact of intravascular signal on quantitative measures of cerebral oxygen extraction and blood volume under normo- and hypercapnic conditions using an asymmetric spin echo approach". In: *Magnetic Resonance in Medicine* 50 (2003), pp. 708–716.

[143] Kamil Uludag, Bernd Muller-Bierl, and Kamil Ugurbil. "An integrative model for neuronal activity-induced signal changes for gradient and spin echo functional imaging". In: *NeuroImage* 48 (2009), pp. 150–165.

[144] Jason M Zhao et al. "Oxygenation and hematocrit dependence of transverse relaxation rates of blood at 3T". In: *Magnetic Resonance in Medicine* 58.3 (2007), pp. 592–597.

[145] Nicholas P Blockley, Valerie E M Griffeth, and Richard B Buxton. "A general analysis of calibrated BOLD methodology for measuring CMRO 2 responses: Comparison of a new approach with existing methods". In: *NeuroImage* 60 (2012), pp. 279–289.

[146] Alexander L Sukstanskii and Dmitriy A Yablonskiy. "Theory of FID NMR Signal Dephasing Induced by Mesoscopic Magnetic Field Inhomogeneities in Biological Systems". In: *Journal of Magnetic Resonance* 151.1 (2001), pp. 107–117. URL: http://linkinghub.elsevier.com/retrieve/pii/S1090780701923638%20http://www.idealibrary.com.

[147] Avery J L Berman and G Bruce Pike. "Transverse signal decay under the weak field approximation: Theory and validation". In: *Magnetic Resonance in Medicine* 00 (2017), pp. 1–10. URL: http://doi.wiley.com/10.1002/mrm.27035.

[148] Avery J.L. Berman et al. "Gas-free calibrated fMRI with a correction for vessel-size sensitivity". In: *NeuroImage* 169.December 2017 (2018), pp. 176–188. URL: http://linkinghub.elsevier.com/retrieve/pii/S1053811917310716.

[149] J H Jensen and Ronil V Chandra. "NMR relaxation in tissues with weak magnetic inhomogeneities". In: *Magnetic Resonance in Medicine* 44.1 (2000), pp. 144–156.

[150] Dmitriy A Yablonskiy. "Quantitation of Intrinsic Magnetic Susceptibility-Related Effects in a Tissue Matrix. Phantom Study". In: *Magnetic Resonance in Medicine* 39 (1998), pp. 417–428.

[151] Wendy Ni et al. "Comparison of R2 measurement methods in the normal brain at 3 tesla". In: *Magnetic Resonance in Medicine* 73.3 (2015), pp. 1228–1236. eprint: NIHMS150003.

[152] Aaron B Simon et al. "A novel Bayesian approach to accounting for uncertainty in fMRI-derived estimates of cerebral oxygen metabolism fluctuations". In: *NeuroImage* 129 (2016), pp. 198–213.

[153] Sebastian Domsch et al. "Oxygen Extraction Fraction Mapping at 3 Tesla Using an Artificial Neural Network: A Feasibility Study". In: *Magnetic Resonance in Medicine* 79.2 (2018), pp. 890–899.

[154] Vitaly G Kiselev and S Posse. "Analytical Theory of Susceptibility Induced NMR Signal Dephasing in a Cerebrovascular Network". In: *Physical Review Letters* 81.25 (1998), pp. 5696–5699.

[155] Alexander L Sukstanskii and Dmitriy A Yablonskiy. "Gaussian approximation in the theory of MR signal formation in the presence of structure-specific magnetic field inhomogeneities". In: *Journal of Magnetic Resonance* 163.2 (2003), pp. 236–247.

[156] Alexander L Sukstanskii and Dmitriy A Yablonskiy. "Gaussian approximation in the theory of MR signal formation in the presence of structure-specific magnetic field inhomogeneities. Effects of impermeable susceptibility inclusions". In: *Journal of Magnetic Resonance* 167.1 (2004), pp. 56–67.

[157] Dean C. Douglass and David W. McCall. "Diffusion in Paraffin Hydrocarbons". In: *The Journal of Physical Chemistry* 62.9 (1958), pp. 1102–1107. eprint: https://doi.org/10.1021/j150567a020. URL: https://doi.org/10.1021/j150567a020.

[158] Jerrold L Boxerman et al. "MR Contrast due to Intravascular Magnetic Susceptibility Perturbations". In: *Magnetic Resonance in Medicine* 34.4 (1995), pp. 555–566.

[159] John D Dickson et al. "Quantitative BOLD: the effect of diffusion." In: *Journal of Magnetic Resonance Imaging* 32.4 (2010), pp. 953–961. URL: http://doi.wiley.com/10.1002/jmri.22151%20http://www.scopus.com/inward/record.url?eid=2-s2.0-79952198166%7B%5C&%7DpartnerID=tZOtx3y1.

[160] John D Dickson et al. "Quantitative phenomenological model of the BOLD contrast mechanism". In: *Journal of Magnetic Resonance Imaging* 212 (2011), pp. 17–25.

[161] Nicolas A Pannetier et al. "Numerical modeling of susceptibility-related MR signal dephasing with vessel size measurement: phantom validation at 3T". In: *Magnetic Resonance in Medicine* 72.3 (2014), pp. 646–658.

[162] Hongyu An and Weili Lin. "Cerebral oxygen extraction fraction and cerebral venous blood volume measurements using MRI: Effects of magnetic field variation". In: *Magnetic Resonance in Medicine* 47.5 (2002), pp. 958–966.

[163] Nicholas P Blockley and Alan J Stone. "Improving the specificity of R2 to the deoxyhaemoglobin content of brain tissue: Prospective correction of macroscopic magnetic field gradients". In: *NeuroImage* 135 (2016), pp. 253–260. URL: http://dx.doi.org/10.1016/j.neuroimage.2016.04.013.

[164] Thomas Christen et al. "Measuring brain oxygenation in humans using a multiparametric quantitative blood oxygenation level dependent MRI approach". In: *Magnetic Resonance in Medicine* 68.3 (2012), pp. 905–911.

[165] Hyunyeol Lee, Erin K Englund, and Felix W Wehrli. "Interleaved quantitative BOLD : Combining extravascular R2 - and intravascular R2 -measurements for estimation of deoxygenated blood volume and hemoglobin oxygen saturation". In: *NeuroImage* 174.February (2018), pp. 420–431. URL: https://doi.org/10.1016/j.neuroimage.2018.03.043.

[166] D N Guilfoyle et al. "Real-time flow measurements using echo-planar imaging". In: *Magnetic Resonance in Medicine* 18.1 (1991), pp. 1–8.

[167] Donald S Williams et al. "Magnetic resonance imaging of perfusion using spin inversion of arterial water." In: *Proceedings of the National Academy of Sciences* 89.1 (1992), pp. 212–216. URL: http://www.pnas.org/cgi/doi/10.1073/pnas.89.1.212.

[168] John A Detre et al. "Perfusion imaging". In: *Magnetic Resonance in Medicine* 23.1 (1992), pp. 37–45. URL: http://eutils.ncbi.nlm.nih.gov/entrez/eutils/elink.fcgi?dbfrom=pubmed%7B%5C&%7Did=1734182%7B%5C&%7Dretmode=ref%7B%5C&%7Dcmd=prlinks%7B%5C%%7D0Apapers3://publication/doi/10.1002/mrm.1910230106.

[169] Richard B. Buxton et al. "A general kinetic model for quantitative perfusion imaging with arterial spin labeling". In: *Magnetic Resonance in Medicine* 40.3 (1998), pp. 383–396.

[170] Weiying Dai et al. "Continuous flow-driven inversion for arterial spin labeling using pulsed radio frequency and gradient fields". In: *Magnetic Resonance in Medicine* 60.6 (2008), pp. 1488–1497.

[171] Feng Xu et al. "On improving the speed and reliability of T 2-relaxation-under- spin-tagging (TRUST) MRI". In: *Magnetic Resonance in Medicine* 68.1 (July 2012), pp. 198–204. arXiv: NIHMS150003. URL: http://doi.wiley.com/10.1002/mrm.23207.

[172] Hanzhang Lu et al. "Calibration and validation of TRUST MRI for the estimation of cerebral blood oxygenation". In: *Magnetic Resonance in Medicine* 67.1 (2012), pp. 42–49.

[173] Xavier Golay et al. "Measurement of tissue oxygen extraction ratios from venous blood T2: Increased precision and validation of principle". In: *Magnetic Resonance in Medicine* 46.2 (2001), pp. 282–291.

[174] Caitlin O'Brien et al. "Volume-localized measurement of oxygen extraction fraction in the brain using MRI". In: *Magnetic Resonance in Medicine* 82.4 (2019), pp. 1412–1423.

[175] A Gelman, G O Roberts, and W R Gilks. "Efficient Metropolis Jumping Rules". In: *Bayesian Statistics*. Ed. by J M Bernardo et al. 1996.

[176] Christopher M Bishop. *Pattern Recognition and Machine Learning*. New York: Springer, 2006.

[177] Carl Edward Rasmussen and Christopher K I Williams. "Gaussian Processes for Machine Learning". In: *Adaptive Computation and Machine Learning*. Ed. by Thomas Dietterich. Cambridge, MA: MIT Press, 2006.

[178] Andrew Gelman et al. *Bayesian Data Analysis*. 3rd ed. Texts in Statistical Science. London: Chapman and Hall, 2013.

[179] David JC MacKay and David JC Mac Kay. *Information theory, inference and learning algorithms*. Cambridge university press, 2003.

[180] Mark W Woolrich and Timothy E J Behrens. "Variational bayes inference of spatial mixture models for segmentation". In: *IEEE Transactions on Medical Imaging* 25.10 (2006), pp. 1380–1391.

[181] Adrian R Groves, Michael A Chappell, and Mark W Woolrich. "Combined spatial and non-spatial prior for inference on MRI time-series". In: *NeuroImage* 45 (2009), pp. 795–809.

[182] Michael A Chappell, Adrian R Groves, and Mark W Woolrich. "The FMRIB Variational Bayes Tutorial: Variational Bayesian inference for a non-linear forward model". In: *FMRIB Analysis Group Technical Reports* 8 (2008), pp. 2–6.

[183] Adrian R Groves. "Bayesian Learning Methods for Modelling Functional MRI". D.Phil Thesis. Oxford: University of Oxford, Dec. 2009.

[184] Michael A Chappell. "Bayesian Inference for (Neuro) Imaging. Bayesian Inference in MRI". In: *Proceedings of the 27th Annual Meeting of the International Society for Magnetic Resonance in Medicine*. ISMRM. Montreal, QC, 2019.

[185] T Bayes. "An Essay towards solving a Problem in the Doctrine of Chances". With annots. by R Price. In: *Philosophical Transactions of the Royal Society of London* 53 (1763), pp. 370–418.

[186] Harold Jeffreys. "Some Tests of Significance, Treated by the Theory of Probability". In: *Mathematical Proceedings of the Cambridge Philosophical Society* 31.2 (1935), pp. 203–222.

[187] Harold Jeffreys. *Theory of Probability*. 3rd ed. Oxford: Oxford University Press, 1961.

[188] Michael Lavine and Mark J Schervish. "Bayes Factors: What They are and What They are Not". In: *The American Statistician* 53.2 (1999), pp. 119–122.

[189] Robert E Kass and Adrian E Raftery. "Bayes factors". In: *Journal of the American Statistical Association* 90.430 (1995), p. 773.

[190] Gideon Schwarz. "Estimating the Dimension of a Model". In: *The Annals of Statistics* 6.2 (1978), pp. 461–464.

[191] David J C MacKay. "Probable networks and plausible predictions - a review of practical Bayesian methods for supervised neural networks". In: *Network: Computation in Neural Systems* 6.3 (1995), pp. 469–505.

[192] William D Penny, Nelson J Trujillo-Barreto, and Karl J Friston. "Bayesian fMRI time series analysis with spatial priors". In: *NeuroImage* (2005).

[193] Christopher M Bishop. "Variational principal components". In: *Proc. International Conference on Artificial Neural Networks* 9 (2005), pp. 509–514.

[194] Karl J Friston. "Bayesian Estimation of Dynamical Systems: An Application to fMRI". In: *NeuroImage* (2002).

[195] Robert E Kass and Duane Steffey. "Approximate Bayesian Inference in Conditionally Independent Hierarchical Models (Parametric Empirical Bayes Models)". In: *Journal of the American Statistical Association* 84.407 (1989), pp. 717–726.

[196] N Metropolis et al. "Equations of state calculations by fast computing machines". In: *Journal of Chemical Physics* 21.21 (1953), pp. 1087–1092.

[197] W K Hastings. "Monte Carlo Sampling Methods Using Markov Chains and Their Applications". In: *Biometrika* 57.1 (1970), pp. 97–109.

[198] Siddhartha Chib and Edward Greenberg. "Understanding the Metropolis-Hastings Algorithm". In: *The American Statistician* 49.4 (1995), pp. 327–335.

[199] Steve Brooks et al. *Handbook of Markov Chain Monte Carlo*. CRC press, 2011.

[200] Anders Eklund, Martin A Lindquist, and Mattias Villani. "A Bayesian heteroscedastic GLM with application to fMRI data with motion spikes". In: *NeuroImage* 155.April (2017), pp. 354–369.

[201] M J Beal. "Variational Algorithms for Approximate Bayesian Inference". PhD Thesis. Gatsby Computational Neuroscience Unit: University College London, 2003.

[202] Karl J Friston and Klaas E Stephan. "Free-energy and the brain". In: *Synthese* 159.3 (2007), pp. 417–458.

[203] Karl J Friston. "The free-energy principle: a rough guide to the brain?" In: *Trends in Cognitive Sciences* 13.7 (2009), pp. 293–301.

[204] William D Penny. "Comparing dynamic causal models using AIC, BIC and free energy". In: *NeuroImage* 59.1 (2012), pp. 319–330.

[205] Y. Zhang, M. Brady, and S. Smith. "Segmentation of Brain MR Images Through a Hidden Markov Random Field Model and the Expectation-Maximization Algorithm". In: *IEEE Transactions on Medical Imaging* 20.1 (2001), pp. 45–57. URL: `https://github.com/tanyanair/HMRF-EM`.

[206] Xiaojin Zhu, John Lafferty, and Zoubin Ghahramani. "Semi-Supervised Learning: From Gaussian Fields to Gaussian Processes". In: *Carnegie Mellon University Technical Reports* 3.175 (2003), pp. 1–19.

[207] Karl J Friston et al. "Classical and Bayesian Inference in Neuroimage: Theory". In: *NeuroImage* 16.2 (2002), pp. 465–483.

[208] William D Penny, Stefan J Kiebel, and Karl J Friston. "Variational Bayesian inference for fMRI time series". In: *NeuroImage* 19.3 (2003), pp. 727–741.

[209] Mark W Woolrich et al. "Fully Bayesian Spatio-Temporal Modeling of FMRI Data". In: *IEEE Transactions on Medical Imaging* (2004).

[210] Mark W Woolrich, Timothy E J Behrens, and Stephen M Smith. "Constrained linear basis sets for HRF modelling using Variational Bayes". In: *NeuroImage* 21.4 (2004), pp. 1748–1761.

[211] Peter Zeidman et al. "Bayesian population receptive field modelling". In: *NeuroImage* 180.9 (2017), pp. 173–187.

[212] Zhenfu Wen et al. "Grouped sparse Bayesian learning for voxel selection in multivoxel pattern analysis of fMRI data". In: *NeuroImage* 184.September 2018 (2018), pp. 417–430.

[213] Jalil Taghia et al. "Bayesian switching factor analysis for estimating time-varying functional connectivity in fMRI". In: *NeuroImage* 155.March (2017), pp. 271–290.

[214] Tian Dai and Ying Guo. "Predicting individual brain functional connectivity using a Bayesian hierarchical model". In: *NeuroImage* 147.November 2016 (2017), pp. 772–787.

[215] Per Sidén et al. "Fast Bayesian whole-brain fMRI analysis with spatial 3D priors". In: *NeuroImage* 146.June 2016 (2017), pp. 211–225.

[216] Quinten Collier et al. "Diffusion kurtosis imaging with free water elimination: A bayesian estimation approach". In: *Magnetic Resonance in Medicine* 80.2 (2018), pp. 802–813.

[217] Marco Reisert et al. "Disentangling micro from mesostructure by diffusion MRI: A Bayesian approach". In: *NeuroImage* 147.June 2016 (2017), pp. 964–975.

[218] Julio Acosta-Cabronero et al. "A robust multi-scale approach to quantitative susceptibility mapping". In: *NeuroImage* 183.February (2018), pp. 7–24. URL: `https://doi.org/10.1016/j.neuroimage.2018.07.065`.

[219] Oscar Gustafsson et al. "Impact of prior distributions and central tendency measures on Bayesian intravoxel incoherent motion model fitting". In: *Magnetic Resonance in Medicine* 79.3 (2018), pp. 1674–1683.

[220] Debra McGivney et al. "Bayesian estimation of multicomponent relaxation parameters in magnetic resonance fingerprinting". In: *Magnetic Resonance in Medicine* 80.1 (2018), pp. 159–170.

[221] P E Roland et al. "Does mental activity change the oxidative metabolism of the brain?" In: *Journal of neuroscience* 7.8 (1987), pp. 2373–89. URL: `http://www.ncbi.nlm.nih.gov/pubmed/3612246`.

[222] G Marchal, P Rioux, and M C Petit-Taboue. "Regional cerebral oxygen consumption, blood flow, and blood volume in healthy human aging". In: *Archives of Neurology* 49 (1992), pp. 1013–1020.

[223] Diana Nicoll et al. *Pocket Guide to Diagnostic Tests*. 6th ed. New York: McGraw-Hill, 2012.

[224] R Fahraeus and T Lindqvist. "The viscosity of the blood in narrow capillary tubes". In: *American Journal of Physiology* 96 (1931), pp. 562–568.

[225] Fernando Calamante et al. “A novel approach to measure local cerebral haematocrit using MRI”. In: *Journal of Cerebral Blood Flow and Metabolism* 36.4 (2016), pp. 768–780.

[226] Fumihiko Sakai et al. “Regional cerebral blood volume and hematocrit measured in normal human volunteers by single-photon emission computed tomography”. In: *Journal of Cerebral Blood Flow and Metabolism* 5.2 (1985), pp. 207–213.

[227] John P Mugler and James R Brookeman. “Three-dimensional magnetization-prepared rapid gradient-echo imaging (3D MP RAGE)”. In: *Magnetic Resonance in Medicine* 15.1 (1990), pp. 152–157.

[228] Mark Jenkinson et al. “Fsl”. In: *NeuroImage* 62.2 (2012), pp. 782–790. URL: `https://linkinghub.elsevier.com/retrieve/pii/S1053811911010603`.

[229] Mark Jenkinson et al. “Improved optimization for the robust and accurate linear registration and motion correction of brain images”. In: *NeuroImage* 17.2 (2002), pp. 825–841. arXiv: `arXiv:1011.1669v3`.

[230] Elias Kellner et al. “Gibbs-ringing artifact removal based on local subvoxel-shifts”. In: *Magnetic Resonance in Medicine* 76.5 (2016), pp. 1574–1581.

[231] Stephen M Smith. “Fast robust automated brain extraction.” In: *Human brain mapping* 17.3 (2002), pp. 143–55. URL: `http://www.ncbi.nlm.nih.gov/pubmed/12391568`.

[232] Mark Jenkinson and Stephen M Smith. “A global optimisation method for robust affine registration of brain images”. In: *Medical Image Analysis* 5.2 (2001), pp. 143–156.

[233] Thomas Christen et al. “MR vascular fingerprinting: A new approach to compute cerebral blood volume, mean vessel radius, and oxygenation maps in the human brain”. In: *NeuroImage* 89 (2014), pp. 262–270.

[234] Nicholas P Blockley et al. “An analysis of the use of hyperoxia for measuring venous cerebral blood volume: comparison of the existing method with a new analysis approach”. In: *Neuroimage* 72 (2013), pp. 33–40.

[235] Michael A Chappell et al. “Partial volume correction of multiple inversion time arterial spin labeling MRI data”. In: *Magnetic Resonance in Medicine* 65.4 (2011), pp. 1173–1183. URL: `http://doi.wiley.com/10.1002/mrm.22641`.

[236] Norihiko Fujita et al. “Quantitative mapping of cerebral deoxyhemoglobin content using MR imaging”. In: *NeuroImage* 20.4 (2003), pp. 2071–2083.

[237] Kenneth P. Whittall et al. “In vivo measurement of T2 distributions and water contents in normal human brain”. In: *Magnetic Resonance in Medicine* 37.1 (1997), pp. 34–43.

[238] Janaka P Wansapura et al. “NMR relaxation times in the human brain at 3.0 Tesla”. In: *Journal of Magnetic Resonance Imaging* 9.4 (1999), pp. 531–538.

[239] Qin Qin. "A simple approach for three-dimensional mapping of baseline cerebrospinal fluid volume fraction". In: *Magnetic Resonance in Medicine* 65.2 (2011), pp. 385–391.

[240] T Ernst, R Kreis, and B D Ross. "Absolute Quantitation of Water and Metabolites in the Human Brain. I. Compartments and Water". In: *Journal of Magnetic Resonance, Series B* 102.1 (1993), pp. 1–8.

[241] Hanzhang Lu et al. "Routine clinical brain MRI sequences for use at 3.0 tesla". In: *Journal of Magnetic Resonance Imaging* 22.1 (2005), pp. 13–22.

[242] Stuart Clare and Peter Jezzard. "Rapid T(1) mapping using multislice echo planar imaging." In: *Magnetic Resonance in Medicine* 45.4 (2001), pp. 630–634.

[243] Greg J Stanisz et al. "T1, T2 relaxation and magnetization transfer in tissue at 3T". In: *Magnetic Resonance in Medicine* 54.3 (2005), pp. 507–512. arXiv: NIHMS150003.

[244] Neil Gelman et al. "Interregional Variation of Longitudinal Relaxation Rates in Human Brain at 3.0 T: Relation to Estimated Iron and Water Contents". In: *Magnetic Resonance in Medicine* 45 (2001), pp. 71–79.

[245] Thomas Ethofer et al. "Comparison of longitudinal metabolite relaxation times in different regions of the human brain at 1.5 and 3 Tesla". In: *Magnetic Resonance in Medicine* 50.6 (2003), pp. 1296–1301.

[246] Andreas Saleh et al. "In vivo MRI of brain inflammation in human ischaemic stroke". In: *Brain* 127.7 (2004), pp. 1670–1677.

[247] J.A. Jones et al. "Optimal Sampling Strategies for the Measurement of Spin–Spin Relaxation Times". In: *Journal of Magnetic Resonance, Series B* 113.1 (Oct. 1996), pp. 25–34. URL: https://www.sciencedirect.com/science/article/pii/S106418669690151X?via%7B%5C%%7D3Dihub.

[248] R I Shrager, G H Weiss, and R G S Spencer. "Optimal time spacings for T2 measurements: Monoexponential and biexponential systems". In: *NMR in Biomedicine* 11.6 (1998), pp. 297–305.

[249] Adrienne N Dula, Daniel F Gochberg, and Mark D Does. "Optimal Echo Spacing for Multi-Echo Imaging Measurements of Bi-exponential T2 Relaxation". In: *Journal of Magnetic Resonance* 196.2 (2009), pp. 149–156.

[250] Kelly H Zou et al. "Statistical Validation of Image Segmentation Quality Based on a Spatial Overlap Index". In: *Academic Radiology* 11.2 (2004), pp. 178–189.

[251] Jesper L R Andersson, Stefan Skare, and John Ashburner. "How to correct susceptibility distortions in spin-echo echo-planar images: Application to diffusion tensor imaging". In: *NeuroImage* 20.2 (2003), pp. 870–888.

[252] Xialing Ulrich and Dmitriy A. Yablonskiy. "Separation of cellular and BOLD contributions to T2 signal relaxation". In: *Magnetic Resonance in Medicine* 75.2 (Feb. 2016), pp. 606–615. URL: http://doi.wiley.com/10.1002/mrm.25610.

[253] Pierre Gillis and Seymour H Koenig. "Transverse Relaxation of Solvent Protons Induced by Magnetized Spheres". In: *Magnetic Resonance in Medicine* 345.5 (1987), pp. 323–345.

[254] Thomas Christen et al. "Quantitative MR estimates of blood oxygenation based on T 2*: A numerical study of the impact of model assumptions". In: *Magnetic Resonance in Medicine* 67.5 (2012), pp. 1458–1468.

[255] B J Bain, S M Lewis, and I Bates. "Basic haematological techniques". In: *Dacie and Lewis Practical Haematology*. Ed. by S M Bates. 10th ed. Philadelphia: Churchill Livingstone, 2006. Chap. 3.

[256] Katrin A Rempp et al. "Quantification of Regional Cerebral Blood Flow and Volume with DSC". In: *Radiology* 193 (1994), pp. 637–641.

[257] Maithili Sharan et al. "A Compartmental Model for Oxygen Transport in Brain Microcirculation". In: *Annals of Biomedical Engineering* 17.1 (1989), pp. 13–38.

[258] Thies H Jochimsen et al. "Whole-brain mapping of venous vessel size in humans using the hypercapnia-induced BOLD effect". In: *NeuroImage* 51.2 (2010), pp. 765–774. URL: `http://dx.doi.org/10.1016/j.neuroimage.2010.02.037`.

[259] Michael A. Germuska, James A. Meakin, and Daniel P. Bulte. "The influence of noise on BOLD-mediated vessel size imaging analysis methods". In: *Journal of Cerebral Blood Flow and Metabolism* 33.12 (2013), pp. 1857–1863.

[260] Frederic Lauwers et al. "Morphometry of the human cerebral cortex microcirculation: General characteristics and space-related profiles". In: *NeuroImage* 39.3 (2008), pp. 936–948.

[261] D Le Bihan, R Turner, and N Patronas. "Diffusion". In: *Diffusion and Perfusion Magnetic Resonance Imaging: Applications to Functional MRI*. Ed. by D Le Bihan. New York: Raven Press, 1995.

[262] Lisbeth Rohl et al. "Viability thresholds of ischemic penumbra of hyperacute stroke defined by perfusion-weighted MRI and apparent diffusion coefficient". In: *Stroke* 32.5 (2001), pp. 1140–1146.

[263] George W Harston et al. "Quantification of serial cerebral blood flow in acute stroke using arterial spin labeling". In: *Stroke* 48.1 (2016), pp. 123–130.

[264] George W. J. Harston et al. "Optimizing image registration and infarct definition in stroke research". In: *Annals of Clinical and Translational Neurology* 4.3 (2017), pp. 166–174.

[265] Archana Purushotham et al. "Apparent diffusion coefficient threshold for delineation of ischemic core". In: *International Journal of Stroke* 10.3 (2015), pp. 348–353.

[266] George WJ Harston et al. "Identifying the ischaemic penumbra using pH-weighted magnetic resonance imaging". In: *Brain* 138.1 (2014), pp. 36–42.

[267] Francis Cassot et al. "A novel three-dimensional computer-assisted method for a quantitative study of microvascular networks of the human cerebral cortex". In: *Microcirculation* 13.1 (2006), pp. 1–18.

[268] Bruno Weber et al. "The microvascular system of the striate and extrastriate visual cortex of the macaque". In: *Cerebral Cortex* 18.10 (2008), pp. 2318–2330.

[269] Kamil Uludag and Pablo Blinder. "Linking brain vascular physiology to hemodynamic response in ultra-high field MRI". In: *NeuroImage* 168.2 (2018), pp. 279–295.

[270] Sriranga Kashyap et al. "Impact of acquisition and analysis strategies on cortical depth-dependent fMRI". In: *NeuroImage* 168.5 (2018), pp. 332–344.

[271] A. Reci, A. J. Sederman, and L. F. Gladden. "Optimising magnetic resonance sampling patterns for parametric characterisation". In: *Journal of Magnetic Resonance* 294 (2018), pp. 35–43. URL: `https://doi.org/10.1016/j.jmr.2018.06.010`.

[272] Chengyan Wang et al. "Simultaneous dynamic R2 R2, and R2 measurement using periodic $\pi$ pulse shifting multiecho asymmetric spin echo sequence moving estimation strategy: A feasibility study for lower extremity muscle". In: *Magnetic Resonance in Medicine* 77.2 (2016), pp. 766–773.

[273] Chengyan Wang et al. "Evaluation of renal oxygenation change under the influence of carbogen breathing using a dynamic R2, R2 and R2* quantification approach". In: *NMR in Biomedicine* 29.11 (2016), pp. 1601–1607.